uOttawa

Exploring Cadmium Sulfide as a Catalyst for the Solvent-Free Conversion of Benzyl Alcohol and 2-Phenoxy-1-Phenylethanol as Model Lignin Derivatives

Kusuma Virginna Adiningtyas

Thesis submitted to the University of Ottawa

in partial fulfilment of the requirements for the

Master of Science degree in Chemistry

Department of Chemistry and Biomolecular Sciences

Faculty of Science

University of Ottawa

Abstract

Concerns about fossil fuel depletion and environmental impact have led to exploring biomass as an energy source and feedstock for value-added chemicals. Lignin, a heterogeneous polymer and an abundant component of lignocellulosic biomass is a byproduct of the papermaking industry commonly burned as raw fuel. The underutilization of lignin stems from its highly aromatic structure and large size, making it challenging to break down and convert to more useful products. To that end, current research has focused on lignin valorization using various catalytic systems. Cadmium sulfide (CdS), a direct band gap semiconductor, is a promising catalyst due to its facile synthesis and favorable properties. The versatility of CdS nanoparticles (NPs) has been demonstrated in studies for applications such as carbon dioxide (CO_2) reduction, hydrogen evolution reactions (HERs) through water splitting, and the decomposition of organic molecules, which include lignin model molecules such as 2-phenoxy-1-phenylethanol (PP-ol). While photocatalytic and electrocatalytic activity of CdS is well-described, unlike other metal sulfides little is known about its thermocatalytic activity.

This Thesis highlights the synthesis of CdS NPs of various crystalline phases and their characterization by X-ray diffraction (XRD), transmission electron microscopy (TEM), and Brunauer-Emmett-Teller (BET) surface area measurements. Ultraviolet and visible light (UV-vis) absorption and attenuated total reflection infrared (ATR-IR) spectra, as well as scanning electron microscopy (SEM) and energy-dispersive X-ray spectroscopy (EDS) measurements were also obtained for some select CdS NPs. The synthesized CdS NPs were used in a series of substrate conversion experiments, with benzyl alcohol and PP-ol as the probed model molecules. The resulting products of conversion were characterized by gas chromatography-mass spectrometry (GC-MS). Through experiments, the difference in catalyst morphology was found to affect photocatalytic activity in UV-assisted PP-ol conversion. In the series of solvent-free experiments employing select CdS NPs, we have demonstrated, for the first time, the catalytic activity of CdS NPs in the conversion

of benzyl alcohol and PP-ol at high temperatures in the dark, and at mild temperatures under UV or visible light irradiation.

More importantly, in the thermal reactions, we have showcased the formation of products through potentially distinct reaction pathways that were not observed under photocatalytic conditions, some of which have not been reported in literature. As the substrate conversions were successfully conducted under solvent-free and inert atmosphere conditions, we have demonstrated that these substrate conversions on CdS are solvent-independent and can take place without external gas. In other words, no air, oxygen (O_2), or hydrogen (H_2) atmosphere was necessary to drive the reactions. These conditions offer significant advantages in future heterogeneous catalysis applications. Where CdS contributions in thermal decomposition reactions have been overlooked, the preliminary results obtained and discussed in this Thesis help fill the existing knowledge gap on this subject and expand the potential use of CdS beyond typical photocatalytic and electrocatalytic applications.

Keywords: cadmium sulfide, lignin valorisation, heterogeneous catalysis, photocatalysis, solvent-free catalysis, benzyl alcohol, 2-phenoxy-1-phenylethanol

Acknowledgements

First and foremost, my most sincere and deepest gratitude to my supervisor Dr. Javier Giorgi. This Thesis would not exist if you had not let me pursue my graduate studies in your lab! I am eternally grateful for your guidance, insight, endless patience, and all the academic and professional support over the years.

Naturally, a substantial part of my work would not have been possible without the expertise and help of my TAC members. I would like to thank Dr. Paul Mayer, who is a member of my TAC and was my temporary, unofficial "co-supervisor" for a short amount of time and who granted me independent access to his lab and facilities, which proved to be vital in the completion of my work. I'd also like to extend my gratitude to Dr. Eva Hemmer, another member of my TAC, who also provided me access to her group's equipment. More importantly, she instilled my knowledge of the nanoparticle world in my undergraduate days, which continued to be valuable during my graduate studies.

I would like to acknowledge and thank the following people: Dr. Sharon Curtis for her training and guidance with the GC-MS, Dr. Jeffrey Ovens for the XRD training, Dr. Yun Liu for acquiring SEM and TEM pictures, and Dr. Wendy Pell for access to the undergraduate lab.

Bien sûr, merci maman et papa. Without their love and support, all the opportunities that I've had in life thus far would have been out of my grasp.

To all my friends, labmates, and colleagues in the department, I'm so glad we've had the opportunity to connect, enjoy BBQ/coffee together, and exchange our experiences and hilarious TA stories.

Finally, to Nicholas, my anchor and the one who has had the [mis]fortune of dealing with me in my happy and sad days: thank you for your endless encouragement, support, and confidence in me.

Table of Contents

List of Figures

List of Schemes

List of Tables

List of Symbols and Abbreviations

Symbol/Abbreviation	Definition
$[M]^+$	molecular ion
Al_2O_3	aluminium oxide
Ar	argon gas
ATR-IR	attenuated total reflectance infrared
BET	Brunauer-Emmett-Teller
CdO	cadmium oxide
CdS	cadmium sulfide
CI	chemical ionization
CO_2	carbon dioxide
DC	direct current
DIBAL-H	diisobutylaluminium hydride
DRS	diffuse reflectance spectroscopy
DSC	differential scanning calorimetry
EDS	energy dispersive X-ray spectroscopy
e^-	electron
EI	electron ionization

ESI-MS	electrospray ionization mass spectrometry
FCC	face-centered cubic
GC	gas chromatography
GC-MS	gas chromatography-mass spectrometry
h^+	hole
H^+	proton
H_2	hydrogen gas
H_2O	water
H_2S	hydrogen sulfide
HCP	hexagonal close-packed
HDN	hydrodenitrogenation
HDO	hydrodeoxygenation
HDS	hydrodesulfurization
HER	hydrogen evolution reaction
HRTEM	high-resolution TEM
hν	photon energy
IR	infrared
LED	light-emitting diode
m/z	mass-to-charge ratio

MS	mass spectrometer
MSD	mass selective detector
NH_3	ammonia
NMR	nuclear magnetic resonance
NOx	nitrogen oxide
NP	nanoparticle
O_2	oxygen gas
OER	oxygen evolution reaction
PDF	powder diffraction file
POP	persistent organic pollutant
PP-ol	2-phenoxy-1-phenylethanol
PP-one	2-phenoxy-1-phenylethanone
pXRD	powder X-ray diffraction
QD	quantum dot
QMS	quadrupole mass spectrometer
RF	radio frequency
scXRD	single crystal X-ray diffraction
SEM	scanning electron microscopy
SOx	sulfur oxide

SSA	specific surface area
TEM	transmission electron microscopy
TGA	thermogravimetric analysis
TMS	transition metal sulfides
TOF	time-of-flight
TPD	temperature-programmed desorption
UV	ultraviolet
UV-vis	ultraviolet-visible
vis	visible light
XPS	X-ray photoelectron spectroscopy
XRD	X-ray diffraction
·	radical
·+	radical cation
λ	wavelength

Statement of Contributions

I hereby declare that I am the sole author of this Thesis.

I performed all synthesis of cadmium sulfide nanoparticles (CdS NPs) as described in Chapters 3 and 4. Through modifications of known procedures, I have also developed a new methodology of obtaining CdS of different crystalline phases from the same precursor materials, through the optimization of synthesis conditions. This was described in Chapter 4 and Appendix F. I performed all the CdS-catalyzed conversion experiments of benzyl alcohol and 2-phenoxy-1-phenylethanol (PP-ol) as described in Chapters 3 and 4. I also designed the experimental procedures for the solvent-free experiments described in Chapter 4.

Regarding CdS characterization, I performed all the X-Ray diffraction (XRD) data collection and analysis, apart from Rietveld refinement on select samples, which was performed by Dr. Jeffrey Ovens. I performed all the Brunauer-Emmett-Teller (BET) surface area measurements after receiving training from Dr. Javier Giorgi. I prepared samples for transmission electron microscopy (TEM) and scanning electron microscopy (SEM) imaging. The TEM and SEM images themselves were collected by Dr. Yun Liu, which were then sent to me once obtained. In some cases, she also collected energy dispersive X-ray spectroscopy (EDS) data for some of the CdS NPs. I conducted the TEM particle size measurements myself. I performed the UV-vis absorption and attenuated total reflectance infrared (ATR-IR) measurements of CdS NPs.

Regarding the use of gas chromatography-mass spectrometry (GC-MS), I received training from Dr. Sharon Curtis to learn how to correctly prepare liquid samples for analysis, how to perform headspace sampling and analysis, and how to operate the instrument both for manual and automated sample injection, including troubleshooting common issues. Afterwards, I performed all the sample preparation, GC-MS experiments, and data analysis, which entails molecule identification and peak quantization, myself. This includes the generation of calibration curves of known compounds, as described in Chapter 2 and Appendix A, as well as the qualitative and quantitative analysis of benzyl alcohol and PP-ol conversion products, as described in Chapters 3 and 4.

Chapter 1. Introduction

1.1. Energy use and demand over the years: from fossil fuels to biomass

Energy demand has been steadily increasing over the years, driven by population growth, economic development, and lifestyle changes. In 2022, demand rose by 1.2% from the previous year, and as of 2023, energy demand is projected to grow by 0.7% yearly until 2030, continuously increasing until 2050.[1] For multiple decades, energy was primarily sourced from fossil fuels, which includes natural gas, oil, and coal. Renewable sources such as geothermal, solar, wind, hydro, and biomass have also been used in a supplementary fashion. As shown in Figure 1.1, in 2023 alone, fossil fuels satisfied over 81% of all global energy consumption.

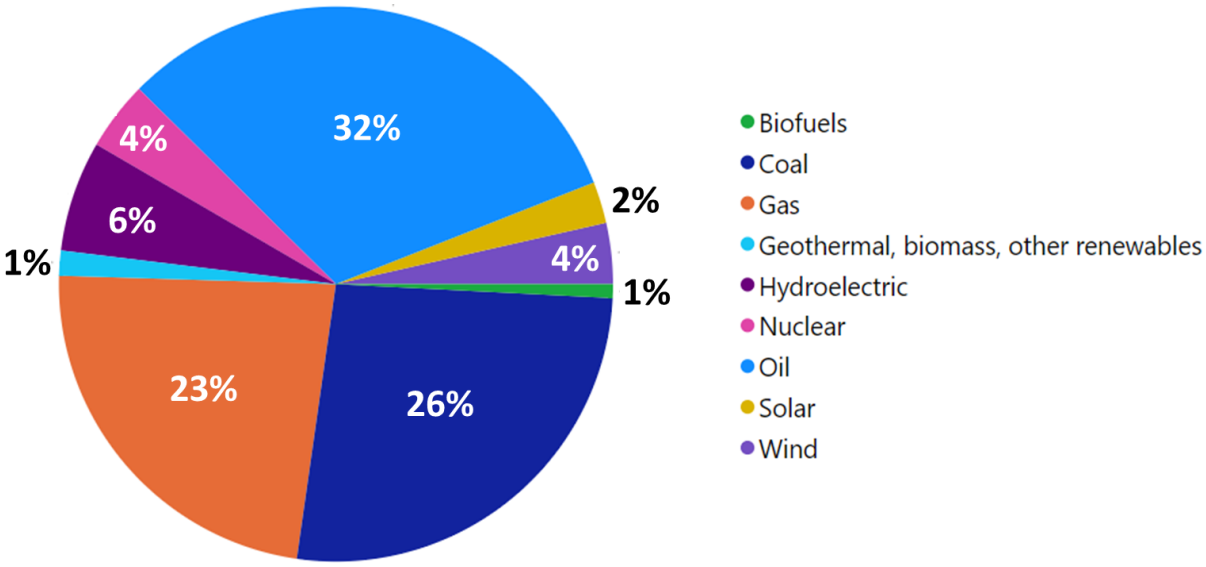

Figure 1.1. Global energy consumption by source, in 2023. Replotted from available data.[2]

Despite fossil fuels acting as the dominant energy source for many years, major concerns regarding their continued use have been raised over time. One important point is that fossil fuel reserves are currently depleting. As of 2020, coal, natural gas, and crude oil reserves are projected to last only for the next 139, 54, and 49 years, respectively.[3] This is problematic, considering fossil fuels require millions of years and harsh conditions to form and accumulate in significant amounts, thereby making it practically impossible

to replenish existing reserves. Incidentally, fossil fuels provide energy through combustion, but unfortunately do not burn cleanly and have played a major role in accelerating climate change, namely through excessive greenhouse gas (GHG) emissions.[4] All these potential problems have led to more research into exploiting sustainable energy sources. Among them is biomass, considered a viable candidate due to its abundance, renewability, flexibility in processing, and cleaner-burning properties.

1.2. Biomass

Biomass is a renewable energy source that refers to any organic matter derived from currently or recently living organisms. This includes plants and wood, along with agricultural and household waste. Because biomass is relatively easy to source and replenish naturally, either through the growth of new plants and fast-growing energy crops, or from other naturally occurring processes such as animal manure, it is considered a renewable source of energy. Furthermore, combustion of biomass remains less environmentally destructive than fossil fuel combustion,[5] in part due to the lower sulfur and nitrogen content in biomass relative to fossil fuels. Incorporation of biomass into a coal feedstock has been shown to reduce sulfur oxide (SO_x) and nitrogen oxide (NO_x) emissions.[6,7]

One of the most common forms of biomass energy is the direct burning of wood or other plant materials for heating, commonly referred to as “traditional biomass”. This has been used for centuries and continues to be used in many rural areas where access to other forms of energy is limited. Nonetheless, the combustion of raw biomass remains an inefficient process for energy generation. For this reason, there has been a shift toward employing “modern biomass” as an energy source. This consists of valorizing biomass sources to produce more energy-dense outputs, such as biofuels, that can be utilized as energy feedstock. While biomass valorization itself does require some energy and resource investment, the energy offset and overall sustainability of the process can be achieved by sourcing biomass from waste materials and bypassing the cultivation of energy crops, leading to net-zero emissions.[8]

1.2.1. Lignocellulosic biomass

Lignocellulosic biomass specifically refers to plant matter consisting of cellulose, hemicellulose, and lignin as its building blocks. Cellulose is the most abundant polymer found in plants and is a linear chain of glucose monomers that is structurally rigid due to the presence of hydroxyl groups in glucose forming hydrogen bonds with each other, allowing it to strengthen the primary cell wall of plants. In terms of use, it is the main feedstock for the paper, pulp, and textile industries, and has been explored for bioplastics, ethanol production, and biomedical applications.[5,9] On the other hand, hemicellulose is a shorter, branched chain of diverse saccharide monomers. Its current uses are limited to the production of xylose, which is a building block for xylitol, a sugar substitute, or other important platform chemicals, including furfurals. Like cellulose, it also has the potential to be used as feedstock for biofuels.[10] While the extraction, derivatization, and use of cellulose and hemicellulose have already been widely applied, lignin, another key polymer found in lignocellulosic biomass, remains severely underutilized.

1.3. Lignin

Lignin is a class of organic polymers found in lignocellulosic biomass that plays a significant role in the structural support of cell walls. It is second only to cellulose in terms of abundance, amounting to 30% of plant-derived polymers. The structure of lignin varies significantly in polymer size and composition of the sub-units, but a model structure can be represented as shown in Figure 1.2 along with representative linkages within it. Evidently, lignin is rich in aromatics and thus highly hydrophobic. As such, there is significant interest in extracting smaller aromatics to obtain more useful compounds.

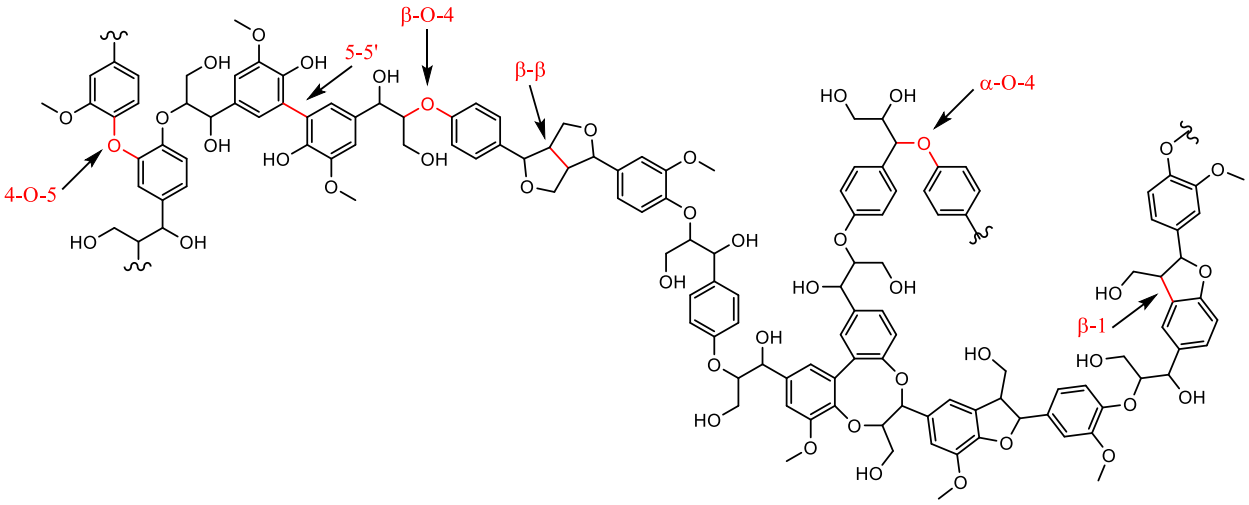

Figure 1.2. Structure of lignin with common linkages highlighted in red. Reproduced with permission from author.[11]

The lignin backbone is formed by cross-linking lignin-specific phenolic monomers called monolignols. These monomers are connected via ether bonds (e.g. α-O-4, 4-O-5, β-O-4) or carbon-carbon bonds (e.g. β-β, 5-5', β-1), as shown in Figure 1.2, with the β-O-4 linkage as the predominant form.[12] The monolignols primarily include the para-coumaryl, coniferyl, and sinapyl alcohols, depicted in Figure 1.3, and are often referred to by their associated aromatic moieties, 4-hydroxyphenyl (H), guaiacyl (G), and syringyl (S), respectively. The proportion of these subunits and their linkages varies depending on the plant species, ultimately leading to variations in lignin structure, properties, and chemistry.[13]

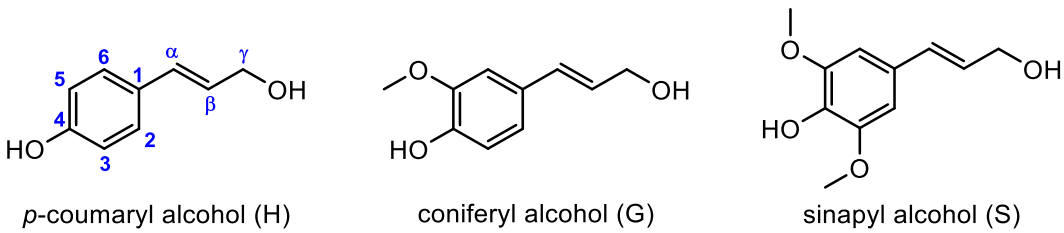

Figure 1.3. Structures of main monolignols in lignin, with annotated carbon atoms to illustrate linkage positions.

Historically, lignin has been considered a waste product of the paper and pulp industry, as it is a byproduct of the process of breaking down wood fibers to make paper and is commonly burnt in its raw state as fuel for pulp and fiber processing plants. However, at an industrial scale, lignin-derived vanillin also accounts for 15% of global vanillin production.[14–16] From an energy perspective, efforts are underway to exploit the

aromatic-rich structure of lignin and use it as a feedstock to produce value-added chemicals, particularly for biofuels and hydrocarbons, with the goal of converting low-grade, crude lignin to more efficient energy sources.[10] Lignin could also be chemically modified to produce other industrial chemicals and aromatic starting materials, which have many applications in the chemical industry. For example, lignin could be used to produce phenolic resins, which are used in the production of adhesives and insulation materials.[17]

The process of decomposing or depolymerizing lignin can be achieved through chemical,[18] bio-catalytic,[19,20] electrochemical,[21] and thermochemical methods,[12] among others.[22–24] Depending on the lignin source, the feedstock may be slightly different due to the variability of guaiacyl-to-syringyl ratios, and thus certain processes are preferred depending on the feedstock and intended product. Moreover, the surrounding conditions also play a role in the decomposition pathways of lignin. While biochemical systems have been well-studied, alternative methods that are more viable at an industrial scale are still being investigated.

1.4. Heterogeneous catalysis

Heterogeneous catalysis occurs when a catalyst and reactants are in different phases. Catalysis generally enables high reaction rates and selectivity. The use of heterogeneous catalysts, specifically in industry, is desirable as it eases the separation of reagents and products from the catalyst, which is important for recycling the catalyst, reducing operational costs, and allowing for less potential waste.[25]

One of the most important aspects of heterogeneous catalysis is the surface chemistry of the catalyst. Reactions occur on the catalyst surface; therefore, the properties of the surface play a critical role in determining the catalytic activity and selectivity, as any potential surface-to-molecule interactions are subject to modifications of the catalyst surface.[25]

Over the years, many types of materials have been used as heterogeneous catalysts. Metal catalysts such as nickel (Ni), platinum (Pt), palladium (Pd), or rhodium (Rh) are highly active and selective catalysts for a wide range of applications, such as the production of ammonia, syngas, methanol, and hydrogen.[26] They are also used in the refining of crude oil and the production of fuels such as gasoline and diesel.[27] The same

types of reactions, notably oxidation and acid-based reactions, can also be done using metal oxide catalysts, such as alumina, silica, or titania, which are often used as supports for metal catalysts, and zeolites.[26,28]

1.4.1. The use of metal sulfides in heterogeneous catalysis

Metal sulfides are a group of compounds that have been widely used or studied as catalysts for certain industrial processes such as hydrotreating.[29,30] However, metal sulfides are generally underutilized and understudied, particularly due to perceived complications with sulfur loss, making them intriguing catalysts for further exploration. Typically, these metal sulfides are supported on other materials such as aluminium oxide (Al_2O_3), but there has been an increasing interest in using unsupported metal sulfides. Typical metal sulfide catalysts are cobalt (Co), nickel (Ni), molybdenum (Mo), and tungsten (W)-based, particularly MoS_2 and CoMoS, however other transition metal sulfides (TMS) have also been explored.[26,31–37] Relevant reactions encompass hydrodesulfurization (HDS),[38–44] hydrodenitrogenation (HDN),[45–48] hydrodeoxygenation (HDO),[49,50] hydrogenation of aromatics,[43,51–53] in addition to hydrogen and oxygen evolution reactions (HERs and OERs, respectively).[54–62]

1.5. Cadmium sulfide (CdS)

1.5.1. Overview

Cadmium sulfide (CdS) is a direct band gap semiconductor with a bulk bandgap of 2.42 eV, one of the lowest among metal sulfides. The band gap is defined as the minimum energy required to excite an electron from the top of the valence band to the bottom of the conduction band. A band gap is said to be “direct” if the top (highest energy state) of the valence band possesses the same momentum as the bottom (lowest energy state) of the conduction band. Electrons can therefore transition between the valence and conduction bands through absorption and emission of photons, without needing any momentum change. This efficiency in light absorption and emission renders direct band gap semiconductors highly sought-after for applications in photovoltaic and optoelectronic devices.[63,64]

Historically, CdS was found in nature in greenockite and sphalerite ores, and the first reported synthesis of CdS occurred in the early 1800s, followed by its eventual popularization as a yellow pigment for paintings and commercial scale dyeing of plastics, glass, ceramics, lacquers, and inks.[65] In 1962, the semiconducting properties of CdS were finally exploited when it was used in the first CdS-based thin-film transistor.[66] Owing to its strong absorption coefficient, good electrical conductivity, and electron mobility,[67] as well as small band gap, CdS has since then been explored as a promising candidate for a variety of optoelectronic and sensing applications, such as photovoltaics and light-emitting diodes (LEDs), as well as radiation and gas sensors. In addition, CdS has been extensively studied for photocatalytic and electrochemical applications in the decomposition of volatile organic compounds (VOCs),[68] hydrogen evolution reactions (HER),[69,70] and carbon dioxide reduction.[68]

There are many methods of obtaining CdS in various size regimes and architectures. CdS nanoparticles (NPs) are of particular interest due to their higher surface area and overall tunability compared to bulk CdS. Reported synthesis methods include, but are not limited to, chemical precipitation,[71,72] solid-state reactions,[73,74] chemical deposition techniques,[75,76] sol-gel synthesis,[77] solvothermal synthesis,[78,79] and hydrothermal synthesis.[80–82] Depending on the chosen method of preparation, reaction conditions, and subsequent treatment, CdS NPs can exhibit phase purity and adopt only one specific crystalline structure. Alternatively, polycrystalline, or mixed phase CdS can also be obtained.

1.5.2. Crystalline phases

Under ambient pressure, CdS exists as two distinct polymorphs, zincblende and wurtzite. Figure 1.4 shows the unit cell of each of the polymorphs. As shown, zincblende CdS (CdS-zb) has a face-centered cubic (FCC) lattice, with each unit cell sharing a Cd^{2+} atom, while wurtzite CdS (CdS-wz) has a hexagonal close-packed (HCP) lattice. Henceforth, mentions of “cubic” and “hexagonal” CdS refer to zincblende and wurtzite CdS, respectively. Owing to the difference in atomic packing arrangements, zincblende CdS is metastable while hexagonal CdS is the thermodynamically stable polymorph. The latter is generally

obtained through high-temperature synthesis or by inducing a phase shift of cubic CdS through annealing. The cubic-to-hexagonal crystalline phase shift generally begins at annealing temperatures of 300°C.[75,83,84]

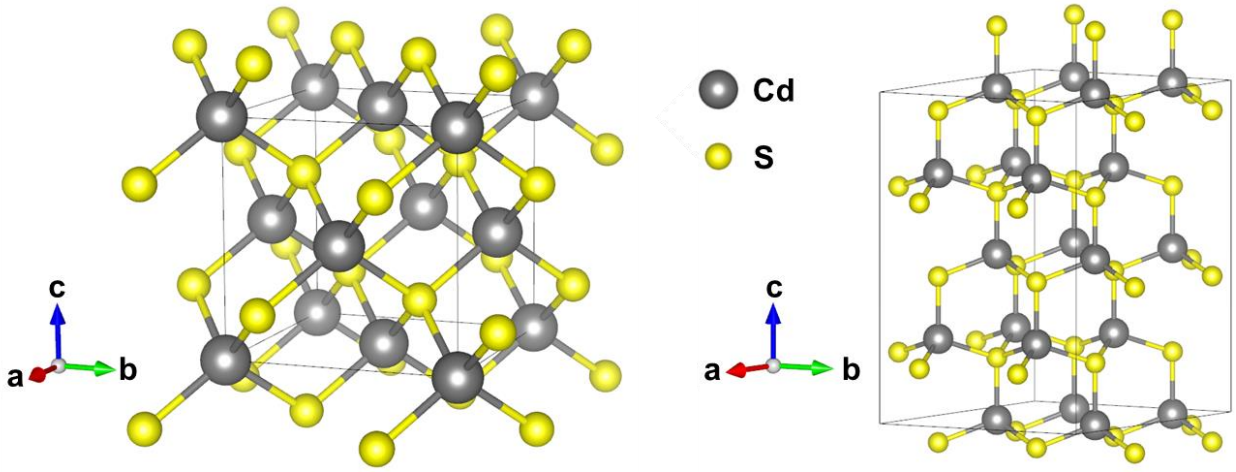

Figure 1.4. Unit cells of zincblende (left) and wurtzite (right) CdS, generated on VESTA using literature values.[85] Cadmium and sulfur atoms are drawn in gray and yellow, respectively.

While both unit cells have a 1:1 ratio of Cd^{2+} to S^{2-} bonded in a tetrahedral conformation, their orientation differs. In the cubic unit cell, the tetrahedral subunit is parallel to the (111) plane, while in the hexagonal unit cell, it is oriented along the (0001) plane. The CdS lattice parameters and relative Cd and S atom positions are outlined in Table 1.1.

Table 1.1. Structural information on the crystal lattices of cubic and hexagonal CdS.[85]

Crystal structure	**Crystalline phase**	**Space group**	**Lattice parameters (Å)**		**Bond angles (°)**		**Relative atom positions**
Zincblende	Cubic (FCC)	$F\bar{4}3m$	5.832	–	90	–	Cd (0, 0, 0) S (0.25, 0.25, 0.25)
Wurtzite	Hexagonal (HCP)	$P6_3mc$	4.130	6.703	90	120	Cd (0.333, 0.667, 0) S (0.667, 0.333, 0.875)

As a result of CdS polymorphism, different facets can form on the surface of the CdS catalyst and within. Each of these facets has varying surface energies, which dictate particle growth directions[86] and exposed facets.[86,87] The impact of surface energies and surface atoms on exposed facets is particularly important in the context of thermal decomposition, as they are highly dependent on catalyst-adsorbate interactions and some exposed facets preferentially facilitate the adsorption of certain molecules.[88] In the case of CdS as a photocatalyst, it is also known that specific facets preferentially attract specific charge carriers.[86] The formation of specific facets in CdS NPs is therefore a subject of interest; controlling crystalline phase, and by extension morphology, theoretically tunes reaction selectivity.

1.5.3. Band structures

As mentioned above, CdS has attracted significant attention due to the potential applications that arise because of its semiconducting properties. However, this requires an understanding of the band position and band structure of the catalyst itself. Often, band positions and band gaps are experimentally measured; cyclic voltammetry (CV) is commonly used to measure redox potentials, while diffuse reflectance spectroscopy (DRS) or UV-vis spectrophotometry can be employed to measure the optical properties of the material and calculate the band gap. Meanwhile, to elucidate the band structures of CdS, which gives more information on the energy levels within the material, theoretical approaches have been taken.[89–92] The band structures of both polymorphs are illustrated in Figure 1.5. Computational values of the band gaps vary according to the functionals used in the first principle calculations, with some functionals like LDA and PBE showing significant deviation from experimental values.[90] That said, close approximations to the bulk band gap value of 2.42 eV were made using DFT+U and PBE0 hybrid functionals. The direct band gap values, measured along the gamma point (Γ), were 2.45 eV (DFT+U) and 2.41 eV (PBE0) for CdS-zb, as well as 2.48 eV (DFT+U) and 2.47 eV (PBE0) for CdS-wz, respectively. Beyond the valence band maximum and conduction band minimum, the band structures show multiple energy states in CdS exist, although CdS-wz has more of these additional states than CdS-zb. Nonetheless, regardless of the

polymorph, the presence of additional energy states should allow other transitions to occur, provided that enough energy is supplied to and absorbed by the CdS catalyst.

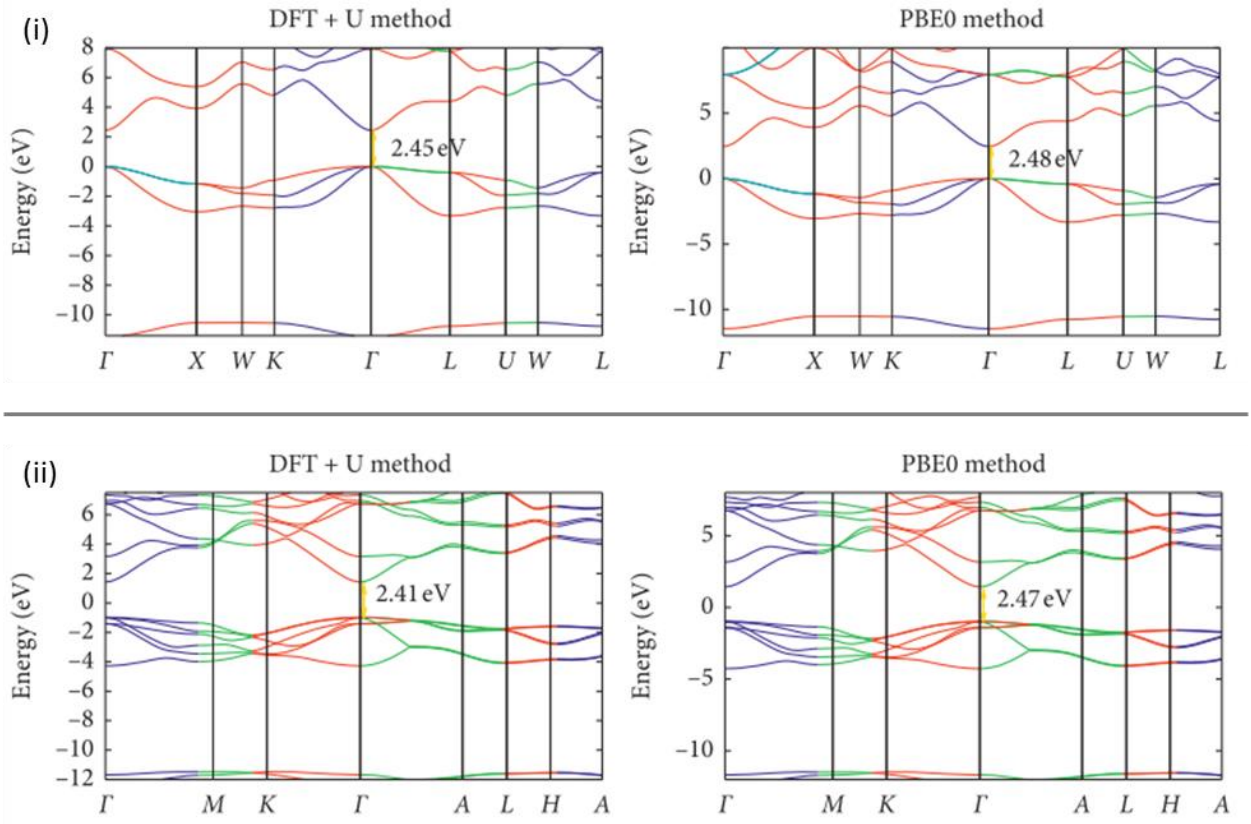

Figure 1.5. Band structure of (i) CdS-zb and (ii) CdS-wz along high symmetry points measured using the DFT+U and PBE0 methods. Adapted from literature under the terms of the Creative Commons Attribution License.[90]

1.6. Literature review: catalytic role of CdS in the conversion of lignin substructures

As a semiconducting material, native and composite CdS materials have been widely explored in the photocatalytic and photoelectrochemical degradation of persistent organic pollutants (POPs) in wastewater, which include organic dyes[76,93–95] and pharmaceuticals.[78,82,96–98] Some of these reactions occur concurrently with HERs, though this can be achieved through dedicated water-splitting reactions. Meanwhile, research in lignin valorization by means of heterogeneous catalysis has been a longstanding topical issue. This literature review focuses on recent advances using CdS as a catalyst for various organic reactions, in particular pertaining to lignin valorization. Other metal sulfide catalysts that have been studied for this purpose are also briefly discussed.

More relevant to this Thesis are current efforts in using CdS in the degradation of lignin and its derivatives. For a more fundamental insight, one should look at the decomposition of lignin model molecules on CdS, beginning with benzyl alcohol as the smallest reactive sub-unit. Indeed, in the last decade alone, tens of publications have been issued on this matter and various CdS-based catalysts have been studied as a photocatalyst for lignin degradation.[99,100,109,101–108] The consensus is that the main product of benzyl alcohol decomposition is benzaldehyde, with varying amounts of side products depending on the architecture and composition of the catalyst, reaction solvents used, and atmospheric conditions. It is generally agreed that decomposition occurs through oxidation via the initial activation of the benzylic C-H bond. Under photocatalytic conditions, CdS absorbs photons and generates electron-hole pairs. Hydrogen abstraction occurs on the benzylic C-H bond to generate a carbon-centered PhCH•OH radical. This species can either undergo further oxidation by photogenerated holes to produce benzaldehyde or can dimerize with another radical through C-C coupling to form hydrobenzoin, which can either desorb as-is, undergo further oxidation to benzoin or benzil, or undergo pinacol rearrangement to deoxybenzoin.

The role of CdS in the activation of C-H bonds has also been reported in the photocatalytic oxidation of toluene,[110–112] which takes place in the presence of oxygen (O_2) atmosphere or air. The general mechanism involves the generation of superoxide radicals ($O_2^{\bullet-}$) through O_2 reduction by photogenerated electrons. In

parallel, photogenerated holes abstract hydrogen from the methyl group to generate the benzyl radical, which reacts with O_2 or $O_2^{-\bullet}$ to form benzaldehyde as the main product. In 2021, Chai *et al.* reported the synthesis and use of CdS catalysts with cubic-hexagonal phase junctions that enhanced selective photocatalytic toluene oxidation. Meaningful toluene oxidation was only found under O_2 atmosphere or air; reactions under nitrogen (N_2) atmosphere resulted in a marginal 0.3% conversion of toluene. More importantly, obtaining an appropriate ratio of cubic and hexagonal CdS was essential to observe the intended increase in photocatalytic activity, and this was accomplished by adjusting the CdS synthesis temperature. Against the other CdS catalysts, the best performing CdS catalyst in this work had the highest surface area, intermediate optical band gap that still absorbed visible light, and an optimal cubic-hexagonal phase ratio that allowed the formation of a type-II junction and increased electron-hole separation efficiency. This work highlighted the importance of controlling the morphological features of the CdS catalysts, as well as the atmospheric conditions of the reaction system.

A similar oxidation pathway is observed when the complexity of the molecule of interest increases. In 2018, Wu *et al.* studied the photocatalytic decomposition of native lignin and various lignin model molecules, namely 2-phenoxy-1-phenylethanol (PP-ol), which is the simplest fragment containing the ubiquitous β-O-4 linkage, using CdS quantum dots (QDs) as a catalyst.[113] They have reported that the photodegradation of PP-ol proceeded via hole-induced oxidation of the benzylic C_α-H bond. They have confirmed that the presence of the C_α-H bond is necessary for the C_α-centered radical intermediate to form, as substituting this hydrogen for a methyl group resulted in no reactions. Further oxidation processes resulted in two competitive pathways; one that produced the ketone analogue of PP-ol, and another that formed acetophenone and the phenoxy anion through C_β-O bond cleavage, effectively breaking the β-O-4 bond. The produced anion was then protonated by abstracted hydrogen species to form phenol. A simplified diagram to represent the major reaction pathway can be seen in Figure 1.6. Their follow-up study in 2019 elucidated the effects of CdS surface ligands on reaction kinetics, specifically for solvated reactions.[114] Briefly, the authors demonstrated that the colloidal stability of catalysts in solution influences CdS contact

with PP-ol, with higher CdS dispersibility potentially enhancing photocatalytic efficiency by improving this contact. They also found that the ligand anchor group and length impact charge transfer from the CdS core to PP-ol. Namely, within the same type of ligands, surface ligands with shorter chain lengths increased charge transfer to PP-ol, increasing catalytic activity. In both selected works, the authors did not report any C-C coupling of intermediate radical species when benzyl alcohol was the probed molecule.

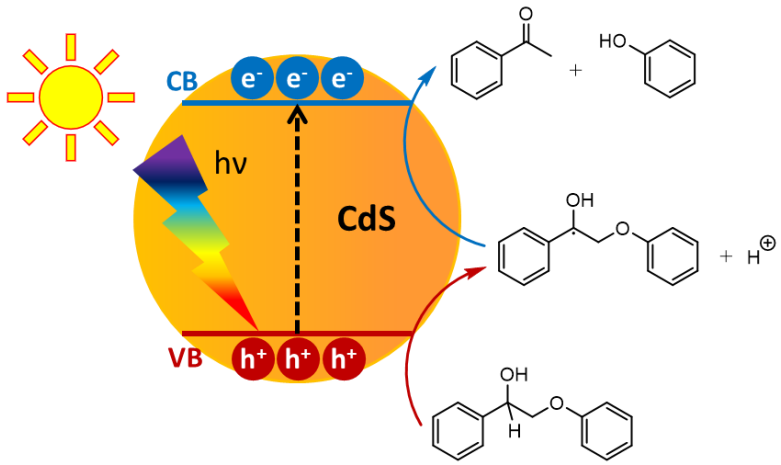

Figure 1.6. The CdS-catalyzed cleavage of the C_β-O bond in PP-ol through the generation of the C_α radical intermediate. Irradiation using visible light excites electrons from the valence band (VB) to the conduction band (CB), generating electron-hole pairs that participate in PP-ol decomposition.[113]

The activation of C(sp^3)-H bonds has been shown to not be a solvent-dependent process. In 2018, Firoozi *et al.* reported the CdS-catalyzed, photoinduced C-H bond activation of N,N-dimethylanilines or alkyl 2-(3,4-dihydroisoquinolin-2(1H)-yl)acetates as a starting step to coupling reactions.[115] The mechanism differs slightly from that of PP-ol due to the presence of nitrogen atoms in the molecules being studied. In each starting material, the nitrogen atom loses an electron to a photogenerated hole, and subsequent deprotonation occurs on the adjacent C(sp^3) atom, resulting in the formation of a C-centered radical, which was then reacted with maleimide, as well as N-aryl and N-alkyl maleimides. For N,N-dimethylanilines, condensation reactions with alkyl but-2-ynedioates and phenyl acetylenes were also explored. It was found that O_2, sourced from pure O_2 gas or air, was necessary for the reactions to occur and that the reactions involved radical species, since employing radical and hole scavengers yielded none of the target products.

To date, the thermal β-O-4 bond cleavage in lignin derivatives has been reported using metal sulfides other than CdS. In 2016, Zhang *et al.* reported the NiMo sulfide-catalyzed conversion of PP-ol under H_2 atmosphere and using methanol as a solvent.[116] The main pathway leading to β-O-4 bond cleavage was the initial dehydroxylation of PP-ol followed by hydrogenation. The main products of the reaction were phenol, along with styrene, ethylbenzene, and ethers resulting from decomposition of the parent reactant as well as reactions with the alcohol solvent. To note, when the reaction was conducted under inert atmosphere, only a conversion of 1% was observed, highlighting the necessity of H_2 to drive the reaction forward. In 2019, Liu *et al.* evaluated the performance of carbon-supported Co_3S_4, NiS, MoS_2, Co_3MoS_6, and $NiMoS_3$ for the hydrogenolysis of 2-(2-methoxyphenoxy)-1-phenylethanol.[117] The main product of the reaction was *o*-guaiacol, which was produced using all catalysts. Other products included ethylbenzene, styrene, benzaldehyde, phenylacetaldehyde, and benzyl mercaptan with varying selectivity depending on the catalyst. CoMo sulfides are very popular, and this material was explored again in 2020, when Song *et al.* reported the use of supported CoMo sulfide for the decomposition of various lignin-derived ethers through an HDO strategy. Under H_2 atmosphere, PP-ol decomposed to phenol, which partially converted to benzene, as well as 1-phenylethanol, which was fully converted to ethylbenzene.[118] Lastly, while ZnS is commonly studied in photocatalysis, in 2023, Guo *et al.* compared the performance of FeS, ZnS, and FeZnS-based catalysts in the thermal decomposition of 2-phenoxy-1-phenylethanone (PP-one).[119] The first pathway, which had a lower activation energy, was the β-O-4 bond cleavage to phenol, methyl benzoate, and methyl benzoylformate. The latter two products were observed as the reactions involved methanol as the solvent. The second pathway was the C_α-C_β bond cleavage to phenol and methyl benzoate. With the highlighted FeZnS/NC 650 catalyst, under N_2 atmosphere, conversion reached 44% with phenol as the main product, as well as methyl benzoate. In air, however, conversion increased to 99%, predominantly producing phenol, as well as smaller amounts of methyl benzoate and methyl benzoylformate, indicating that $O_2^{-\bullet}$ was formed and pushed the conversion of the starting PP-one, showcasing the importance of the reaction system's atmospheric conditions. To demonstrate the synergistic effects of FeS and ZnS sites, the same decomposition experiments were conducted using FeS/NC 650 and ZnS/NC 650, which showed slightly

lower conversion at around 61% and 64%, respectively. DFT calculations ultimately concluded that, in FeZnS/NC 650, O_2 and PP-one preferentially adsorbed on the FeS and ZnS sites, respectively, resulting in elevated PP-one conversion. It is worth considering that these synergistic effects of heterostructures would likely extend to CdS, as it is also a metal sulfide, and PP-ol because of the similarity of substrate structure.

Despite the important results and mechanistic insight these past studies have provided, to the best of our knowledge, the use of CdS as a catalyst in the thermal decomposition of lignin has not been reported. As a result, any distinction in decomposition or other surface reaction mechanisms, if any, between thermal and photocatalytic conditions remains unclear. Furthermore, there are currently no studies that investigate the interaction of lignin model molecules with CdS, through thermal or photocatalytic decomposition, under solvent-free (neat) conditions.

1.7. Objectives

Despite existing applications of cadmium sulfide as potential photocatalysts for lignin valorization, the use of pristine CdS as a catalyst in the thermal decomposition of lignin, to the best of our knowledge, remains unreported. As such, the main objective of this Thesis was to investigate the decomposition of lignin model molecules on CdS NPs under thermal conditions, generate a potential decomposition pathway, and compare the resulting products to photocatalysis products. The criteria for an appropriate catalyst in this case are a combination of high surface area, ideally leading to a higher number of adsorption sites, and a high number of active sites, particularly towards hydrogen abstraction or dehydrogenation of the target substrate.

1.7.1. Approach

Our approach to studying the decomposition of lignin model molecules on CdS focuses on the application of heterogeneous catalysis. The first step is the obtention of the catalysts. Solid CdS NPs were synthesized in-house using a variety of precipitation methods and characterized through various techniques. The rationale for using NPs is due to the higher surface-to-volume ratio relative to bulk CdS, which is a desirable property since this should increase the number of active sites on the catalyst surface. The surface

architecture of the NPs was indirectly controlled during the synthesis step by targeting specific crystalline phases, achieved by controlling reaction temperature to obtain cubic, hexagonal, and mixed phase CdS.

Next, lignin model molecules, illustrated in Figure 1.7, were selected for thermal catalysis experiments. Benzyl alcohol was chosen because previous photocatalysis studies have reported its decomposition on a CdS surface. 2-phenoxy-1-phenylethanol was chosen because it contains the β-O-4 linkage, ubiquitous in lignin and therefore of significant interest, and its photocatalytic decomposition has also been reported. In the thermal catalysis experiments, the lignin model molecules were introduced to the CdS catalysts in liquid or gas phase in a sealed system, followed by heating at specified temperatures and time.

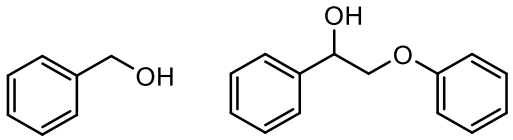

Figure 1.7. The two selected lignin model molecules: benzyl alcohol (left) and 2-phenoxy-1-phenylethanol (right).

Following the reactions, the products of decomposition of lignin model molecules under thermal conditions were characterized using gas chromatography-mass spectrometry (GC-MS) and compared to products obtained through photodecomposition. Because we were mainly interested in the surface-molecule interactions between the solid CdS and liquid/gaseous model molecules, the reactions were conducted under neat conditions to disregard solvent effects. In addition, solvent-free conditions are also ideal from the heterogeneous catalysis perspective; removing solvents from processes generates less potential waste and is more environmentally friendly. To note, some kinetics studies were done in solvated conditions under UV irradiation, employing different CdS catalysts to compare their photocatalytic activity and selectivity. This step also functioned as a screening step in choosing a specific CdS catalyst to use in the thermal catalysis experiments, under the assumption that reactivity trends would be comparable between neat and solvated conditions. Decomposition pathways were proposed through the identification of reaction products. The effect of catalyst crystalline phase on reactivity was also explored.

Chapter 2. Experimental and Theoretical Background

2.1. Synthesis of CdS nanoparticles (NPs)

2.1.1. Fundamentals of nanoparticle formation

Nanoparticles (NPs) are defined as particles with sizes in the nanometer range (between 1 to 100 nanometers). Due to their small size and large surface-to-volume ratio relative to bulk materials, they are of significant interest for catalysis.[120,121] Their preparations can be achieved through top-down and bottom-up approaches. In the top-down approach, bulk materials are physically broken down to the nanoscale, through methods like mechanical milling or nanolithography, among others.[122–124] In this work, however, a bottom-up approach was taken, in which NPs are synthesized from atomic or molecular precursors. This approach is achievable through various wet chemical methods, including but not limited to precipitation methods,[71,72] hydrothermal synthesis,[80,82] the sol-gel method,[77] or biosynthesis.[125]

There are multiple theories to explain the mechanisms of NP formation in a bottom-up approach. Broadly speaking however, these mechanisms involve two key steps: nucleation and growth. Nucleation is the process where free atoms or ions are produced and aggregate to form small clusters which act as nuclei, or "seeds" for larger crystals. Nucleation is followed by particle growth, which can occur because of the aggregation of the clusters, or individual atoms depositing on the surfaces of the seed. A subset of the latter growth process is Ostwald ripening, where larger particles grow at the expense of smaller particles that more readily redissolve in solution.[126] The bottom-up approach to NP formation has the added advantage of additional control on particle shape, size, and composition. Because the NPs are built atom by atom, reaction kinetics can be tailored to direct NP formation towards specific architectures. Furthermore, bottom-up approaches also enable the formation of NPs of uniform shapes, sizes, and distributions. Several parameters can be controlled in the synthesis of NPs, including but not limited to the choice of precursor materials and their concentrations, solvent, temperature, time, and the presence of stabilizing agents.

2.1.2. Effects of synthesis parameters

Because reaction parameters directly affect the nucleation and growth of particles, effective design of nanomaterials can be achieved by tuning NP synthesis conditions. The generation of atoms in solution depends on the choice of starting materials, as different precursors have different decomposition, dissociation, or reaction rates, which dictate nucleation and growth kinetics.[127,128] The solubility of the starting materials can also be altered by changing the solvent. More importantly, however, increasing concentration early in the synthesis step can lead to supersaturation, which is the driving force behind nucleation.[120,124,129] High temperatures increase the kinetic of nucleation typically leading to smaller NPs,[130] but faster kinetics can also cause excessive agglomeration if not controlled. That said, high temperatures drive reactions to form the thermodynamically stable product. Therefore, the formation of specific polymorphs and degree of crystallinity can be directed by tuning temperature.[128,131,132] Reducing reaction time can reduce aggregation but can also limit particle growth, resulting in smaller NPs. Lastly, surfactants, ligands, or stabilizing agents can be used to control particle size and prevent aggregation by forming a protective layer around the nanoparticles. They can also adsorb on specific facets, directing anisotropic growth which results in specific NP shapes.[126] Evidently, the interplay between different reaction parameters and their effects on NP synthesis can be complex, thus these parameters must be optimized to achieve desired results.

2.1.3. Synthesis methods

All CdS NPs synthesized in this work were prepared through various chemical precipitation methods. Chemical precipitation is straightforward, does not require any specialized equipment, and can relatively easily be scaled up. Throughout the course of the project, several different procedures were employed to synthesize CdS NPs of various shapes, sizes, and crystalline phases. Given the variety of procedures used throughout this work, the exact synthesis steps for each of these NPs will be further outlined in their respective Chapters.

2.2. Characterization techniques

This section provides an outline of all techniques mentioned throughout this work. However, only the techniques that were extensively used and the instruments directly operated by the Author of this work (as stated in the Statement of Contributions) are explained in detail.

2.2.1. Powder X-ray diffraction (pXRD)

2.2.1.1. Overview

X-ray diffraction (XRD) is a non-destructive technique used to determine the crystallinity of a solid sample under the principle that different crystalline structures diffract incident X-rays at specific angles. Single crystal X-ray diffraction (scXRD) is used to analyze single crystals, while powder X-ray diffraction (pXRD), represented in Figure 2.1, involves analyzing solid samples composed of many crystallites. Throughout this work, only the latter was used and is therefore the focus of this sub-chapter. Henceforth, any mention of XRD in subsequent chapters is used specifically to refer to pXRD.

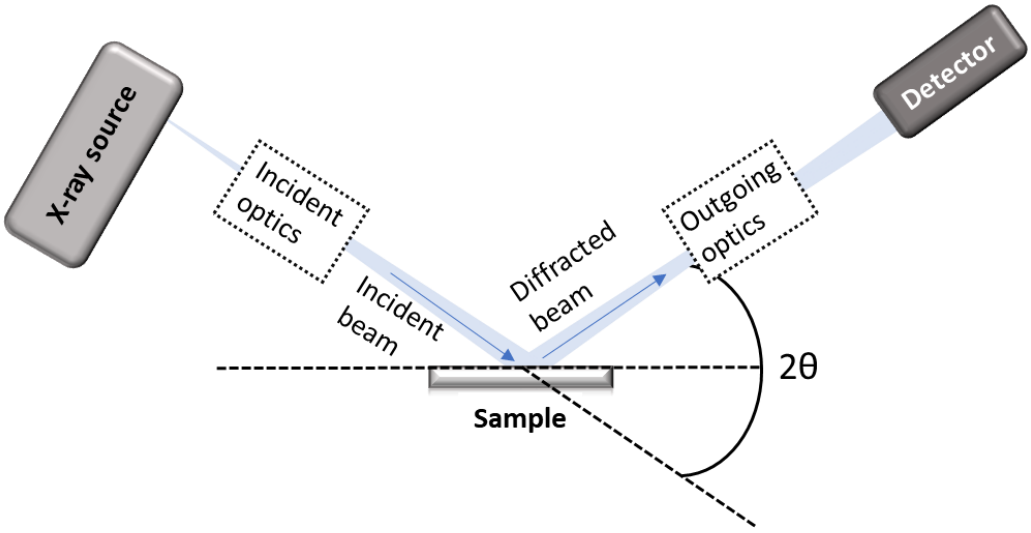

Figure 2.1. Simple visualization of pXRD setup.

In a typical X-ray diffraction setup pictured in Figure 2.1, the solid sample is mounted on a sample holder. An X-ray source is used to generate electromagnetic radiation since X-rays have the appropriate wavelength to probe interatomic distances. The X-ray beam hits atoms in the sample at an angle θ and gets diffracted

through a process of elastic scattering by the same angle. This phenomenon is described as Bragg's law, pictured in Figure 2.2, and Bragg's equation is defined by Equation **(1)** as:

$$n\lambda = 2d\sin\theta \quad \textbf{(1)}$$

where n is the diffraction order, λ is the wavelength of the incident beam, and d is the distance between each plane of the crystal lattice. 2dsinθ represents the total path difference between X-rays scattered by adjacent planes in the crystal. The intensities of these diffracted beams are plotted as a function of the detector angle (equal to 2θ), generating an XRD pattern corresponding to a specific crystalline structure of the analyzed sample. More specifically, this pattern illustrates the crystalline phase of the sample.[133]

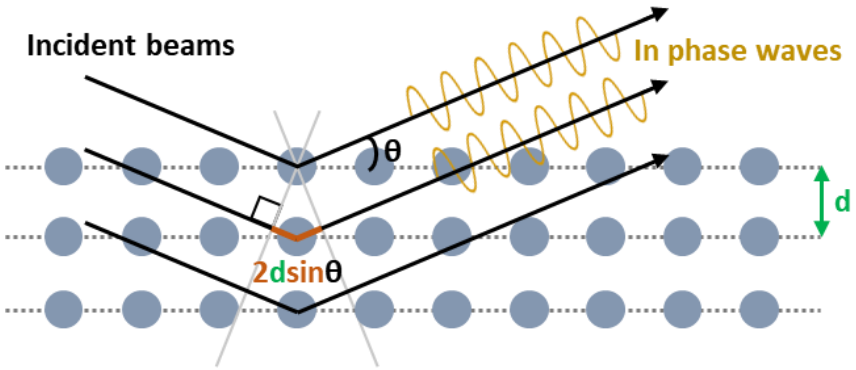

Figure 2.2. Visualization of Bragg's equation.[134]

It is worth noting that Bragg's condition needs to be satisfied for peaks to be observed in a diffractogram. This condition states that Bragg diffraction only occurs when the scattered beams are in phase with each other, achieved only through constructive interference. Diffracted beams that are out of phase experience destructive interference, and no diffraction peaks are recorded in the XRD pattern as a result.

In the specific case of pXRD, the powdered sample contains multiple crystals. Due to the random orientation of individual crystals, for a given probed plane, the incident X-ray beam may get diffracted in multiple directions. Only crystals oriented such that their planes satisfy the Bragg condition for the incident X-ray wavelength and angle will contribute to the diffraction peaks; crystals that do not meet this condition for a particular plane will not contribute to that diffraction peak. This also means that a statistically

significant number of crystals need to be present in the sample to contribute to diffraction peaks with an acceptable signal-to-noise ratio. From a technical perspective, rotating the sample can change the orientation of crystals relative to the incident beam, therefore increasing the number of probed planes that can exhibit Bragg diffraction and increase the peak intensity in the XRD pattern.

2.2.1.2. Analysis methods and parameters

pXRD patterns were recorded on all CdS samples for crystalline phase identification using a Rigaku Ultima IV diffractometer (Cu Kα, λ = 1.5401 Å) with a scan range (2θ) set from 20° to 80° at a scan speed of 1°/min and with a sample rotation speed of 30 rpm. The resulting experimental patterns were compared to Powder Diffraction Files (PDFs) obtained from the International Centre for Diffraction Data (ICDD) database for analysis.

2.2.2. Transmission electron microscopy (TEM)

TEM is a method of microscopy that employs a focused beam of electrons interacting with and transmitted through a thin sample. The image resulting from the beam-sample interaction is then focused onto an imaging device, allowing for atomic-level resolution imaging for structures at the nanoscale region.[121]

As stated in the Statement of Contributions, images of CdS nanoparticles were collected by Dr. Yun Liu, using an FEI Tecnai G2 Spirit Twin transmission electron microscope (TEM), or a JEOL JEM-2100F field-emission transmission electron microscope (FETEM). The nanoparticles were dispersed on a carbon film supported on a 300-mesh copper grid. Analysis of the collected TEM images was conducted by the Author, where a minimum of 100 particles per sample were measured against the provided scale bar using the ImageJ software to determine particle sizes and size distributions.

2.2.3. Brunauer–Emmett–Teller (BET) surface area measurements

2.2.3.1. Overview

The BET method is the standard method used to determine the specific surface area of a given solid material. It was first introduced in 1938 and works under the principle of measuring physical adsorption

(physisorption) of an inert gas (adsorbate) onto the surface of a solid sample.[135] Because the BET theory is an extension of the Langmuir theory, the following BET equation can be derived:

$$\frac{1}{W\left(\left({}^{P_0}/_{P}\right)-1\right)} = \frac{C-1}{W_m C}\left({}^{P}/_{P_0}\right) + \frac{1}{W_m C} \qquad \textbf{(2)}$$

where W is the mass of adsorbed gas at a relative pressure P/P_0, and W_m is the weight of one monolayer of adsorbed gas. C represents the BET constant and is proportional to the adsorption energy of the monolayer. In other words, C reflects the magnitude of adsorbent/adsorbate interactions.

A linear multipoint BET plot can be generated with a minimum of three data points, provided that the P/P_0 ratio lies between 0.05 and 0.35. Outside of this range, the linearity of the adsorption isotherm is no longer preserved. Using Equation **(2)** above, W_m can be calculated from the experimentally measured slope, m, and y-intercept of the line, b, with the rearranged equation, shown by Equation **(3)**, defined as:

$$W_m = \frac{1}{m+b} \qquad \textbf{(3)}$$

Knowing the mass of adsorbed gas that constitutes a monolayer, the total surface area of the sample, S_T, can be calculated using Equation **(4)**:

$$S_T = \frac{W_m N A_{CS}}{M} \quad \textbf{(4)}$$

where N represents Avogadro's number (6.022×10^{23}), A_{CS} is the cross-section of the adsorbate gas (in the case of nitrogen, this value is equal to 16.2 $Å^2$), and M is the molar mass of the adsorbate (28.02 g/mol for nitrogen gas). The specific surface area, S, is then calculated by dividing the total surface area by the mass of the solid sample.

2.2.3.2. Analysis methods and parameters

The BET surface areas of CdS samples were measured using a Quantachrome Autosorb-1 Analyzer. Some samples were omitted from these measurements due to low synthesis yield; for reliable measurements, a minimum quantity of 75.0 mg of solid was required for each surface area measurement. CdS solids were

finely ground and loaded into a 9mm quartz sample cell and outgassed at 100°C for five hours or until the outgassing test showed a gas flow below 30 microns per second. After sufficient outgassing, three-point BET measurements were taken relative to a blank P_0 cell using the pre-set Physisorption Analysis program of the instrument's corresponding Quantachrome analysis software. Nitrogen (N_2) was used as the adsorbate gas and a temperature of 77K was maintained, achieved by submerging the two cells in liquid nitrogen contained by a Dewar. The final specific surface areas (in m^2/g) of analyzed samples were recorded.

2.2.4. Gas chromatography-mass spectrometry (GC-MS)

2.2.4.1. Principles of gas chromatography (GC)

Gas chromatography (GC) is a chromatography technique for volatile substances that employs a mobile and stationary phase (the carrier gas and the column, respectively) to separate various compounds in a sample. In a typical setup, as shown in Figure 2.3, a gaseous or liquid sample is injected into an inlet and vaporized. This vaporized sample is then carried to the column by a carrier gas, whose flow can be controlled. The carrier gas is normally an inert gas such as nitrogen, hydrogen, helium, or argon, though the use of the latter two gasses has become less popular with their increasing prices over the years. As the gas carries the vaporized sample, it passes through the column, whose temperature is controlled by an oven. Depending on the nature of the compounds in the sample (volatility, polarity, etc.) and how they interact with the column, they exit the stationary phase at different times and are identified by a detector. A chromatograph then plots the detector response, proportional to the number of analytes in the sample, as a function of retention time. This plot is called a chromatogram and it can be used to quantify the number of analytes in a sample by integrating the area under the curve.[136]

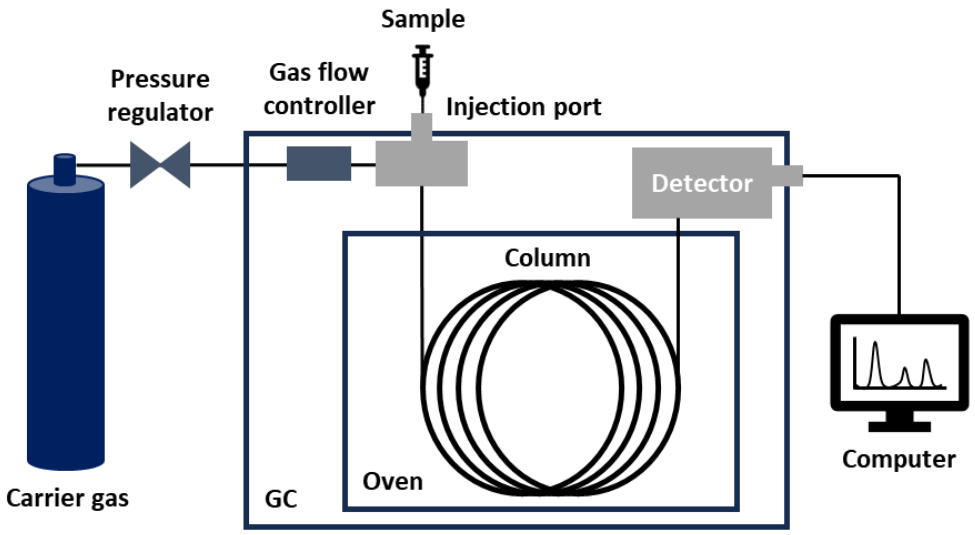

Figure 2.3. Simplified diagram of a typical gas chromatography (GC) system.[137]

A simple way of quantifying an analyte is by measuring its area under the curve at different concentrations. The caveat with this method, however, is that GC signals often have fluctuating response factors, and no two injections are perfectly identical. In the interest of keeping measurements reproducible, throughout this work, analyte quantification was done by measuring their response factor relative to an internal standard.

2.2.4.2. Principles of mass spectrometry (MS)

Mass spectrometry (MS) is an analytical technique that measures the mass-to-charge (*m/z*) ratio of ions. Different types of mass spectrometers exist with varying functionalities and constituent elements. However they will always have the following four components: a sample inlet, an ionization source, one or multiple mass analyzers, and an ion detector.[138] Some of these components can be combined depending on the instrumentation. Fundamentally, a mass spectrometer functions as follows: a sample (the analyte) is introduced into the system via an inlet, either through direct injection or from a gas chromatograph. The analyte is then ionized by an ionization source. Various ionization methods exist; depending on the desired degree of fragmentation, the sample can simply be ionized to produce the molecular ion with little fragmentation (soft ionization) or fragmented further to produce ions with a smaller *m/z* than the molecular ion (hard ionization). For gases and vapors, chemical ionization (CI) and electron ionization (EI) are

common techniques for soft and hard ionization, respectively. In the case of EI, the ion source consists of a heated metal filament that emits electrons, which are then accelerated by an applied potential, commonly 70 V, and bombard the analyte and expel an electron from the analyte. This forms the molecular ion ($[M]^{+\cdot}$) of the analyte, also called the parent ion. Because the electrons generated by the ion source possess high kinetic energy, other bonds in the analyte molecule can be broken, leading to extensive fragmentation by generating smaller ions.

Resulting ions are then separated according to their *m/z value* by a mass analyzer. This separation of ions stems from the fact that ions with different *m/z value*s will have different trajectories. Ion separation is accomplished differently depending on the type of mass analyzer used. The most common, single analyzer MS techniques incorporate the use of a sector-type, time-of-flight (TOF), or quadrupole mass analyzer. A sector mass analyzer uses an electric or magnetic field to bend the path of ions according to their masses. Lighter ions will get deflected more from their original trajectory compared to heavier ions. A TOF mass analyzer uses an electric field to accelerate ions and measures the time needed for these ions to reach the detector. The separation of ions stems from the different velocities exhibited by ions of different masses.

A quadrupole mass analyzer uses an oscillating quadrupole electric field to stabilize or destabilize the trajectory of ions. It consists of four parallel rods with two pairs of opposing charges, connected electrically in a parallel configuration. An oscillating radio frequency (RF) voltage with a direct (DC) offset voltage is applied to the rods; one pair of rods has a positive DC voltage, and the other has a negative DC voltage and out-of-phase RF voltage. The generated oscillating electric field alters the path of ions travelling through the quadrupole. Only ions with specific *m/z value*s and stable trajectories will avoid collision with the rods and successfully exit the mass analyzer. Alternating the oscillating frequency of the applied voltage on the rods allows for a scan of a range of *m/z* values rather than a single *m/z* value. The ions that emerge from the mass analyzer travel to the detector, typically an electron multiplier, which measures the abundance of ions as a function of their *m/z* values. These measured signals are sent to a computer, which then generates a

mass spectrum of the injected sample.[139] Figure 2.4 depicts a quadrupole mass spectrometer (QMS) using EI as the ionization method.

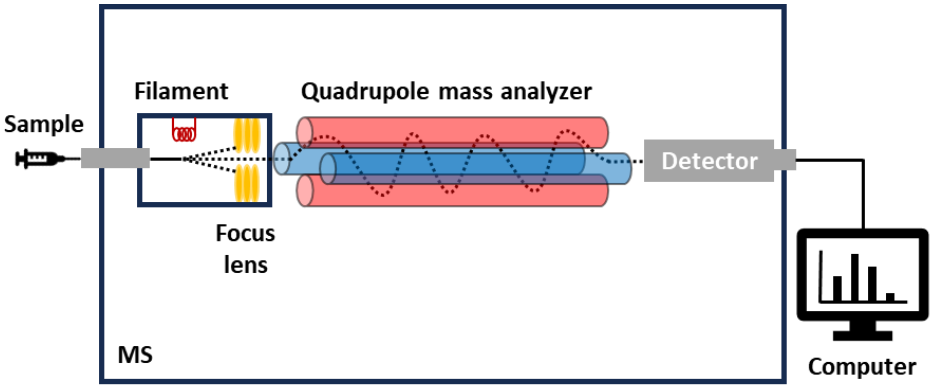

Figure 2.4. Simplified diagram of a quadrupole mass spectrometry (QMS) system.[140]

2.2.4.3. Overview of GC-MS

GC-MS combines gas chromatography and mass spectrometry to identify the chemical composition of volatile samples. In a typical experiment, a gaseous or liquid sample is injected into the inlet of the GC instrument. Throughout this work, the GC used was equipped with a split/splitless inlet, where the sample was injected into a built-in heated chamber through a septum. In this chamber, either all (splitless mode) or a pre-defined portion (split mode) of the vaporized sample was swept by the carrier gas into the column. The eluate enters the mass spectrometer and undergoes ionization. Because our MS operated under EI mode, the ion source is depicted as a filament emitting electrons, ionizing the eluate. The resulting fragment ions were filtered through a single quadrupole mass analyzer and reached the detector. A GC chromatogram of all eluted species and their corresponding mass spectra are generated at the end of the run.[141] A representative diagram of the system is depicted in Figure 2.5.

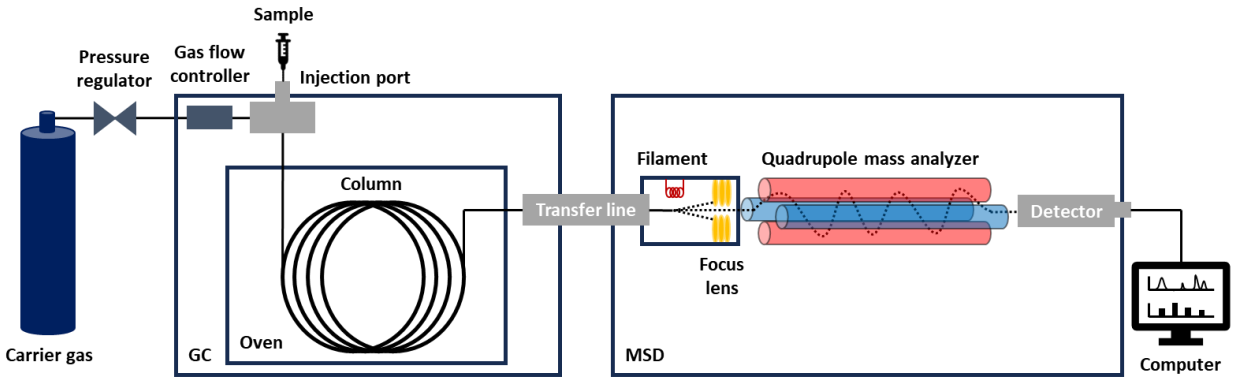

Figure 2.5. Simplified diagram of a gas chromatography-mass spectrometry (GC-MS) system.

The main reason GC-MS was used for characterization purposes was our interest in volatile products potentially produced by the decomposition of lignin-like molecules on CdS. As emphasized in Chapter 1, one of the target applications of these reactions is in the production of value-added organic compounds such as biofuels, which are generally volatile and have low molecular masses. GC-MS was therefore a suitable characterization method for this purpose. In addition, we expected reactions on CdS to produce multiple products that we wanted to identify and quantify relatively easily. Considering the small scale of reactions, some of these products may be unknown. Attempts at separating them would be difficult and identifying individual molecules in a sample containing various unknown products using other methods such as nuclear magnetic resonance (NMR) would be less straightforward and more time-consuming. Finally, GC-MS also allows for the analysis of samples or reaction mixtures of reactions conducted in both neat and solvated conditions, removing the need for solvent evaporation and modification. This reduces workup time and any additional errors from sample manipulation and/or processing.

2.2.4.4. Analysis methods and parameters

To identify the products of thermal and photocatalytic decomposition of lignin model molecules, chemical analyses of assays were conducted in an Agilent 7820A Gas Chromatography (GC) instrument coupled with an Agilent 5975 Series Mass Selective Detector (MSD). An Agilent J&W DB-5 column was used as the GC stationary phase. The GC inlet temperature was set to 250°C, and liquid sample injection volumes were maintained at 0.2µL with a 10:1 split ratio. Helium was used as the carrier gas. For each run, the GC

oven temperature program was set as follows: (i) the oven was maintained at 40°C for 1 minute, followed by (ii) heating to 300°C at a rate of 10°C/min, and finally (iii) maintained at 300°C for 1 minute. At the end of each run, the oven underwent rapid cooling back to 40°C. A 2-minute temperature equilibration period was programmed between runs. The MSD was set to record compounds above the cutoff *m/z value* of 33 to prevent detection of nitrogen and oxygen (*m/z value*s of 28 and 32, respectively), which are present in air. For each run, a 3.5-minute solvent delay was applied to ensure no solvent was present in the chromatogram and to avoid damage to the MS filament.

For qualitative headspace analysis, the GC inlet was operated under splitless mode. The assays were extracted through adsorption onto a solid phase microextraction (SPME) sampler for 2 minutes, followed by manual injection to the GC inlet. The same GC temperature program was used for data acquisition, with the following changes: (i) the solvent delay was omitted, and data acquisition was started upon sample injection, and (ii) chromatogram recording was stopped at the 10-minute mark, in the interest of time and accounting for the volatility of adsorbed species.

2.2.4.5. Generation of GC-MS calibration curves of known species

Calibration curves for all known species were generated for quantification purposes. To this end, known amounts of each species were diluted in acetonitrile with 1.0 mg/mL pentachlorobenzene as the internal standard of the aliquot. Using the aforementioned GC-MS parameters, several chromatograms were collected with varying concentrations of organic species, with blanks run in between samples whenever necessary. Data acquisition and peak analysis were done using the Agilent GC-MS software. Further data processing was done on Origin Pro 8.5 and Excel. The resulting calibration curves for all known species and their experimental mass spectra, to be used as reference mass spectra, can be found in Appendix A.

Chapter 3. Selection of CdS Catalyst for Decomposition Experiments

3.1. Background and objective

Many procedures exist to synthesize CdS nanoparticles (NPs) depending on the targeted crystalline phase, size, and other structural considerations. As there currently is no literature on the effects of CdS particle architecture on catalytic activity from a thermal decomposition perspective, there was uncertainty about the most optimal "type" of CdS to use, namely, which CdS synthesis procedure to adopt.

Therefore, the main objective of this subproject was to determine an adequate CdS synthesis procedure to use for the remainder of the project. An exploration of synthesis techniques and CdS NPs was undertaken to determine the most suitable catalyst. The selected catalyst would then be used in Chapter 4 to determine catalytic activity and performance in biomass valorization.

Firstly, a variety of CdS NPs were individually synthesized and characterized. Next, these synthesized NPs were used in a series of photocatalytic reactions to determine activity and compare with state-of-the-art literature. Two targets were used for photodegradation: Rhodamine B, an organic dye and commonly used standard for testing CdS photocatalytic activity, and 2-phenoxy-1-phenylethanol (PP-ol), a commonly studied lignin model molecule. Photodegradation of Rhodamine B was monitored using UV-vis spectrophotometry as part of a proof-of-concept experiment. The products of PP-ol conversion were characterized using GC-MS. The values of PP-ol conversion were compared across all synthesized CdS NPs. From these experiments, one CdS catalyst was chosen as the viable candidate for use in subsequent decomposition experiments.

The following criteria was used to shortlist the best-performing CdS photocatalyst for thermal decomposition applications. While the most effective photocatalyst may not always excel in thermal catalysis, a strong photocatalyst is likely to exhibit some thermal activity. This serves as a starting point for demonstrating CdS thermal activity and comparing the resulting substrate decomposition products. Other key considerations included CdS size, as thermal catalysis highly depends on catalyst surface area, and the

synthesis procedure. Priority was given to methods producing bare or pristine CdS NPs, without capping agents or ligands, and procedures offering tunability, as catalyst optimization could be part of future work. As the interest of the work is study CdS-substrate interactions and how they lead to the decomposition of the substrate of choice, a bare, ligand-free, and uncapped catalyst surface ensures that only direct interactions between the substrate and CdS are probed. The synthesis tunability aspect is important because of the need to obtain CdS catalysts with different crystalline phases, while maintaining the bare CdS surface. This means that the procedure must be tunable enough to allow for different crystalline phases to be obtained without the use of surface ligands or capping agents, and possibly without changing the precursors. The validity of this approach is supported by the apparent thermal activity of the chosen catalyst, as demonstrated in Chapter 4.

3.2. Experimental

The synthesis of CdS NPs reported in this Chapter is centered on exploring a wide variety of synthesis methods to obtain a diverse set of CdS NPs to test, as opposed to fine-tuning and optimizing one specific procedure. This was achieved through the exploration of synthesis procedures that employ different precursor materials, solvents, and reaction temperatures, as these reaction parameters play key roles in the resulting CdS NPs.[123] Using different starting materials affects the local environment of the reaction, and solvent selection contributes to this by reducing surface tension whenever precursor-solvent interactions are favorable.[142] Certain procedures also employ surfactants and capping agents, which can protect the NPs from aggregation or direct particle growth to form specific shapes.[122,143] Lastly, temperature drives the kinetics and thermodynamics of the reactions, affecting nucleation rates and particle growth, as well as dictating the thermodynamically accessible polymorphs.

3.2.1. Chemicals

All chemicals were used without further purification unless stated otherwise. Ethylenediamine (99%), sodium sulfide nonahydrate ($Na_2S \cdot 9H_2O$, 98+%), and cadmium acetate dihydrate ($CdOAc_2 \cdot 2H_2O$, 98%) were purchased from Alfa Aesar. Thiourea ($SC(NH_2)_2$ ≥99.0%) was purchased from J. T. Baker. Sodium hydroxide (NaOH) was purchased from Merck. Cetyltrimethylammonium bromide (CTAB), ethylene glycol (EG, 99+%), 1-octadecene (ODE, 99%), myristyltrimethylammonium bromide (MYTAB, 99%), triethylenetetramine (TETA, 60%), oleylamine (70%), cadmium nitrate tetrahydrate ($Cd(NO_3)_2 \cdot 4H_2O$, 98%), and thioacetamide (98%) were purchased from Sigma Aldrich. Benzyl alcohol was purchased from TCI America. Triethylene glycol (TriEG, 99%), was purchased from Thermo Scientific. 2-phenoxy-1-phenylethanol (PP-ol) was purchased from Toronto Research Chemicals. Pentachlorobenzene (99.9%) was purchased from Fluka Analytical.

3.2.2. Synthesis of CdS-1, CdS-2, and CdS-3

CdS quantum dots (QDs) were synthesized according to a reported approach with modifications.[144] Thiourea (5.0 mmol) was dissolved in 30 mL of ethylene glycol to prepare a sulfur stock solution. In a separate flask, anhydrous $CdCl_2$ (5.0 mmol) and tetramethylammonium hydroxide (10.0 mmol) were dissolved in 30 mL of ethylene glycol and heated to 100 °C. Under vigorous stirring, the sulfur precursor solution was quickly injected into the flask. The reaction was heated to 155 °C and stirring was maintained for 2 hours, followed by refluxing at 194 °C for an additional hour before cooling down to room temperature. The solution was then centrifuged and washed with water and methanol to obtain solid CdS, which was dried under vacuum at 60 °C for 4 hours. The procedure was repeated to verify reproducibility and increase yield, resulting in the synthesis of CdS-2 and CdS-3.

3.2.3. Synthesis of CdS-4

CdS QDs were synthesized according to a reported approach with modifications.[145] $Cd(OAc)_2 \cdot 2H_2O$ (2.0 mmol, 0.533 g) was dissolved in 20 mL of ethanol until the solution became clear. Afterwards, thiourea (6.0 mmol, 0.457 g) was slowly added into the solution, and the pH was tuned to 10 with a 0.20 M NaOH solution. Stirring was maintained at room temperature for 12 hours. The nanoparticles were collected through centrifugation and washed multiple times with distilled water and acetone. Finally, the powder was dried under vacuum at 60 °C for 4 hours.

3.2.4. Synthesis of CdS-5

CdS nanoflorets were synthesized according to a reported approach.[146] $Cd(OAc)_2 \cdot 2H_2O$ (1.0 mmol, 0.266 g) was dissolved in 50 mL ethylene glycol until a clear solution was obtained. Then, thiourea (2.0 mmol, 0.152 g) was added to the reaction mixture, and subsequently refluxed at 80 °C for 6 hours. The suspension was centrifuged and washed with distilled water and ethanol three times, respectively, and dried at 70 °C in an oven overnight.

3.2.5. Synthesis of CdS-6

CdS microspheres were synthesized according to a reported approach.[147,148] $Cd(NO_3)_2 \cdot 4H_2O$ (2.4 mmol, 0.750 g) and thioacetamide (6.7 mmol, 0.500 g) were dissolved in 25 ml of distilled water and stirred for 30 min until clear. The solution was heated to 105 °C and refluxed for 30 min. The yellow precipitate was collected by centrifugation and washed several times using distilled water and ethanol, followed by drying in an oven at 70 °C overnight.

3.2.6. Synthesis of CdS-7

CdS NPs were synthesized according to a reported approach with modifications.[86] Synthesis was done under inert atmosphere. $Na_2S \cdot 9H_2O$ (40.0 mmol, 9.607 g) was dissolved in 40 mL of ethylene glycol and heated to 175 °C for over 10 min to evaporate any remaining water content and maintained at that temperature afterwards. Subsequently, $Cd(OAc)_2 \cdot 2H_2O$ (2.5 mmol, 0.666 g) was dissolved in 20 mL of ethylene glycol and purged with argon. Once clear, the cadmium stock solution was injected into the sulfur stock solution using a mechanical syringe pump at a rate of 0.5 mmol/h and the solution was refluxed for an additional 5 hours. The solids were collected by centrifugation, washed twice with distilled water and acetone, and dried at 50 °C for 24 hours.

3.2.7. Synthesis of CdS-8

CdS NPs were synthesized according to a reported approach with modifications.[80] $Cd(NO_3)_2 \cdot 4H_2O$ (3.0 mmol, 0.709 g), triethylenetetramine (12.0 mmol, 1.754 g), SDS (2.1 mmol, 0.600 g), and thiourea (6.0 mmol, 0.457 g) were added into 60 mL of distilled water and stirred for 30 min. The resulting solution was heated to 100 °C and stirred for 5 hours. The solids were collected via centrifugation and washed using distilled water and ethanol before drying in an oven at 60 °C overnight.

3.2.8. Synthesis of CdS-9, CdS-10, CdS-12, and CdS-13

CdS nanoflorets were synthesized according to literature.[149] $Cd(OAc)_2 \cdot 2H_2O$ (1.5 mmol, 0.400 g), thioacetamide (1.5 mmol, 0.113 g), and CTAB (1.5 mmol, 0.365 g) were dissolved in 30 mL of distilled

water. The solution was then heated to 90 °C and stirred for 30 minutes, followed by cooling to room temperature. The resulting solids were collected by centrifugation and washed three times with distilled water and ethanol before drying in an oven at 60 °C overnight. This procedure was repeated to verify reproducibility and increase yield, resulting in the synthesis of CdS-12 and CdS-13. For the synthesis of CdS-10, the procedure above was repeated using MYTAB as the surfactant instead of CTAB to elucidate the effects of changing surfactants on the resulting CdS NPs.

3.2.9. Synthesis of CdS-11

CdS NPs were synthesized according to literature.[150] $Cd(NO_3)_2 \cdot 4H_2O$ (2.5 mmol, 0.771 g) and $Na_2S \cdot 9H_2O$ (2.5 mmol, 0.600 g) were separately dissolved in 25 mL of distilled water. Afterwards, the sulfur stock solution was added dropwise to the cadmium stock solution under vigorous stirring. The reaction was maintained at room temperature for 6 hours. The precipitates were collected via centrifugation and washed three times with ethanol, followed by drying under air overnight.

3.2.10. Photocatalysis experiments

In this Chapter, the photocatalysis experiments were conducted using two light sources, namely a 6 mW nitrogen laser ($\lambda = 337$ nm, 400 μJ max. energy per pulse) or 8 W UV LED bars ($\lambda = 352$ nm). These light sources were selected based on the absorption range of the CdS NPs, as well as the sufficient energy provided by the light sources to induce the photocatalytic decomposition of substrates, as described in subsequent sections. The reaction vessels were placed no more than 5 mm in front of the light source.

3.2.10.1. Photocatalytic decomposition of Rhodamine B

While it is known that CdS is photoactive in the UV and visible light range, a rapid proof-of-concept experiment under UV irradiation ($\lambda = 337$ nm) was conducted to experimentally confirm this photoactivity. In brief, the experiment consisted of irradiating a solution of Rhodamine B, a well-known organic dye, and monitoring its photodecomposition using UV-vis spectrophotometry. This dye is commonly used due to its susceptibility to photodecomposition, which can easily be monitored both using UV-vis measurements and

quantitatively, as RhoB degradation is visually marked by a fade in the dye's color. RhoB was thus considered appropriate for a proof-of-concept experiment. To this end, an 8.35×10^{-5} M aqueous solution of Rhodamine B was prepared. One of the synthesized CdS samples was chosen at random and dispersed in the dye solution at a concentration of 1.0 mg/mL in a quartz cuvette. The dispersion was then irradiated under constant stirring, and aliquots were taken at regular intervals for UV-vis measurements. A control experiment was also conducted without any CdS.

3.2.10.2. Photocatalytic conversion of PP-ol

To compare the performance of all the synthesized CdS samples, a series of photocatalysis experiments were conducted under UV irradiation ($\lambda = 352$ nm). A 0.02 M stock solution of PP-ol in acetonitrile (MeCN) was prepared. In a typical reaction, a glass vial was loaded with a stir bar, the CdS catalyst (4.0 mg), and 2 mL of the PP-ol stock solution. The vial was then capped, and the mixture was degassed under argon for 5 min. The cap was sealed with parafilm, and the vial was placed on a stirring plate, 5 mm in front of the light source. The vial was irradiated under constant stirring and a light shield was employed to isolate the reaction setup from external light sources. After 24 hours, the dispersion was centrifuged. The supernatant at the reaction end ($t_f = 24$ h) was analyzed by GC-MS and compared with PP-ol solution at the reaction start (t_0). No assays were collected in between these reaction times. A typical reaction setup is depicted in Figure 3.1.

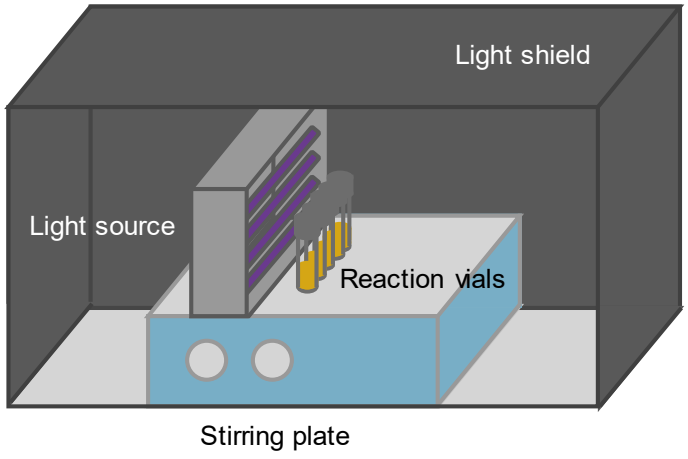

Figure 3.1. Typical experiment setup. The front side of the light shield is illustrated with increased transparency to visualize the elements inside (stirring plate, sample vials loaded with different CdS catalysts, and light source).

3.2.10.3. Kinetics experiments

To elucidate the conversion pathways of PP-ol under UV irradiation (λ = 352 nm), some kinetics experiments were conducted using the previously synthesized CdS samples. In this case, PP-ol conversion was monitored over time, at regular time intervals, using the same reaction setup as depicted in Figure 3.1 with some modifications. In a glass vial, 15.0 mg of the chosen CdS catalyst was dispersed in 8 mL of a 0.02 M solution of PP-ol in MeCN. The dispersion was degassed with argon for 10 minutes. The vial was sealed and irradiated under constant stirring. Aliquots were taken at regular time intervals and analyzed by GC-MS.

3.3. Results and discussion

3.3.1. Characterization of catalysts

As expected, the variety of synthesis methods resulted in CdS of various crystalline phase, particle size, and specific surface area. Other synthesized NPs were not used for any photocatalytic reactions but are described in Appendix G. XRD patterns and TEM images for the catalysts are shown in Figure 3.2 and compared with reference XRD patterns of cubic and hexagonal CdS. All catalysts, except for CdS-2, demonstrated either a cubic or a mixed crystalline phase. As expected, the use of various synthesis procedures yielded NPs of different shapes and sizes, though this would be discussed further in the section. In cases where the same CdS NPs synthesis procedure was repeated, it was observed that the resulting products differed on more than one occasion. One example is the synthesis of CdS-1, CdS-2, and CdS-3. Despite being synthesized using the same procedure, the reaction environments were not fully reproducible, as demonstrated by the experimental XRD patterns. It is well-reported that high temperatures encourage the formation of the thermodynamically stable hexagonal CdS provided that the growth of NPs along specific planes was not directed, and assuming ambient pressure. However, only CdS-2 showed diffraction peaks consistent with hexagonal CdS, which was expected based on the reaction temperature that was employed, while CdS-1 and CdS-3 displayed mixed crystalline phases.

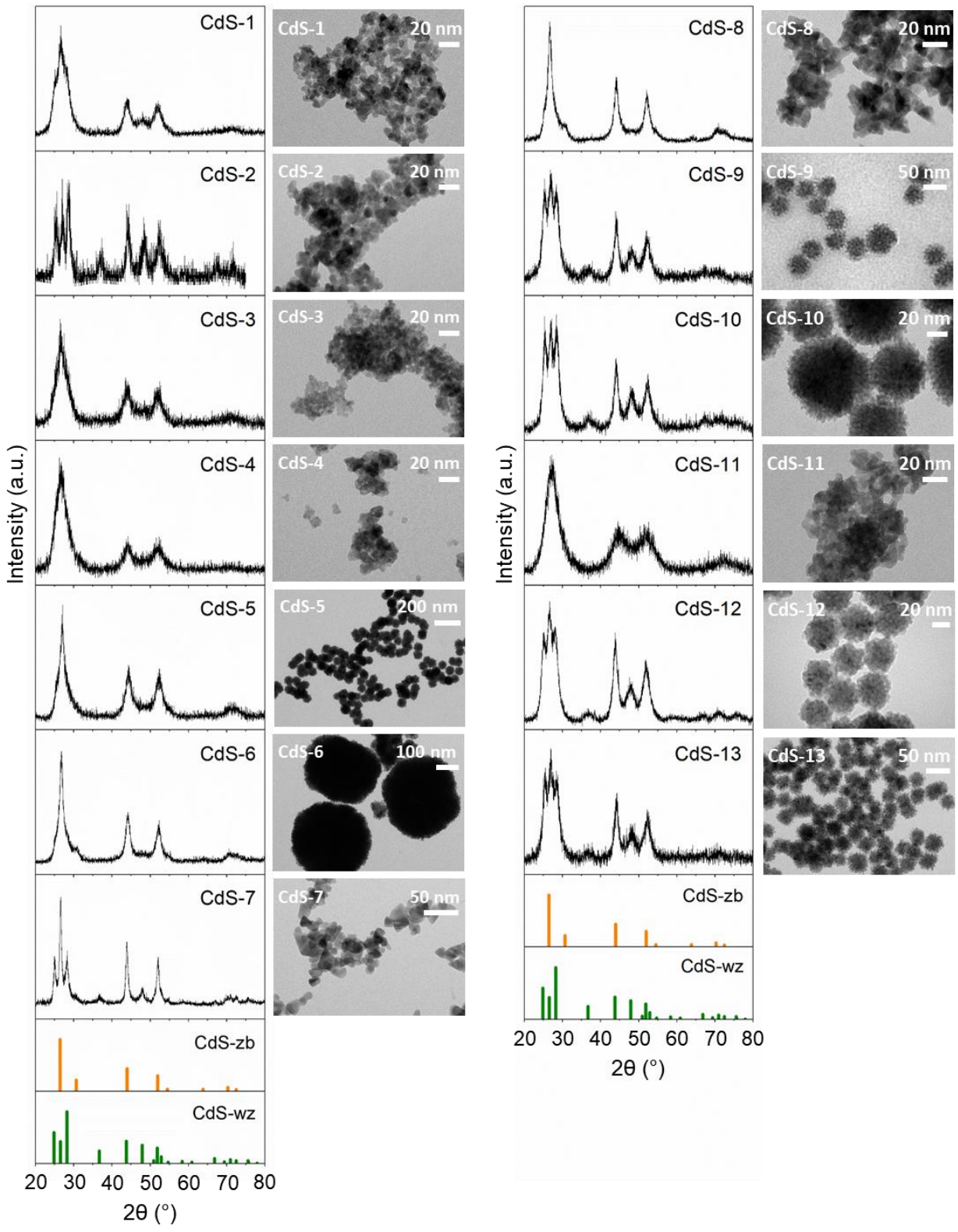

Figure 3.2. XRD patterns of synthesized CdS catalysts compared with reference XRD patterns of cubic CdS (CdS-zb, in orange, PDF card no. 01-089-0440) and hexagonal CdS (CdS-wz, in green, PDF card no. 01-074-9663).

The next series of catalysts, comprised of CdS-9, CdS-12, and CdS-13, employed the same procedure, using CTAB as a surfactant to direct the growth of the nanoflorets. To note, the synthesis of CdS-10 also followed the same procedure, with the exception that the surfactant used was MYTAB, which is a derivative of CTAB with a longer alkyl chain. XRD patterns showed mixed phases for these catalysts. However, CdS-10 displayed a subtle difference in relative peak intensities. Specifically, the 24°, 26°, and 28° peak intensities are equal, indicating a different phase composition (cubic-to-hexagonal ratio) compared to CdS-9, CdS-12, and CdS-13. This discrepancy suggests that variations in crystalline phase are expected when increasing the chain length of a surfactant, consistent with literature. Despite this, no significant differences were observed solely from XRD analysis.

As one of the key aspects of the work was to find a simple, scalable, and straightforward procedure, two catalysts, CdS-4 and CdS-11, were synthesized at room temperature. Due to the mild conditions (ambient temperature and pressure), a cubic or mixed phase was anticipated, which aligned with their respective XRD patterns. In the case of CdS-4, precipitation was facilitated through the addition of NaOH, which raised the pH of the reaction environment. To note, CdS precipitates under basic conditions. Aggregation was noted for both CdS-4 and CdS-10 as no capping or stabilizing agents were employed. The XRD patterns for these catalysts were not well resolved, indicating a lack of crystallinity. The broadness of the XRD peaks is also indicative of small particle sizes.

On another front, the use of other heated synthetic procedures was also explored. CdS-5 exhibited an XRD pattern indicative of a cubic structure, but with sharper peaks compared to CdS-4 and CdS-11. This increase in crystallinity is likely due to the higher reaction temperatures. The same observation can be said about CdS-6 and CdS-8, even though these were synthesized using two other different procedures. CdS-7, which was synthesized at a slightly higher temperature, showed a mixed cubic-hexagonal phase with high crystallinity. From the TEM images that were collected, particles were measured, and their size distributions were plotted as shown in Figure 3.3. Beginning with CdS-1, CdS-2, and CdS-3 as they were synthesized using the same procedure, it was found that the mixed phase CdS-1 and CdS-3 were smaller and have

similar sizes, while the hexagonal CdS-2 had a larger particle size. This is consistent with what is known about hexagonal NPs; since they are the thermodynamic product and sufficient time was provided for the reaction at high temperature, it was likely that surface energy reduction favored particle growth, leading to larger size. In this case, difference in size seemed to be minor, which could, in part, be attributed to the presence of hexagonal CdS in the CdS-1 and CdS-3 crystalline lattices, indicating that a phase shift could have possibly occurred. The shapes and agglomeration behavior of the NPs were similar. Looking at the other series of CdS NPs, comprised of CdS-9, CdS-10, CdS-12, and CdS-13, it is expected that CdS-10 would show a difference in particle size. The primary distinction between CdS-9, CdS-12, and CdS-13, with CdS-10 lies in the surfactants used: CTAB for the three and MYTAB for the latter. Both surfactants have the same polar head (N^+), but CTAB has a longer alkyl chain (16 carbons) compared to MYTAB (14 carbons). This difference in chain length is expected to influence particle size and architecture.[151,152] The sizes of CdS-9, CdS-12, and CdS-13 are similar, exhibiting a consistent morphology of nanoflorets across the samples. In contrast, CdS-10, which used MYTAB, is larger than the other three samples. While the floret-like shape is preserved, the change in surfactant impacts particle growth, leading to size differences. The shorter alkyl chain of MYTAB results in reduced spacing between nuclei during nucleation, promoting self-assembly and aggregation, which favors larger particle sizes. This trend aligns with literature observations on selenium nanoparticles synthesized with similar surfactants (n-alkyl trimethylammonium bromides),[153] where an inverse relationship between surfactant chain length and nanoparticle size has been noted. Given that sulfur (S) is in the same group as selenium (Se) and that the surfactants share similar characteristics, it is reasonable to expect similar behavior in CdS NP synthesis.

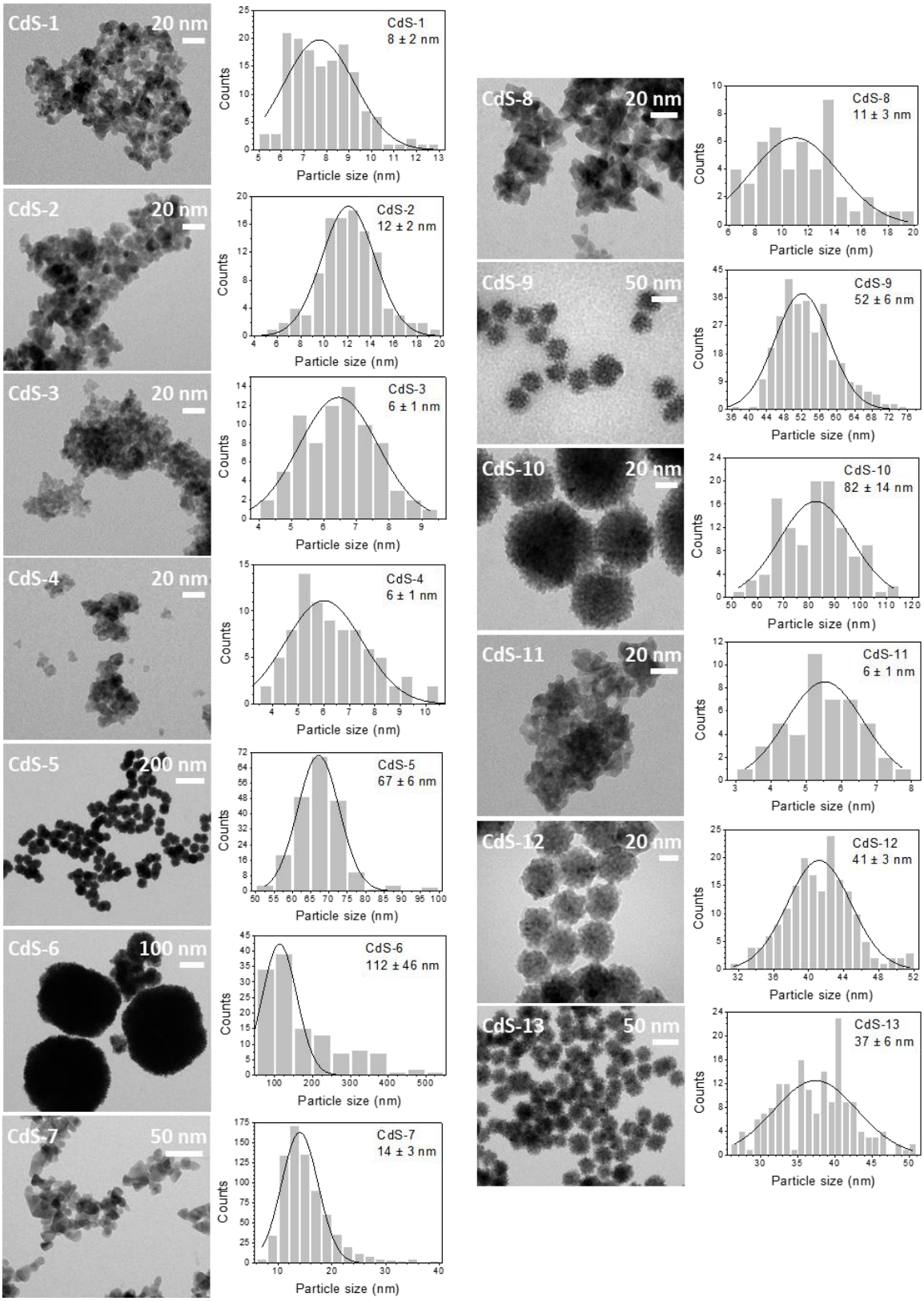

Figure 3.3. TEM images and associated particle size distributions of CdS-1 to CdS-13.

With regards to the catalysts synthesized at room temperature, the cubic CdS-4 and CdS-11 have the same particle sizes and size distributions despite being synthesized using different procedures. This implies that the mild conditions employed have similar reaction kinetics which favored the formation of small NPs. On the other hand, the higher temperature reactions showed a wider variety of particle sizes. The CdS-5 nanoflorets were formed in large, uniform shapes and sizes, which was expected considering the reaction time. To note, the formation of nanoflorets was observed despite the absence of additional surfactants. It is possible that the interaction between thiourea as the sulfur source and ethylene glycol as the solvent may have facilitated that growth mechanism, but this remains to be confirmed. Meanwhile, the procedure for CdS-6 was meant to produce microspheres. While the resulting product was still at the nanoscale, they were indeed formed at larger size regimes with broad size distributions and non-uniform particle shapes. Lastly, CdS-7 and CdS-8 exhibited small particles with a medium size distribution. Particularly in the case of CdS-8, there seemed to be a higher degree of agglomeration.

The results of CdS characterization are summarized in Table 3.1. As expected, room temperature CdS precipitation procedures generally resulted in cubic phase CdS, while higher temperature procedures yielded mostly mixed phase CdS and a hexagonal phase CdS. Particle size fluctuation overall was high at around 20%, except for CdS-6, whose particle size distribution was broader than the rest at 41%. However, obtaining uniform CdS NPs or optimization of synthesis methods was not a focus of this work. Specific surface areas (SSAs) were measured for most of the synthesized CdS, with some samples omitted due to insufficient quantities (75.0 mg minimum) for surface area measurements. Since specific surface areas did not consistently increase as particle size decreased, various factors such as porosity, vacancies or defects, aggregation, or surface reconstruction, to name a few, could have influenced specific surface areas.[154–156]

Table 3.1 Summary of synthesized CdS XRD, TEM, and surface area measurements.

Catalyst designation	Crystalline phase	Particle size (nm)	SSA (m^2/g)
CdS-1	Mixed	8 ± 2	98.9
CdS-2	Hexagonal	12 ± 2	125
CdS-3	Mixed	6 ± 1	256
CdS-4	Cubic	6 ± 1	Not measured
CdS-5	Cubic	67 ± 6	36.2
CdS-6	Cubic	112 ± 46	54.3
CdS-7	Mixed	14 ± 3	78.1
CdS-8	Cubic	11 ± 3	24.2
CdS-9	Mixed	52 ± 6	Not measured
CdS-10	Mixed	82 ± 16	Not measured
CdS-11	Cubic	6 ± 1	165
CdS-12	Mixed	41 ± 4	85.8
CdS-13	Mixed	37 ± 6	75.0

One apparent problem was present in some of the catalysts that could allude to potential reproducibility issues in the synthesis process. Namely, CdS-1, CdS-2, and CdS-3 all exhibited different properties despite being synthesized following the same high temperature procedure, and only CdS-2 was successfully obtained as hexagonal phase CdS, likely caused by temperature fluctuations (Appendix C-1). Reproducibility issues were also seen with CdS-9, CdS-12, and CdS-13 (Appendix C-2), where it is possible that the added use of surfactants or capping agents rendered the synthesis process more susceptible to variations, leading to apparent disparities in CdS architecture, notably pertaining to particle size which is affected by particle growth.[157,158]

3.3.2. Photocatalysis experiments

Figure 3.4 illustrates a representative proof-of-concept experiment using CdS to catalyze the photodecomposition of Rhodamine B (RhoB). Evidently, in the span of 60 minutes, RhoB (Figure 3.4(i)) showed a gradual decrease in absorbance, while in the control experiment (Figure 3.4(ii)), the dye was shown to be stable under UV irradiation. This experimentally confirms CdS was photoactive and could thus be used as a catalyst for other reactions involving more relevant substrates, namely lignin model molecules.

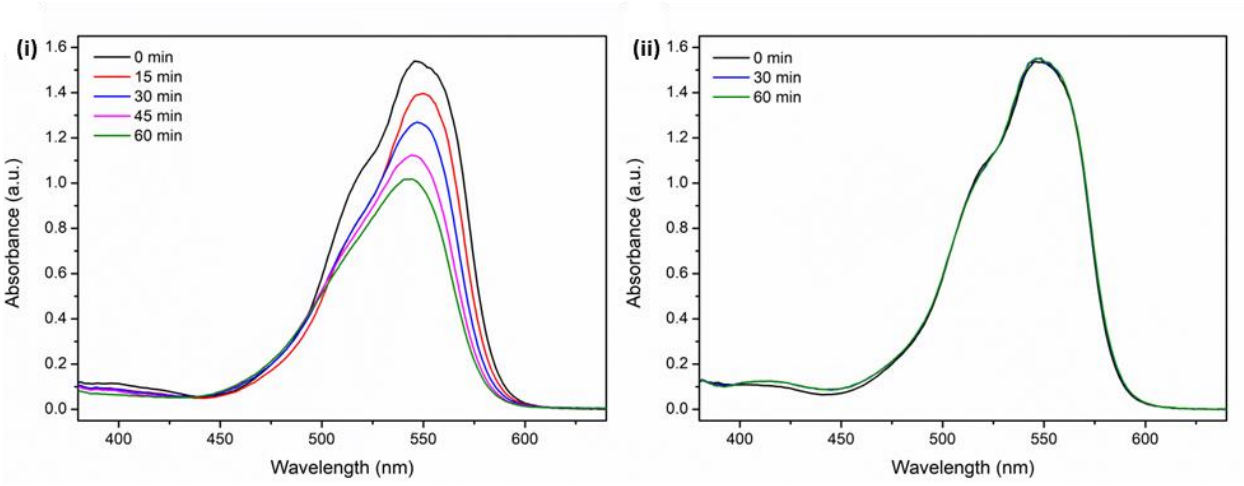

Figure 3.4. *(i) Photodecomposition of Rhodamine B with 1.0 mg/mL CdS and (ii) without CdS. Reaction conditions: 8.35 × 10^{-5} M RhoB in H_2O, t = 60 min, λ = 337 nm.*

For the preliminary kinetics experiments using CdS for photocatalytic PP-ol conversion, CdS-13 was initially selected based on catalyst availability and its acceptable surface area. In this experiment, only the major products of PP-ol conversion were quantified, which were phenol, acetophenone, and 2-phenoxy-1-phenylethanone (PP-one) as they were the main products of interest, and they were also present in observable amounts. The conversion of the substrate and yield of products over time is shown in Figure 3.5.

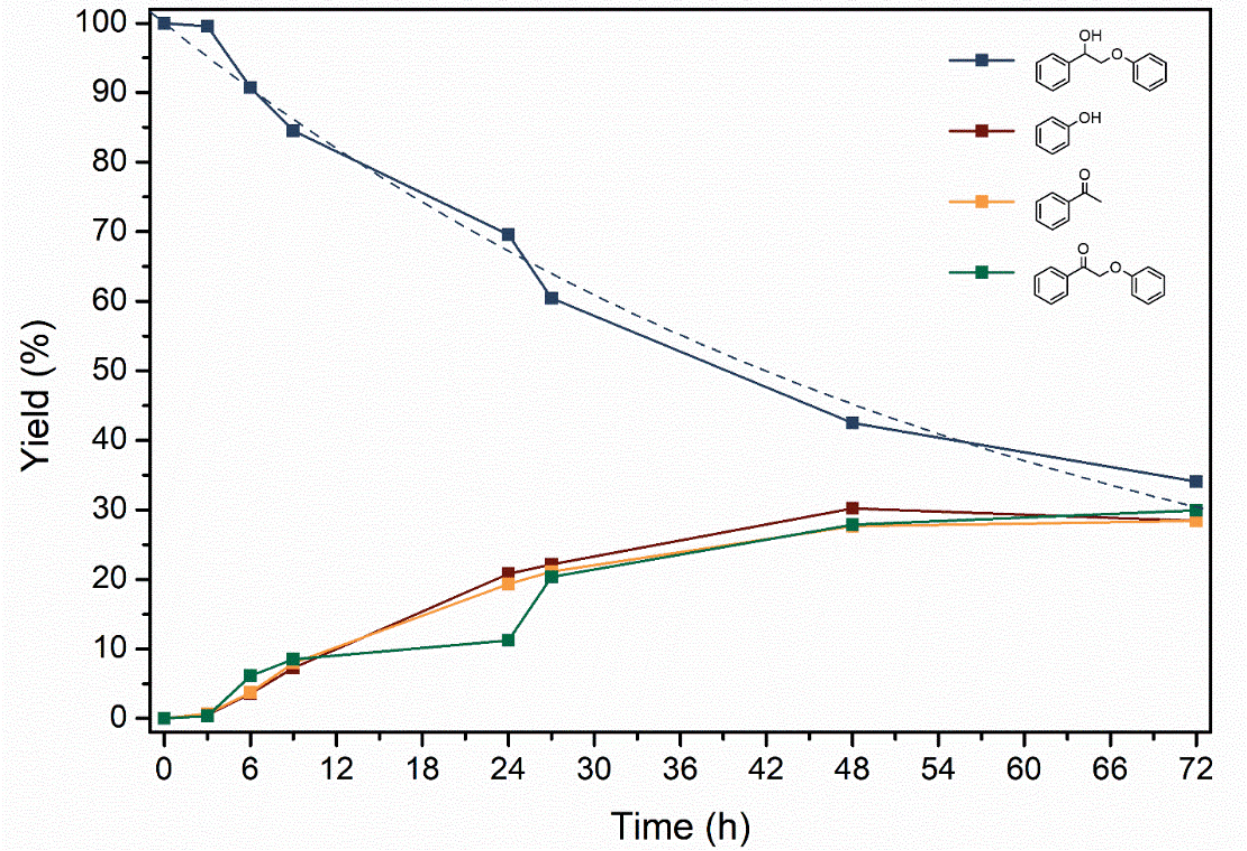

Figure 3.5. Photocatalytic decomposition of PP-ol under UV irradiation over 72 h. The fitted curve (dashed line) represents the calculated rate of PP-ol decomposition. Reaction conditions: 0.02 M PP-ol in MeCN, 15.0 mg catalyst (CdS-13), λ = 352 nm, Ar atmosphere.

As seen from the reaction profiles, the production of acetophenone and phenol occurs simultaneously with PP-one. There does not seem to be any subsequent decrease in the concentration of PP-one, suggesting that the two reaction pathways are competitive rather than sequential and that β-O-4 bond cleavage did not occur via a PP-one intermediate in our reaction system, as illustrated in Scheme 3.1. Using CdS-13 as the catalyst, PP-ol conversion after 72 hours was determined to be 66%, with phenol, acetophenone, and PP-one yields at 28%, 28%, and 30%, respectively. The rate constant for PP-ol conversion was approximated through line fitting, assuming first-order reaction kinetics, and has a value of $1.604 \times 10^{-2}\ h^{-1}$.

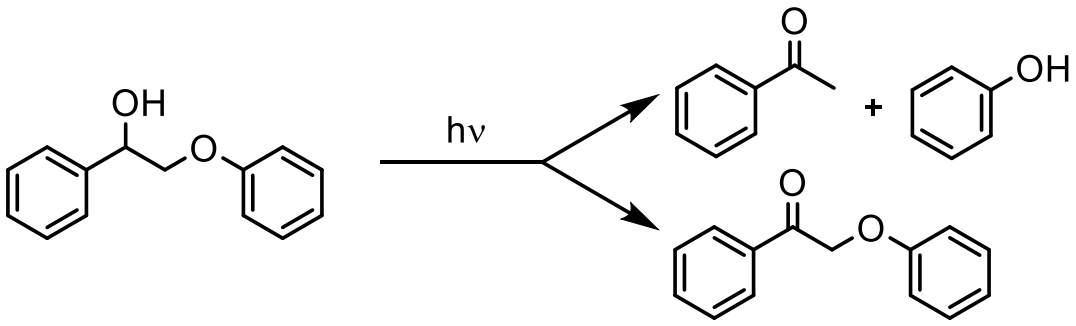

Scheme 3.1. The two major pathways of CdS-catalyzed PP-ol photocatalytic decomposition.

The first sign that catalyst activity could be influenced by inconsistent catalyst synthesis emerged during a replicated kinetic experiment with CdS-12. Despite being prepared using the same techniques as CdS-13, CdS-12 evidently had different physical properties than CdS-13 which were not obvious based on the XRD and TEM characterization results alone, meaning that the synthesis of these CdS NPs was not reproducible. This difference across batches was reflected by the altered catalyst activity in the photodecomposition of PP-ol. As seen in Figure 3.6, PP-ol conversion with CdS-12 was slower, meaning the rate constant for PP-ol conversion was lower, estimated to be $1.128 \times 10^{-2}\ h^{-1}$. Notably, the two parallel PP-ol decomposition pathways did not proceed at the same rate. Instead, using CdS-12 as a photocatalyst seemed to favor decomposition to PP-one rather than β-O-4 bond cleavage to phenol and acetophenone, and the concentration of PP-one was around three times higher than that of the phenol-acetophenone pair, compared to the near equimolar concentrations observed with CdS-13. PP-ol conversion after 77 hours reached 56%, with phenol, acetophenone, and PP-one yields at 12%, 10%, and 35%, respectively. Around 9% of the converted PP-ol was unaccounted for at the 77-hour mark and is attributed to byproducts of PP-ol conversion that were not identified nor quantified in this series of experiments.

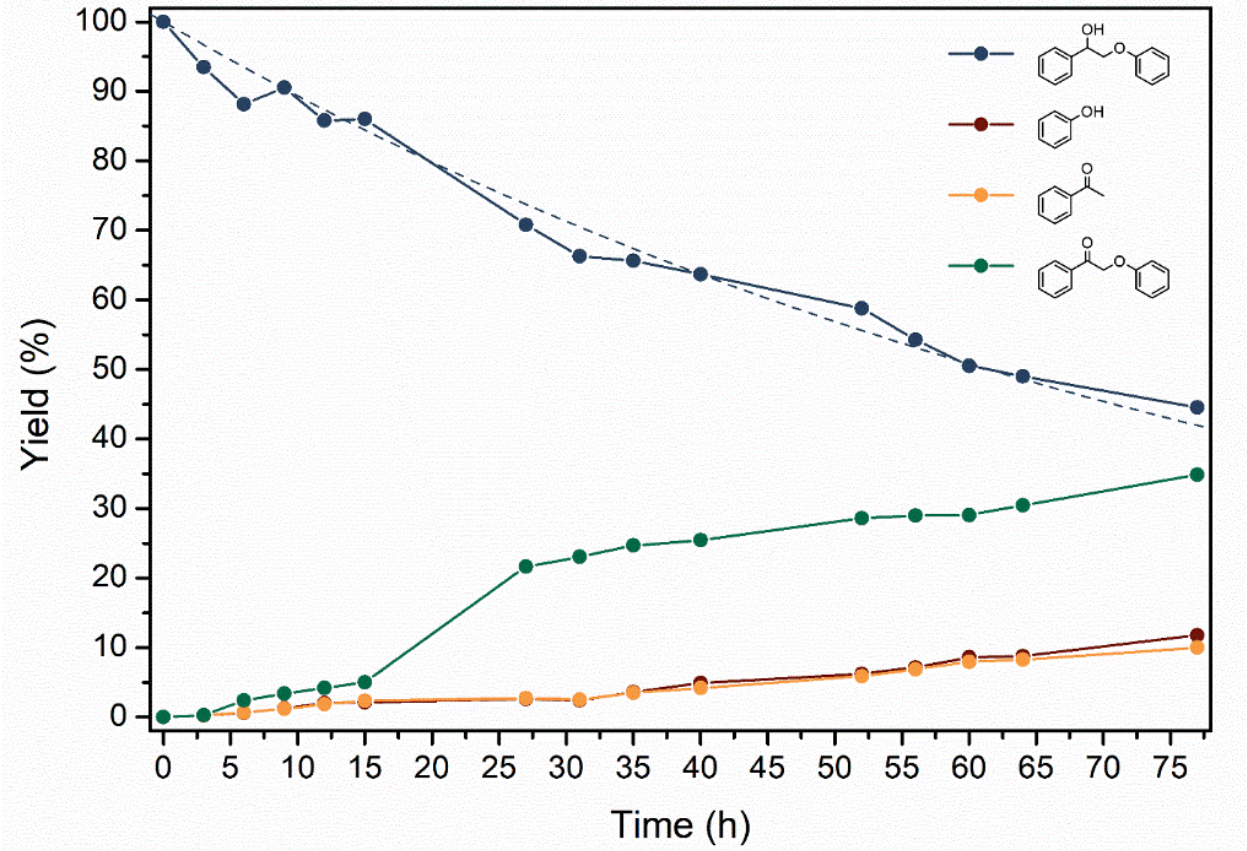

Figure 3.6. Photocatalytic decomposition of PP-ol under UV irradiation over 77 h. The fitted curve (dashed line) represents the calculated rate of PP-ol decomposition. Reaction conditions: 0.02 M PP-ol in MeCN, 15.0 mg catalyst (CdS-12), λ = 352 nm, Ar atmosphere.

With the results of the preliminary kinetics experiments in mind and before proceeding further, a series of photocatalytic experiments were conducted using all the CdS catalysts to determine the better-performing CdS candidate for use in further studies. A representative GC chromatogram (Figure B.1) shows all possible peaks that can be observed in the CdS-catalyzed decomposition of PP-ol under UV. The results of the experiments were summarized in Table 3.2, where PP-ol conversion varied from 4% to 86%. Across all catalysts, the common products of PP-ol decomposition were phenol, acetophenone, and PP-one, consistent with existing literature reports.[99] Byproducts of the reaction include anisole and benzaldehyde, as well as 1,4-diphenylbutan-1,4-dione in some cases. Two unknown compounds, each exhibiting a set of GC twin peaks at retention times of around 17.67 minutes and 23.56 minutes, were also observed and attributed to a dimer and phenolic oligomer, respectively. These unknown compounds were not identified in this Chapter.

However, further discussion on their possible structures can be found in Chapter 4. The concentration of the unknown dimer and phenolic oligomer was estimated using the acetophenone and PP-ol calibration curve, respectively, as it is expected that each of the unknown products would exhibit similar structures as those reference molecules. Within the same class of catalysts, that is, catalysts that were synthesized using the same procedure, some of the results suggested that PP-ol conversion increased with increasing surface area, namely in the case of CdS-1, CdS-2, and CdS-3, as expected. However, this observation was not reflected by CdS-12 and CdS-13. Without the surface area measurements of CdS-9 and CdS-10, which are in the same class as CdS-12 and CdS-13, it was difficult to deduce whether there was a direct correlation between specific surface area and PP-ol conversion. Furthermore, crystalline phase or particle size individually were not the sole factors that affect PP-ol conversion, because it was observed that decreasing particle size, increasing surface area, or changing crystalline phase did not necessarily lead to increased PP-ol conversion. This is in line with current understanding that multiple factors in CdS architecture play a role in photocatalytic activity.

The formation of oligomers was found to be random and did not follow any specific pattern (Figure B.3). However, the β-O-4 cleavage-to-oxidation ratio, obtained through the ratio of phenol or acetophenone to PP-one, showed a general upward trend with increasing PP-ol conversion (Figure B.2). This would imply that highly active CdS photocatalysts favor the cleavage of PP-ol instead of its oxidation to PP-one. Finally, as PP-ol conversion increased, a slight increase in the phenol-to-acetophenone ratio was observed, suggesting that active CdS photocatalysts also facilitated the reaction of acetophenone to form byproducts.

Table 3.2. Summary of PP-ol conversion rates and product compositions (0.02 M PP-ol in MeCN, 4.0 mg CdS catalyst, λ = 352 nm, t = 24 h, Ar atmosphere).

Catalyst	**Conversion (%)**	**Product composition (%)**							
						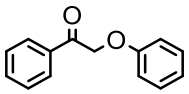	**Unknown dimer**	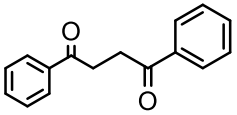	**Unknown phenolic oligomer**
CdS-1	19			27	30	43			
CdS-2	64			37	31	25	3	1	2
CdS-3	74			35	33	28	2		2
CdS-4	85			40	30	17	6	< 1	7
CdS-5	19			27	31	42			< 1
CdS-6	33	< 1	6	29	30	34		1	
CdS-7	86			41	32	14	6	< 1	6
CdS-8	4					100			
CdS-9	61	< 1		40	36	18	3		2
CdS-10	35	< 1		40	32	21	3	1	3
CdS-11	24			33	30	30	4	3	< 1
CdS-12	15			17	21	60		2	
CdS-13	30			40	37	22	1	< 1	< 1

In parallel, the effect of catalyst loading was also briefly studied. Figure 3.7(i) illustrates the GC chromatograms of PP-ol conversion experiments using 4.0 mg and 1.0 mg of CdS-4, as the best performing catalyst, as well as the control experiment where no CdS was used. After UV irradiation for 24 hours, the control experiment showed no PP-ol conversion. Under catalyzed conditions, PP-ol conversion was estimated to be 89% and 23% when using 4.0 mg and 1.0 mg of the catalyst, respectively. It was observed that β-O-4 cleavage was favored with increased CdS loading, as demonstrated by the increase in phenol and acetophenone composition. Surprisingly, PP-one was produced in similar concentrations in the two catalyzed experiments. As it was previously stipulated that β-O-4 cleavage does not occur in PP-one, catalyst loading did not seemingly affect the rate of PP-one formation, and it is possible that the oxidation of PP-ol to PP-one was not the dominant reaction. In terms of PP-ol conversion to larger oligomers, the uncharacterized dimer and phenolic oligomer were produced at low concentrations under 4.0 mg catalyst loading, while none were detected under lower CdS loading. However, 1,4-diphenylbutan-1,4-dione was only detected at slightly higher concentrations when using 1.0 mg CdS. No other byproducts were detected.

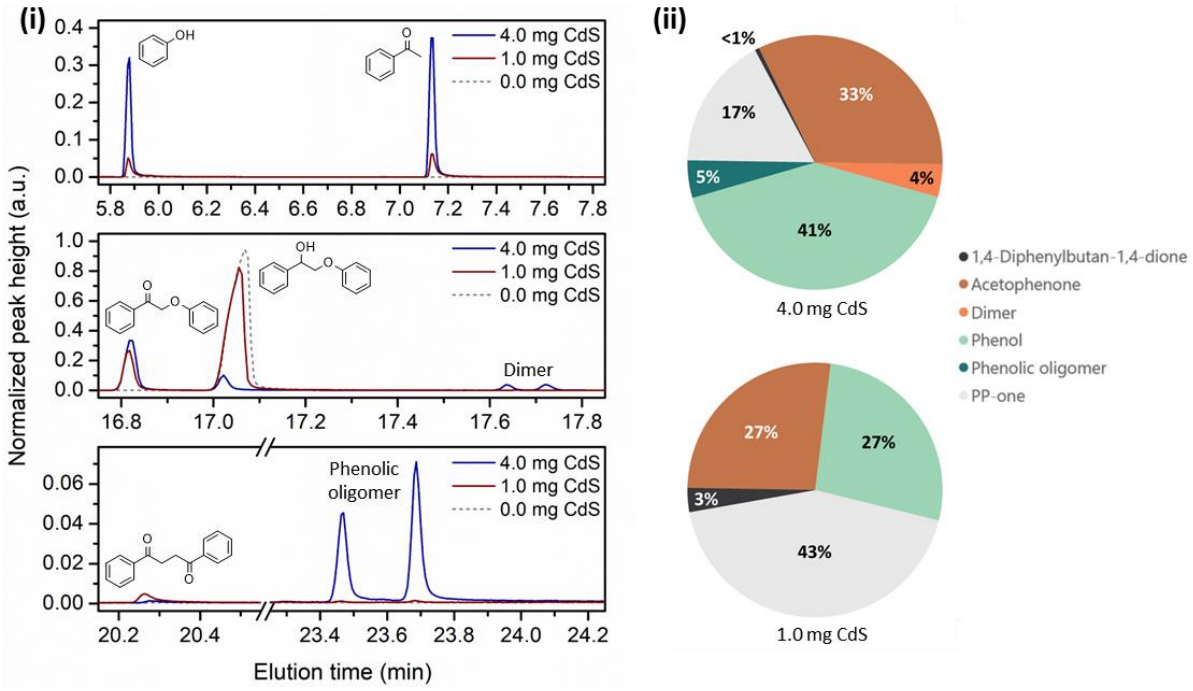

Figure 0.1. (i) GC chromatograms and (ii) product compositions of PP-ol conversion based on catalyst loading (0.02 M PP-ol in MeCN, catalyst (0.0 mg, 1.0 mg, and 4.0 mg CdS-4), λ = 352 nm, t = 24 h, Ar atmosphere).

The product composition is depicted in Figure 3.7(ii). When 4.0 mg of CdS was used to catalyze PP-ol conversion, the composition of acetophenone, at 33%, was lower than that of phenol, at 41%, indicating further reaction of acetophenone to byproducts. The relative stability of phenol after 24 hours also implies that it was likely not involved in side reactions. Therefore, part of the phenolic oligomer likely originated from either PP-ol or PP-one. Under lower catalyst loading, β-O-4 cleavage did not progress as far, reflected by the lower proportion of cleavage products to PP-one. Phenol and acetophenone were present at equimolar amounts, each encompassing 27% of the final reaction mixture, and 1,4-diphenylbutan-1,4-dione was the only byproduct that was observed. The exact reason for the latter's apparent favored formation under low catalyst loading remained unclear, and further insights could be obtained by monitoring the PP-ol conversion over time. However, at this stage, studying PP-ol conversion under neat conditions became the larger priority, and further photocatalysis experiments under solvated conditions were not continued.

Based on PP-ol conversion, the two most viable catalysts for use in further studies were CdS-4 and CdS-7. Every subsequent attempt to repeat CdS-4 synthesis resulted in failure to isolate a usable amount of product, and it is likely that the reproducibility issues stemmed from pH fluctuations during synthesis, which generally affect nanostructure formation.[159] In addition, because the procedure involved using a low boiling point solvent and emphasized chemical precipitation, there would have been issues in modifying the procedure to yield other CdS polymorphs. Notably, hexagonal CdS can generally only be obtained from high-temperature synthesis, and the reference work for the synthesis of CdS-7 demonstrated the possibility of hexagonal CdS being easily produced. As such, the focus was shifted to reproducing CdS-7 synthesis. This attempt was successful, and further experiments involving this catalyst are discussed in Chapter 4.

3.4. Conclusion

This Chapter explored the synthesis of various catalysts to assess their impact on PP-ol conversion under photocatalytic conditions and select one based on specific criteria: high specific surface area, easy crystalline phase modification, high PP-ol conversion rate, and a relatively narrow particle size distribution. Furthermore, it was crucial to ensure the reproducibility of the synthesis procedure, considering variations

in the architectural features of the synthesized CdS catalysts influence their catalytic activity, emphasizing the need for synthesis of CdS catalysts with comparable characteristics.

To this end, various CdS catalysts were synthesized using different existing methods. In some cases, reproducibility issues were observed, where the same procedure can result in CdS NPs possessing different physical properties, namely with regard to polymorphism, particle size, and specific surface area. Minor fluctuations in these features were shown to visibly impact catalytic activity in the photocatalytic conversion of PP-ol. Using the synthesized CdS catalysts in a series of photocatalytic experiments, PP-ol conversion under UV irradiation for 24 hours ranged from 4% to 86%. The main products of PP-ol conversion were phenol, acetophenone, and PP-one. Observed byproducts included anisole, benzaldehyde, 1,4-diphenylbutan-1,4-dione, an unidentified dimer, and an unidentified phenolic oligomer. Kinetic experiments have demonstrated that PP-ol decomposition occurs in two separate pathways: the oxidative β-O-4 bond cleavage to produce phenol and acetophenone, and the oxidation of PP-ol to PP-one. A side experiment also showed that PP-ol conversion varied proportionally with catalyst loading, although this may change depending on the exact CdS catalyst used.

Considering the acceptable specific surface area of the catalyst, its relatively high activity in PP-ol conversion, and a high rate of β-O-4 bond cleavage, CdS-7 was selected for use in subsequent studies. Namely, the synthesis of CdS-7 is reproducible and results in little to no variation of crystalline phases and particle size between batches. Furthermore, the synthesis method itself offers potential for crystalline phase tuning, depending on the synthesis solvent and temperature, as well as architecture modifications, which depend on the rate of addition of the cadmium precursor solution. In addition, the photocatalytic decomposition of PP-ol using CdS-7 progressed at a satisfactory rate. Assuming the relative decomposition rates across all catalysts remain unchanged in thermal conditions and disregarding potential solvent effects, CdS-7 was chosen as the viable catalyst for future experiments.

Chapter 4. The Solvent-free Conversion of Benzyl Alcohol and 2-Phenoxy-1-phenylethanol on CdS

4.1. Introduction

With increasing concerns over the depletion and environmental impact of fossil fuels, biomass has been explored as a source of energy fuel and feedstock for value-added chemicals. Namely, lignin has garnered significant interest due to its under-utilization in large-scale applications.[13–15,17] It is an abundant byproduct of the papermaking industry, which processes cellulose from biomass feedstocks, and is mostly burned as raw fuel.[10] As such, lignin valorization has become a subject of great interest over the years with different catalytic systems and materials having been explored.[12,13,18–24]

Cadmium sulfide (CdS), an n-type II-VI semiconductor with a direct band gap of 2.42 eV, has become a viable candidate for these systems, amongst other metal sulfides.[160] The facile synthesis of CdS is evidenced by the numerous CdS architectures successfully obtained.[161] It has also been established that the electronic properties of CdS are closely related to their structural properties and are therefore tunable by changing their morphology, crystalline phase, size, and composition.[162] Generally, the relatively narrow band gap and band position of CdS make it a versatile catalyst for a multitude of important practical applications, such as in water splitting reactions,[70,163,164] CO_2 reduction,[165–167] and more importantly, decomposition of organic molecules. The latter can encompass the removal of organic pollutants[76,78,82,93–98] or lignin valorization with hydrogen evolution reactions (HERs) occasionally occurring in tandem.[99,100,109,113,114,101–108] Typically, CdS is used as a photocatalyst or electrocatalyst, and while these applications are currently limited to laboratory settings, ongoing research aims to scale up these applications for industrial and commercial use.

Despite this, CdS as a catalyst often suffers from several shortcomings. CdS is generally thermally stable, but it is prone to photocorrosion, especially in aqueous systems.[99,168] Several methods exist to inhibit CdS

photocorrosion,[78,162,169] but generally involve morphological control, including the introduction of dopants and/or co-catalysts,[170,171] the formation of junctions,[112,172] and synthesis of a core-shell structure.[160,173] In a photocatalytic water-splitting system, the addition of hole scavengers or sacrificial agents is also a commonly exploited strategy to inhibit CdS degradation.[79,160,174,175] While effective, this may not be a desirable strategy at a larger scale. To note, using a hole scavenger in a system meant for lignin photodegradation would be counterproductive, as hole generation by CdS is the driving force of these reactions.[176113] Another consideration of metal sulfide-catalyzed redox processes is the contribution of the solvent to the final product of the organic transformations. Occasionally, these contributions are warranted, for example with the solvent acting as a necessary hydrogen donor or enabling better catalyst-substrate interactions, but in other cases, the solvent acts as a reagent, contributing to the generation of byproducts and decreasing reaction selectivity. In the context of lignin valorization, 2-phenoxy-1-phenylethanol (PP-ol) is a typical model molecule used for mechanistic studies, as it contains the β-O-4 linkage ubiquitous in lignin. Through various studies, the effects of different solvents on catalyzed PP-ol decomposition have been reported.[113,116,177–179] However, the CdS-driven conversion of lignin and its derivatives in solvent-free conditions remains unreported to date. In addition, there have also been no reports of pristine CdS being used strictly under thermal conditions.

In this Chapter, the synthesis of ligand-free CdS nanoparticles (NPs) in different crystalline phases is described. Furthermore, the activities of the synthesized CdS NPs in catalyzing the conversion of benzyl alcohol and PP-ol was investigated under various solvent-free conditions. Apart from allowing the investigation of reaction mechanisms by focusing exclusively on the CdS-substrate interaction, the absence of solvents eliminates harmful or unproductive solvent effects, including solvent-promoted photocorrosion. Benzyl alcohol as a substrate has been studied and was chosen in this work for experiment validation purposes, while PP-ol was selected as the substrate and model molecule as it possesses the β-O-4 bond linkage, ubiquitous in lignin.

4.2. Experimental procedures

4.2.1. Synthesis and characterization of CdS nanoparticles (NPs)

CdS NPs were synthesized using the procedure for CdS-7 as described in Chapter 3, which was selected due to the tunability of the procedure itself, as well as the performance of the resulting CdS NPs in the conversion of PP-ol. As described in Appendix F, the procedure was repeated to ensure reproducibility, while further modifications and optimizations to the procedure were done to obtain cubic CdS NPs and hexagonal CdS NPs without changing precursor materials.

Synthesis was done under argon atmosphere. A cadmium stock solution was prepared by dissolving cadmium acetate dihydrate ($Cd(OAc)_2 \cdot 2H_2O$, 2.50 mmol) in 40 mL of ethylene glycol (EG). Separately, sodium sulfide nonahydrate ($Na_2S \cdot 9H_2O$, 40.0 mmol) was dissolved in 40 mL of EG, and the solution was degassed with argon for 10 minutes. To remove all water from the starting material, the sulfur-containing solution was heated to 100°C under vacuum for 30 minutes. This solution was then cooled to 80°C for synthesis of the cubic phase NPs (**CdS-c**). Under rapid stirring, the cadmium stock solution was quickly injected into the sulfur solution. The mixture was left to react at the set temperature for 5 hours. Upon cooling to room temperature, the reaction mixture was diluted with water (1:3 v/v ratio of reaction mixture to water) and centrifuged at 10,000 rpm for 15 minutes, followed by two subsequent washes with water/acetone (1:2 v/v) and finally methanol. The solid was dried under vacuum at 80°C for 10 hours to obtain the final yellow-orange product and stored for further characterization and use. Similar procedures were followed when synthesizing CdS NPs of different crystalline phases. For the synthesis of the mixed phase NPs (**CdS-m**), the reaction temperature was maintained at 175°C. For the synthesis of the hexagonal phase NPs (**CdS-h**), the reaction temperature was maintained at 260°C. To accommodate the increased temperature, EG was substituted with triethylene glycol (triEG), which has a higher boiling point. The washing and drying procedures were identical. The samples were then analyzed by X-ray diffraction (XRD) and transmission electron microscopy (TEM) as per procedures outlined in Section 2.2. EDS spectra and SEM images were collected (Appendix D).

4.2.1.1. Ultraviolet-visible (UV-vis) spectrophotometry

The solid CdS samples were dispersed in acetonitrile (MeCN) and loaded into a quartz cuvette. The spectra were recorded on an Agilent Cary 100 UV-vis spectrophotometer at absorption wavelengths of 200 – 900 nm and at ambient temperature, against the reference solvent using double beam mode.

4.2.1.2. Attenuated Total Reflectance Infrared (ATR-IR) spectroscopy

IR spectra were obtained using an Agilent Cary 630 FTIR Spectrometer equipped with the ATR sampling module. Interfacing and data processing was conducted using the instrument's corresponding Agilent Microlab software. The solid CdS samples were finely ground prior to analysis. Atmospheric corrections were done by recording the background spectra before each sample. The solid samples were loaded onto the ATR crystal and pressed to ensure good contact.

4.2.2. Reaction of benzyl alcohol on CdS NPs

To study the thermal decomposition of benzyl alcohol on CdS, the previously synthesized **CdS-c** (5.0 mg) and benzyl alcohol (0.05 mmol) were loaded into a reaction vial. The neat mixture was purged with argon and the vial was then crimp-sealed. The vessel was heated to 200°C and left to react in the dark for 20 hours. The same procedures were repeated using **CdS-m** and **CdS-h** as the reaction catalyst, and without any catalysts as a reference. For experiments under UV (LED, 5W, $\lambda = 352$ nm) or visible light (LED, 30W, $\lambda \geq 400$ nm), the same amount of catalyst and benzyl alcohol were loaded into the reaction vial, purged with argon, and sealed, followed by irradiation at room temperature for the same length of time as stated above. Following the thermal and photocatalytic experiments, the products of the reactions were analyzed by headspace and liquid GC-MS.

4.2.3. Reaction of 2-phenoxy-1-phenylethanol on CdS NPs

To study the decomposition of 2-phenoxy-1-phenylethanol (PP-ol) on CdS under various conditions, the same procedure was followed as outlined in Section 4.2.2. with a few changes. Namely, for the thermal decomposition experiments, the reaction vials were heated to 250°C instead of 200°C to compensate for

the higher boiling point of PP-ol. For the photocatalytic experiments (UV or visible light), the vials were heated to 60°C during irradiation to melt solid PP-ol and ensure its adsorption on the catalyst surface. A representative diagram of the reaction setups for the solvent-free, CdS-catalyzed conversion of benzyl alcohol and PP-ol is illustrated in Figure 4.1. For the thermal conversion reactions (Figure 4.1(i)), the vial was placed in a preheated sand bath equipped with a thermometer. For the UV (Figure 4.1(ii)) and visible light (Figure 4.1(iii)) conversion reactions, the vial was placed 5 mm in front of the light source. A light shield was employed to isolate the reaction setups from external light sources.

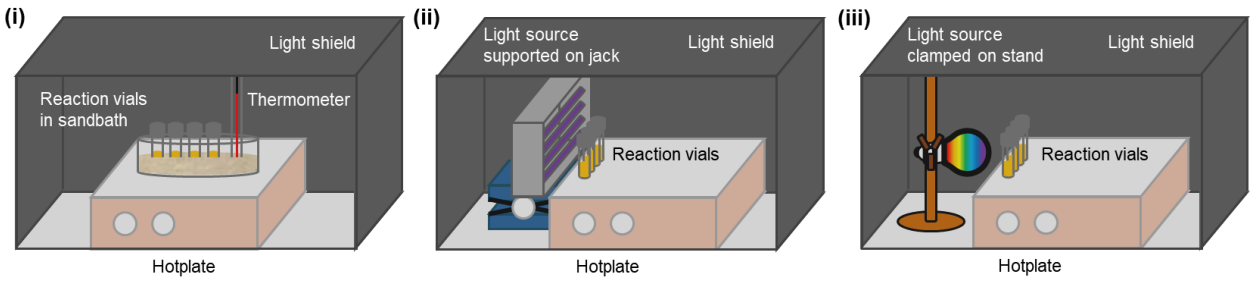

Figure 4.1. Typical reaction setups for the (i) thermal, (ii) UV, and (iii) visible light conversion of benzyl alcohol and PP-ol. The front side of the light shields are illustrated with increased transparency for clarity.

4.2.4. Preparation of liquid GC-MS samples

GC-MS analysis was conducted using methods described in Section 2.2.4.4. After completion of headspace analysis, the neat mixtures were diluted in a 1.0 mg/mL solution of pentachlorobenzene in acetonitrile. The mixture was centrifuged at 12,000 rpm for 10 min and the supernatant was analyzed with GC-MS.

4.3. Experimental results

4.3.1. Characterization of CdS NPs

Through XRD analysis, the crystalline phases of all synthesized NPs were determined. As illustrated in Figure 4.2, the diffraction patterns of **CdS-c** and **CdS-h** matched the reference diffraction patterns of cubic and hexagonal phase CdS, respectively. Both **CdS-c** and **CdS-h** showed phase purity. In addition, the low signal-to-noise ratio of the experimental **CdS-h** pattern suggests that it has the highest order of crystallinity. **CdS-m** shows a noticeable difference compared to the pure hexagonal CdS reference, in that its peaks at

25.02°, 26.48°, and 28.22° have different relative heights. This is caused by the overlap of the cubic (111) peak with the hexagonal (002) peak, which is only possible if both cubic and hexagonal phases are present. Furthermore, the presence of small bumps at 30.62°, as well as at 36.64° and 47.86°, indicates the presence of the cubic (002) plane, along with the hexagonal (102) and (103) planes, respectively. All of this confirms the polycrystalline structure of **CdS-m**. Regarding the phase composition of **CdS-m**, Rietveld analysis of the sample showed a cubic-to-hexagonal phase ratio of approximately 3:7.

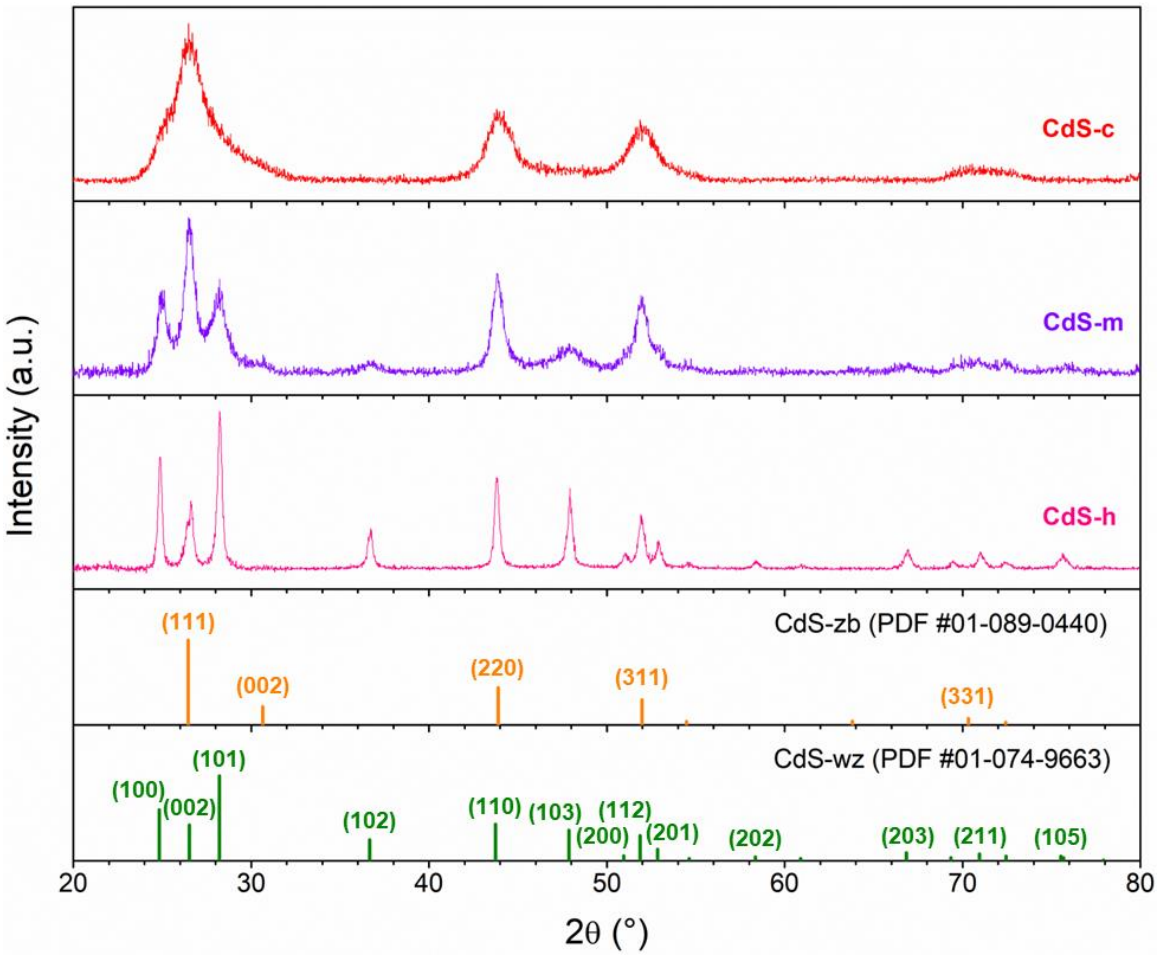

*Figure 4.2. Experimental XRD patterns of **CdS-c**, **CdS-m**, and **CdS-h** compared with reference XRD patterns of cubic CdS (CdS-zb, PDF card no. 01-089-0440) and hexagonal CdS (CdS-wz, PDF card no. 01-074-9663).*

TEM photographs shown in Figure 4.3 show NPs forming aggregates in all cases, and particle measurements found that all the catalysts had various size distributions. **CdS-c** had the smallest average particle size at 9 ± 1 nm. The NPs had the narrowest size distribution and generally amorphous, uniform

geometry. As the synthesis temperature increased, so did the average particle size and size distribution. In the case of **CdS-m**, the particle size was determined to be 15 ± 3 nm. At this temperature, the formation of larger rhombic NPs was observed, implying that particle growth proceeded along specific planes, although these larger NPs did not dominate the synthesized solids. Similar phenomena are observed in **CdS-h**, where particle size averaged at 32 ± 11 nm, and more of the large, less amorphous NPs were observed.

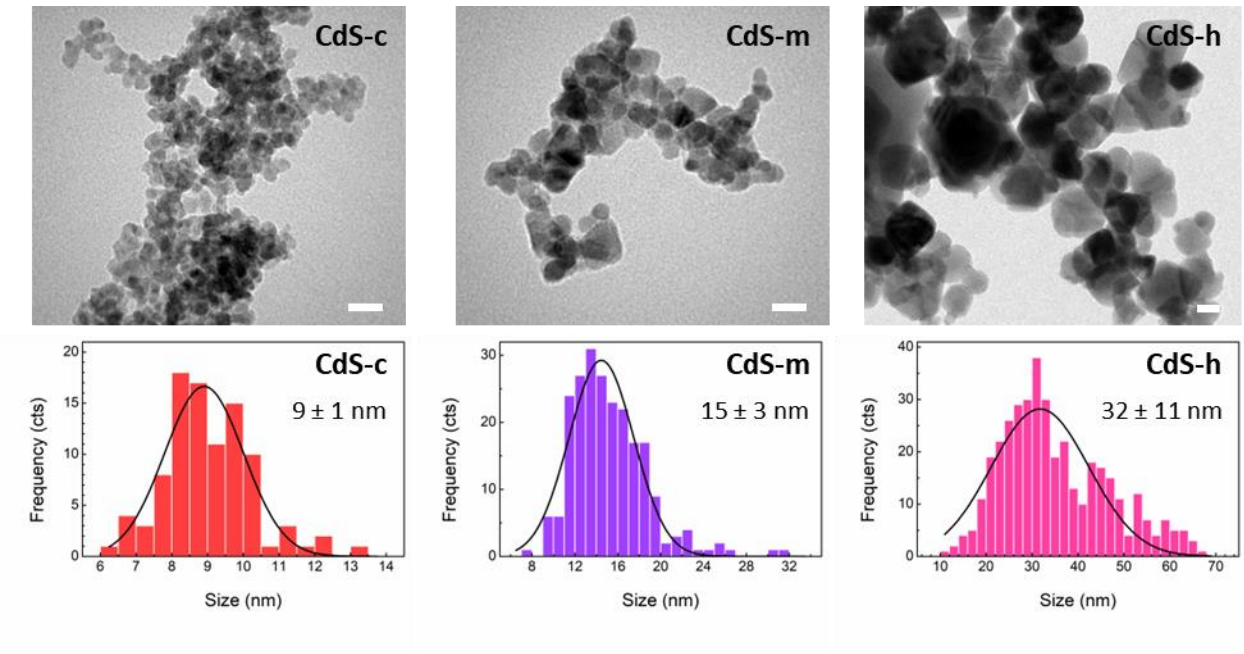

Figure 4.3. Top: TEM images of synthesized CdS catalysts with white bar indicating scale (20 nm). Bottom: size distribution histograms (bottom) of synthesized CdS catalysts with Gaussian fitting curves (black solid lines).

Solid-state ATR-IR measurements were conducted to identify functional groups on the CdS surface, if any. An IR spectrum of the cadmium starting material was also recorded as a reference and to confirm its absence in the final products. The collected spectra, similar to commercial CdS,[180] are shown in Figure 4.4. Across all catalysts, IR measurements show a peak at 1013 cm^{-1} and two shouldering peaks centered at 1115 and 1148 cm^{-1}, typical of CdS.[181–185] These peaks are potentially associated with S-O stretching modes,[186,187] either due to surface sulfur oxidation or interactions with adsorbed atmospheric water. This may also allude to sulfur being the exposed atoms on the catalyst surface. While not confirmed by the spectrum due to instrument measurement range limitations, based on reported values, the Cd-S stretching mode is expected

to be observed at 670 cm^{-1} and below.[180,181,188,189] The samples show a decrease in transmittance at the 650 cm^{-1} cutoff point, but it was not possible to confirm if this is a real peak. The presence of a noisy peak around 1620 cm^{-1} and a broad hump centered at 3370 cm^{-1} represent H-O-H bending and O-H stretching modes respectively, from atmospheric water adsorption.[181,189,190] It is also evident, based on the disappearance of the carboxylate O-C-O stretching modes between 1300 to 1600 cm^{-1}, that none of the $Cd(OAc)_2 \cdot 2H_2O$ starting material remained in the synthesized CdS. The similarity between all the IR spectra and the absence of C-H vibration modes suggest that ethylene glycol and triethylene glycol, which were used as synthesis solvents, are not present as surface ligands. The peaks between 1900 to 2700 cm^{-1} appear in all spectra as they are instrument artifacts due to atmospheric variations and are not associated with any functional groups.

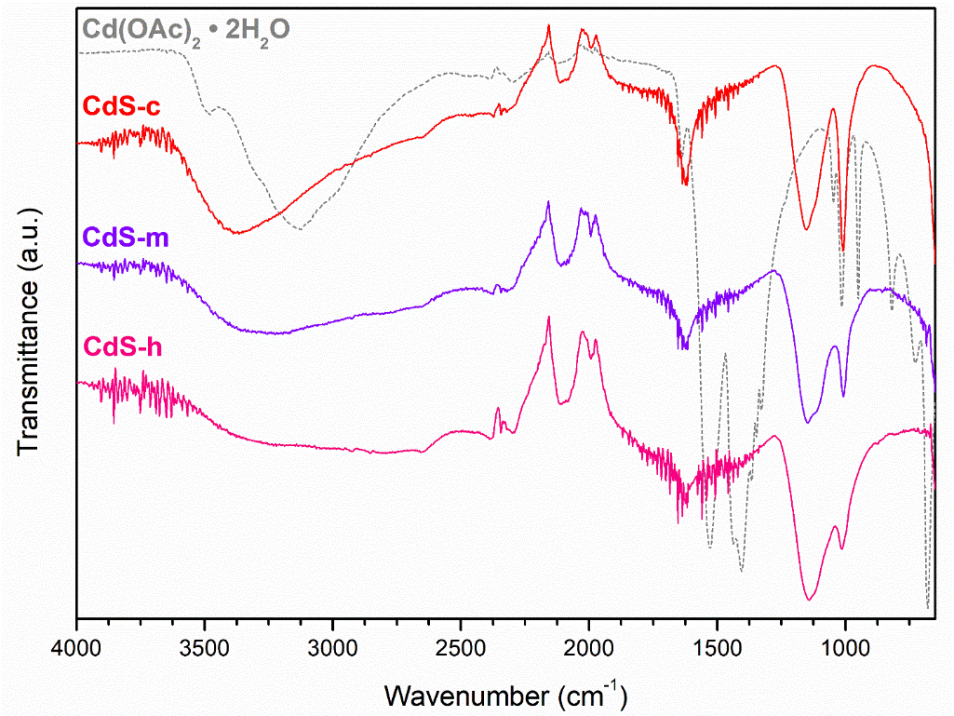

*Figure 4.4. Experimental ATR-IR spectra of $Cd(OAc)_2 \cdot H_2O$, **CdS-c**, **CdS-m**, and **CdS-h**.*

Figure 4.5 depicts the solution-state UV-vis absorbance spectra of the catalysts, suspended in acetonitrile (MeCN) at a concentration of 8.65×10^{-4} mol L^{-1}. In all cases, broad absorption bands with trailing edges were observed, in particular **CdS-c**, whose absorption profile was nearly flat and not very well resolved.

Incidentally, it was observed that in acetonitrile, **CdS-h** dispersed relatively well, while the other two catalysts did not, especially **CdS-c**. As it was established through IR that the CdS NPs do not possess any surface ligands, this increase in dispersibility may also insinuate that **CdS-h** contained additional exposed facets that favor nanoparticle-solvent interactions with acetonitrile, therefore preventing NP aggregation,[191] though the increased particle size of **CdS-h** may have also contributed to this increased dispersion stability. The positions of absorption edges for the CdS NPs lie between 500 – 600 nm, making them suitable for use under visible light irradiation.

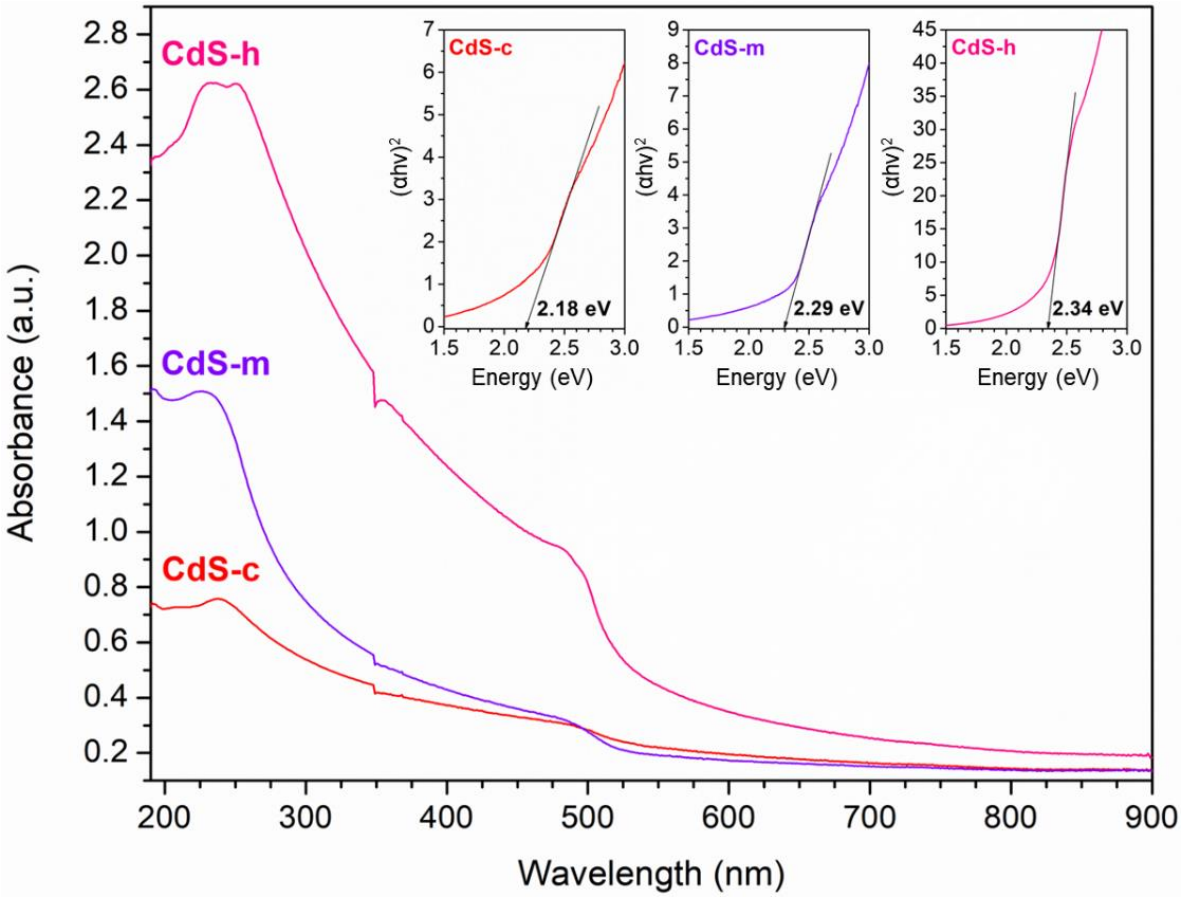

*Figure 4.5 UV-vis absorption spectra of **CdS-c**, **CdS-m**, and **CdS-h** dispersed in MeCN ([C] = 8.65×10^{-4} mol L^{-1}). Inset represents the respective Tauc plot of the CdS NPs.*

To estimate optical band gaps (E_g) of the CdS NPs, graphs of $(\alpha h\nu)^2$ versus hν were plotted based on the Tauc equation for direct allowed transitions of semiconductors:

$$(\alpha h\nu)^2 = B(h\nu - E_g) \quad \textbf{(5)}$$

where α is the absorption coefficient, $h\nu$ is the incident photon energy, B is a constant, and E_g is the band gap energy. The value of α was calculated based on the Beer-Lambert law:

$$\alpha = 2.303A/d \quad \textbf{(6)}$$

where A is the experimentally measured absorbance of the sample and d is the length of the light path, in this case the width of the cuvette. The value of E_g can be obtained by extrapolating the linear part of the curve to the x-axis.[192] The optical band gaps of **CdS-c**, **CdS-m**, and **CdS-h** were estimated to be 2.18, 2.29, and 2.34 eV, corresponding to wavelengths of 569, 541, and 530 nm, respectively. The band gap calculated above is around the same ballpark as the values that were reported in the source literature.[86] The instrument light source switchover point was set to 350 nm, accounting for the sudden jump in intensities.

The spectra in Figure 4.5 show that all three CdS NPs can absorb light in the UV and visible light regions, shown by a peak below 300 nm and a minor peak close to the absorption edge around the 500 nm mark. This highlights the fact that there are at least two accessible energy bands, each in different energy regimes, provided that enough energy is supplied to the system. In other words, the CdS NPs showcase photoactivity in the UV and visible light regions, and electron transitions to higher energy states should be possible. This is corroborated by theoretical approaches taken to determine CdS band structures, where both polymorphs of CdS show multiple accessible energy states, particularly through a direct transition along the same symmetry point.[89–92] From the catalysis perspective, this opens the possibility of observing additional substrate reaction pathways that require a higher energy input, which could differ from reaction pathways observed through the lower-energy, band gap excitation. Furthermore, it was experimentally observed that the band gap increased when going from **CdS-c** to **CdS-h**. This trend is like what has been reported in literature, where increasing wurtzite content also increased the band gap.

Surface areas for each of the catalysts were measured and it was found that increasing hexagonal NP content further decreased surface area. **CdS-c**, **CdS-m**, and **CdS-h** were found to have surface areas of 166.2, 74.95,

and 43.90 m^2/g, respectively. This is consistent with the TEM particle size measurements further summarized in Table 4.1, since it is expected that smaller particle sizes will result in higher surface areas. EDS results (Figure D.1) were obtained to determine the elemental composition of the CdS NPs and SEM images (Figures D.2 to D.4) were also collected to obtain grain images but little relevant information was extracted due to the small size regime of the synthesized CdS NPs.

Table 4.1. Summary of characterization results of synthesized CdS NPs.

Catalyst	Crystalline phase	Particle size (nm)	Surface area (m^2/g)	Band gap (eV)	Absorption edge (nm)
CdS-c	Cubic	9 ± 1	166.2	2.18 eV	569
CdS-m	Mixed	15 ± 3	74.95	2.29 eV	541
CdS-h	Hexagonal	32 ± 11	43.90	2.34 eV	530

4.3.2. Thermal conversion of benzyl alcohol on CdS

Figure 4.6 shows the GC chromatograms of the benzyl alcohol conversion reactions. After 20 hours of heating at 200 °C, benzyl alcohol on its own does not decompose (Figure E.1). However, this is not the case in the presence of CdS NPs as catalysts. From the experiments, it was found that decomposition products include anisole (**1a**), benzaldehyde (**1b**), and benzoic acid (**1d**). We also observed some of the starting material, in this case unreacted benzyl alcohol (**1c**), and some condensation products, which consisted of dibenzyl ether (**1e**), benzyl benzoate (**1f**), dibenzyl sulfide (**1g**), and a coupled product with a fragment ion mass spectrum (MS) peak at m/z 197 (**1h**). Evidently, the CdS NPs catalyze bond cleavages followed by certain condensation reactions to varying degrees depending on the catalyst. While the reactivity of each catalyst varies, the reaction products do not differ. Conversion was estimated to be around 64% for **CdS-c**, 71% for **CdS-m**, and 56% for **CdS-h**.

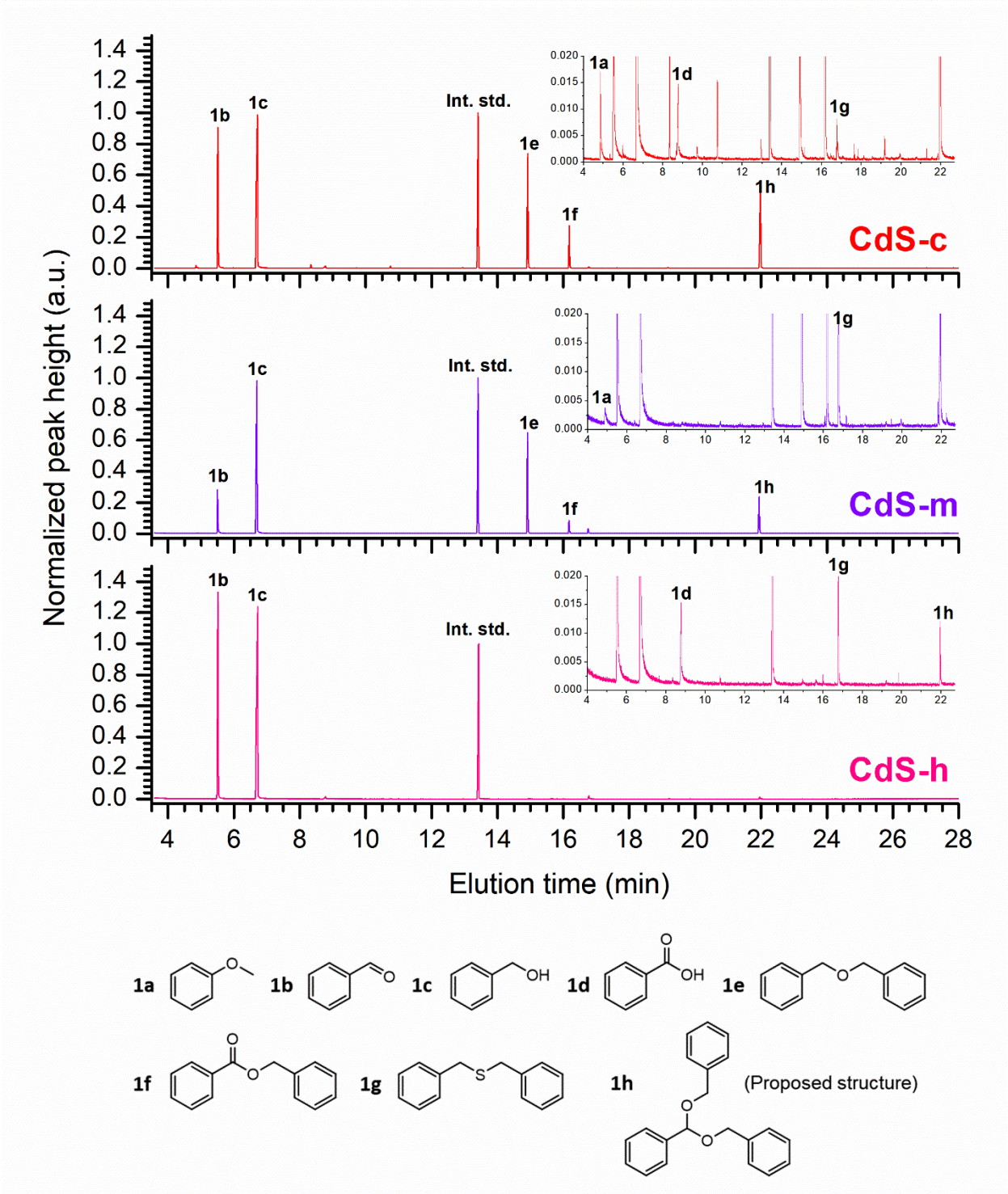

*Figure 4.6. Full GC chromatograms of benzyl alcohol thermal conversion on **CdS-c, CdS-m,** and **CdS-h** (T = 200°C). Insets represent the magnified full spectra to show relevant peaks with very low peak heights. Relevant peaks are labelled, and peak heights are normalized relative to the internal standard.*

Headspace analysis (Figure 4.7) showed that toluene was also produced when the benzyl alcohol conversion was catalyzed with CdS NPs, while the control experiment showed no toluene production.

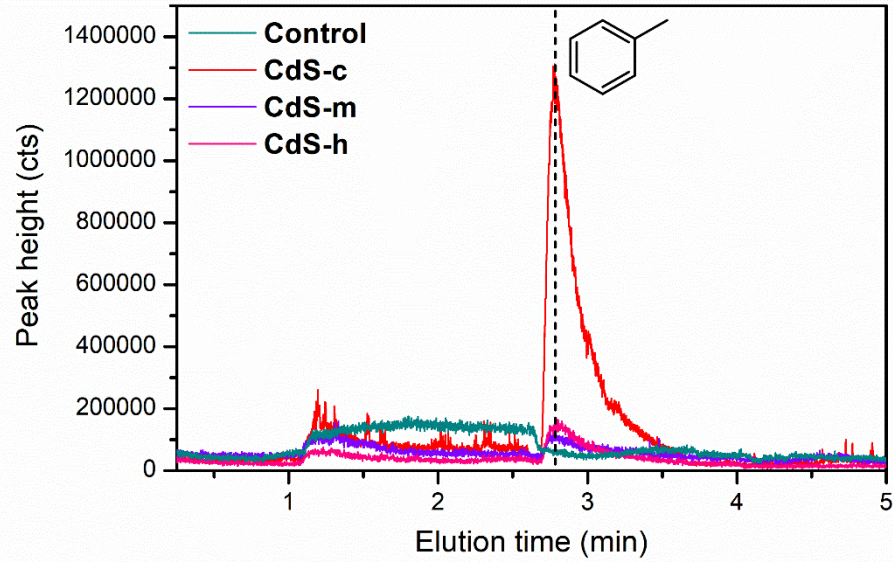

*Figure 4.7. Headspace GC chromatogram of uncatalyzed (control experiment) and catalyzed (**CdS-c, CdS-m,** and **CdS-h**) benzyl alcohol conversion (T = 200°C). Dashed line represents the retention time of toluene.*

Amounts of each reaction product were estimated through peak quantification, except for toluene. Figure 4.8 illustrates the percentage composition of the products after the thermal decomposition reactions were left to run for 20 hours, ignoring loss of products by evaporation. Looking at the decomposition products and beginning with anisole, this product was generally observed in very small amounts and was not involved in any further reactions, as shown by the absence of products bearing phenolic moieties. Furthermore, it was only observed for reactions on **CdS-c** and **CdS-m**, implying the necessity of a cubic crystalline phase of the catalyst for the decomposition pathway to proceed this way. As expected, the main decomposition product of benzyl alcohol, benzaldehyde, was observed in all catalyzed reactions. Amongst all catalysts, benzaldehyde composition is the highest with **CdS-h**. This would suggest that **CdS-c** and **CdS-m** facilitate not only benzyl alcohol conversion, but also any subsequent reactions involving benzaldehyde. Gauging the reactivity of the catalyst was also done by comparing percentage conversion of benzyl alcohol after 20 hours. It was found that the lowest benzyl alcohol conversion occurred with **CdS-**

h, suggesting this catalyst has the lowest catalytic conversion relative to **CdS-c** and **CdS-m**. However, benzyl alcohol decomposition to benzaldehyde was more selective with **CdS-h** than the other catalysts. With regards to the catalyst activity of **CdS-c** and **CdS-m**, it would be reasonable to estimate that **CdS-c** more readily converts benzyl alcohol despite its lower apparent conversion rate, since it was able to produce higher concentrations of the conversion products. Looking at the next product of benzyl alcohol conversion, benzoic acid was detected with **CdS-c** and **CdS-h** but not with **CdS-m**. There currently is no clear correlation between CdS crystalline phase and benzoic acid formation.

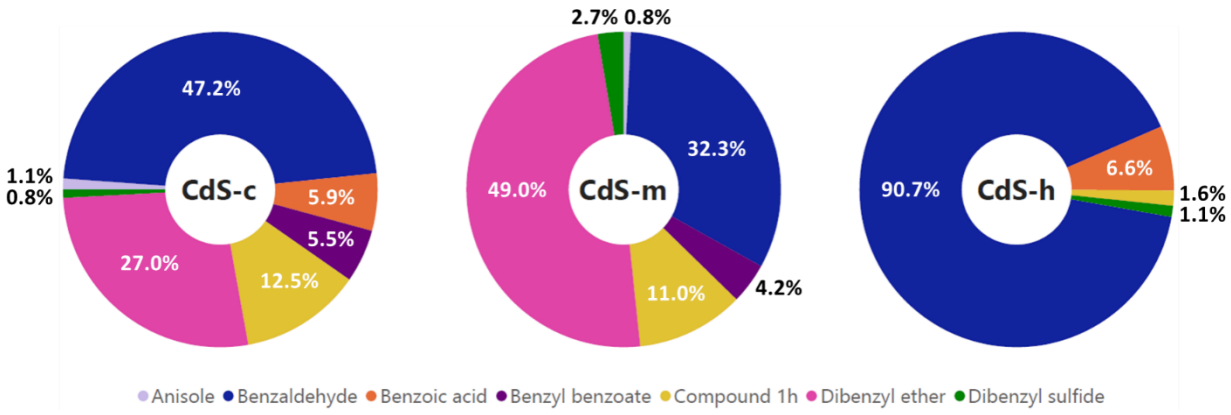

Figure 4.8. Comparison of product compositions of thermal benzyl alcohol conversion (T = 200°C) catalyzed by ***CdS-c, CdS-m,*** *and* ***CdS-h****.*

As elaborated in Chapter 1, numerous studies have reported the coupling reactions of benzyl alcohol on CdS upon light irradiation. We have found that CdS can also catalyze condensation reactions under strictly thermal conditions. More importantly, the resulting coupling products seem to differ from light-catalyzed reactions reported in literature.[99] First, in the case of **CdS-c** and **CdS-m**, the formation of dibenzyl ether and benzyl benzoate was observed. Because these products were not observed in quantitative amounts with **CdS-h**, it implies the necessary presence of a cubic phase, as seen with anisole. Furthermore, the catalysts seem to show a degree of thermal decomposition through sulfur leaching, demonstrated by the formation of dibenzyl sulfide. This supports the notion that sulfur atoms were exposed on the surface[160] and imply the presence of carbon-sulfur interactions favored under thermal conditions. Surprisingly, the lowest degree of decomposition was observed in **CdS-c**, which was synthesized under relatively mild temperature

conditions. The reasons for the difference in dibenzyl sulfide formation remain unclear. A possible mechanism leading to its formation is further discussed in Section 4.4.1.

Lastly, the product **1h** was observed using all catalysts, prominently with **CdS-c** and **CdS-m**, and to a lesser extent with **CdS-h**. Because this product was observed at significantly higher retention times, it is reasonable to deduce that it must contain at least three phenyl rings, which would visibly increase its boiling point relative to all known products (**1a** – **1g**). With regards to its mass spectrum (Figure 4.9(i)), the base peak corresponds to the tropylium cation at m/z 91. A small peak was observed with m/z 197. Considering benzyl alcohol was the starting material, this fragment can only correspond to either a dibenzyl ether or 1,2-diphenylethanol cation. There were weak signals at m/z 105, 106, and 107, all of which are related to the benzaldehyde and benzyl alcohol ions. To note, the mass spectrum for **1h** strongly resembles that of dibenzyl ether. Therefore, we have identified that the most likely structure for **1h** is (dibenzyloxymethyl)benzene (Figure 4.9(ii)). As reported by Kariofilis *et al.*, this compound possesses a fragment ion peak for the $[M\text{-}BnOH]^{\cdot+}$ species at m/z 197 but no molecular ion peak,[193] consistent with our findings. It is worth noting that while the synthesis of **1h** through the catalytic coupling of benzyl alcohol and/or benzaldehyde has been extensively studied, none have employed CdS as the catalyst.[194–198]

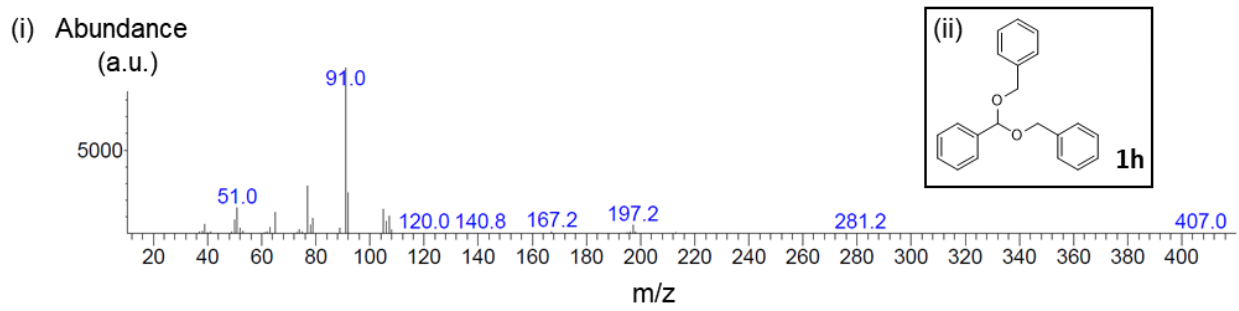

*Figure 4.9. (i) Mass spectrum of compound **1h** (retention time, t = 21.94 min on corresponding chromatogram) and (ii) the proposed structure of compound **1h**.*

4.3.3. Photocatalytic conversion of benzyl alcohol on CdS

To determine whether the conversion of benzyl alcohol proceeds in the same manner under photocatalytic conditions, photocatalytic experiments using single-wavelength UV and visible light were conducted at room temperature. Figure 4.10 shows the GC chromatogram of the benzyl alcohol conversion reactions. It was found that decomposition products include anisole (**1a**), benzaldehyde (**1b**), and benzoic acid (**1d**). Some unreacted benzyl alcohol (**1c**) was also present. With regards to coupled products, benzyl benzoate (**1f**) and compound **1h** were formed; however, UV irradiation of benzyl alcohol did not result in the production of dibenzyl ether or dibenzyl sulfide. Notable differences compared to the thermal experiments are the production of hydrobenzoin (**1i**) and a distinct coupled product (**1j**) with an MS base peak at m/z 196. There seemingly was no difference in products across catalysts; only the concentration of products after 20 h of UV irradiation differed. Furthermore, unlike the thermal reactions, the control experiment under UV irradiation also showed benzyl alcohol conversion, albeit to a limited extent. Benzyl alcohol conversion, calculated from the concentration of products, was 9% in the control experiment, versus 45%, 36%, and 30% with **CdS-c**, **CdS-m**, and **CdS-h**, respectively. Headspace analysis showed no observable amounts of toluene or any other product in any of the reaction mixtures, regardless of the presence of CdS NPs (Figure E.3). No organic sulfur species were observed in any of the UV experiments, hinting that the catalysts underwent little to no photocorrosion.

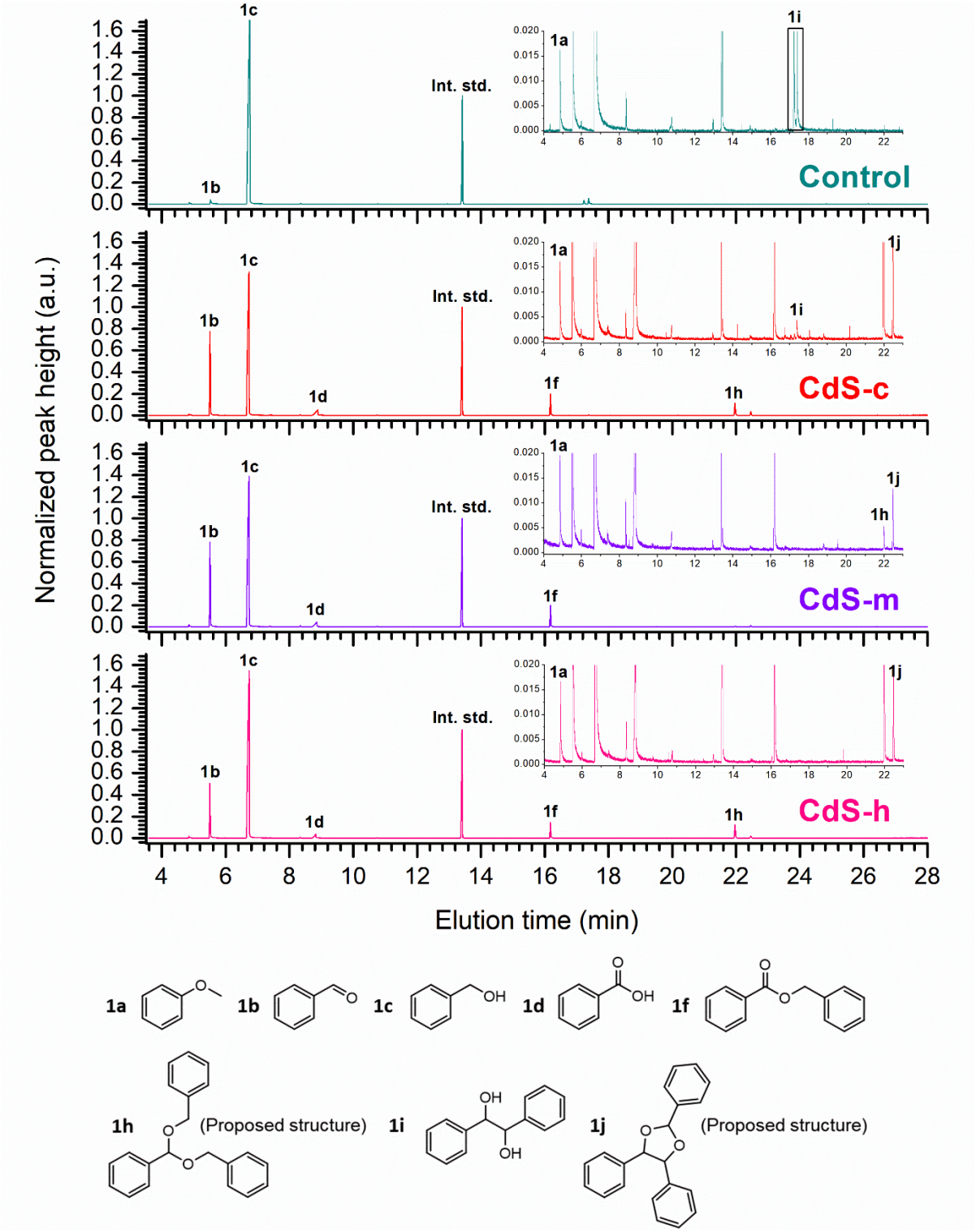

Figure 4.10. Full GC chromatograms of benzyl alcohol photocatalytic conversion, uncatalyzed and with ***CdS-c,*** ***CdS-m,*** *and* ***CdS-h*** *(UV, λ = 352 nm). Insets represent the magnified full spectra to show relevant peaks with very low peak heights. Relevant peaks are labelled, and peak heights are normalized relative to the internal standard.*

Figure 4.11 illustrates the composition of the final reaction mixtures upon UV irradiation. To note, a minimal temperature increase due to irradiation was observed and was not sufficient to induce thermal reactions. Anisole was once again observed across all catalysts and in slightly higher amounts relative to the thermal experiments. Nonetheless this pathway remains unfavorable, and there were no significant differences in final anisole yield across all catalysts. Interestingly, when CdS is absent, anisole was also produced in similar concentrations, which implies this minor decomposition pathway via UV irradiation was intrinsic to the parent molecule. Indeed, benzaldehyde was the dominant product of benzyl alcohol decomposition. **CdS-m** proportionally produced more benzaldehyde than **CdS-c** and **CdS-h**. Benzoic acid proportions were roughly equal across all catalysts. For condensation products, benzyl benzoate proportions were similar with **CdS-m** and **CdS-h**, and slightly lower with **CdS-c**.

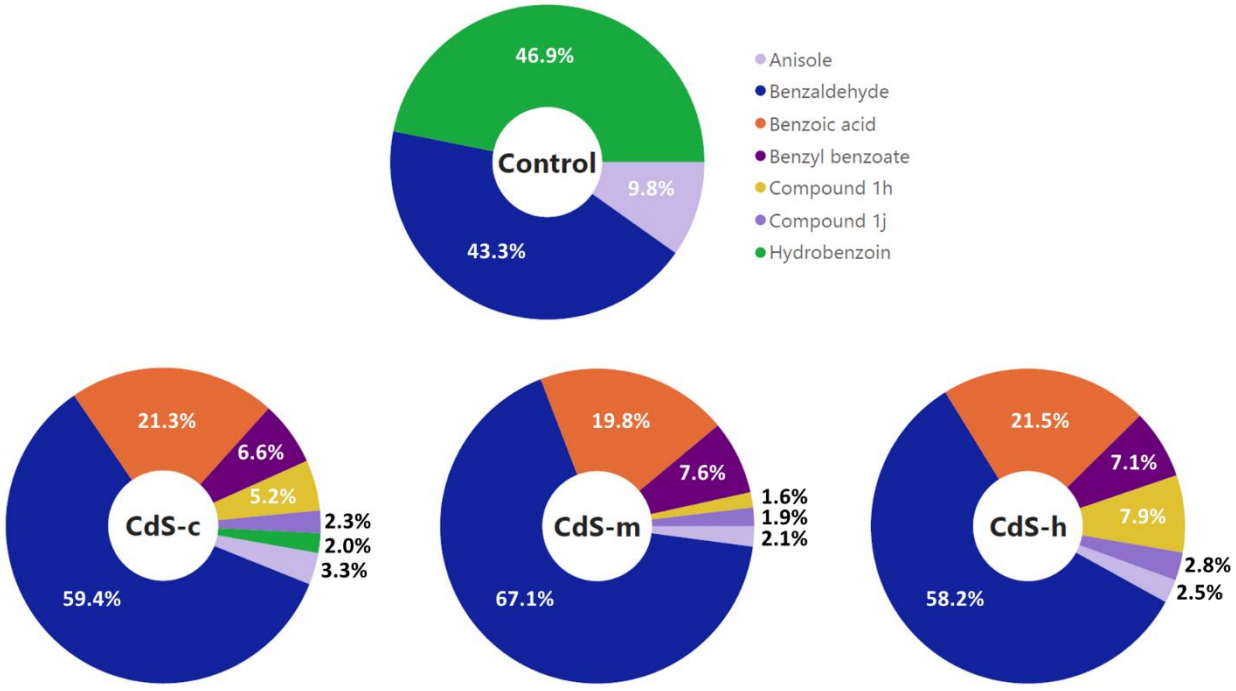

*Figure 4.11. Comparison of product compositions of photocatalytic benzyl alcohol conversion (UV, λ = 352 nm) of the control experiment and under catalysis by **CdS-c, CdS-m,** and **CdS-h**.*

Near negligible amounts of hydrobenzoin were observed using **CdS-c**, while **CdS-m** and **CdS-h** did not seem to favor the formation of this product at all. Most likely, the CdS NPs catalyzed its subsequent conversion to compounds **1h** and **1j**, although **CdS-c** seemed to have stabilized this product. Conversely,

hydrobenzoin was the predominant product in the control experiment, indicating that the carbon-centered radical species generated through the UV irradiation of benzyl alcohol undergo oxidative C-C coupling by default. Because hydrobenzoin concentration was the highest in the control experiment, this would suggest that further reaction pathways towards larger molecules are not accessible unless benzyl alcohol conversion is catalyzed. The presence of compound **1h** upon UV irradiation itself is interesting. This suggests that the CdS NPs can catalyze thermal reaction pathways to a limited extent. Under UV conditions, **CdS-m** catalyzes the formation of **1h** only slightly. Since benzaldehyde proportions were higher with said catalyst, and benzaldehyde is one of the starting materials for **1h**, the smaller proportion of **1h** could be attributed to the faster desorption of benzaldehyde from **CdS-m**, leading to less **1h** formation compared to **CdS-c** and **CdS-h.** The higher accessibility of other pathways could have contributed to the lower proportion of **1h**.

The last product observed was a different coupled product **1j** with an MS base peak at m/z 196 (Figure 4.12(i)). It was observed as a minor product across all catalysts at later retention times. Interestingly, this compound was seen eluting at two distinct retention times in the case of **CdS-m**. Looking at the mass spectrum of compound **1j**, spectrum matching to the database suggested either 2,3-diphenyloxirane or 2,4,5-triphenyl-1,3-dioxolane as potential products. However, based on the long retention time, it is more likely that **1j** is a large molecule with at least three phenyl rings. Therefore, we propose that 2,4,5-triphenyl-1,3-dioxolane (Figure 4.12(ii)) is the more viable structure of **1j**, and this choice can be further rationalized since this molecule can be formed through the acetalization of benzaldehyde and hydrobenzoin.[199] The fragmentation pattern of **1j** also matches those reported for 2,4,5-triphenyl-1,3- dioxolane in literature.[200]

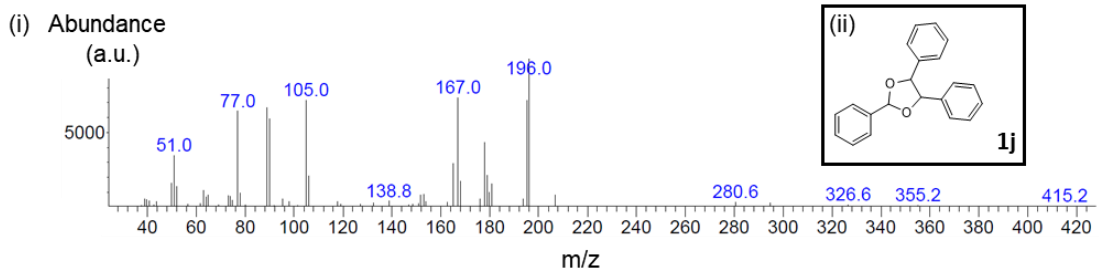

*Figure 4.12. (i) Mass spectrum of compound **1j** (retention time, t = 22.46 min on corresponding chromatogram) and (ii) the proposed structure of compound **1j**.*

In the second series of photocatalysis experiments, this time employing visible light, the control experiment showed that benzyl alcohol does not undergo any sort of conversion. The GC headspace chromatogram, depicted in Figure 4.13, showed that toluene was only present under catalysis of **CdS-m**.

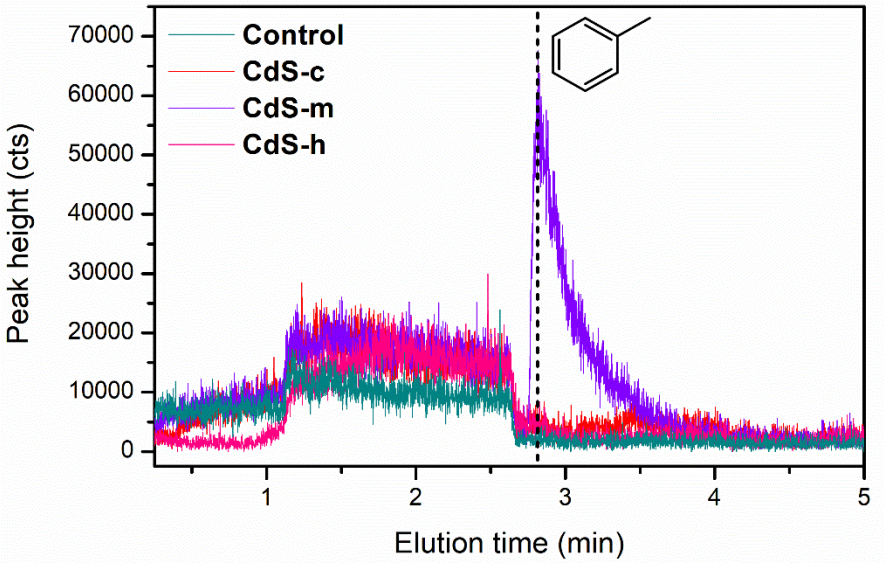

*Figure 4.13. Headspace GC chromatogram of uncatalyzed (control experiment) and catalyzed (**CdS-c, CdS-m,** and **CdS-h**) benzyl alcohol conversion (visible light, $\lambda \geq 400$ nm). Dashed line represents the retention time of toluene.*

Figure 4.14 shows the GC chromatogram of benzyl alcohol conversion under visible light. The control experiment showed no other products (Figure E.2). In this series of experiments, anisole, dibenzyl ether, and dibenzyl sulfide were completely absent from the final reaction mixture, while benzaldehyde (**1b**), and benzoic acid (**1d**), in addition to some unreacted benzyl alcohol (**1c**) and minor amounts of benzyl benzoate (**1f**) were detected. Instead of generating smaller decomposition products, many coupling products were observed, such as deoxybenzoin (**1k**), benzoin (**1l**), benzil (**1m**), and hydrobenzoin (**1i**), as well as various coupling products that are currently unidentified, labelled **1n** and **1o**, for which proposed structures were discussed below. A quick glimpse of the chromatograms shows a significantly higher rate of conversion in comparison to the thermal and UV experiments, regardless of the CdS NPs used. Benzyl alcohol conversion was shown to be highest with **CdS-m** at 97%, followed by **CdS-c** at 95% and finally **CdS-h** at 83%. Once again, little to no photocorrosion was observed based on the absence of organic sulfur species.

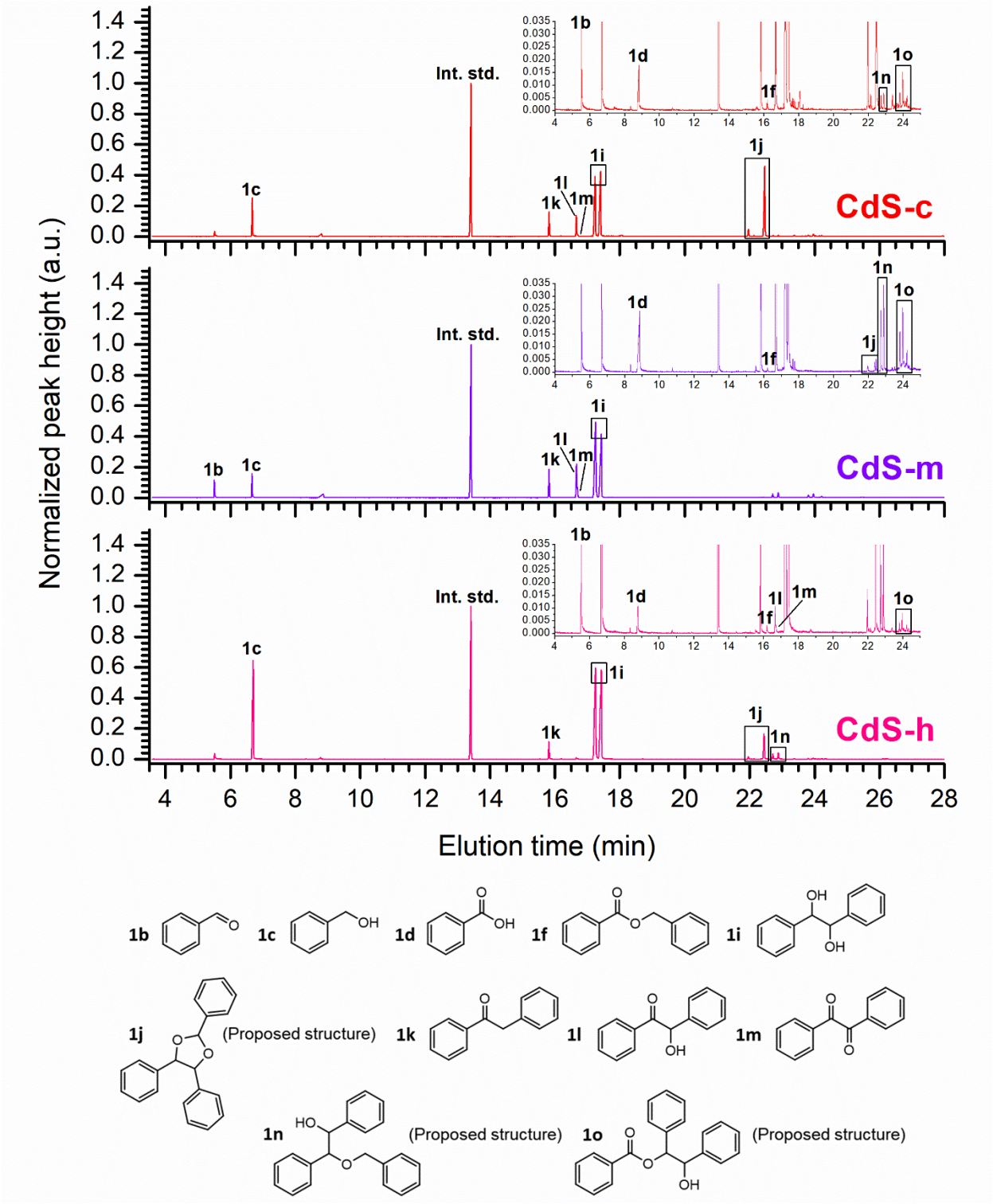

*Figure 4.14. Full GC chromatograms of benzyl alcohol photocatalytic decomposition on **CdS-c, CdS-m,** and **CdS-h** (visible light, $\lambda \geq 400$ nm). Insets represent the magnified full spectra to show relevant peaks with very low peak heights. All relevant peaks are labelled, and peak heights are normalized relative to the internal standard.*

Looking at benzyl alcohol conversion products (Figure 4.15), benzaldehyde in the **CdS-m** reaction mixture was proportionally the highest across all catalysts, around double that of the **CdS-c** and **CdS-h** mixtures, implying that **CdS-m** might have been better at inhibiting its conversion to other products. Benzyl benzoate was produced in small amounts and in similar concentrations across all catalysts. Benzoic acid was observed with all catalysts, with no clear dependence on crystalline phase.

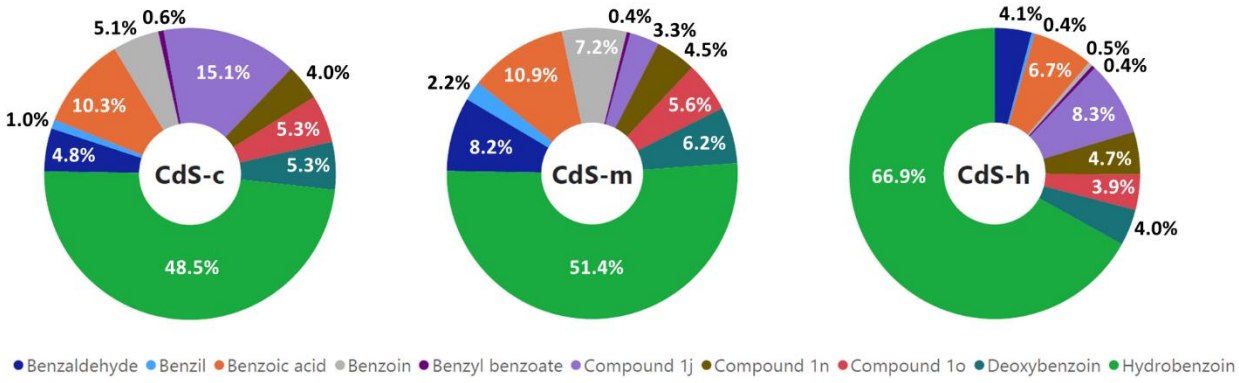

*Figure 4.15. Comparison of product compositions of photocatalytic benzyl alcohol conversion (visible light, $\lambda \geq 400$ nm) catalyzed by **CdS-c**, **CdS-m**, and **CdS-h**.*

To compare the overall yield of coupling products, they were first grouped into two categories. The intermediate size products consist of hydrobenzoin, benzoin, benzil, and deoxybenzoin. Large coupling products encompass all products with retention times longer than 21 minutes on the chromatogram. Looking at the intermediate-size products, diastereomers of hydrobenzoin were observed in increasing proportions with **CdS-c**, **CdS-m**, and **CdS-h**. Because a portion of the hydrobenzoin underwent further oxidation in this series of photocatalytic experiments, this trend would suggest that the purely hexagonal crystalline phase of the CdS NPs may play a role in stabilizing hydrobenzoin and inhibiting its subsequent conversion. The oxidation of hydrobenzoin was reflected through the presence of benzoin in the reaction mixture, produced from the oxidation of one alcohol group of hydrobenzoin. Subsequent oxidation of the other alcohol led to benzil, also observed. As with the two previously-mentioned products, deoxybenzoin, likely via pinacol rearrangement of hydrobenzoin, was formed in order of increasing proportions using **CdS-h**,

then **CdS-c**, and finally **CdS-m**. This trend suggests that the mixed phase crystalline structure may have played a role in the further oxidation of hydrobenzoin.

The appearance of large coupling products began with **1j**, at retention times of 21.96 and 22.46 minutes. The fact that this product does not appear under thermal conditions suggests its formation can only proceed under photocatalytic conditions. Looking at the mass spectra of peaks with retention times above 22.50 minutes, there were generally two distinct fragmentation patterns. As such, the compounds with the same mass spectra were grouped together, resulting in two general assignments, **1n** and **1o**. Beginning with **1n** (Figure 4.16(i)), this compound was observed eluting at 22.71 and 22.88 minutes with all catalysts. While some similarities with the mass spectra of previous products were observed, major distinctions can be made, namely through the appearance of fragment ion peaks with m/z 270 and m/z 213. The latter can be attributed to a deprotonated hydrobenzoin fragment. The presence of m/z 105 ions in the mass spectrum suggests fragmentation to benzoyl fragments, and noticeable tropylium fragments at m/z 91 suggest a benzylic moiety in the structure of **1n**. We propose that **1n** corresponds to 2-benzyloxy-1,2-diphenylethanol (Figure 4.16(ii)). This prediction can be rationalized by the fact that it elutes not too long after **1j**, which under reductive conditions has been shown to convert to **1n**. Currently, reported reduction methods involve the use of a reducing agent such as diisobutylaluminium hydride (DIBAL-H). However, it follows that photoreduction or hydrogenation by adsorbed hydrogen may also be possible.[201–203] To note, the ketone analogue of the proposed structure could also be considered due to the presence of the *m/z* 105 fragment ion in the mass spectrum. Confirming exactly which analogue is formed strictly based on GC-MS data is not trivial; to date, there is little to no data on the fragmentation patterns of either form (alcohol or ketone) in literature.

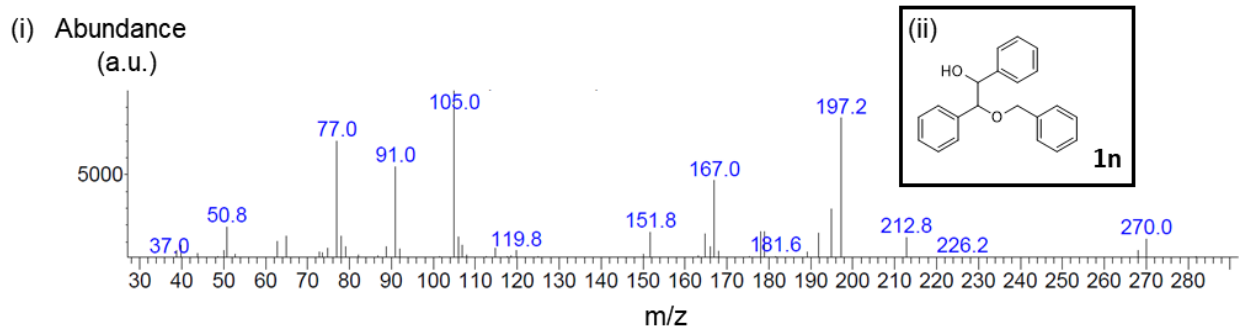

*Figure 4.16. (i) Mass spectrum of compound **1n** (retention time, t = 22.71 min on corresponding chromatogram) and (ii) the proposed structure of compound **1n**.*

Meanwhile, the second unidentified compound, **1o** (Figure 4.17(i)) eluted beginning at 23.81 minutes. Despite its similar mass spectrum to **1n**, there were some important distinctions in the fragmentation pattern. Firstly, the relative abundance of the tropylium ion (m/z 91) in the mass spectrum of **1o** is lower than in **1n**. This would imply that **1o** does not have a "free" benzylic moiety. In addition, there were no m/z 197 fragment ions; they were instead replaced by a m/z 195 fragment ion, which can correspond to deprotonated 1,2-diphenylethanone. The m/z 167 fragment ion also has a higher relative abundance compared to **1n**, indicating a difference in structure. In combination with its slightly higher retention time, most likely due to a higher molar mass, and based on available literature, we propose **1o** to be 2-benzoyloxy-1,2-diphenylethanol (Figure 4.17(ii)),[204,205] although with the currently available experimental data, the ketone analogue should not be dismissed.[206–208]

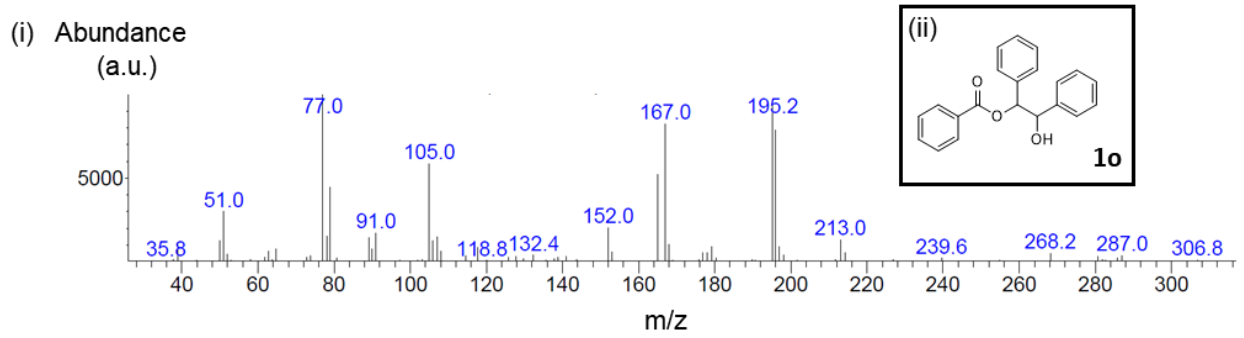

*Figure 4.17. (i) Mass spectrum of compound **1o** (retention time, t = 23.80 min on corresponding chromatogram) and (ii) the proposed structure of compound **1o**.*

4.3.4. Thermal decomposition of PP-ol on CdS

Following thermal and photocatalytic conversion studies of benzyl alcohol on CdS, a similar set of experiments were conducted on 2-phenoxy-1-phenylethanol (PP-ol) as a model molecule containing the β-O-4 linkage, ubiquitous in lignin. As seen in Figure 4.18, the headspace GC peak at 4.41 minutes was attributed to styrene, which was only formed under CdS-catalyzed conditions, based on the absence of the styrene peak in the control experiment. No other volatile products were detected.

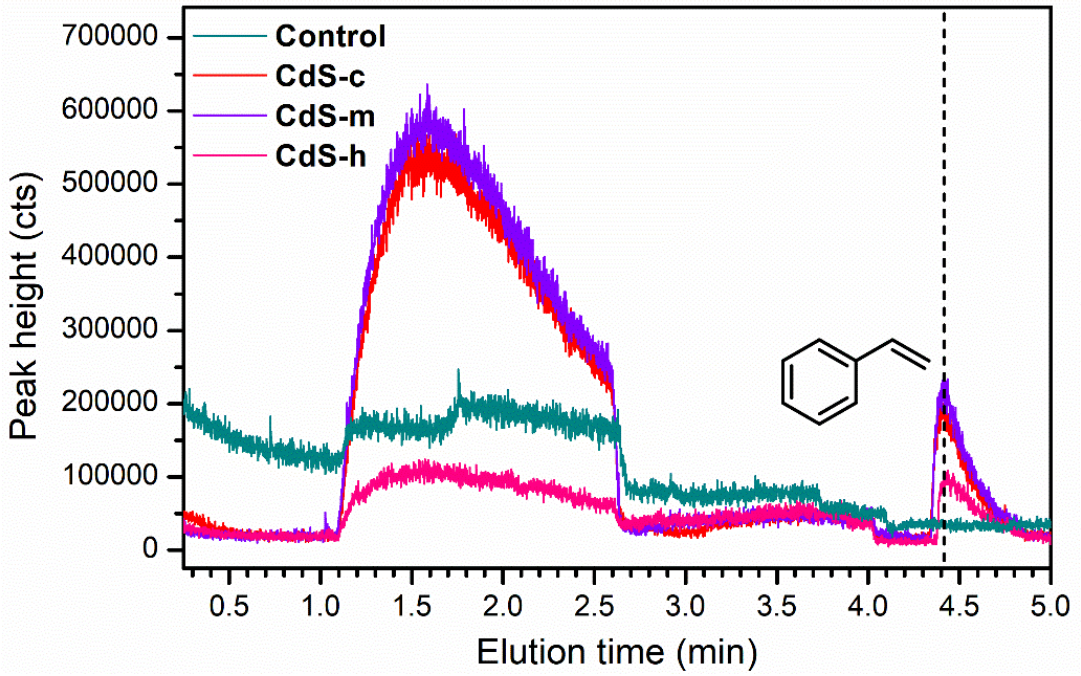

*Figure 4.18. Headspace GC chromatogram of uncatalyzed (control experiment) and catalyzed (**CdS-c**, **CdS-m**, and **CdS-h**) PP-ol conversion (T = 250°C) Dashed line represents the retention time of styrene.*

Figure 4.19 shows the GC-MS spectra of the PP-ol decomposition reactions. It was found that products of decomposition include anisole (**1a**), benzaldehyde (**1b**), phenol (**2a**), acetophenone (**2b**), benzoic acid (**1d**), phenyl benzoate (**2c**), and 2-phenoxy-1-phenylethanone, PP-one (**2h**). Unreacted PP-ol (**2i**) was also present, along with other proposed decomposition products (**2d** – **2f**). Solely when using **CdS-m**, an unknown product (**2j**) was observed. The control experiment, where PP-ol was heated on its own, produced a negligible amount of PP-one as the sole conversion product of the parent molecule (Figure E.1). PP-ol conversion was calculated to be 27%, 24%, and 11% with **CdS-c**, **CdS-m**, and **CdS-h**, respectively.

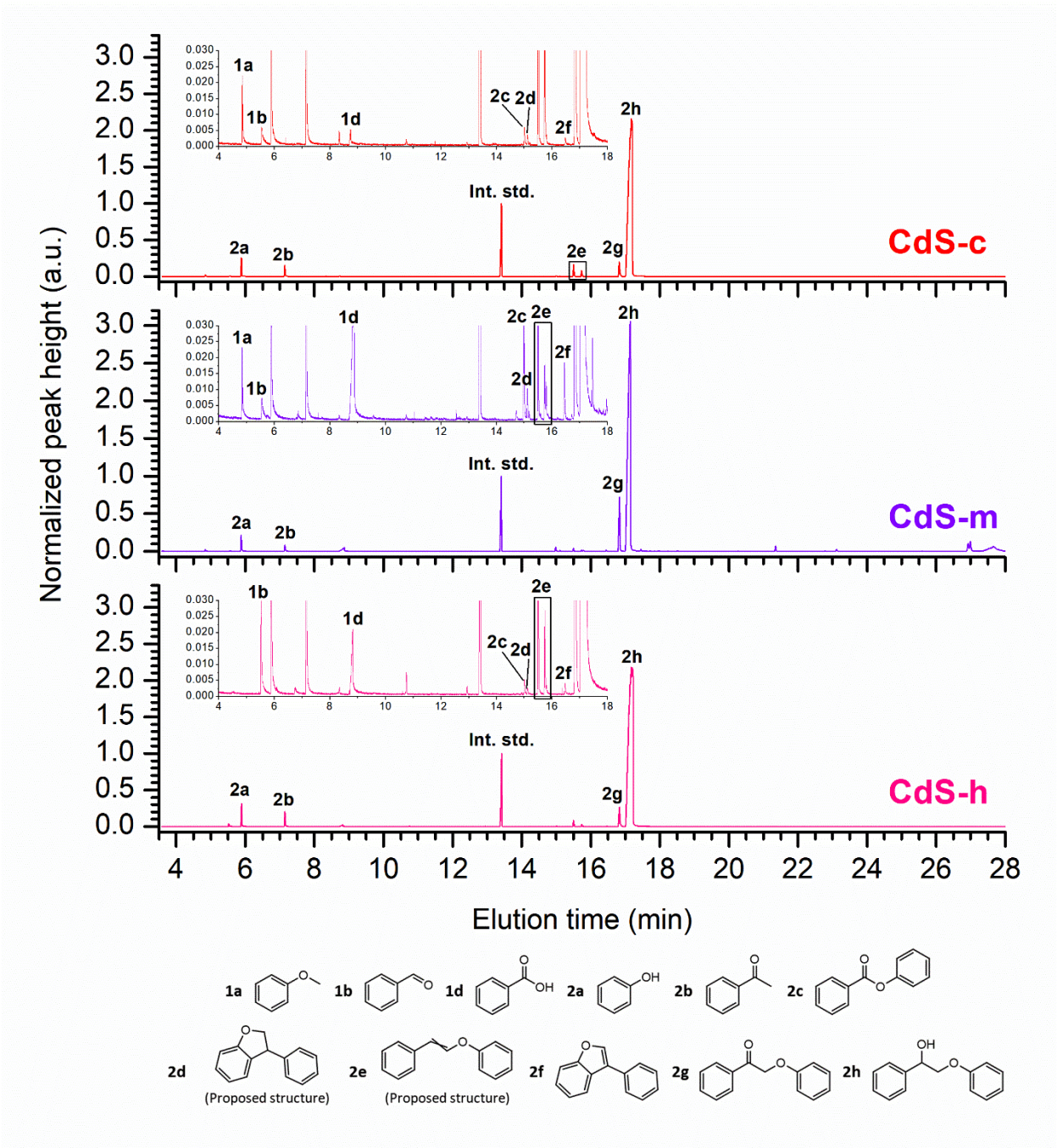

*Figure 4.19. Full GC chromatograms of PP-ol thermal conversion on **CdS-c**, **CdS-m**, and **CdS-h** (T = 250°C). Insets represent the magnified full spectra to show relevant peaks with very low peak heights. Relevant peaks are labelled, and peak heights are normalized relative to the internal standard.*

The peaks for each product were quantified, except for styrene. Figure 4.20 illustrates the percentage composition of the products after the thermal conversion reactions were left to run for 20 hours, ignoring all loss of products by evaporation. Anisole was only observed for reactions on **CdS-c** and **CdS-m**, and like the thermal decomposition of benzyl alcohol, the presence of the cubic crystalline phase seemed to lead to anisole formation. However, the mechanism for its formation may be different due to structural differences of the parent substrate. Benzaldehyde was detected in all catalyzed reactions, with the highest proportion found with **CdS-h** at roughly the same proportion as **CdS-c**. Benzoic acid was more prominent in reactions using **CdS-m**, although **CdS-c** and **CdS-h** seemed to also facilitate its formation. The expected products of the β-O-4 bond cleavage, phenol and acetophenone, were observed across all catalysts. However, in all cases, the amount of phenol after 20 hours is always more than twice the amount of acetophenone.

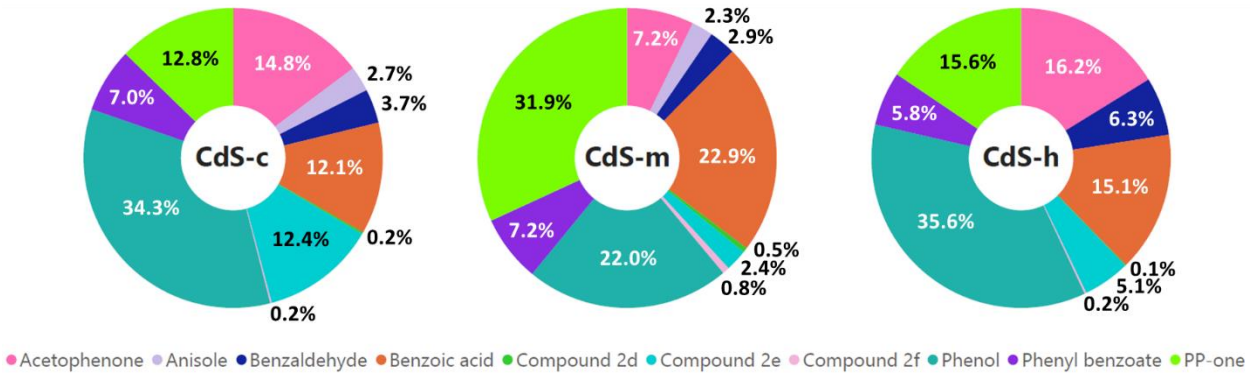

*Figure 4.20. Comparison of product compositions of thermal PP-ol conversion (T = 250°C) catalyzed by **CdS-c**, **CdS-m**, and **CdS-h**.*

Looking at other GC chromatogram peaks, phenyl benzoate was assigned to the peak at 15.00 minutes through database spectral matching. This product was a result of benzoic acid and phenol condensation and was found to have been catalyzed by **CdS-c** and **CdS-m** roughly to the same extent, and slightly less by **CdS-h** based on its proportions relative to other products of PP-ol conversion. Phenyl benzoate made up around 6-7% of the final products of PP-ol conversion and, while a minor byproduct, was not negligible.

The next unidentified peaks on the chromatograms are those around 15.50 and 15.74 minutes. The associated mass spectrum for each peak is depicted in Figure 4.21(i) and 4.21(ii). Evidently, despite the

slightly different retention times on the column, the fragmentation patterns are identical. Thus, the chromatogram peaks likely refer to the same compound with different isomers. For brevity, the two peaks were grouped as those belonging to compound **2e**. Analyzing the mass spectra themselves, the m/z 196 ion is most likely the molecular ion $[M]^{\cdot+}$, considering the retention time. Though not annotated, there is a distinguishable ion peak at m/z 103, which is indicative of a $[M - PhO]^{\cdot+}$ fragment. The ion with m/z 94 corresponds to a phenol molecular ion, while the m/z 91 ion corresponds to a tropylium ion. This would suggest the presence of phenoxy and benzyl moieties in the structure of compound **2e**. Based on the experimental data, it is suspected that compound **2e** corresponds to *cis* and *trans* isomers of β-phenoxystyrene (Figure 4.21(iii)). Indeed, the fragmentation pattern closely matches those reported in literature. Furthermore, **2e** has been reported as one possible product of PP-ol thermal decomposition.[116] Based on the product proportions in Figure 4.19, the formation of **2e** dominated with **CdS-c**, followed by **CdS-h**, and finally **CdS-m**.

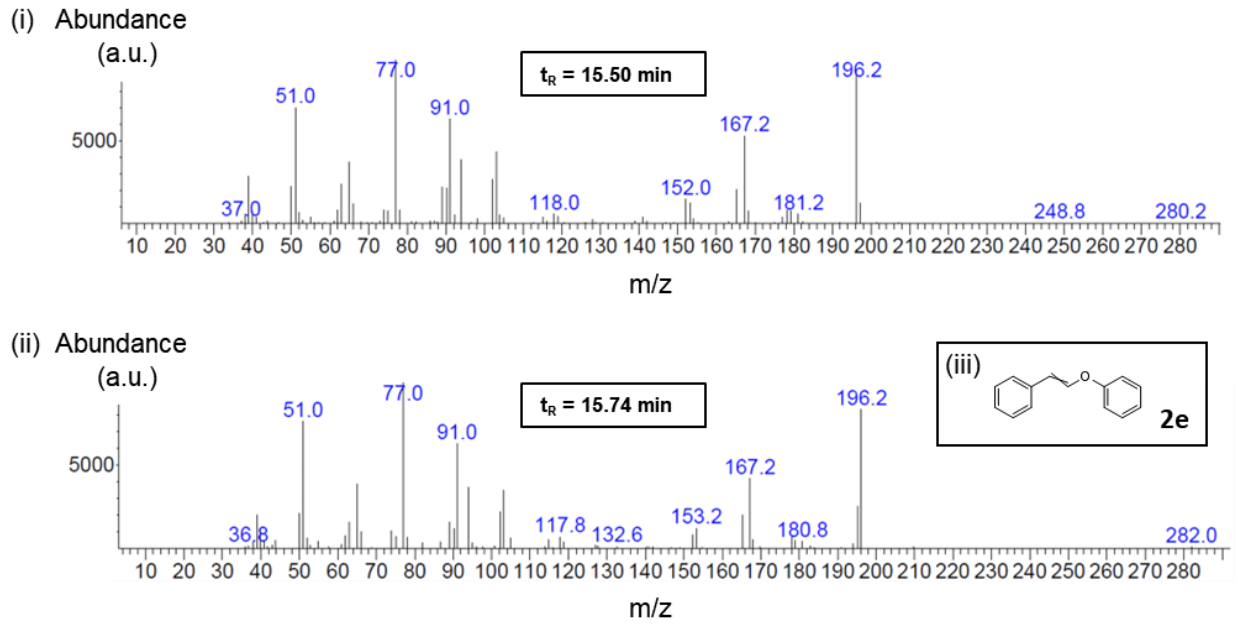

*Figure 4.21. Representative mass spectra of chromatogram peaks with retention times of (i) 15.50 and (ii) 15.74 minutes, as well as (iii) the suggested structure of compound **2e**.*

Byproducts that were present in even smaller amounts in the final reaction mixtures were compounds **2d** and **2f**, making up less than 1% of all PP-ol conversion products regardless of the catalyst used. The

identification of **2f** was slightly more straightforward and is therefore discussed first. The chromatogram peak assigned to compound **2f** was observed at 16.46 minutes. Its associated mass spectrum is shown in Figure 4.22(i). Stipulating that the molecular ion peak is at m/z 194 and considering all observed products of PP-ol conversion, through spectral matching and based on literature searches, it is likely that the structure of **2f** can be attributed to 2-phenylbenzofuran[209,210] or 3-phenylbenzofuran,[211,212] formed from the cyclodehydration of PP-one. It is worth noting that the two isomers exhibit similar fragmentation patterns and are difficult to distinguish[213] without the use of additional characterization methods or through direct comparison with a known standard.[49] It is generally reported that in PP-one cyclodehydration, 3-phenylbenzofuran is produced first. Harsh reaction conditions such as higher temperatures, increased strength and/or number of acid sites in heterogeneous catalysts, or increased acidity of homogeneous catalysts tend to drive the subsequent isomerization of 3-phenylbenzofuran to 2-phenylbenzofuran.[214–216] Although our PP-ol thermal decomposition experiments were conducted at high temperatures, CdS seemed to inherently be inefficient for cyclodehydration reactions, shown by the low concentrations of **2f**. Because the formation of the kinetic product is favored, 3-phenylbenzofuran was assigned to **2f** (Figure 4.22(ii)).

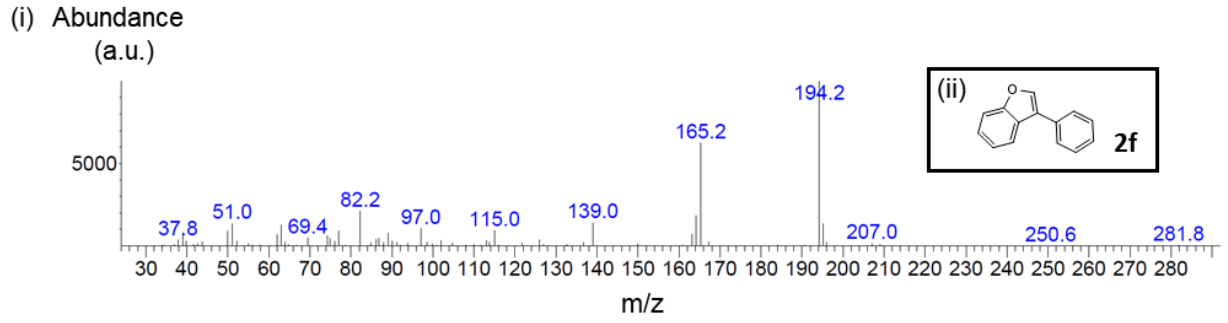

*Figure 4.22. (i) Mass spectrum of compound **2f** (retention time, t = 16.46 min on corresponding chromatogram) and (ii) the proposed structure of compound **2f**.*

Lastly, compound **2d** was detected in the GC chromatogram through a peak appearing at 15.11 minutes. As shown by the mass spectrum in Figure 4.23(i), compound **2d** has a molecular ion peak at m/z 196. Database spectral matching suggested a molecule similar to 6,7-dihydrodibenzo[b,d]oxepine. However, there exists no literature on the preparation of this molecule from PP-ol or its derivatives. Instead, literature searches

suggested a possible structure of **2d** to be 3-phenyl-2,3-dihydrobenzofuran (Figure 4.23(ii)).[217] The reduction and hydrogenation of phenyl-substituted benzofurans have been reported in literature.[209,210,218]

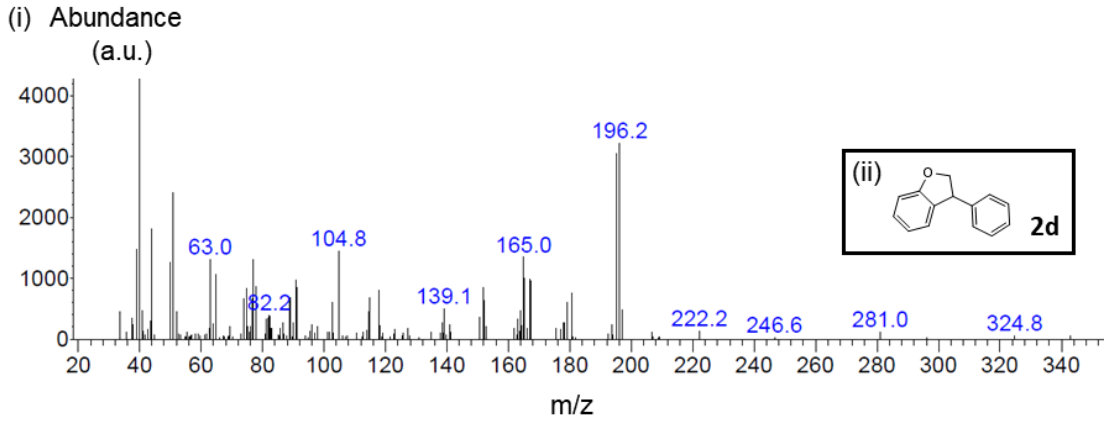

*Figure 4.23. (i) Mass spectrum of compound **2d** (retention time, t = 15.11 min on corresponding chromatogram) and (ii) the proposed structure of compound **2d**.*

4.3.5. Photocatalytic decomposition of PP-ol on CdS

To determine whether the conversion of PP-ol proceeds in the same manner under photocatalytic conditions, photocatalytic experiments using UV and visible light were conducted. Figure 4.24 shows the GC chromatogram of the PP-ol conversion reactions. The expected products of decomposition, phenol (**2a**) and PP-one (**2g**) were observed. However, acetophenone (**2b**) was not detected when using **CdS-h**. Byproducts such as anisole (**1a**), benzaldehyde (**1b**), and benzoic acid (**1d**), as well as compounds **2e** and **2f** were also detected. Much of the parent PP-ol (**2h**) was also present. As with the thermal experiments, no molecules with higher molecular masses were detected. The control experiment also seemed to show PP-ol conversion, albeit to a much lesser extent than the CdS-catalyzed reactions. Headspace analysis showed no observable amounts of styrene or other volatile species in either the control or catalyzed reactions (Figure E.3). PP-ol conversion in the control experiment, as well as in the **CdS-c**, **CdS-m**, and **CdS-h**-catalyzed reactions were calculated as 3%, 13%, 10%, and 4%, respectively. The low catalyst activity under UV conditions was rather surprising, notably in the case of **CdS-h**, which did not seem to increase conversion by much when compared to uncatalyzed conditions. The key difference between the two, however, lies in the amount of acetophenone and PP-one produced.

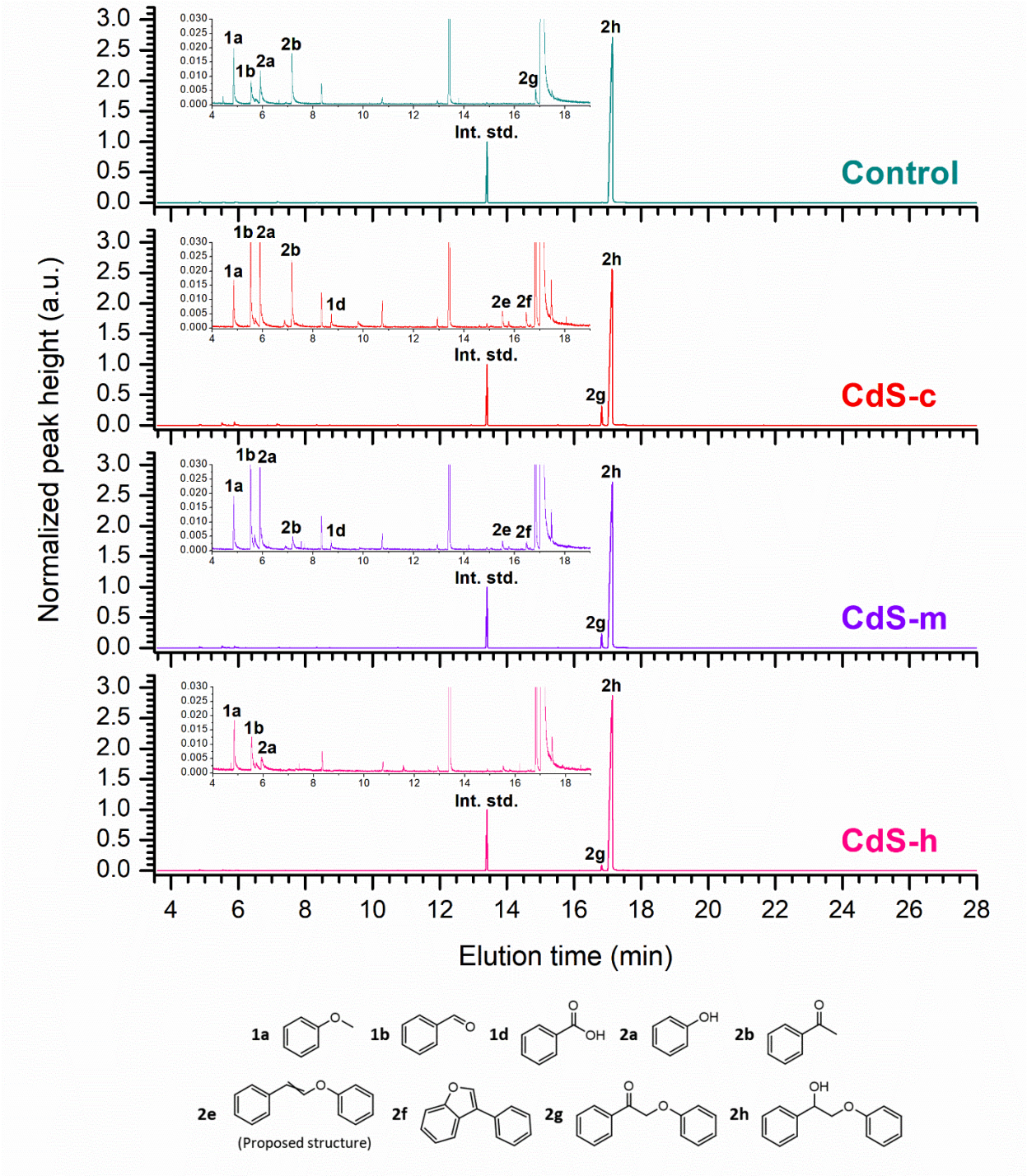

*Figure 4.24. Full GC chromatograms of PP-ol photocatalytic conversion, uncatalyzed and with **CdS-c**, **CdS-m**, and **CdS-h** (UV, λ = 352 nm). Insets represent the magnified full spectra to show relevant peaks with very low peak heights. Relevant peaks are labelled, and peak heights are normalized relative to the internal standard.*

Figure 4.25 illustrates the percentage composition of the products of PP-ol conversion under UV irradiation for 20 hours. Unlike in thermal conditions, even without the use of any catalysts, PP-ol only underwent decomposition to a variety of smaller compounds under UV irradiation. Hence, no byproducts with molar masses larger than the parent substrate were detected. Looking at the products of PP-ol decomposition, PP-one only contributed to 3% of the total product composition, while the rest were comprised of cleavage products. Namely, the acetophenone and phenol pair resulting from β-O-4 bond cleavage, as well as anisole and benzaldehyde, presumably from C_α-C_β bond cleavage. Selectivity towards β-O-4 bond cleavage was slightly higher than the other cleavage reaction. In contrast, catalyzed reactions increased PP-one formation significantly, raising its selectivity up to 35%. Significant amounts of benzoic acid were formed with **CdS-c** and **CdS-m**. Evidently, the increased rate of PP-ol conversion and perhaps higher catalyst activity, observed with **CdS-c** and **CdS-m**, was important in the formation of benzoic acid, as well as the minor amounts of **2f**. Another minor byproduct, **2e**, was also present in the catalyzed reactions.

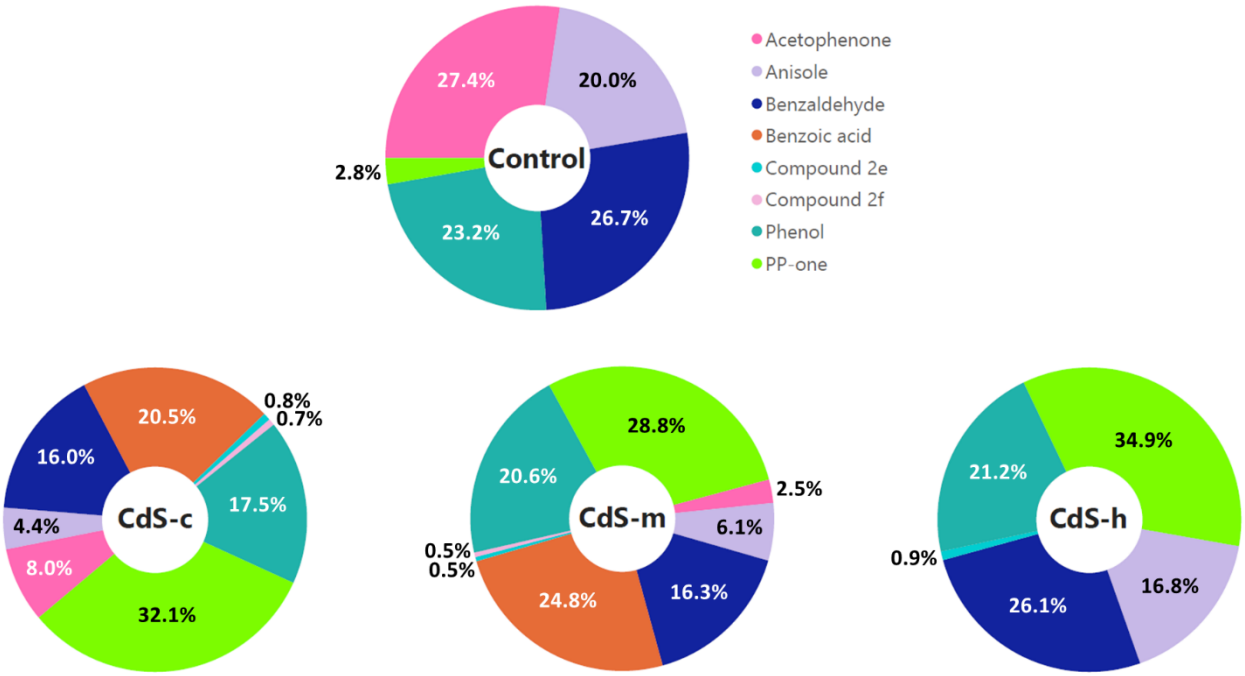

*Figure 4.25. Comparison of product compositions of photocatalytic PP-ol conversion (UV, λ = 352 nm) of the control experiment and under catalysis by **CdS-c**, **CdS-m**, and **CdS-h**.*

More importantly, unlike in the control experiment, anisole composition was always lower than benzaldehyde, and acetophenone composition was always lower than phenol across all catalysts. In the case of **CdS-h**, acetophenone was totally absent from the final reaction mixture, though this could be explained by low PP-ol conversion. Nonetheless, the acetophenone-to-phenol and anisole-to-benzaldehyde non-equimolar ratios would suggest that acetophenone and anisole underwent further separate reactions, or additional phenol and benzaldehyde were formed through other unspecified reaction pathways.

When looking at the product composition of PP-ol decomposition under UV conditions, they seemingly did not differ much from the thermal decomposition experiments. What distinguished the two were merely the PP-ol decomposition rates, which were higher under thermal conditions, and selectivity towards specific reaction pathways. Under catalysis of **CdS-c** and **CdS-h**, PP-one formation was the dominant reaction under thermal conditions, while **CdS-m** facilitated this reaction roughly to the same extent in both thermal and UV conditions.

The last part in the series of photocatalytic, neat PP-ol conversion experiments involved repeating the previous experiment under visible light irradiation. Figure 4.26 shows the GC chromatogram of PP-ol conversion under visible light conditions. In this series of experiments and across all catalysts, nearly all the parent PP-ol (**2h**) had been converted. Observed products include phenol (**2a**), acetophenone (**2b**), and PP-one (**2g**), as well as some later-eluting byproducts (**2i** – **2k**). Unlike the experiments under thermal and UV conditions, this series of experiments did not result in the production of **2c** – **2f**, and other cleavage pathways, namely the ones resulting in anisole and benzaldehyde, seemingly did not occur. The absence of benzoic acid in the final reaction mixtures further supports the notion that it is formed from the oxidation of benzaldehyde. The control experiment showed no changes to the parent PP-ol (Figure E.2), and headspace analysis did not detect observable amounts of styrene or any other volatile products (Figure E.3). PP-ol conversion for **CdS-c**, **CdS-m**, and **CdS-h** reactions were calculated as 96%, 99%, 99%, respectively.

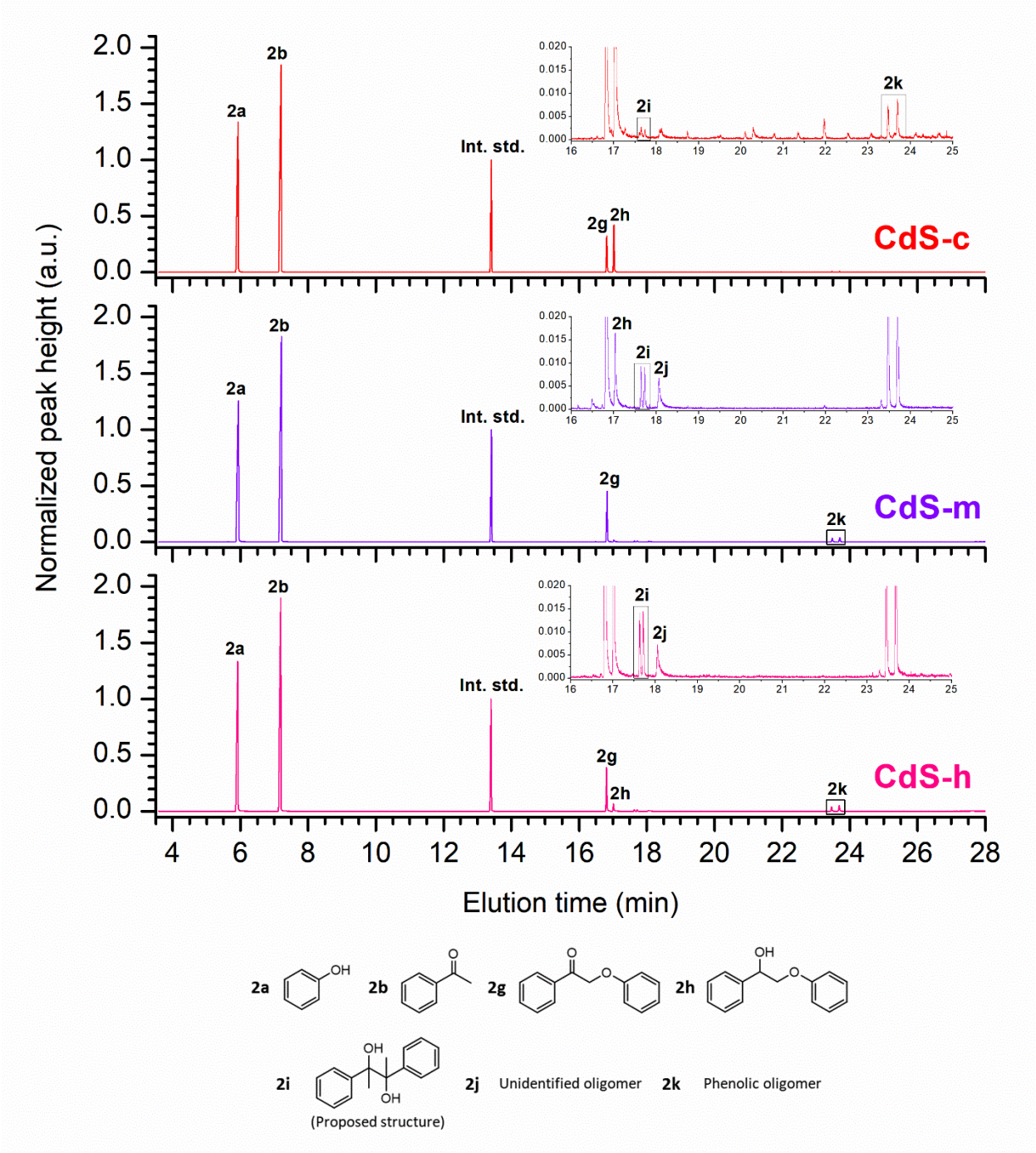

*Figure 4.26. Full GC chromatograms of PP-ol photocatalytic decomposition on **CdS-c**, **CdS-m**, and **CdS-h** (visible light, $\lambda \geq 400$ nm). Insets represent the magnified full spectra to show relevant peaks with very low peak heights. All relevant peaks are labelled, and peak heights are normalized relative to the internal standard.*

In line with previous experiments, the products of PP-ol conversion under visible light were quantified and the product proportions were compared. Figure 4.27 shows that the β-O-4 bond cleavage reaction dominates over PP-ol oxidation to PP-one regardless of the catalyst used. This is a distinct observation compared to the thermal and UV experiments. Furthermore, unlike previous experiments, phenol and acetophenone were present in the final reaction mixtures in near equimolar amounts. However, the final amount of acetophenone was always slightly lower than phenol. This would imply that some of the produced acetophenone was involved in side reactions, though it is likely that it did not decompose further, judging by the absence of smaller byproducts, notably styrene. Indeed, the visible light series of experiments showed the presence of later-eluting products, presumably with the same molar mass as the parent PP-ol or larger. Nonetheless, these larger byproducts collectively represent less than 1% of the final product composition across all catalysts. For example, compound **2i** made up 0.2% of the final product composition when catalyzed by **CdS-c** and **CdS-m**, and 0.3% when catalyzed by **CdS-h**. Compound **2j** was absent in the CdS-c mixture but made up 0.1% of products in the **CdS-m** and **CdS-h** assays. Finally, compound **2k** made up 0.1%, 0.4%, and 0.6% of products in the **CdS-c**, **CdS-m**, and **CdS-h** assays, respectively.

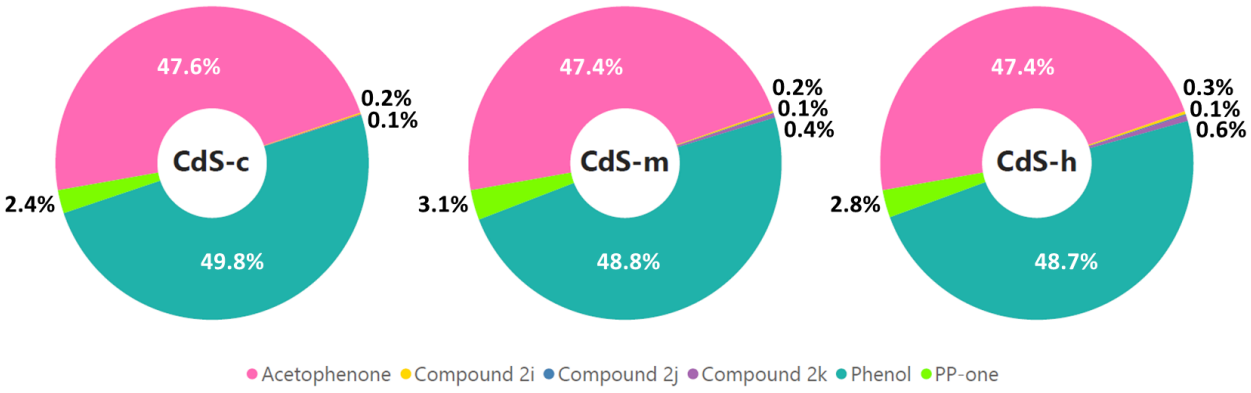

*Figure 4.27 Comparison of product compositions of photocatalytic PP-ol conversion (visible light, λ ≥ 400 nm) catalyzed by **CdS-c**, **CdS-m**, and **CdS-h**.*

To determine the structures of the presently unidentified molecules, their associated mass spectra were analyzed. Beginning with compound **2i**, this molecule was assigned to the GC chromatogram peaks at 17.63 and 17.72 minutes. As seen in Figure 4.28(i) and Figure 4.28(ii), the mass spectra associated with the

chromatogram peaks were very similar, sometimes identical. Therefore, both products were referred to as **2i**. The MS base peak has m/z 43, which can be associated with the $[COCH_3]^+$ ion. One possible way to generate this ion is through cleavage of the $[PhCHOCH_3]^+$ ion, which has m/z 121 and is incidentally the second most abundant fragment ion. Thus, it stands to reason that **2i** possesses this moiety. The visible ion peak with m/z 105 suggests fragmentation of **2i** to $[PhCO]^+$ and/or $[PhCH_2CH_2]^+$. The smaller m/z 103 and m/z 107 ion peaks possibly indicate the presence of $[PhC{=}CH_2]^+$ and $[PhCHOH]^+$ fragment ions, respectively. Based on available literature, the best approximation to the structure of **2i** is 2,3-diphenylbutan-2,3-diol, pictured in Figure 4.28(iii).[219–221] The molecular ion with m/z 242 was not visible, but a $[M-34]^+$ peak was seen at m/z 208, which was the largest stable MS fragment.

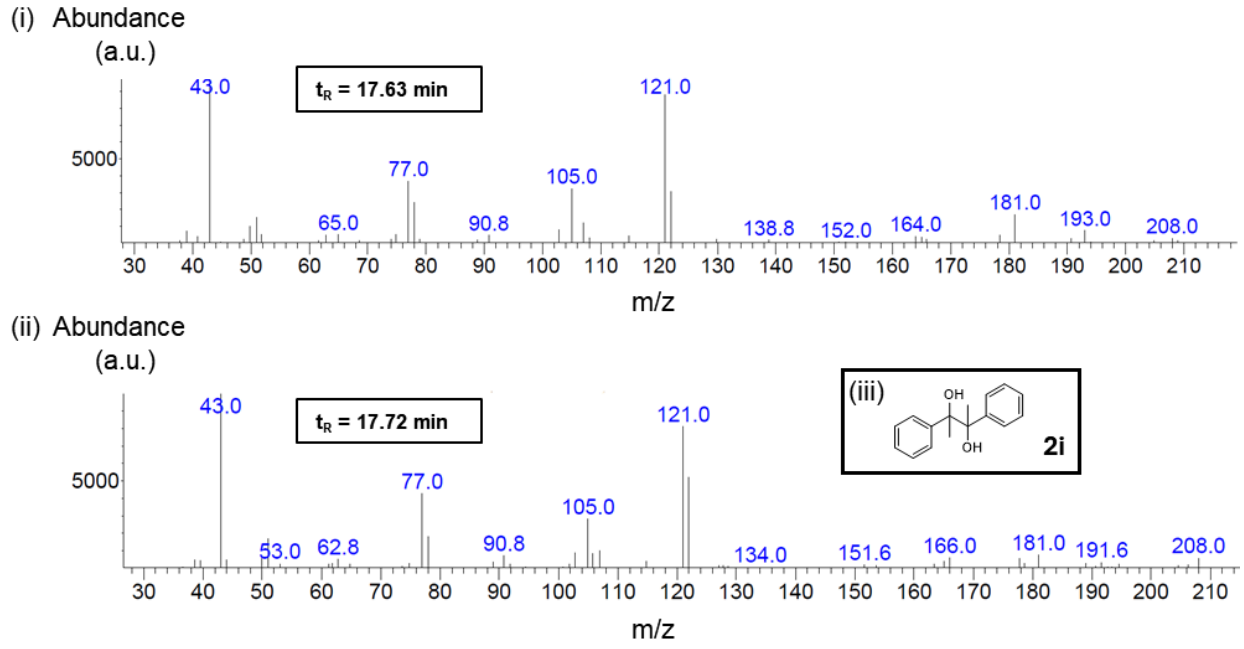

*Figure 4.28. Representative mass spectra of chromatogram peaks with retention times of (i) 17.63 and (ii) 17.72 minutes, as well as (iii) the suggested structure of compound **2i**.*

The next product of PP-ol conversion that was uniquely found in visible light irradiation, compound **2j**, had a retention time of 18.04 minutes and was only observed in the presence of **CdS-m** and **CdS-h**. Its fragmentation pattern (Figure 4.29(i)) was very similar to that of PP-one, but differences in peak intensities may suggest a different structure. It showed a base peak at m/z 105, possibly from a $[PhCO]^+$ and/or

$[PhCH_2CH_2]^+$ ion. Fragments with m/z 51 and 77 were present but not m/z 65, which suggests that all substituted benzene rings in **2j** cannot fragment to the $[C_5H_4]^+$ ion. Combined with the absence of a peak at m/z 93, this eliminates the likelihood of a phenoxy moiety. The absence of m/z 91 peak suggests that whatever benzyl group is present, if any, would be branched. Peaks with m/z 139, 165, and 194 suggest that **2j** fragments to phenylbenzofuran in the GC-MS system. Based on the lack of visible carbon isotope peaks, the peak at m/z 212 is likely a fragment ion, also considering **2j**'s elution time in the GC column. Currently, no specific structure has been assigned to **2j**, but several compounds (Figure 4.29(ii)) have been eliminated from consideration based on further literature reviews.[222,223,232–237,224–231]

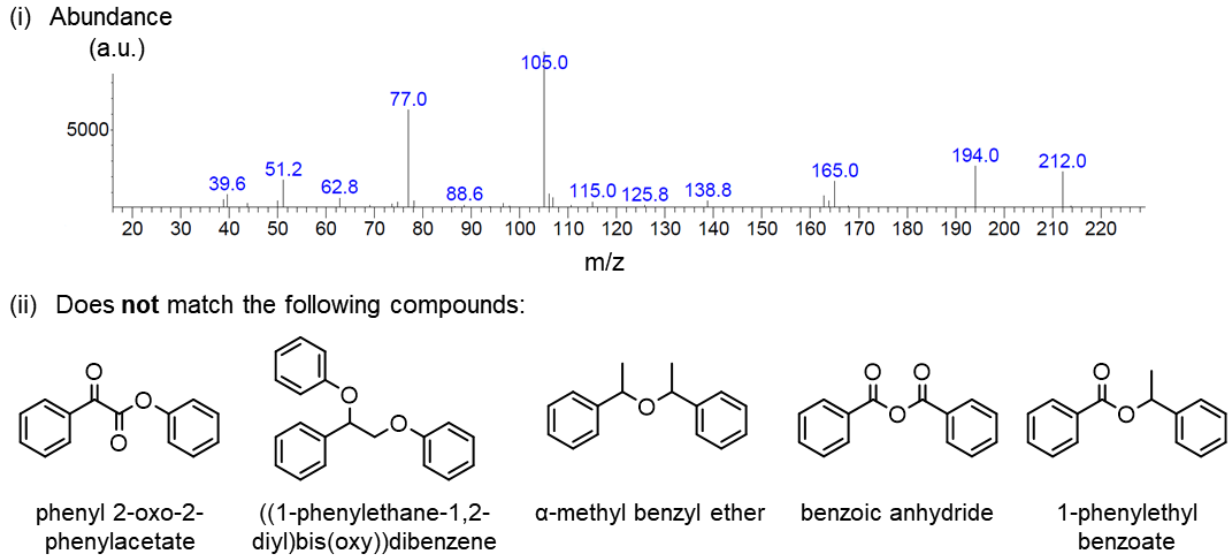

*Figure 4.29. (i) Representative mass spectrum of chromatogram peak with retention time of 18.06 minutes, attributed to compound **2j**, and (ii) compounds whose fragmentation patterns do not match that of compound **2j**.*

Lastly, mass spectra were recorded for larger products that were seen eluting around 23.48 (Figure 4.30(i)) and 23.70 minutes (Figure 4.30(ii)). The fragmentation patterns appear to be similar, and as such, they are collectively referred to as compound **2k**. The molecular ion was very difficult to distinguish but was very likely to be the m/z 316 ion, meaning **2k** likely contained three phenyl groups. The structure of the molecule was deduced based on fragment ions. The m/z 43 peak was likely the $[COCH_3]^+$ ion. The presence of phenyl groups is reflected by the m/z 51, 62, and 77 peaks. Furthermore, the presence of the m/z 62 peak

specifically indicates that α cleavage of at least one benzene ring within **2k** is not possible. The m/z 91 and m/z 94 peaks correspond to the tropylium ion and the phenol radical cation, respectively, suggesting that **2k** contained both a benzylic and phenolic moiety. A distinguishable m/z 105 peak likely corresponded to $[PhCO]^+$ and/or $[PhCHCH_3]^+$. The m/z 120 ion could correspond to the acetophenone fragment ion. The m/z 121 fragment ion is also present, which is normally a result of C_α or O cleavage and corresponds to the $[PhC(OH)CH_3]^+$ or $[PhCHOCH_3]^+$ ion, respectively. Lastly, the weak m/z 213 and 214 could be derivatives of the parent PP-ol. Ultimately, no specific structure has been assigned to **2k**. However, analysis of its mass spectrum would surmise that it is a phenolic oligomer.

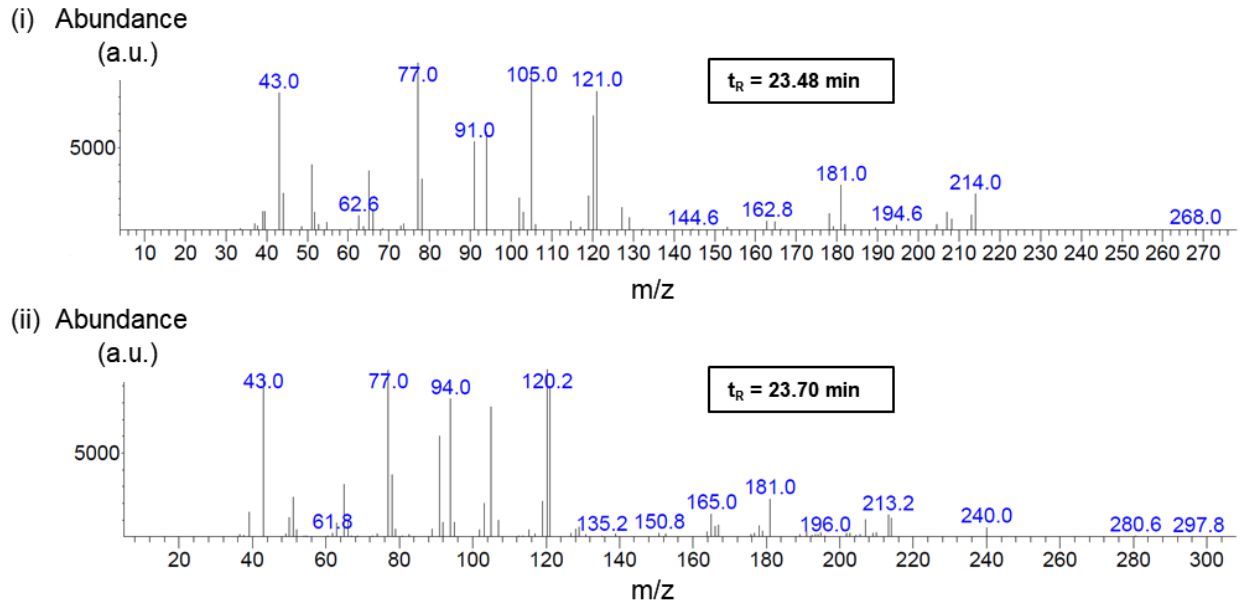

*Figure 4.30. Representative mass spectra of chromatogram peaks with retention times of (i) 23.48 and (ii) 23.70 minutes, attributed to compound **2k**.*

4.4. Discussion

4.4.1. Conversion of benzyl alcohol on CdS NPs

Table 4.2 summarizes all benzyl alcohol conversion products along with the reaction conditions under which they are observed. Overall, within the same reaction conditions, all catalysts afforded the same products in differing concentrations. In addition, unreacted benzyl alcohol was still observed in the final

mixtures across all experiment conditions. Experiments showed that thermal and photocatalytic conditions afforded the same decomposition products, with key differences in some of the coupled products. While benzyl benzoate was common to all experimental conditions, and **1h** was found under heating and UV irradiation, the experiments clearly showed that C-C coupled products occurred strictly only under UV and visible light irradiation. None of the characterized or proposed products contained any alkene moieties capable of participating in addition reactions. As such, C-C coupling could only have taken place through photogenerated radical intermediates. The absence of C-C-coupled products in the high-temperature experiments suggests that reactions under these conditions proceeded through radical-free pathways. Conversely, only photocatalytic conditions produced the C-C coupled products, suggesting that radical species were produced only under UV and visible light irradiation. Toluene, an unquantified product, was observed primarily under thermal conditions, but **CdS-m** was able to catalyze its formation in small amounts under visible light irradiation.

Table 4.2. Summary of all observed benzyl alcohol decomposition and coupled products.

Entry	Compound	Catalytic conditions	Entry	Compound	Catalytic conditions
1a	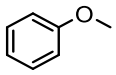	Thermal, UV	**1i**	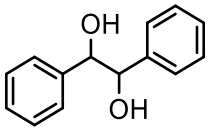	UV, Vis
1b	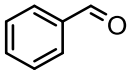	Thermal, UV, Vis	**1j**	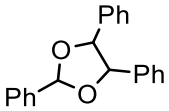	UV, Vis
1c	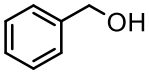	N/A (parent molecule)	**1k**	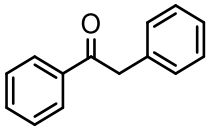	Vis
1d	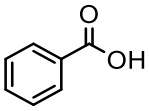	Thermal, UV, Vis	**1l**	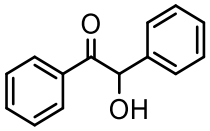	Vis
1e	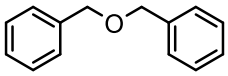	Thermal	**1m**	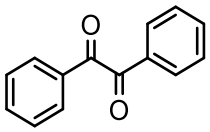	Vis
1f	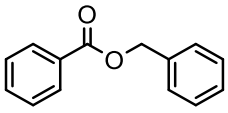	Thermal, UV, Vis	**1n[i]**	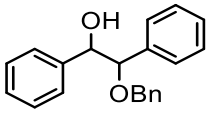	Vis
1g	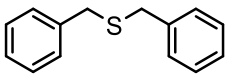	Thermal	**1o[i]**	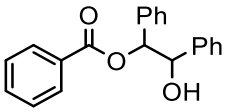	Vis
1h[i]	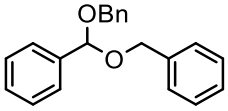	Thermal, UV			

[i]Proposed structures.

Scheme 4.2 illustrates the proposed conversion pathways of benzyl alcohol at high temperatures, under UV irradiation, and under visible-light irradiation. All reactions were conducted under inert atmosphere and neat conditions, meaning no contribution of external gas or solvent. Prior to any reaction, benzyl alcohol was adsorbed and activated on the CdS surface.

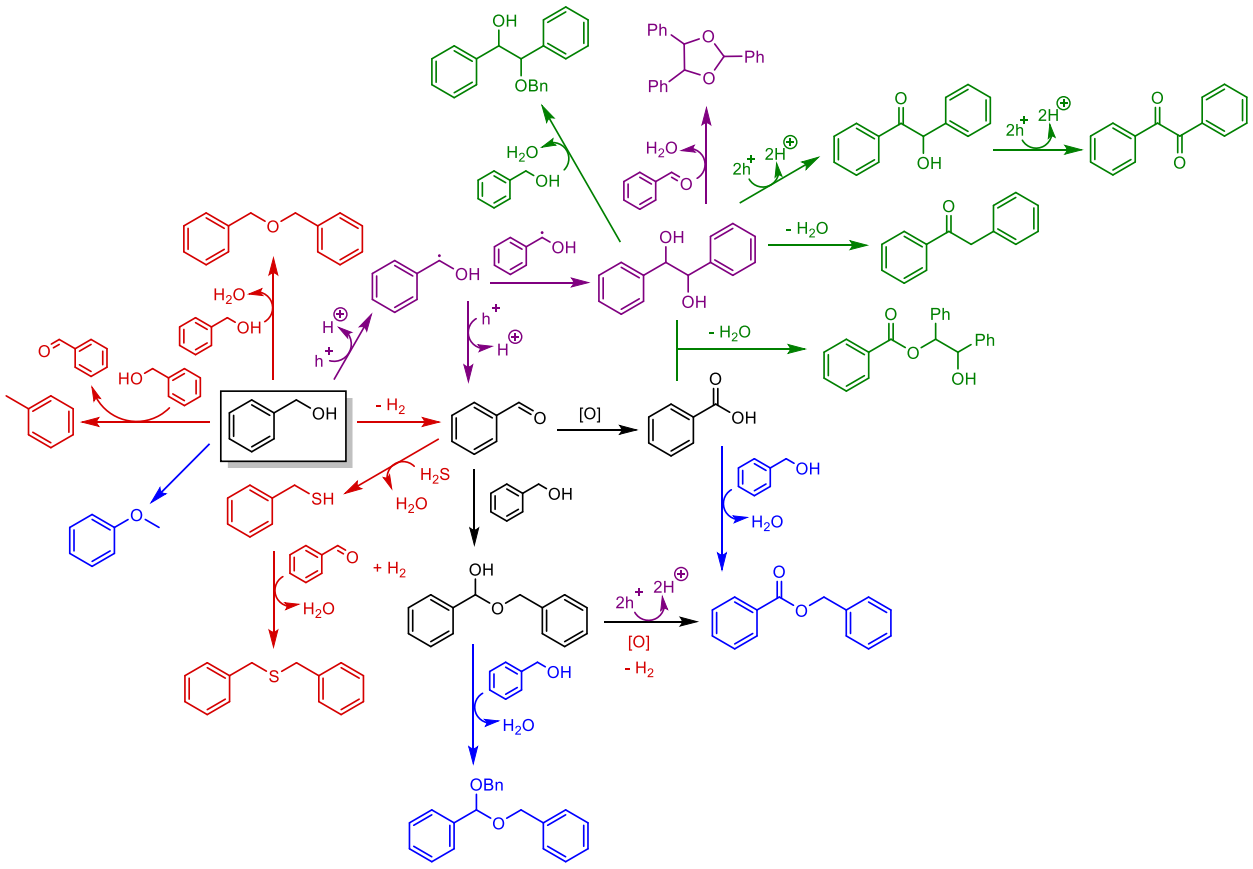

Scheme 4.2. The proposed CdS-catalyzed pathways of benzyl alcohol conversion, grouped as thermal-only (red), thermal and UV-only (blue), photocatalytic-only (purple), and visible light-only (green) products and pathways. Molecules and pathways depicted in black occur under all (thermal and photocatalytic) conditions.

In the thermal experiments, as it was established that no radical species were thermally generated, benzaldehyde was most likely produced through a dehydrogenation process. Abstracted hydrogen adsorbed on the CdS surface acted as hydrogen donors for reactions or desorbed as H_2. The subsequent reaction of benzaldehyde and the starting benzyl alcohol occurred, leading to an intermediate hemiacetal. Acyclic hemiacetals are generally unstable, and this was showcased by the absence of the intermediate hemiacetal

in the final reaction mixtures. Due to the high temperatures imposed on the system, the hemiacetal can quickly react with excess benzyl alcohol to form the proposed acetal **1h**.[194,196,198,238] There is also a possibility that the hemiacetal underwent oxidative dehydrogenation to benzyl benzoate, although, to date, this reaction was only reported in one instance using H_2O_2 as an oxidant and no catalyst.[239] The alternative pathway to benzyl benzoate formation is the thermal oxidation of benzaldehyde to benzoic acid, followed by condensation with benzyl alcohol, where dehydration was favored by elevated temperatures.

Thermocatalysis resulted in several side reactions. Firstly, dibenzyl ether was obtained from benzyl alcohol self-condensation. While typically an acid-catalyzed reaction, adsorption on CdS active sites would activate benzyl alcohol and, along with high temperature, drive the direct substitution of the hydroxyl group.[163,194,240,241] In addition, toluene was also observed, which likely came from the disproportionation of benzyl alcohol to toluene and benzaldehyde. This mechanism has been widely reported on other heterogeneous catalysts and competes with oxidative dehydrogenation.[105,242–245] It is worth noting that disproportionation has not yet been reported on CdS-based catalysts.

As evidenced by the presence of dibenzyl sulfide, some degree of sulfur leaching or sulfur insertion into the benzyl alcohol substrate occurred. The exact mechanism leading to dibenzyl sulfide formation is not known, but a carbocation-free pathway was suggested as a speculative attempt to elucidate its formation in our reaction systems.[246] As water was a byproduct of some reactions illustrated in Scheme 4.2, it is possible that the presence of water vapor partially degraded the CdS catalysts, forming cadmium oxide (CdO) and hydrogen sulfide (H_2S), the latter acting as the sulfur source. The formation of organic sulfur as a result of H_2S production at high temperatures has been observed with other metal sulfide catalysts.[117] In the absence of benzylic halides, thioetherification through hydrogen borrowing has been reported on a CoMo sulfide catalyst with benzyl alcohol and H_2S as the starting materials.[247] Stipulating that the same mechanism is possible on CdS, this overall mechanism involves the initial oxidative dehydrogenation of benzyl alcohol to benzaldehyde, with the evolved hydrogen adsorbed on CdS. Some of the benzaldehyde reacted with H_2S to form benzyl mercaptan, which quickly reacted with another adsorbed benzaldehyde. This nucleophilic

attack on the carbonyl generated an intermediate hemithioacetal species that was reduced to dibenzyl sulfide by CdS-adsorbed hydrogen. Benzyl mercaptan and dibenzyl disulfide, another possible byproduct, were not observed in our systems. To note, the formation of disulfides requires a lower activation energy compared to the formation of thioethers, meaning that at lower temperatures, the disulfide is favored.[247,248] Specifically in the context of our experiments, the formation of dibenzyl sulfide is reported to also necessitate an excess of benzyl alcohol. These conditions were satisfied; our starting material was benzyl alcohol rather than benzaldehyde, and the reaction temperature was sufficiently high to supply the requisite energy for dibenzyl sulfide generation. By generating organosulfur byproducts, our CdS catalysts exhibited a distinct selectivity towards thioethers. Given that the catalytic formation of C-S bonds remains largely unexplored, this unexpected performance by our CdS NPs warrants further study.

The conversion of benzyl alcohol under photocatalytic conditions, to some extent, involved the same pathways seen in the thermal experiments. The key difference is that in the absence of heat, benzyl alcohol did not undergo direct dehydrogenation. Instead, there exist numerous reports of electron-hole pair generation through photoexcitation of CdS NPs, inducing benzyl alcohol oxidation to its benzylic radical intermediate.[99,102,108,113,249] The benzylic radical intermediate can undergo further oxidation to benzaldehyde and benzoic acid. The latter can react with excess benzyl alcohol to form benzyl benzoate. Alternatively, two equivalents of the benzylic radical intermediates can undergo C-C coupling to produce hydrobenzoin. Subsequent oxidation would lead to the formation of benzoin and benzil.[101,102,108,249] The reaction of hydrobenzoin with benzaldehyde to yield **1j**, with benzyl alcohol to yield **1n**, or with benzoic acid to yield **1o**, have been reported in literature and generally takes place under acid catalysis, but none have been reported with CdS as the catalyst. In our reaction systems, active acid sites would drive these reactions. Pinacol rearrangement to deoxybenzoin can also occur at these sites or through a redox pathway implicating photogenerated electron-hole pairs.[101,108,249]

Compound **1h** was observed in thermal conditions and UV irradiation but not upon visible light irradiation. It is possible that the formation of this product requires conditions harsher than those provided by visible

light irradiation.[250] It is noteworthy to mention that no other sulfur-containing compounds were detected in the photocatalytic experiments, which were conducted at room temperature, noting the CdS catalysts were photostable. With regards to toluene, which under photocatalytic conditions was only observed when employing **CdS-m** and visible light, a possible reason for this is the presence of both cubic and hexagonal phases in the crystalline structure, which introduces interphase regions where benzyl alcohol can adsorb at different states[242] and disproportionation can occur. That said, toluene selectivity generally increases with temperature,[245,251] explaining why the room temperature conditions imposed during photocatalytic reactions did not favor this pathway relative to the thermocatalysis experiments.

4.4.2. Conversion of PP-ol on CdS NPs

Table 4.3 summarizes the PP-ol conversion products and their reaction conditions. Under the same conditions, all catalysts yielded the same products in different concentrations. Thermal and UV conditions yielded smaller products, while larger products appeared only under visible light. Phenol, acetophenone, and PP-one were the main decomposition products across all conditions, with varying selectivity.

Table 4.3. Summary of all possible PP-ol decomposition and coupled products.

Entry	Compound	Catalytic conditions	Entry	Compound	Catalytic conditions
1a	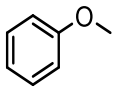	Thermal, UV	**2e[l]**	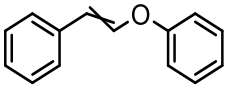	Thermal, UV
1b	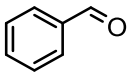	Thermal, UV	**2f**	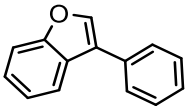	Thermal, UV
1d	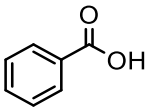	Thermal, UV	**2g**	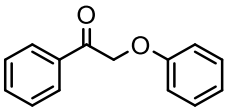	Thermal, UV, Vis
2a	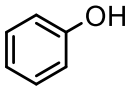	Thermal, UV, Vis	**2h**	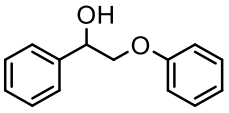	N/A (parent molecule)
2b	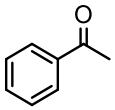	Thermal, UV, Vis	**2i**	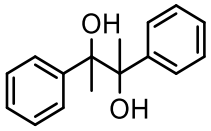	Vis
2c	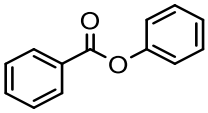	Thermal	**2j**	Unidentified oligomer	Vis
2d[l]	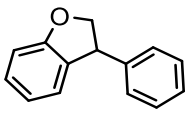	Thermal	**2k**	Phenolic oligomer	Vis

[l]*Proposed structures*

In thermal conditions, the selectivity varies among different compounds. In **CdS-c** and **CdS-h**, phenol is slightly over twice as abundant as acetophenone, and acetophenone is marginally higher than PP-one. In **CdS-m**, PP-one is almost 50% more abundant than phenol, while phenol is slightly over twice as abundant as acetophenone. On **CdS-h**, anisole is not detected, but benzaldehyde is present, suggesting an alternative formation mechanism for benzaldehyde since no byproducts of anisole were detected. Compounds **2d** and **2f** were present in trace amounts. Compound **2e** concentrations were higher under thermal conditions in comparison to the UV-induced reactions, suggesting that **2e** formation was likely favored by dehydration, notably at high temperatures, but mild heating can drive this reaction pathway to a limited extent. Styrene was only observed under thermal conditions, indicating the necessity of elevated temperatures. Based on available literature, all of which do not involve the use of CdS as a catalyst, there could be three possible pathways of styrene production. The first pathway would involve the direct deoxygenation or reduction of acetophenone, produced from β-O-4 bond cleavage, to styrene. That said, most studies report overwhelmingly low yields for this reaction,[51,252,253] and selectivity tended to products not observed in our series of experiments, namely 1-phenylethanol and ethylbenzene. The second pathway would be through the reduction of acetophenone to 1-phenylethanol,[254] followed by the dehydration of 1-phenylethanol to styrene.[255,256] Considering the absence of any 1-phenylethanol, this pathway was also ruled out. The third possible pathway, which we considered most plausible, would be the direct decomposition of PP-ol or PP-one to phenol and styrene,[116,257–259] which also explains the increased concentration of phenol.

Under UV irradiation, control experiments show phenol to be produced at a roughly equal concentration as acetophenone. Indeed, the β-O-4 cleavage products were almost ten times more abundant than PP-one. However, with all CdS catalysts, there was higher reaction selectivity towards PP-one rather than the phenol-acetophenone pair. Furthermore, acetophenone, totally absent in the **CdS-h** assay, was observed in lower amounts than phenol. It is unclear if the acetophenone decomposed further or if phenol was formed through an alternative pathway. Concentrations of compounds **2e** and **2f** were minimal. Under visible light, phenol and acetophenone were observed at near equimolar amounts, with selectivity towards PP-one

significantly reduced. This experimental condition evidently favored some coupling reactions over the generation of diverse decomposition byproducts. Namely, C_α-C_β cleavage did not seem to occur, as reflected by the absence of benzaldehyde and anisole from the assays.

In terms of overall trends, for benzoic acid to be observed, benzaldehyde was necessary, and conversion rates seemingly needed to exceed a certain threshold. This was evident in the **CdS-h** assay under UV irradiation, where no benzoic acid was observed. Phenyl benzoate, generally formed through condensation of benzoic acid and phenol, was only observed under thermal conditions, suggesting the necessity of higher temperatures for this reaction to occur in our systems.[260]

Scheme 4.3 illustrates the proposed conversion pathways of PP-ol. Prior to any reactions, PP-ol adsorbs on the surface of the CdS NPs, leading to the activation of bonds within the molecule, notably the C_α-H_α and C_αO-H bonds.[116,179,261–263] In studies involving CdS as a catalyst, the decomposition of lignin model molecules commonly takes place through the generation of radical species.[264] A redox-neutral pathway has been reported on Pd/C,[265] though the applicability of this pathway in CdS is uncertain. In our systems, PP-ol decomposition was proposed to proceed through oxidative hydrogen abstraction on the C_α atom, leading to the generation of a C_α-centered radical or active intermediate, which can undergo further oxidation to PP-one. Alternatively, acetophenone (via its enol form) and phenol are produced through a separate pathway. Under thermal conditions, the active species reacts with adsorbed hydrogen to cleave the β-O-4 bond. Under photocatalytic conditions, it is reported that the radical intermediate reacts with a photogenerated electron. The resulting phenolate ion reacts with hydrogen to form phenol.

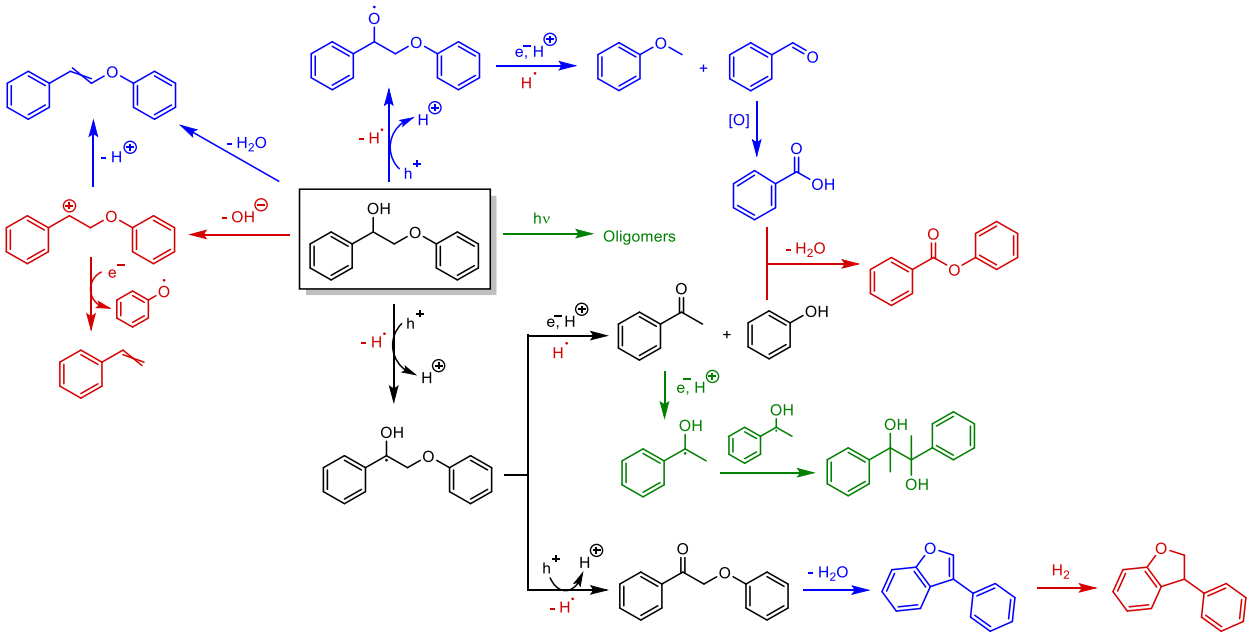

Scheme 4.3. The proposed CdS-catalyzed pathways of PP-ol conversion, grouped as thermal-only (red), thermal and UV-only (blue), and visible light-only (green) products and pathways. Molecules and pathways depicted in black occur under all (thermal and photocatalytic) conditions.

The generation of the O-centered radical as an intermediate to PP-one production has been reported in literature, though these involve catalysts other than CdS. Furthermore, the bond dissociation energy to cleave the C_α-H bond is lower than that of the C_αO-H bond,[266,267] making the latter pathway a minor one. For this reason, the pathway involving the O-centered radical or activated intermediate leading to PP-one, acetophenone, and phenol was not illustrated.

Some byproducts were observed from PP-ol decomposition. Heterolytic dehydroxylation at high temperatures has been reported to occur using a NiMo sulfide catalyst, leading to the formation of a carbocation. This carbocation could either lose a hydrogen atom at C_β and produce β-phenoxystyrene or undergo reductive C_β-O cleavage to styrene and phenoxy radical, the latter being hydrogenated to form phenol.[116] To note, β-phenoxystyrene was observed, without styrene, in small amounts under UV without heat. Thus, it is possible that an alternative pathway, like the direct dehydration of PP-ol,[268] was more accessible under these conditions. A side reaction involving the cleavage of the C_α-C_β bond was observed, resulting in the production of anisole and benzaldehyde. Current literature reports this bond cleavage

typically occurs in PP-ol rather than PP-one,[269–271] as the oxidation of PP-ol to PP-one raises the C_α-C_β bond energy from 264.3 to 294.2 kJ mol^{-1}.[272] Consequently, it was stipulated that the main pathway for the generation of these byproducts originated from PP-ol, where the C_αO-H bond in the activated PP-ol species was broken, generating an O-centered radical intermediate or active species, followed by β scission. Mechanisms have been elucidated under photocatalytic and thermal conditions, but none involved CdS. Meanwhile, under thermal and UV conditions, further oxidation of benzaldehyde resulted in benzoic acid, the latter further reacting with phenol to form phenol benzoate, specifically under high temperatures. Under visible light irradiation, **2j** and **2k**, whose structures were not identified and were labelled as oligomers in Scheme 4.3, were estimated to have also been produced from PP-ol. Some PP-one was supposedly dehydrated to form the 3-phenylbenzofuran species under thermal and UV conditions.[214,273–275] It was also proposed that this species underwent some hydrogenation process to form 2,3-dihydro-3-phenylbenzofuran under high temperatures. Lastly, 2,3-diphenylbutan-2,3-diol was proposed to have been formed through reductive pinacol coupling of acetophenone through the generation of a C-centered 1-phenylethanol radical intermediate, immediately followed by radical C-C coupling. This mechanism is reported using various metallic catalysts, none being CdS.[276–279]

Overall, PP-ol conversion was lower under UV irradiation compared to thermal conditions. PP-ol conversion was highest under visible light, possibly due to more stable lower energy charge carriers, higher light power, or efficiency of multi-wavelength visible light source compared to single-wavelength UV light. Furthermore, while CdS was a more efficient photocatalyst rather than a thermal catalyst, the use of CdS in thermal catalysis should not be discounted, owing to its non-negligible catalytic activity at high temperatures and substrate decomposition pathways otherwise not accessible photocatalytically.

4.4.2.1. Comparison with solvated conditions

Table 4.4 provides a side-by-side overview of the observed products of **CdS-m**-catalyzed PP-ol conversion under UV irradiation in acetonitrile, per the series of experiments discussed in Chapter 3, under UV irradiation in solvent-free conditions, as well as under visible light irradiation in solvent-free conditions. It

is worth noting that in this Chapter, where the PP-ol conversion experiments were solvent-free, 2,3-diphenylbutan-2,3-diol was unique to visible light conditions. However, it was previously detected and identified under UV and solvated conditions, as described in Chapter 3. Conversion was determined to be 86%, 10%, and 99%, respectively.

Table 4.4. Summary of observed products of PP-ol conversion under UV (in solution and neat) and visible light (neat) irradiation.

Retention time (min)	Compound	Product composition (%)			Retention time (min)	Compound	Product composition (%)		
		CH_3CN, UV	Neat, UV	Neat, vis			CH_3CN, UV	Neat, UV	Neat, vis
4.85	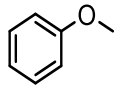		6		16.47	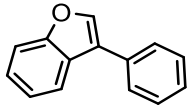		< 1	
5.52	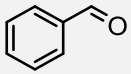		16		16.82	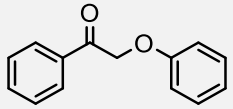	14	29	3
5.90	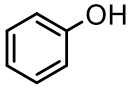	41	21	49	17.64 17.72	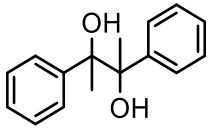	6		< 1
7.20	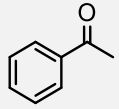	32	3	47	18.06	Unidentified oligomer			< 1
8.72	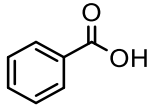		25		20.26	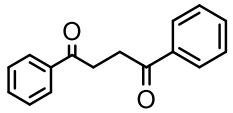	< 1		
15.52 15.77	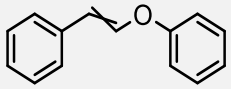		< 1		23.46 23.69	Phenolic oligomer	6		< 1

The products of PP-ol β-O-4 bond cleavage and oxidation were observed in all cases. Under UV irradiation, the ratio of PP-one to cleavage products was lower relative to neat conditions. This was slightly unexpected; PP-one is soluble in acetonitrile, therefore, in solution, any PP-one formed could easily desorb from the CdS surface and would not be further converted, which would theoretically result in a higher proportion of PP-one at the end of the reaction. Instead, the opposite was observed. Under solvent-free conditions, where PP-one would likely linger on the CdS surface, PP-one was found in higher proportions than the phenol-acetophenone pair. This may suggest that in solvent, β-O-4 bond cleavage of the radical intermediate was favored over the subsequent hole-induced oxidation to PP-one. Also, in solvent-free conditions, PP-one decomposition into smaller products seemed to be a minor pathway. Further validation can be done by conducting control experiments using PP-one as the substrate.

With relation to byproducts, reactions under UV irradiation visibly led to a higher proportion of byproducts. Under neat conditions, these UV-induced byproducts were small molecules, and the presence of anisole and benzaldehyde suggests there was enough energy for PP-ol C_α-C_β bond cleavage. On the other hand, in solvent, the UV-induced byproducts were larger than the starting PP-ol, suggesting coupling reactions. It is likely that solvation effects stabilized the starting PP-ol and any photogenerated radical species, further enabling coupled byproducts rather than decomposition byproducts. The production of styrene or any other volatiles under solvated conditions remains to be confirmed.

Under visible light irradiation, the proposed 2,3-diphenylbutan-2,3-diol and phenolic oligomer were observed. It is possible that lower energy excitation may have led to more stable radicals. These products were not seen under neat UV conditions, but they were present under solvated UV conditions, alluding once again to increased stabilization of photogenerated radical species by the surrounding solvent. Finally, 1,4-diphenylbutan-1,4-one was unique to UV-solvated conditions, albeit in trace amounts, and was attributed to the dimerization of acetophenone.[280–282] Phenol and acetophenone were practically produced in equimolar amounts, with no detectable byproducts in the headspace GC-MS (Figure E.3). Larger byproducts likely originated from PP-ol or PP-one, with some acetophenone potentially involved.

The equimolar ratio of acetophenone and phenol became less obvious under other photocatalytic conditions. In solvated UV conditions, acetophenone was observed at visibly lower molar concentrations than phenol. The presence of 2,3-diphenylbutan-2,3-diol and 1,4-diphenylbutan-1,4-one in this assay would suggest that acetophenone was consumed. Meanwhile, in neat UV conditions, acetophenone amounts were significantly lower than phenol. This insinuates two things: phenol was generated as a product of a different PP-ol and/or PP-one decomposition pathway,[177,178,271,283,284] or the generated acetophenone decomposed to other products. While there are reports of phenol formation through other mechanisms, the experimental conditions that surround those reactions do not match those in this Thesis. Furthermore, products generated by alternative pathways described in literature were not observed in our series of experiments. Regarding acetophenone decomposition, experimental conditions were likely not conducive for this, as no volatile products were detected through headspace GC-MS. Thus, further studies are needed to elucidate the non-equimolar ratio of phenol and acetophenone.

4.4.3. General trends in the CdS-catalyzed conversion of benzyl alcohol and PP-ol

Across experimental conditions, benzyl alcohol and PP-ol conversion and product compositions were mainly governed by the excitation source. It was previously established that radical intermediates were not generated thermally in our systems, as evidenced by the absence of C-C radical coupling products in the high-temperature-assisted experiments. Rather, the radical species were only produced under photocatalytic conditions through hole-induced oxidation of the parent substrates, implying that electron-hole pairs were solely generated via photocatalysis. Thus, thermocatalytic conversion was primarily influenced by substrate activation and surface interactions; photocatalytic conversion was more complex with the added consideration of photogenerated charge carriers. Particularly under UV irradiation, excess photon energy can excite electrons to higher states. These higher-energy electrons can then lose the excess energy in the form of heat as they relax to lower energy states within the conduction band, in a process referred to as electron thermalization,[285–289] which might explain the generation of benzyl alcohol and PP-ol thermal conversion products under UV.

Nonetheless, the architecture of the synthesized CdS NPs played a key role in influencing substrate conversion and product composition. Initially, it was expected that the catalyst with the largest specific surface area would have a larger number of active sites and would show the highest substrate conversion. However, the ability of CdS to convert substrates also depends on the nature of the surface active site itself. It is known that surfaces with different crystalline orientations have different surface energies, leading to different adsorption energies and reaction selectivity.[86,165,176] Thus, in each catalyst, if the surface or exposed facet is incompatible with a substrate or intermediate product, or inactive towards a specific reaction, increasing the surface area of this inactive facet would not necessarily result in a meaningful increase in substrate conversion. In this Chapter, NP synthesis did not make use of capping agents or ligands to specifically inhibit NP nucleation or growth along a particular plane.[79,81] Rather, reaction temperatures were selected in a way that would result in the formation of CdS in the cubic or hexagonal phase or a mix of both. These crystalline phases dictated the facet content of the resulting CdS NPs and their morphologies.

In the specific case of **CdS-m**, the existence of both cubic and hexagonal phases may have increased conversion, where coexposed facets can act as additional active sites. Notably, under photocatalytic conditions, tight interfaces between cubic-specific and hexagonal-specific facets facilitate charge migration. As specific facets preferentially attract charge carriers, the increased charge migration enables better charge separation, reducing electron-hole recombination and driving substrate conversion.

Another physical property that relates to facets and influences the performance of the catalysts is the presence of defects. Specific details regarding surface defects were unknown as surface topologies were not experimentally measured. However, some predictions can be made from the obtained XRD patterns, which provide information about bulk crystallinity through the shape of the XRD peaks. Amorphous solids have a disordered crystal lattice and exhibit peak broadening, as seen in the XRD pattern of **CdS-c**, which is usually the first indicator of defect presence in the bulk. One of the implications of defects is the formation of additional surfaces, which increase overall surface area, and this was observed with the CdS NPs; as the samples became more crystalline, specific surface area decreased. That said, the effect of these changes

may vary depending on reaction conditions. In the thermocatalysis experiments, assuming the benzyl alcohol and PP-ol adsorb easily on the catalyst and disregarding any steric hindrance, introducing more surfaces through defects could lead to increased substrate adsorption, leading to higher conversion. In the photocatalysis experiments, however, an excess number of defects could be detrimental because they would act as recombination centers for photogenerated electrons and holes. As hole generation is the driving force for the photocatalytic conversion of benzyl alcohol and PP-ol, substrate conversion would decrease with increasing defects.

The actual overall trends of benzyl alcohol and PP-ol conversion across all catalysts and experimental conditions were summarized in Figure 4.31. Conversion using **CdS-h** was generally lower than with the larger NPs, except for the visible light irradiation of PP-ol (Figure 4.31(ii)), where conversion using **CdS-h** was equal to **CdS-m** at 99%. A possible explanation for this perceived equal performance is that PP-ol conversion using these catalysts may have already been complete by the 20-hour mark, but because the reaction was not monitored at regular intervals, it is unclear if PP-ol conversion occurred at the same rate. While it is reasonable to speculate that PP-ol conversion was slower with **CdS-h** due to its smaller specific surface area, this remains to be experimentally confirmed.

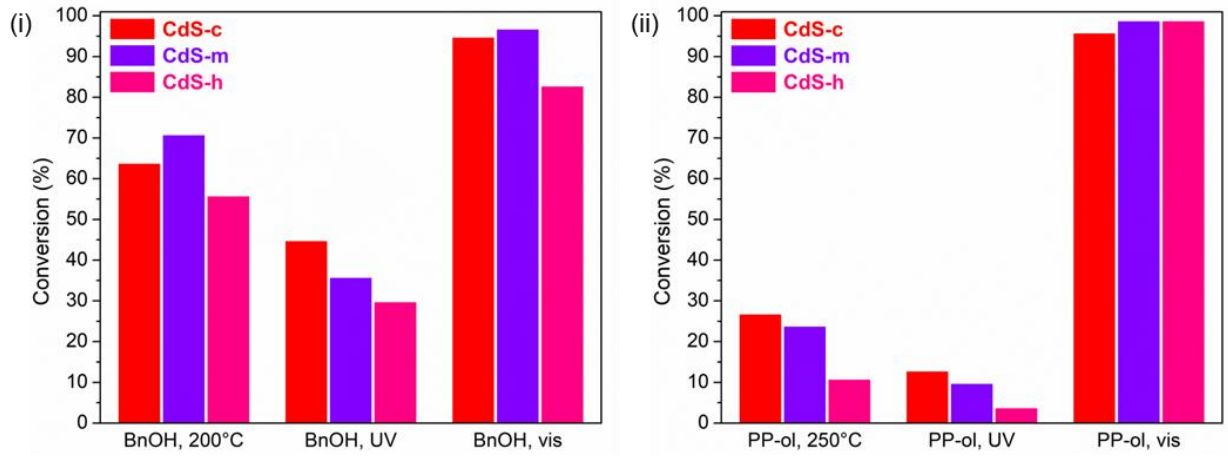

Figure 4.31. Trends of (i) benzyl alcohol and (ii) PP-ol conversion under different conditions and CdS catalysts.

The positive impact of increasing surface area seemed less important in reactions catalyzed by **CdS-c** and **CdS-m**. Considering the specific surface area of **CdS-c** was significantly higher than the other two catalysts, it was expected that conversion with **CdS-c** would be much higher, but this is not the case. Under visible light, **CdS-m** marginally outperformed **CdS-c**, where benzyl alcohol and PP-ol conversion were higher by 2% and 3% respectively. Considering that conversions of the parent substrates were near completion and satisfactory conversion was achieved despite the variations in CdS architecture, from a practical standpoint, these small differences in conversion were considered insignificant. Looking at cases where **CdS-c** outperformed **CdS-m**, such as benzyl alcohol under visible light, PP-ol at high temperature, and PP-ol under UV, the increases in conversion were marginal at 3%. These increases fall within a standard 5% margin of error, and since the effects of random fluctuations in the reaction systems could not be ruled out, these increases were considered insignificant.

The equal performance of **CdS-c** and **CdS-m** was contrary to expectations; it was speculated that conversion with **CdS-m** would distinctly increase. However, this was only true for benzyl alcohol at high temperatures. For PP-ol, it is possible that its bulky structure was a limiting factor in highlighting the added benefits of cubic-hexagonal interfaces, either through ineffective adsorption or blockage of active sites by PP-ol itself. Under UV, the reason for the lower conversion of benzyl alcohol using **CdS-m** remains unclear and warrants further study. Overall, it is likely that the cubic and hexagonal phase content in **CdS-m** requires further optimization.

Beyond catalytic activity, a primary objective of this work in studying the CdS NPs is to evaluate their potential applicability for lignin valorization, involving the breakdown of polymeric structures to their monomeric constituents. In the context of the following discussion, monomers are defined as all products containing a single phenyl group, while oligomers encompass products that contain two or more phenyl groups. Experimentally, in the absence of solvents, CdS catalyzed potentially unproductive reactions, such as C-C coupling reactions, condensation reactions, and the formation of ethers or organosulfur compounds. Thus, an important aspect in assessing the differences between catalysts was to compare the proportions of

monomeric products to the larger, oligomeric products (Figure 4.32), from which the monomer-to-oligomer (M:O) molar ratios can be deduced. A high M:O ratio is desired, as monomeric derivatives are economically significant as organic precursors. Toluene and styrene were not discussed as they were not quantified.

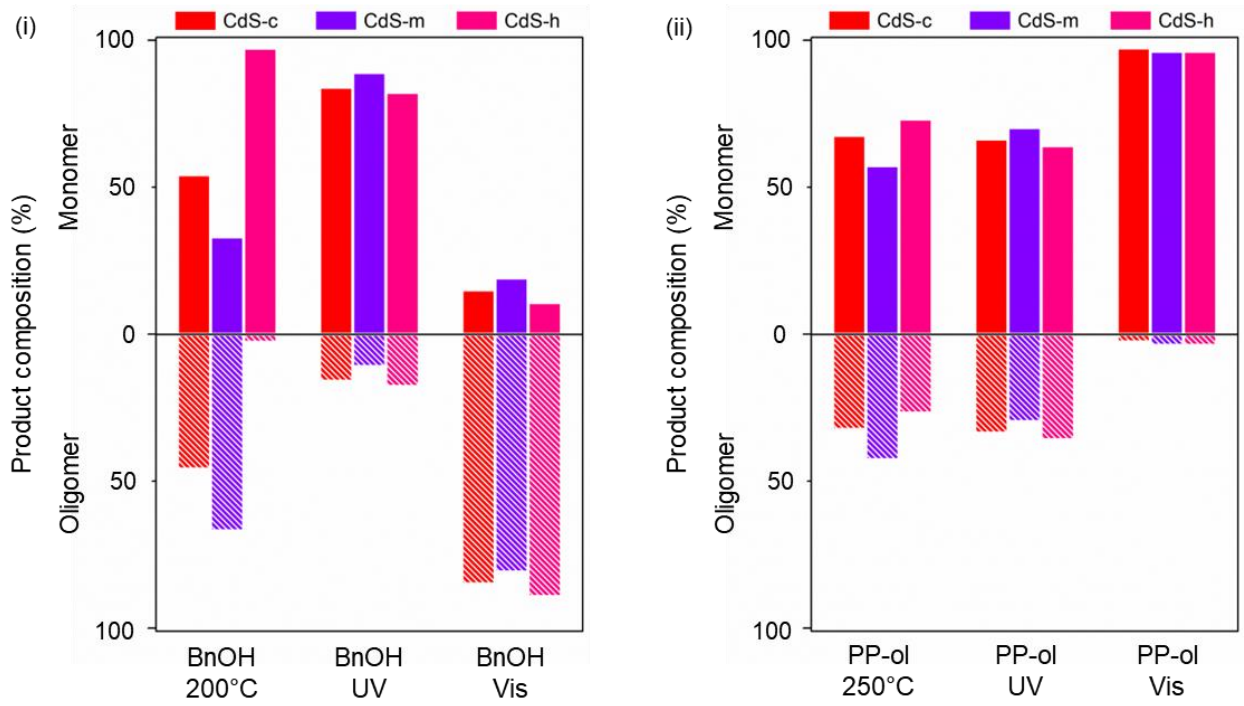

Figure 4.32. Proportion of monomers and oligomers produced through (i) benzyl alcohol and (ii) PP-ol conversion, under different conditions and CdS catalysts.

In benzyl alcohol conversion (Figure 4.32(i)), at high temperatures, monomers were overwhelmingly favored by **CdS-h**, while **CdS-m** facilitated more of the condensation reactions to larger byproducts, namely the dehydration of benzyl alcohol to dibenzyl ether. **CdS-c** favored the monomers slightly more, though this M:O ratio might be higher considering toluene production. Under photocatalytic conditions, the M:O ratio was highest with **CdS-m**, followed by **CdS-c** and finally **CdS-h**. Specifically under UV, monomers dominated the products, while under visible light, oligomers were significantly more prominent.

In the case of PP-ol conversion (Figure 4.32(ii)), the expected monomeric products of decomposition were acetophenone and phenol in equimolar amounts. However, other monomeric products were also observed, and in many cases, phenol was unexpectedly observed in much higher amounts relative to acetophenone.

Therefore, general M:O ratios were used to compare the catalysts' ability to preferentially catalyze cleavage reactions, as opposed to catalyzing dehydrogenation, dehydration, or coupling reactions, as these do not result in a significant decomposition of large parent molecules. At high temperatures, **CdS-h** showed the highest M:O ratio, indicating superior bond cleavage performance, while **CdS-m** favored more of the dimeric products. This followed the same trend as benzyl alcohol, although **CdS-h** did not overwhelmingly favor bond cleavages at the same degree. Also, the M:O ratio for the thermal decomposition of PP-ol might increase slightly due to styrene production, notably with **CdS-c** and **CdS-m**. Under UV, the M:O ratio from PP-ol conversion was highest with **CdS-m**, followed by **CdS-c** and finally **CdS-h**, like benzyl alcohol conversion. Under visible light, however, the trend breaks down, with the highest M:O ratio observed with **CdS-c**, followed by **CdS-m** and then **CdS-h**, the latter two being very close in value.

With limited data on the CdS properties, it is difficult to rationalize the trends in M:O ratios. That said, some information can be derived regarding the reaction systems based on observed products. First, based on high-temperature benzyl alcohol conversion, there seems to be a structural property unique to **CdS-h** that hinders the formation of larger products. It is also worth noting that in both benzyl alcohol and PP-ol, thermocatalysis with **CdS-m** generally favors oligomers. Since this was not observed with **CdS-c** or **CdS-m**, it is possible that oligomer formation was facilitated by cubic-hexagonal interfaces.

In addition, the high M:O ratio in the visible light-assisted conversion of PP-ol indicated that photogenerated electrons were not inhibited from participating in the reductive cleavage of the C_β-O bond in PP-ol. Indeed, after the hole-induced generation of the C_α-centered radical, electrons drove β-O-4 bond cleavage. Selectivity towards cleavage also suggests that the band positions of the synthesized CdS NPs were appropriately aligned with the redox potentials for PP-ol conversion.

Finally, it is important to note that the variation in benzyl alcohol and PP-ol conversion rates and products attributed to physical differences between **CdS-c**, **CdS-m**, and **CdS-h** were generally minor within the same reaction conditions. An exception was observed, notably with the considerable increase in M:O ratio, seen with **CdS-h** in the high-temperature conversion of benzyl alcohol. Ultimately, to significantly tune

catalytic activity and selectivity independently of reaction conditions, more drastic morphological changes need to be induced on the CdS NP architecture.

4.5. Conclusion

In this Chapter, we have successfully synthesized pristine, ligand-free CdS NPs of various crystalline phases by using the same precursors and tuning the synthesis temperature. Furthermore, we have showcased their catalytic activities in the conversion of benzyl alcohol and PP-ol at high temperatures, under UV irradiation, and under visible light irradiation. While some observable differences in substrate conversion rates and products were attributed to the differences in the physical properties of the synthesized CdS NPs, these differences did not drastically change the outcomes of substrate conversion. Our preliminary findings suggest that significant differences in substrate conversion and resulting products were largely governed by substrate structure and excitation sources. The selection of a viable CdS catalyst for lignin valorization purposes, among the ones synthesized in this Chapter, remains subject to further discussion and would depend on optimum reaction conditions, as well as finding a delicate balance between high conversion rate and an increased ratio of monomeric products relative to larger polymeric products. Nonetheless, as the substrate conversions were successfully conducted under solvent-free and inert atmosphere conditions, we have demonstrated that these substrate conversions on CdS are solvent-independent and can take place without external gas feedstock. In other words, the reactions were able to proceed without added oxidants, normally air or O_2 atmosphere, and no hydrogen gas (H_2) was necessary to drive reductive reactions. The solvent-independence offers a significant advantage in future heterogeneous catalysis applications. Most importantly, we have showcased that CdS can catalyze substrate conversion under high temperature conditions in the absence of light, which also resulted in the observation of distinct reaction pathways that have not been reported. In other words, CdS contributions to thermal decomposition reactions have been overlooked. Our results highlight an existing knowledge gap in this subject and expand the potential use of CdS beyond typical photocatalytic and electrocatalytic applications.

Chapter 5. Summary and Outlook

5.1. Summary

Chapter 1 highlighted the necessity of exploring renewable energy sources to meet increasing energy demands due to depleting reserves of non-renewable energy sources. In line with this, some context was provided regarding lignocellulosic biomass and how it can be valorized through heterogeneous catalysis, focusing on metal sulfides as the catalyst class of interest due to their widely reported potential applications for a variety of reactions. More specifically, recent progress in the use of CdS as a catalyst and current knowledge gaps were pinpointed. This helped set the scope of the work conducted in this Thesis. Chapter 2 outlines the working principles, procedures, and parameters behind some of the characterization methods used throughout the Thesis, notably regarding XRD, BET, and GC-MS. All chemicals were listed, and other characterization methods were briefly described in this Chapter as well.

In Chapter 3, the synthesis of CdS NPs through various reported procedures yielding NPs at various sizes, shapes, and crystalline phases was described. They were then characterized through the collection of their TEM images, XRD patterns, and BET surface areas. These CdS NPs were used in a series of preliminary experiments as photocatalysts for the decomposition of PP-ol in solution. Some photocatalytic kinetics experiments were also done in solution to highlight the difference in catalyst performance, depicted by the difference in PP-ol conversion rates, and to confirm the competitive nature of the two dominant PP-ol decomposition pathways. In other words, through the kinetics experiments, PP-ol decomposition to its ketone analogue, PP-one, was shown to occur in parallel with the β-O-4 bond cleavage to produce phenol and acetophenone, rather than the two pathways being sequential. Based on the results of CdS synthesis and photocatalysis experiments, a specific CdS synthesis procedure was selected for subsequent work.

In Chapter 4, a new set of CdS synthesis procedures was developed by modifying the procedure selected at the end of Chapter 3, with the aim of obtaining CdS NPs at the cubic, hexagonal, and mixed phases, followed by characterization as described in Chapter 3, with the additional collection of UV-vis adsorption

and IR spectra, as well as SEM images. These CdS NPs were then used in the catalytic conversion of benzyl alcohol and PP-ol under solvent-free conditions and inert atmosphere, under high temperature, UV irradiation, and visible light irradiation. The preliminary results of these experiments showed that excitation source played a larger role in dictating the possible products of substrate conversion. However, structural differences across CdS NPs did affect the extent of substrate conversion. While overall conversion under thermal conditions was not the highest, the experiments showcased that even in the dark, CdS can catalyze organic reactions at high temperatures. Furthermore, some of the resulting substrate conversion products were distinct from those observed in photocatalytic pathways, opening new avenues for potential applications. It was deduced that CdS merits consideration for further study in thermal lignin valorization.

5.2. Outlook

While the preliminary results of the work described in this Thesis are promising, it should be noted that considerable time was spent in optimizing experimental conditions, troubleshooting technical difficulties, and literature searches to speculate on the proposed structures of the uncharacterized molecules and elucidate the pathways leading to their formation. As a result, experimental work was prioritized to obtain results that would begin to address knowledge gaps mentioned in Chapter 1. Further work can be done to solidify the results that have already been obtained, and based on lessons learned, this Thesis has yielded several recommendations for future work. As the main driver for the project has been the exploration of CdS as a thermal catalyst for the decomposition of lignin in solvent-free conditions, the following recommendations were made based on that scope.

5.2.1. Additional characterization of CdS NPs

Beginning with the CdS catalysts themselves, thermogravimetric analysis (TGA) of the synthesized CdS NPs should be conducted to determine the maximum temperature at which the catalysts can operate before decomposing or undergoing other structural changes. As organic sulfur was observed in the thermal decomposition of benzyl alcohol and was speculated to have formed because of H_2S formation, this hypothesis can also be verified using TGA. A complementary technique that can be used is differential

scanning calorimetry (DSC), where phase transitions, if any, can be monitored by measuring sample temperature and heat flow. These analyses can also be done in different atmospheres to experimentally determine the influence of atmosphere on CdS stability. To get a better idea of the morphologies of the CdS NPs, high-resolution TEM (HRTEM) images should be collected to more decisively determine the catalysts' exposed facets, which may help rationalize the surface reactions leading to the observed products. To better understand the absorption geometry or orientation of the molecules of interest, in our case benzyl alcohol and PP-ol, first principle calculations can be done involving facets that were experimentally observed to be exposed. Raman spectroscopy can be conducted to provide more information on the vibrational modes not observed through the ATR-IR measurements, whether due to being out of scanning range or resulting from being IR inactive. Furthermore, Raman spectroscopy is also complementary to XRD, as it is possible to distinguish different polymorphs due to the difference in crystal lattice vibrations. For elemental analysis of surface atoms in the CdS NPs and a determination of their chemical states, X-ray photoelectron spectroscopy (XPS) can be used. While UV-vis absorption was measured for dispersed CdS to estimate the optical band gaps of the CdS NPs, a more fitting approach would have been diffuse reflectance spectroscopy (DRS) measurements on the solid CdS NPs instead. It should be noted that while optical band gap is not directly relevant to thermal catalysis, it does provide some insight into the presence of defects in the CdS NPs. Finally, since thermal catalysis reactions depend on the number and nature of active sites, one may find utility in subjecting the CdS NPs to temperature-programmed desorption (TPD) experiments using ammonia (NH_3) and CO_2 gas for the detection of acidic and basic active sites, respectively. The characterization techniques outlined in the Thesis body, alongside additional ones proposed in this Chapter, can be applied both pre- and post-catalyst usage in reactions. These measurements can be compared and discussed to assess the viability of the synthesized CdS NPs more holistically.

5.2.2. Additional experiments

Once the substrate conversion experiment protocols were established, duplicate experiments were initiated, but due to unforeseen difficulties, the products could not be characterized. That said, instead of performing

triplicates of the experiments elaborated in Chapter 4, a more useful exercise in the future would be to conduct solvent-free kinetics experiments to not only measure overall conversion of the substrates, but also estimate conversion rates. Monitoring product formation over time will also lead to a better understanding of the mechanisms and reaction pathways at play. This series of experiments, however, would require the reactions to be conducted at a larger scale, so further optimizations to the reaction setups may be needed.

Another immediate next step in the work involves catalyst longevity studies, where the lifetime and reusability of CdS NPs are assessed based on how well they maintain their performance after repeated cycles of benzyl alcohol and PP-ol conversion. This could be evaluated by measuring substrate conversion and monitoring product compositions, as well as characterizing CdS NPs in between each cycle to monitor physical changes to the catalysts themselves. However, implementing these studies presents challenges given current experimental procedures. As described in Chapter 4, the small scale of the substrate conversion experiments complicates the recovery of CdS NPs after each cycle, resulting in a gradual decrease in the quantity of available catalysts. Additionally, the small quantity of catalyst used for the experiments precludes complete characterization of the CdS NPs post-reaction, as a sizeable quantity is required for XRD characterization, and allocating part of the sample for TEM imaging, which would also include EDS, further diminishes the amount of catalyst available for the next cycle of catalysis experiments. A reaction scale-up would be the simplest solution to resolve this challenge.

In terms of validating the proposed reaction pathways and mechanisms, some control experiments using other substrates can be done. For example, one could use benzaldehyde as the substrate to determine if it experimentally undergoes reduction at all, or if it takes part in the formation of larger products despite the absence of benzyl alcohol. Thermal conversion of PP-one could also be monitored to definitively determine if it decomposes into any of the observed monomeric products from PP-ol conversion. 2-phenoxyethanol could be used as a substrate to elucidate the effect of removing one phenyl group on β-O-4 bond cleavage. Using PP-ol derivatives that are fully substituted on the C_α and C_β positions and monitoring their decomposition products, if any, would provide insight into the positions of abstracted hydrogen, or if the

reactions would proceed at all. Finally, monitoring β-phenoxystyrene decomposition for the absence of styrene would support the current proposed reaction pathways and mechanism.

One lingering uncertainty relates to the identities of the large coupling products. Because of the ionization methods employed throughout this work, it was not always possible to observe the molecular ions in the mass spectra of larger molecules. While we have proposed plausible molecular structures of large unidentified compounds, they still need to be experimentally confirmed. Aside from comparing GC-MS data with known standards, which were unavailable in-lab at the time of this Thesis publication, electrospray ionization mass spectrometry (ESI-MS) would be useful to obtain the molecular masses of the unknown products. In the case of certain compounds with multiple possible isomers, running assays in a GC-MS system coupled with a chiral column may provide more certainty during the qualitative analysis of reaction products. For additional characterization, these coupling products could be isolated, requiring column chromatography and the use of a rotary evaporator, and characterized by nuclear magnetic resonance (NMR). However, this may not be viable unless the scale of the experiments is increased. The unknown byproducts also need to be produced in sufficient amounts for isolation and characterization.

The thermal decomposition reactions were held at fairly high temperatures and a near-stoichiometric CdS-substrate ratio was used. Taking into consideration the scalability of the thermal decomposition reactions, there is value in exploring the effect of lower catalyst loading and lower reaction temperatures, as well as catalyst turnover and reusability. It is worth reiterating that all experiments reported in Chapter 4 were conducted under inert atmosphere. Therefore, future experiments studying the impact of H_2, O_2, or air on substrate conversion and resulting products is of great interest.

5.3. Future work

To end, an expansion of the current scope of study can take place in multiple directions. However, to move away from photocatalytic applications of CdS, which are already widely reported, follow-up studies involving the modification of the CdS architecture, comparison of CdS with other metal chalcogenides not

commonly reported for thermal catalysis, and performing the same studies using other lignin model molecules with different linkages or substitutions on the phenyl groups would greatly contribute to current progress in using CdS for lignin valorization.

References

(1) International Energy Agency. *World Energy Outlook 2023*; 2023.

(2) Energy Institute. *Statistical Review of World Energy 2024 (73rd Edition)*; 2024.

(3) BP. *Statistical Review of World Energy 2022 (71st Edition)*; 2022.

(4) Martins, T.; Barreto, A. C.; Souza, F. M.; Souza, A. M. Fossil Fuels Consumption and Carbon Dioxide Emissions in G7 Countries: Empirical Evidence from ARDL Bounds Testing Approach. *Environ. Pollut.* **2021**, *291*, 118093.

(5) Goldemberg, J. Ethanol for a Sustainable Energy Future. *Science (80-.).* **2007**, *315* (5813), 808–810.

(6) Margaritis, N.; Evaggelou, C.; Grammelis, P.; Yiannoulakis, H.; Papageorgiou, P.; Puschnigg, S.; Lindorfer, J. Use of Biomass as Alternative Fuel in Magnesia Sector. *Fuels* **2022**, *3* (4), 642–666.

(7) Li, L.; Liu, G. K.; Li, Y.; Zhu, Z.; Xu, H.; Chen, J.; Ren, X. Release of Sulfur and Nitrogen during Co-Pyrolysis of Coal and Biomass under Inert Atmosphere. *ACS Omega* **2020**, *5* (46), 30001–30010.

(8) Joshi, N. C.; Sinha, S.; Bhatnagar, P.; Nath, Y.; Negi, B.; Kumar, V.; Gururani, P. A Concise Review on Waste Biomass Valorization through Thermochemical Conversion. *Curr. Res. Microb. Sci.* **2024**, *6*, 100237.

(9) Aziz, T.; Farid, A.; Haq, F.; Kiran, M.; Ullah, A.; Zhang, K.; Li, C.; Ghazanfar, S.; Sun, H.; Ullah, R.; Ali, A.; Muzammal, M.; Shah, M.; Akhtar, N.; Selim, S.; Hagagy, N.; Samy, M.; Al Jaouni, S. K. A Review on the Modification of Cellulose and Its Applications. *Polymers (Basel).* **2022**, *14* (15), 3206.

(10) Cheng, C.; Wang, J.; Shen, D.; Xue, J.; Guan, S.; Gu, S.; Luo, K. H. Catalytic Oxidation of Lignin

in Solvent Systems for Production of Renewable Chemicals: A Review. *Polymers (Basel).* **2017**, *9* (6), 38–50.

(11) Hamou, C. A. O. Decomposition Mechanism of Lignin Models on Pt(111) : Combining Single Crystal Experiments and First-Principles Calculations, 2018.

(12) Pandey, M. P.; Kim, C. S. Lignin Depolymerization and Conversion: A Review of Thermochemical Methods. *Chem. Eng. Technol.* **2011**, *34* (1), 29–41.

(13) Behling, R.; Valange, S.; Chatel, G. Heterogeneous Catalytic Oxidation for Lignin Valorization into Valuable Chemicals: What Results? What Limitations? What Trends? *Green Chem.* **2016**, *18* (7), 1839–1854.

(14) Fache, M.; Boutevin, B.; Caillol, S. Vanillin Production from Lignin and Its Use as a Renewable Chemical. *ACS Sustain. Chem. Eng.* **2016**, *4* (1), 35–46.

(15) Zevallos Torres, L. A.; Lorenci Woiciechowski, A.; de Andrade Tanobe, V. O.; Karp, S. G.; Guimarães Lorenci, L. C.; Faulds, C.; Soccol, C. R. Lignin as a Potential Source of High-Added Value Compounds: A Review. *J. Clean. Prod.* **2020**, *263*, 121499.

(16) Boeriu, C. G.; Bravo, D.; Gosselink, R. J. A.; Van Dam, J. E. G. Characterisation of Structure-Dependent Functional Properties of Lignin with Infrared Spectroscopy. *Ind. Crops Prod.* **2004**, *20* (2), 205–218.

(17) Gao, Z.; Lang, X.; Chen, S.; Zhao, C. Mini-Review on the Synthesis of Lignin-Based Phenolic Resin. *Energy and Fuels* **2021**, *35* (22), 18385–18395.

(18) Wang, H.; Tucker, M.; Ji, Y. Recent Development in Chemical Depolymerization of Lignin: A Review. *J. Appl. Chem.* **2013**, *2013*, 1–9.

(19) Weng, C.; Peng, X.; Han, Y. Depolymerization and Conversion of Lignin to Value-Added Bioproducts by Microbial and Enzymatic Catalysis. *Biotechnol. Biofuels* **2021**, *14* (1), 1–22.

(20) Bugg, T. D. H.; Williamson, J. J.; Rashid, G. M. M. Bacterial Enzymes for Lignin Depolymerisation: New Biocatalysts for Generation of Renewable Chemicals from Biomass. *Curr. Opin. Chem. Biol.* **2020**, *55*, 26–33.

(21) Du, X.; Zhang, H.; Sullivan, K. P.; Gogoi, P.; Deng, Y. Electrochemical Lignin Conversion. *ChemSusChem* **2020**, *13* (17), 4318–4343.

(22) Sun, Z.; Fridrich, B.; De Santi, A.; Elangovan, S.; Barta, K. Bright Side of Lignin Depolymerization: Toward New Platform Chemicals. *Chem. Rev.* **2018**, *118* (2), 614–678.

(23) Wong, S. S.; Shu, R.; Zhang, J.; Liu, H.; Yan, N. Downstream Processing of Lignin Derived Feedstock into End Products. *Chem. Soc. Rev.* **2020**, *49* (15), 5510–5560.

(24) Chio, C.; Sain, M.; Qin, W. Lignin Utilization: A Review of Lignin Depolymerization from Various Aspects. *Renew. Sustain. Energy Rev.* **2019**, *107*, 232–249.

(25) Mukhtar, A.; Saqib, S.; Lin, H.; Hassan Shah, M. U.; Ullah, S.; Younas, M.; Rezakazemi, M.; Ibrahim, M.; Mahmood, A.; Asif, S.; Bokhari, A. Current Status and Challenges in the Heterogeneous Catalysis for Biodiesel Production. *Renew. Sustain. Energy Rev.* **2022**, *157*, 112012.

(26) Thomas, J. M.; Thomas, W. J. *Principles and Practice of Heterogeneous Catalysis*, 2nd ed.; Wiley-VCH Verlag GmbH & Co. KGaA: Weinheim, 2015.

(27) Xia, Y.; Yang, X. Toward Cost-Effective and Sustainable Use of Precious Metals in Heterogeneous Catalysts. *Acc. Chem. Res.* **2017**, *50* (3), 450–454.

(28) Védrine, J. C. Heterogeneous Catalysis on Metal Oxides. *Catalysts* **2017**, *7* (11), 341.

(29) Eijsbouts, S.; Mayo, S. W.; Fujita, K. Unsupported Transition Metal Sulfide Catalysts: From Fundamentals to Industrial Application. *Appl. Catal. A Gen.* **2007**, *322*, 58–66.

(30) Chianelli, R. R.; Berhault, G.; Torres, B. Unsupported Transition Metal Sulfide Catalysts: 100 Years

of Science and Application. *Catal. Today* **2009**, *147* (3–4), 275–286.

(31) Pecoraro, T. A.; Chianelli, R. R. Hydrodesulfurization Catalysis by Transition Metal Sulfides. *J. Catal.* **1981**, *67* (2), 430–445.

(32) Hermann, N.; Brorson, M.; Topsøe, H. Activities of Unsupported Second Transition Series Metal Sulfides for Hydrodesulfurization of Sterically Hindered 4,6-Dimethyldibenzothiophene and of Unsubstituted Dibenzothiophene. *Catal. Letters* **2000**, *65* (4), 169–174.

(33) Quartararo, J.; Mignard, S.; Kasztelan, S. Hydrodesulfurization and Hydrogenation Activities of Alumina-Supported Transition Metal Sulfides. *J. Catal.* **2000**, *192* (2), 307–315.

(34) Eijsbouts, S.; H.J. de Beer, V.; Prins, R. Periodic Trends in the Hydrodenitrogenation Activity of Carbon-Supported Transition Metal Sulfide Catalysts. *J. Catal.* **1988**, *109* (1), 217–220.

(35) Vít, Z.; Zdražil, M. Simultaneous Hydrodenitrogenation of Pyridine and Hydrodesulfurization of Thiophene over Carbon-Supported Platinum Metal Sulfides. *J. Catal.* **1989**, *119* (1), 1–7.

(36) Xing, M.; Xu, W.; Dong, C.; Bai, Y.; Zeng, J.; Zhou, Y.; Zhang, J.; Yin, Y. Metal Sulfides as Excellent Co-Catalysts for H_2O_2 Decomposition in Advanced Oxidation Processes. *Chem* **2018**, *4* (6), 1359–1372.

(37) Wang, M.; Zhang, L.; He, Y.; Zhu, H. Recent Advances in Transition-Metal-Sulfide-Based Bifunctional Electrocatalysts for Overall Water Splitting. *J. Mater. Chem. A* **2021**, *9* (9), 5320–5363.

(38) Weise, C. F.; Falsig, H.; Moses, P. G.; Helveg, S.; Brorson, M.; Hansen, L. P. Single-Atom Pt Promotion of Industrial Co-Mo-S Catalysts for Ultra-Deep Hydrodesulfurization. *J. Catal.* **2021**, *403*, 74–86.

(39) Cortés-Jácome, M. A.; Escobar, J.; Angeles Chávez, C.; López-Salinas, E.; Romero, E.; Ferrat, G.; Toledo-Antonio, J. A. Highly Dispersed CoMoS Phase on Titania Nanotubes as Efficient HDS Catalysts. *Catal. Today* **2008**, *130* (1), 56–62.

(40) Lebeau, B.; Bonne, M.; Comparot, J. D.; Rousseau, J.; Michelin, L.; Blin, J. L.; Brunet, S. HDS of 4,6-Dimethyldibenzothiophene over CoMoS Supported Mesoporous SiO_2-TiO_2 Materials. *Catal. Today* **2020**, *357*, 675–683.

(41) de León, J. N. D.; Kumar, C. R.; Antúnez-García, J.; Fuentes-Moyado, S. Recent Insights in Transition Metal Sulfide Hydrodesulfurization Catalysts for the Production of Ultra Low Sulfur Diesel: A Short Review. *Catalysts* **2019**, *9* (1), 87.

(42) Kouzu, M.; Uchida, K.; Kuriki, Y.; Ikazaki, F. Micro-Crystalline Molybdenum Sulfide Prepared by Mechanical Milling as an Unsupported Model Catalyst for the Hydrodesulfurization of Diesel Fuel. *Appl. Catal. A Gen.* **2004**, *276* (1–2), 241–249.

(43) Okamoto, Y.; Maezawa, A.; Imanaka, T. Active Sites of Molybdenum Sulfide Catalysts Supported on Al_2O_3 and TiO_2 for Hydrodesulfurization and Hydrogenation. *J. Catal.* **1989**, *120* (1), 29–45.

(44) Yu, L.; Cui, W. G.; Zhang, Q.; Li, Z. F.; Shen, Y.; Hu, T. L. Atomic Layer Deposition of Nano-Scale Molybdenum Sulfide within a Metal-Organic Framework for Highly Efficient Hydrodesulfurization. *Mater. Adv.* **2021**, *2* (4), 1294–1301.

(45) Curtis, C. W.; Cahela, D. R. Hydrodenitrogenation of Quinoline and Coal Using Precipitated Transition-Metal Sulfides. *Energy and Fuels* **1989**, *3* (2), 168–174.

(46) Ho, T. C.; Jacobson, A. J.; Chianelli, R. R.; Lund, C. R. F. Hydrodenitrogenation-Selective Catalysts I. Fe Promoted Mo/W Sulfides. *J. Catal.* **1992**, *138* (1), 351–363.

(47) Eijsbouts, S.; De Beer, V. H. J.; Prins, R. Hydrodenitrogenation of Quinoline over Carbon-Supported Transition Metal Sulfides. *J. Catal.* **1991**, *127* (2), 619–630.

(48) Eijsbouts, S.; Sudhakar, C.; De Beer, V. H. J.; Prins, R. Hydrodenitrogenation of Decahydroquinoline, Cyclohexylamine and O-Propylaniline over Carbon-Supported Transition Metal Sulfide Catalysts. *J. Catal.* **1991**, *127* (2), 605–618.

(49) Jiang, S.; Ji, N.; Diao, X.; Li, H.; Rong, Y.; Lei, Y.; Yu, Z. Vacancy Engineering in Transition Metal Sulfide and Oxide Catalysts for Hydrodeoxygenation of Lignin-Derived Oxygenates. *ChemSusChem* **2021**, *14* (20), 4377–4396.

(50) Arun, N.; Sharma, R. V.; Dalai, A. K. Green Diesel Synthesis by Hydrodeoxygenation of Bio-Based Feedstocks: Strategies for Catalyst Design and Development. *Renew. Sustain. Energy Rev.* **2015**, *48*, 240–255.

(51) Cooper, B. H.; Donnis, B. B. L. Aromatic Saturation of Distillates: An Overview. *Appl. Catal. A Gen.* **1996**, *137* (2), 203–223.

(52) Fu, W.; Zhang, L.; Wu, D.; Xiang, M.; Zhuo, Q.; Huang, K.; Tao, Z.; Tang, T. Mesoporous Zeolite-Supported Metal Sulfide Catalysts with High Activities in the Deep Hydrogenation of Phenanthrene. *J. Catal.* **2015**, *330*, 423–433.

(53) Vogelgsang, F.; Shi, H.; Lercher, J. A. Toward Quantification of Active Sites and Site-Specific Activity for Polyaromatics Hydrogenation on Transition Metal Sulfides. *J. Catal.* **2021**, *403*, 98–110.

(54) Qin, J. F.; Yang, M.; Chen, T. S.; Dong, B.; Hou, S.; Ma, X.; Zhou, Y. N.; Yang, X. L.; Nan, J.; Chai, Y. M. Ternary Metal Sulfides MoCoNiS Derived from Metal Organic Frameworks for Efficient Oxygen Evolution. *Int. J. Hydrogen Energy* **2020**, *45* (4), 2745–2753.

(55) Zhang, R.; Gong, K.; Cao, S.; Du, F. Amorphous Sulfur-Rich CoSx Nanodots as Highly Efficient Cocatalyst to Promote Photocatalytic Hydrogen Evolution over TiO_2. *Int. J. Hydrogen Energy* **2022**, *47* (94), 39875–39885.

(56) Gao, T.; Nie, M.; Luo, J.; Huang, Z.; Sun, H.; Guo, P.; Xue, Z.; Liao, J.; Li, Q.; Teng, L. Nickel Sulfides Supported by Carbon Spheres as Efficient Catalysts for Hydrogen Evolution Reaction. *Electrochem. commun.* **2021**, *129*, 107076.

(57) Han, C.; Li, W.; Shu, C.; Guo, H.; Liu, H.; Dou, S.; Wang, J. Catalytic Activity Boosting of Nickel Sulfide toward Oxygen Evolution Reaction via Confined Overdoping Engineering. *ACS Appl. Energy Mater.* **2019**, *2* (8), 5363–5372.

(58) Ding, Y.; Xue, Q.; Hong, Q. L.; Li, F. M.; Jiang, Y. C.; Li, S. N.; Chen, Y. Hydrogen and Potassium Acetate Co-Production from Electrochemical Reforming of Ethanol at Ultrathin Cobalt Sulfide Nanosheets on Nickel Foam. *ACS Appl. Mater. Interfaces* **2021**, *13* (3), 4026–4033.

(59) Irshad, A.; Munichandraiah, N. Electrodeposited Nickel-Cobalt-Sulfide Catalyst for the Hydrogen Evolution Reaction. *ACS Appl. Mater. Interfaces* **2017**, *9* (23), 19746–19755.

(60) Cui, M.; Yang, C.; Li, B.; Dong, Q.; Wu, M.; Hwang, S.; Xie, H.; Wang, X.; Wang, G.; Hu, L. High-Entropy Metal Sulfide Nanoparticles Promise High-Performance Oxygen Evolution Reaction. *Adv. Energy Mater.* **2021**, *11* (3), 1–8.

(61) Guo, Y.; Park, T.; Yi, J. W.; Henzie, J.; Kim, J.; Wang, Z.; Jiang, B.; Bando, Y.; Sugahara, Y.; Tang, J.; Yamauchi, Y. Nanoarchitectonics for Transition-Metal-Sulfide-Based Electrocatalysts for Water Splitting. *Adv. Mater.* **2019**, *31* (17), 1–34.

(62) Fu, G.; Lee, J. M. Ternary Metal Sulfides for Electrocatalytic Energy Conversion. *J. Mater. Chem. A* **2019**, *7* (16), 9386–9405.

(63) Sutherland, B. R. Solar Materials Find Their Band Gap. *Joule* **2020**, *4* (5), 984–985.

(64) Ogoshi, E.; Popolin-Neto, M.; Acosta, C. M.; Nascimento, G. M.; Rodrigues, J. N. B.; Oliveira, O. N.; Paulovich, F. V.; Dalpian, G. M. Learning from Machine Learning: The Case of Band-Gap Directness in Semiconductors. *Discov. Mater.* **2024**, *4* (1).

(65) Cited, L.; October, A. Cadmium Pigments. *Nature* **1939**, *143* (3630), 891–891.

(66) Weimer, P. K. The TFT - A New Thin-Film Transistor. In *Proceedings of the IRE*; 1962; Vol. 50, pp 1462–1469.

(67) Yang, X.; Xu, C.; Giles, N. C. Intrinsic Electron Mobilities in CdSe, CdS, ZnO, and ZnS and Their Use in Analysis of Temperature-Dependent Hall Measurements. *J. Appl. Phys.* **2008**, *104* (7), 73727.

(68) Abdullah, U.; Ali, M.; Pervaiz, E. An Inclusive Review on Recent Advancements of Cadmium Sulfide Nanostructures and Its Hybrids for Photocatalytic and Electrocatalytic Applications. *Mol. Catal.* **2021**, *508*, 111575.

(69) Yuan, Y. J.; Chen, D.; Yu, Z. T.; Zou, Z. G. Cadmium Sulfide-Based Nanomaterials for Photocatalytic Hydrogen Production. *J. Mater. Chem. A* **2018**, *6* (25), 11606–11630.

(70) Chen, X.; Shangguan, W. Hydrogen Production from Water Splitting on CdS-Based Photocatalysts Using Solar Light. *Front. Energy* **2013**, *7* (1), 111–118.

(71) Koumanakos, E.; Dalas, E.; Koutsoukos, P. G. The Precipitation of Cadmium Sulphide in Aqueous Solutions. *J. Chem. Soc. Faraday Trans.* **1990**, *86* (6), 973–977.

(72) Singh, V.; Chauhan, P. Structural and Optical Characterization of CdS Nanoparticles Prepared by Chemical Precipitation Method. *J. Phys. Chem. Solids* **2009**, *70* (7), 1074–1079.

(73) Du, K. Z.; Chaturvedi, A.; Wang, X. Z.; Zhao, Y.; Zhang, K. K.; Iqbal Bakti Utama, M.; Hu, P.; Jiang, H.; Xiong, Q. H.; Kloc, C. Plasma-Enhanced Microwave Solid-State Synthesis of Cadmium Sulfide: Reaction Mechanism and Optical Properties. *Dalt. Trans.* **2015**, *44* (30), 13444–13449.

(74) Baláž, P.; Baláž, M.; Dutková, E.; Zorkovská, A.; Kováč, J.; Hronec, P.; Kováč, J.; Čaplovičová, M.; Mojžiš, J.; Mojžišová, G.; Eliyas, A.; Kostova, N. G. CdS/ZnS Nanocomposites: From Mechanochemical Synthesis to Cytotoxicity Issues. *Mater. Sci. Eng. C* **2016**, *58*, 1016–1023.

(75) Zelaya-Angel, O.; Hernandez, L.; de Melo, O.; Alvarado-Gil, J. J.; Lozada-Morales, R.; Falcony, C.; Vargas, H.; Ramirez-Bon, R. Band-Gap Shift in CdS: Phase Transition from Cubic to Hexagonal on Thermal Annealing. *Vacuum* **1995**, *46* (8–10), 1083–1085.

(76) Zhang, Y.; Shi, Z.; Luo, L.; Liu, Z.; Macharia, D. K.; Duoerkun, G.; Shen, C.; Liu, J.; Zhang, L.

Construction of Titanium Dioxide/Cadmium Sulfide Heterojunction on Carbon Fibers as Weavable Photocatalyst for Eliminating Various Contaminants. *J. Colloid Interface Sci.* **2020**, *561*, 307–317.

(77) Sonker, R. K.; Yadav, B. C.; Gupta, V.; Tomar, M. Synthesis of CdS Nanoparticle by Sol-Gel Method as Low Temperature NO_2 Sensor. *Mater. Chem. Phys.* **2020**, *239*, 121975.

(78) Wang, J.; Yang, J.; Yang, H.; Huang, H.; Yang, X.; Wei, L. Solvothermal Synthesis of CdS at Different Solvents and Its Photocatalytic Activity for Antibiotics. *Opt. Mater. (Amst).* **2023**, *135*, 113303.

(79) Lang, D.; Xiang, Q.; Qiu, G.; Feng, X.; Liu, F. Effects of Crystalline Phase and Morphology on the Visible Light Photocatalytic H_2-Production Activity of CdS Nanocrystals. *Dalt. Trans.* **2014**, *43* (19), 7245–7253.

(80) Yang, X.; Wang, B.; Mu, Y.; Zheng, M.; Wang, Y. Photocatalytic Performance of Cubic and Hexagonal Phase CdS Synthesized via Different Cd Sources. *J. Electron. Mater.* **2019**, *48* (5), 2895–2901.

(81) Zhang, J.; Song, Y.; Dong, X.; Jiang, H.; Tang, J.; Li, H. Umbrella-like CdS Single Crystal: Exposed (002) Facets and Enhanced Photocatalytic Properties. *J. Mater. Sci.* **2020**, *55* (25), 11167–11176.

(82) Senasu, T.; Ruengchai, N.; Khamdon, S.; Lorwanishpaisarn, N.; Nanan, S. Hydrothermal Synthesis of Cadmium Sulfide Photocatalyst for Detoxification of Azo Dyes and Ofloxacin Antibiotic in Wastewater. *Molecules* **2022**, *27* (22), 7944.

(83) Bu, W.; Zhang, Y.; Qin, Q.; Li, Y.; Zhou, Z.; Hu, C.; Chuai, X.; Wang, T.; Sun, P.; Lu, G. Homojunction between Cubic/Hexagonal CdS Nanocrystal for High and Fast Response to n-Propanol. *Sensors Actuators B Chem.* **2022**, *369*, 132281.

(84) Bandaranayake, R. J.; Wen, G. W.; Lin, J. Y.; Jiang, H. X.; Sorensen, C. M. Structural Phase Behavior in II-VI Semiconductor Nanoparticles. *Appl. Phys. Lett.* **1995**, *67*, 831.

(85) Isik, M.; Gullu, H. H.; Delice, S.; Parlak, M.; Gasanly, N. M. Structural and Temperature-Dependent Optical Properties of Thermally Evaporated CdS Thin Films. *Mater. Sci. Semicond. Process.* **2019**, *93*, 148–152.

(86) Wang, X.; Liu, M.; Zhou, Z.; Guo, L. Toward Facet Engineering of CdS Nanocrystals and Their Shape-Dependent Photocatalytic Activities. *J. Phys. Chem. C* **2015**, *119* (35), 20555–20560.

(87) Xiao, C.; Lu, B. A.; Xue, P.; Tian, N.; Zhou, Z. Y.; Lin, X.; Lin, W. F.; Sun, S. G. High-Index-Facet- and High-Surface-Energy Nanocrystals of Metals and Metal Oxides as Highly Efficient Catalysts. *Joule* **2020**, *4* (12), 2562–2598.

(88) Qiu, X.; Ding, L.; Zhang, C.; Ouyang, Z.; Jia, H.; Guo, X.; Zhu, L. Exposed Facets Mediated Interaction of Polystyrene Nanoplastics (PSNPs) with Iron Oxides Nanocrystal. *J. Hazard. Mater.* **2022**, *435*, 128994.

(89) Chang, K. J.; Froyen, S.; Cohen, M. L. Electronic Band Structures for Zinc-Blende and Wurtzite CdS. *Phys. Rev. B* **1983**, *28* (8), 4736–4743.

(90) Edossa, T. G.; Woldemariam, M. M. Electronic, Structural, and Optical Properties of Zinc Blende and Wurtzite Cadmium Sulfide (CdS) Using Density Functional Theory. *Adv. Condens. Matter Phys.* **2020**, *2020*.

(91) Heiba, Z. K.; Mohamed, M. B.; Badawi, A. Structure, Optical and Electronic Characteristics of Iron-Doped Cadmium Sulfide under Nonambient Atmosphere. *Appl. Phys. A Mater. Sci. Process.* **2021**, *127* (3), 1–11.

(92) Naseri, M.; Bafekry, A.; Faraji, M.; Hoat, D. M.; Fadlallah, M. M.; Ghergherehchi, M.; Sabbaghi, N.; Gogova, D. Two-Dimensional Buckled Tetragonal Cadmium Chalcogenides Including CdS, CdSe, and CdTe Monolayers as Photo-Catalysts for Water Splitting. *Phys. Chem. Chem. Phys.* **2021**, *23* (21), 12226–12232.

(93) Iqbal, M.; Ali, A.; Nahyoon, N. A.; Majeed, A.; Pothu, R.; Phulpoto, S.; Thebo, K. H. Photocatalytic Degradation of Organic Pollutant with Nanosized Cadmium Sulfide. *Mater. Sci. Energy Technol.* **2019**, *2* (1), 41–45.

(94) Upadhyay, R. K.; Sharma, M.; Singh, D. K.; Amritphale, S. S.; Chandra, N. Photo Degradation of Synthetic Dyes Using Cadmium Sulfide Nanoparticles Synthesized in the Presence of Different Capping Agents. *Sep. Purif. Technol.* **2012**, *88*, 39–45.

(95) Manzoor, S.; Malana, M. A.; Alshahrani, T.; Gohar, R. S.; Khan, W. Q.; Najam-ul-Haq, M.; Ehsan, M. F.; Shah, A.; Ashiq, M. N.; Ahmed, S. Visible-Light-Driven Zirconium Oxide/Cadmium Sulfide Nanocomposite for Degradation of Textile Dyes. *Int. J. Environ. Sci. Technol.* **2022**, *19* (5), 4037–4046.

(96) Feitosa, M. H. A.; Prado, T. M.; Santos, A. M.; Silva, L. P.; Grosseli, G. M.; Fadini, P. S.; Fatibello-Filho, O.; Moraes, F. C. Titanium Dioxide/Cadmium Sulfide Photoanode Applied to Photoelectrodegradation of Naproxen in Wastewater. *J. Electroanal. Chem.* **2021**, *897*, 115571.

(97) Wang, Y.; Feng, S.; Ma, C.; Zhou, Y.; Ye, Z.; Dai, X.; Cao, X. Synthesis of Z-Type Heterojunction Bifunctional Composites with Mn-Doped CdS Nanoparticles Supported on NH_2-MIL-125(Ti) for Hydrogen Evolution and Antibiotic Degradation under Visible Light. *Opt. Mater. (Amst).* **2023**, *135*, 113087.

(98) Liu, Q.; Wang, K.; Huan, J.; Zhu, G.; Qian, J.; Mao, H.; Cai, J. Graphene Quantum Dots Enhanced Electrochemiluminescence of Cadmium Sulfide Nanocrystals for Ultrasensitive Determination of Pentachlorophenol. *Analyst* **2014**, *139* (11), 2912–2918.

(99) Li, J. Y.; Li, Y. H.; Qi, M. Y.; Lin, Q.; Tang, Z. R.; Xu, Y. J. Selective Organic Transformations over Cadmium Sulfide-Based Photocatalysts. *ACS Catal.* **2020**, *10* (11), 6262–6280.

(100) Jiang, D.; Chen, X.; Zhang, Z.; Zhang, L.; Wang, Y.; Sun, Z.; Irfan, R. M.; Du, P. Highly Efficient

Simultaneous Hydrogen Evolution and Benzaldehyde Production Using Cadmium Sulfide Nanorods Decorated with Small Cobalt Nanoparticles under Visible Light. *J. Catal.* **2018**, *357*, 147–153.

(101) Lee, S. G.; Kang, M. J.; Park, M.; Kim, K. jeong; Lee, H.; Kim, H. S. Selective Photocatalytic Conversion of Benzyl Alcohol to Benzaldehyde or Deoxybenzoin over Ion-Exchanged CdS. *Appl. Catal. B Environ.* **2022**, *304*, 120967.

(102) Mitkina, T.; Stanglmair, C.; Setzer, W.; Gruber, M.; Kisch, H.; König, B. Visible Light Mediated Homo- and Heterocoupling of Benzyl Alcohols and Benzyl Amines on Polycrystalline Cadmium Sulfide. *Org. Biomol. Chem.* **2012**, *10* (17), 3556–3561.

(103) Dimeglio, J. L.; Breuhaus-Alvarez, A. G.; Li, S.; Bartlett, B. M. Nitrate-Mediated Alcohol Oxidation on Cadmium Sulfide Photocatalysts. *ACS Catal.* **2019**, *9* (6), 5732–5741.

(104) Qi, M. Y.; Lin, Q.; Tang, Z. R.; Xu, Y. J. Photoredox Coupling of Benzyl Alcohol Oxidation with CO_2 Reduction over CdS/TiO_2 Heterostructure under Visible Light Irradiation. *Appl. Catal. B Environ.* **2022**, *307*, 121158.

(105) Xiang, X.; Zhu, B.; Zhang, J.; Jiang, C.; Chen, T.; Yu, H.; Yu, J.; Wang, L. Photocatalytic H_2-Production and Benzyl-Alcohol-Oxidation Mechanism over CdS Using Co^{2+} as Hole Cocatalyst. *Appl. Catal. B Environ.* **2023**, *324*, 122301.

(106) Zhang, K.; Lu, G.; Xi, Z.; Li, Y.; Luan, Q.; Huang, X. Covalent Organic Framework Stabilized CdS Nanoparticles as Efficient Visible-Light-Driven Photocatalysts for Selective Oxidation of Aromatic Alcohols. *Chinese Chem. Lett.* **2021**, *32* (7), 2207–2211.

(107) She, H.; Li, L.; Sun, Y.; Wang, L.; Huang, J.; Zhu, G.; Wang, Q. Facile Preparation of Mixed-Phase CdS and Its Enhanced Photocatalytic Selective Oxidation of Benzyl Alcohol under Visible Light Irradiation. *Appl. Surf. Sci.* **2018**, *457*, 1167–1173.

(108) McClelland, K. P.; Weiss, E. A. Selective Photocatalytic Oxidation of Benzyl Alcohol to Benzaldehyde or C-C Coupled Products by Visible-Light-Absorbing Quantum Dots. *ACS Appl. Energy Mater.* **2019**, *2* (1), 92–96.

(109) Li, P.; Yan, X.; Gao, S.; Cao, R. Boosting Photocatalytic Hydrogen Production Coupled with Benzyl Alcohol Oxidation over CdS/Metal–Organic Framework Composites. *Chem. Eng. J.* **2021**, *421*, 129870.

(110) Chai, Z. M.; Wang, B. H.; Tan, Y. X.; Bai, Z. J.; Pan, J. B.; Chen, L.; Shen, S.; Guo, J. K.; Xie, T. L.; Au, C. T.; Yin, S. F. Enhanced Photocatalytic Activity for Selective Oxidation of Toluene over Cubic-Hexagonal CdS Phase Junctions. *Ind. Eng. Chem. Res.* **2021**, *60* (30), 11106–11116.

(111) Liu, F.; Xiao, C. X.; Meng, L. H.; Chen, L.; Zhang, Q.; Liu, J. Bin; Shen, S.; Guo, J. K.; Au, C. T.; Yin, S. F. Facile Fabrication of Octahedral CdS-ZnS by Cation Exchange for Photocatalytic Toluene Selective Oxidation. *ACS Sustain. Chem. Eng.* **2020**, *8* (2), 1302–1310.

(112) Tan, Y. X.; Chai, Z. M.; Wang, B. H.; Tian, S.; Deng, X. X.; Bai, Z. J.; Chen, L.; Shen, S.; Guo, J. K.; Cai, M. Q.; Au, C. T.; Yin, S. F. Boosted Photocatalytic Oxidation of Toluene into Benzaldehyde on $CdIn_2S_4$-CdS: Synergetic Effect of Compact Heterojunction and S-Vacancy. *ACS Catal.* **2021**, *11* (5), 2492–2503.

(113) Wu, X.; Fan, X.; Xie, S.; Lin, J.; Cheng, J.; Zhang, Q.; Chen, L.; Wang, Y. Solar Energy-Driven Lignin-First Approach to Full Utilization of Lignocellulosic Biomass under Mild Conditions. *Nat. Catal.* **2018**, *1* (10), 772–780.

(114) Wu, X.; Xie, S.; Liu, C.; Zhou, C.; Lin, J.; Kang, J.; Zhang, Q.; Wang, Z.; Wang, Y. Ligand-Controlled Photocatalysis of CdS Quantum Dots for Lignin Valorization under Visible Light. *ACS Catal.* **2019**, *9* (9), 8443–8451.

(115) Firoozi, S.; Hosseini-Sarvari, M.; Koohgard, M. Solvent-Free and Room Temperature Visible Light-

Induced C-H Activation: CdS as a Highly Efficient Photo-Induced Reusable Nano-Catalyst for the C-H Functionalization Cyclization of t-Amines and C-C Double and Triple Bonds. *Green Chem.* **2018**, *20* (24), 5540–5549.

(116) Zhang, C.; Lu, J.; Zhang, X.; Macarthur, K.; Heggen, M.; Li, H.; Wang, F. Cleavage of the Lignin β-O-4 Ether Bond: Via a Dehydroxylation-Hydrogenation Strategy over a NiMo Sulfide Catalyst. *Green Chem.* **2016**, *18* (24), 6545–6555.

(117) Liu, S.; van Muyden, A. P.; Bai, L.; Cui, X.; Fei, Z.; Li, X.; Hu, X.; Dyson, P. J. Metal-Sulfide Catalysts Derived from Lignosulfonate and Their Efficient Use in Hydrogenolysis. *ChemSusChem* **2019**, *12* (14), 3271–3277.

(118) Song, W.; Lai, W.; Lian, Y.; Jiang, X.; Yang, W. Sulfated ZrO_2 Supported CoMo Sulfide Catalyst by Surface Exsolution for Enhanced Hydrodeoxygenation of Lignin-Derived Ethers to Aromatics. *Fuel* **2020**, *263*, 116705.

(119) Guo, H.; Chen, Z.; Yin, Q.; Sun, T.; Liu, Y.; Ren, G.; Li, C. Waste to Wealth: H_2S-Free Fabrication of Fe-ZnS/NC by Industrial Lignin Self S-Doping for Efficient Lignin Aerobic Oxidation. *Appl. Catal. B Environ.* **2023**, *339*, 123129.

(120) Ghasempour, A.; Dehghan, H.; Ataee, M.; Chen, B.; Zhao, Z.; Sedighi, M.; Guo, X.; Shahbazi, M. A. Cadmium Sulfide Nanoparticles: Preparation, Characterization, and Biomedical Applications. *Molecules* **2023**, *28* (9), 1–32.

(121) Ozcan, A.; Meral, H. *Introduction to Fundamentals of Nanoparticle Synthesis, Characterization, and Properties*; INC, 2024.

(122) Burlec, A. F.; Corciova, A.; Boev, M.; Batir-Marin, D.; Mircea, C.; Cioanca, O.; Danila, G.; Danila, M.; Bucur, A. F.; Hancianu, M. Current Overview of Metal Nanoparticles' Synthesis, Characterization, and Biomedical Applications, with a Focus on Silver and Gold Nanoparticles.

Pharmaceuticals **2023**, *16* (10), 1410.

(123) Kumari, S.; Raturi, S.; Kulshrestha, S.; Chauhan, K.; Dhingra, S.; András, K.; Thu, K.; Khargotra, R.; Singh, T. A Comprehensive Review on Various Techniques Used for Synthesizing Nanoparticles. *J. Mater. Res. Technol.* **2023**, *27*, 1739–1763.

(124) Nam, N. H.; Luong, N. H. Nanoparticles: Synthesis and Applications. In *Materials for Biomedical Engineering*; Elsevier, 2019; Vol. 2507, pp 211–240.

(125) Sweeney, R. Y.; Mao, C.; Gao, X.; Burt, J. L.; Belcher, A. M.; Georgiou, G.; Iverson, B. L. Bacterial Biosynthesis of Cadmium Sulfide Nanocrystals. *Chem. Biol.* **2004**, *11* (11), 1553–1559.

(126) Seisenbaeva, G. A.; Kessler, V. G. Precursor Directed Synthesis - "Molecular" Mechanisms in the Soft Chemistry Approaches and Their Use for Template-Free Synthesis of Metal, Metal Oxide and Metal Chalcogenide Nanoparticles and Nanostructures. *Nanoscale* **2014**, *6* (12), 6229–6244.

(127) Qutub, N.; Pirzada, B. M.; Umar, K.; Sabir, S. Synthesis of CdS Nanoparticles Using Different Sulfide Ion Precursors: Formation Mechanism and Photocatalytic Degradation of Acid Blue-29. *J. Environ. Chem. Eng.* **2016**, *4* (1), 808–817.

(128) Halimi, I.; Rodrigues, E. M.; Maurizio, S. L.; Sun, H. Q. T.; Grewal, M.; Boase, E. M.; Liu, N.; Marin, R.; Hemmer, E. Pick Your Precursor! Tailoring the Size and Crystal Phase of Microwave-Synthesized Sub-10 Nm Upconverting Nanoparticles. *J. Mater. Chem. C* **2019**, *7* (48), 15364–15374.

(129) Thanh, N. T. K.; Maclean, N.; Mahiddine, S. Mechanisms of Nucleation and Growth of Nanoparticles in Solution. *Chem. Rev.* **2014**, *114* (15), 7610–7630.

(130) Abid, N.; Khan, A. M.; Shujait, S.; Chaudhary, K.; Ikram, M.; Imran, M.; Haider, J.; Khan, M.; Khan, Q.; Maqbool, M. Synthesis of Nanomaterials Using Various Top-down and Bottom-up Approaches, Influencing Factors, Advantages, and Disadvantages: A Review. *Adv. Colloid*

Interface Sci. **2022**, *300*, 102597.

(131) Persano, F.; Nobile, C.; Piccirillo, C.; Gigli, G.; Leporatti, S. Monodisperse and Nanometric-Sized Calcium Carbonate Particles Synthesis Optimization. *Nanomaterials* **2022**, *12* (9), 1–13.

(132) Kim, M. G.; Kang, J. M.; Lee, J. E.; Kim, K. S.; Kim, K. H.; Cho, M.; Lee, S. G. Effects of Calcination Temperature on the Phase Composition, Photocatalytic Degradation, and Virucidal Activities of TiO_2 Nanoparticles. *ACS Omega* **2021**, *6* (16), 10668–10678.

(133) Harrington, G. F.; Santiso, J. Back-to-Basics Tutorial: X-Ray Diffraction of Thin Films. *J. Electroceramics* **2021**, *47* (4), 141–163.

(134) Seibt, S.; Ryan, T. Microfluidics for Time-Resolved Small-Angle X-Ray Scattering. In *Advances in Microfluidics and Nanofluids*; INTECH: London, 2021.

(135) Brunauer, S.; Emmett, P. H.; Teller, E. Adsorption of Gases in Multimolecular Layers. *J. Am.Chem.Soc.* **1938**, *60* (2), 309–319.

(136) Harvey, D. *Modern Analytical Chemistry*, 1st ed.; McGraw-Hill Higher Education, 2000.

(137) Obeidat, Y. The Most Common Methods for Breath Acetone Concentration Detection: A Review. *IEEE Sens. J.* **2021**, *21* (13), 14540–14558.

(138) de Hoffmann, E.; Stroobant, V. *Mass Spectrometry: Principles and Applications*, 3rd ed.; John Wiley & Sons Ltd: Chichester, 2007.

(139) Gross, J. H. *Mass Spectrometry: A Textbook*, 3rd ed.; Springer International Publishing AG, 2017.

(140) *Food Analysis*; Nielsen, S. S., Ed.; Food Science Text Series; Springer International Publishing: Cham, 2017.

(141) Sparkman, O. D.; Penton, Z.; Kitson, F. *Gas Chromatography and Mass Spectrometry: A Practical Guide*, 2nd ed.; Elsevier Inc., 2011.

(142) Lahav, M.; Leiserowitz, L. The Effect of Solvent on Crystal Growth and Morphology. *Chem. Eng. Sci.* **2001**, *56* (7), 2245–2253.

(143) Bakshi, M. S. How Surfactants Control Crystal Growth of Nanomaterials. *Cryst. Growth Des.* **2016**, *16* (2), 1104–1133.

(144) Wang, A.; Wang, W.; Chen, J.; Mao, R.; Pang, Y.; Li, Y.; Chen, W.; Chen, D.; Hao, D.; Ni, B. J.; Saunders, M.; Jia, G. Dominant Polar Surfaces of Colloidal II-VI Wurtzite Semiconductor Nanocrystals Enabled by Cation Exchange. *J. Phys. Chem. Lett.* **2020**, *11* (13), 4990–4997.

(145) Qian, S.; Wang, C.; Liu, W.; Zhu, Y.; Yao, W.; Lu, X. An Enhanced CdS/TiO_2 Photocatalyst with High Stability and Activity: Effect of Mesoporous Substrate and Bifunctional Linking Molecule. *J. Mater. Chem.* **2011**, *21* (13), 4945–4952.

(146) Oskoui, M. S.; Khatamian, M.; Haghighi, M.; Yavari, A. Photocatalytic Hydrogen Evolution from Water over Chromosilicate-Based Catalysts. *RSC Adv.* **2014**, *4* (38), 19569–19577.

(147) Rengaraj, S.; Ferancova, A.; Jee, S. H.; Venkataraj, S.; Kim, Y.; Labuda, J.; Sillanpää, M. Physical and Electrochemical Characterization of CdS Hollow Microspheres Prepared by a Novel Template Free Solution Phase Method. *Electrochim. Acta* **2010**, *56* (1), 501–509.

(148) Rengaraj, S.; Jee, S. H.; Venkataraj, S.; Kim, Y.; Vijayalakshmi, S.; Repo, E.; Koistinen, A.; Sillanpää, M. CdS Microspheres Composed of Nanocrystals and Their Photocatalytic Activity. *J. Nanosci. Nanotechnol.* **2011**, *11* (3), 2090–2099.

(149) Mao, J.; Chen, X. M.; Du, X. W. Facile Synthesis of Three Dimensional CdS Nanoflowers with High Photocatalytic Performance. *J. Alloys Compd.* **2016**, *656*, 972–977.

(150) Khan, Z. R.; Zulfequar, M.; Khan, M. S. Chemical Synthesis of CdS Nanoparticles and Their Optical and Dielectric Studies. *J. Mater. Sci.* **2011**, *46* (16), 5412–5416.

(151) Suárez-López, R.; Puntes, V. F.; Bastús, N. G.; Hervés, C.; Jaime, C. Nucleation and Growth of

Gold Nanoparticles in the Presence of Different Surfactants. A Dissipative Particle Dynamics Study. *Sci. Rep.* **2022**, *12* (1), 1–12.

(152) Liu, C.; Wang, X.; Lee, S.; Pfefferle, L. D.; Haller, G. L. Surfactant Chain Length Effect on the Hexagonal-to-Cubic Phase Transition in Mesoporous Silica Synthesis. *Microporous Mesoporous Mater.* **2012**, *147* (1), 242–251.

(153) Olutas, E. B. Alkyl Chain Length and Headgroup Dependent Stability and Agglomeration Properties of Surfactant-Assisted Colloidal Selenium Nanoparticles. *Colloids Surfaces A Physicochem. Eng. Asp.* **2023**, *661* (January), 130935.

(154) Knözinger, E.; Diwald, O.; Sterrer, M. Chemical Vapour Deposition - A New Approach to Reactive Surface Defects of Uniform Geometry on High Surface Area Magnesium Oxide. *J. Mol. Catal. A Chem.* **2000**, *162* (1–2), 83–95.

(155) Zhang, Q. P.; Xu, X. N.; Liu, Y. T.; Xu, M.; Deng, S. H.; Chen, Y.; Yuan, H.; Yu, F.; Huang, Y.; Zhao, K.; Xu, S.; Xiong, G. A Feasible Strategy to Balance the Crystallinity and Specific Surface Area of Metal Oxide Nanocrystals. *Sci. Rep.* **2017**, *7*, 1–12.

(156) Niu, J.; Shao, R.; Liang, J.; Dou, M.; Li, Z.; Huang, Y.; Wang, F. Biomass-Derived Mesopore-Dominant Porous Carbons with Large Specific Surface Area and High Defect Density as High Performance Electrode Materials for Li-Ion Batteries and Supercapacitors. *Nano Energy* **2017**, *36*, 322–330.

(157) Iravani, S. Surfactant-Free Synthesis of Metal and Metal Oxide Nanomaterials: A Perspective. *RSC Sustain.* **2023**, *1* (1), 72–82.

(158) Lu, L.; Zou, S.; Fang, B. The Critical Impacts of Ligands on Heterogeneous Nanocatalysis: A Review. *ACS Catal.* **2021**, *11* (10), 6020–6058.

(159) Flores, N. M.; Pal, U.; Galeazzi, R.; Sandoval, A. Effects of Morphology, Surface Area, and Defect

Content on the Photocatalytic Dye Degradation Performance of ZnO Nanostructures. *RSC Adv.* **2014**, *4* (77), 41099–41110.

(160) Wu, X.; Xie, S.; Zhang, H.; Zhang, Q.; Sels, B. F.; Wang, Y. Metal Sulfide Photocatalysts for Lignocellulose Valorization. *Adv. Mater.* **2021**, *33* (50), 1–20.

(161) Prakash, J.; Kumar, P.; Saxena, N.; Pu, Z.; Chen, Z.; Tyagi, A.; Zhang, G.; Sun, S. CdS Based 3D Nano/Micro-Architectures: Formation Mechanism, Tailoring of Visible Light Activities and Emerging Applications in Photocatalytic H_2 Production, CO_2 Reduction and Organic Pollutant Degradation. *J. Mater. Chem. A* **2023**, *11* (19), 10015–10064.

(162) Cheng, L.; Xiang, Q.; Liao, Y.; Zhang, H. CdS-Based Photocatalysts. *Energy Environ. Sci.* **2018**, *11* (6), 1362–1391.

(163) Hao, X.; Hu, Y.; Cui, Z.; Zhou, J.; Wang, Y.; Zou, Z. Self-Constructed Facet Junctions on Hexagonal CdS Single Crystals with High Photoactivity and Photostability for Water Splitting. *Appl. Catal. B Environ.* **2019**, *244*, 694–703.

(164) Jiang, J.; Ye, K.; Zhang, W.; Ren, H.; Chen, H.; Hu, Y.; Wang, F.; Hou, J.; Diao, G.; Chen, M. High Index Lattice Plane of CdS to Enhance Photocatalytic Hydrogen Production. *J. Mater. Sci.* **2022**, *57* (47), 21667–21679.

(165) Cheng, L.; Li, Y.; Chen, A.; Zhu, Y.; Li, C. Impacts on Carbon Dioxide Electroreduction of Cadmium Sulfides: Via Continuous Surface Sulfur Vacancy Engineering. *Chem. Commun.* **2020**, *56* (4), 563–566.

(166) Wang, H. Y.; Hu, R.; Lei, Y. J.; Jia, Z. Y.; Hu, G. L.; Li, C. B.; Gu, Q. Highly Efficient and Selective Photocatalytic CO_2 Reduction Based on Water-Soluble CdS QDs Modified by the Mixed Ligands in One Pot. *Catal. Sci. Technol.* **2020**, *10* (9), 2821–2829.

(167) Feng, Y. X.; Wang, H. J.; Wang, J. W.; Zhang, W.; Zhang, M.; Lu, T. B. Stand-Alone CdS

Nanocrystals for Photocatalytic CO_2 Reduction with High Efficiency and Selectivity. *ACS Appl. Mater. Interfaces* **2021**, *13* (22), 26573–26580.

(168) Zajac, W.; Rozycka, A.; Trenczek-Zajac, A. Rational Design of the Electronic Structure of CdS Nanopowders. *Inorg. Chem.* **2023**, *62* (28), 10955–10964.

(169) Zheng, X.; Liu, Y.; Yang, Y.; Song, Y.; Deng, P.; Li, J.; Liu, W.; Shen, Y.; Tian, X. Recent Advances in Cadmium Sulfide-Based Photocatalysts for Photocatalytic Hydrogen Evolution. *Renewables* **2023**, *1* (1), 39–56.

(170) Nagakawa, H.; Tatsuma, T. Highly Crystalline Wurtzite CdS Prepared by a Flux Method and Application to Photocatalysis. *ACS Appl. Energy Mater.* **2022**, *5* (12), 14652–14657.

(171) Yang, Y.; Wang, X.; Xia, Y.; Dong, M.; Zhou, Z.; Zhang, G.; Li, L.; Hu, Q.; Zhu, X.; Yi, J. The Role of Facet Engineered Surface and Interface in CdS Nanostructures toward Solar Driven Hydrogen Evolution. *Appl. Surf. Sci.* **2023**, *615*, 156402.

(172) Ai, Z.; Zhao, G.; Zhong, Y.; Shao, Y.; Huang, B.; Wu, Y.; Hao, X. Phase Junction CdS: High Efficient and Stable Photocatalyst for Hydrogen Generation. *Appl. Catal. B Environ.* **2018**, *221*, 179–186.

(173) Liu, Y.; Zhang, P.; Tian, B.; Zhang, J. Core-Shell Structural CdS@SnO_2 Nanorods with Excellent Visible-Light Photocatalytic Activity for the Selective Oxidation of Benzyl Alcohol to Benzaldehyde. *ACS Appl. Mater. Interfaces* **2015**, *7* (25), 13849–13858.

(174) Ning, X.; Lu, G. Photocorrosion Inhibition of CdS-Based Catalysts for Photocatalytic Overall Water Splitting. *Nanoscale* **2020**, *12* (3), 1213–1223.

(175) Nasir, J. A.; Rehman, Z. U.; Shah, S. N. A.; Khan, A.; Butler, I. S.; Catlow, C. R. A. Recent Developments and Perspectives in CdS-Based Photocatalysts for Water Splitting. *J. Mater. Chem. A* **2020**, *8* (40), 20752–20780.

(176) Yue, Z.; Shao, S.; Yu, J.; Lu, G.; Wei, W.; Huang, Y.; Zhang, K.; Wang, K.; Fan, X. Improved Lignin Conversion to High-Value Aromatic Monomers through Phase Junction CdS with Coexposed Hexagonal (100) and Cubic (220) Facets. *ACS Appl. Mater. Interfaces* **2024**, *16* (23), 29991–30009.

(177) Song, W. L.; Dong, Q.; Hong, L.; Tian, Z. Q.; Tang, L. N.; Hao, W.; Zhang, H. Activating Molecular Oxygen with Au/CeO_2 for the Conversion of Lignin Model Compounds and Organosolv Lignin. *RSC Adv.* **2019**, *9* (53), 31070–31077.

(178) Tian, H. R.; Liu, Y. W.; Zhang, Z.; Liu, S. M.; Dang, T. Y.; Li, X. H.; Sun, X. W.; Lu, Y.; Liu, S. X. A Multicentre Synergistic Polyoxometalate-Based Metal-Organic Framework for One-Step Selective Oxidative Cleavage of β-O-4 Lignin Model Compounds. *Green Chem.* **2020**, *22* (1), 248–255.

(179) Hossain, M. A.; Saelee, T.; Tulaphol, S.; Rahaman, M. S.; Phung, T. K.; Maihom, T.; Praserthdam, P.; Praserthdam, S.; Yelle, D. J.; Sathitsuksanoh, N. Catalytic Hydrogenolysis of Lignin into Phenolics by Internal Hydrogen over Ru Catalyst. *ChemCatChem* **2022**, *14* (20), 1–9.

(180) Ghayeni, H. R.; Razeghi, R.; Olyaei, A. Synthesis and Characterization of Novel Poly(HAzPMA-Co-SA)/RDX/CdS Nanocomposite as a Polymer Bonded Explosive. *Can. J. Chem.* **2020**, *98* (12), 755–763.

(181) Ge, L.; Zuo, F.; Liu, J.; Ma, Q.; Wang, C.; Sun, D.; Bartels, L.; Feng, P. Synthesis and Efficient Visible Light Photocatalytic Hydrogen Evolution of Polymeric G-C_3N_4 Coupled with CdS Quantum Dots. *J. Phys. Chem. C* **2012**, *116* (25), 13708–13714.

(182) Shi, J. W.; Wang, Z.; He, C.; Wang, H.; Chen, J. W.; Fu, M. L.; Li, G.; Niu, C. CdS Quantum Dots Modified N-Doped Titania Plates for the Photocatalytic Mineralization of Diclofenac in Water under Visible Light Irradiation. *J. Mol. Catal. A Chem.* **2015**, *399*, 79–85.

(183) Yang, H.; Liu, Z.; Wang, K.; Pu, S.; Yang, S.; Yang, L. A Facile Synthesis of TiO_2–CdS Heterostructures With Enhanced Photocatalytic Activity. *Catal. Letters* **2017**, *147* (10), 2581–2591.

(184) Wu, X.; Zhao, J.; Wang, L.; Han, M.; Zhang, M.; Wang, H.; Huang, H.; Liu, Y.; Kang, Z. Carbon Dots as Solid-State Electron Mediator for $BiVO_4$/CDs/CdS Z-Scheme Photocatalyst Working under Visible Light. *Appl. Catal. B Environ.* **2017**, *206*, 501–509.

(185) Jiang, F.; Yan, T.; Chen, H.; Sun, A.; Xu, C.; Wang, X. A G-C_3N_4-CdS Composite Catalyst with High Visible-Light-Driven Catalytic Activity and Photostability for Methylene Blue Degradation. *Appl. Surf. Sci.* **2014**, *295*, 164–172.

(186) Elbaum, R.; Vega, S.; Hodes, G. Preparation and Surface Structure of Nanocrystalline Cadmium Sulfide (Sulfoselenide) Precipitated from Dimethyl Sulfoxide Solutions. *Chem. Mater.* **2001**, *13* (7), 2272–2280.

(187) Awatani, T.; McQuillan, A. J. Adsorbed Thiosulfate Intermediate of Cadmium Sulfide Aqueous Photocorrosion Detected and Characterized by in Situ Infrared Spectroscopy. *J. Phys. Chem. B* **1998**, *102* (21), 4110–4113.

(188) Rong, X.; Qiu, F.; Zhao, H.; Yan, J.; Zhu, X.; Yang, D. Fabrication of Single-Layer Graphitic Carbon Nitride and Coupled Systems for the Photocatalytic Degradation of Dyes under Visible-Light Irradiation. *Eur. J. Inorg. Chem.* **2015**, *2015* (8), 1359–1367.

(189) Chen, Y.; Zhai, B.; Liang, Y.; Li, Y.; Li, J. Preparation of CdS/g-C_3N_4/MOF Composite with Enhanced Visible-Light Photocatalytic Activity for Dye Degradation. *J. Solid State Chem.* **2019**, *274*, 32–39.

(190) Liji Sobhana, S. S.; Vimala Devi, M.; Sastry, T. P.; Mandal, A. B. CdS Quantum Dots for Measurement of the Size-Dependent Optical Properties of Thiol Capping. *J. Nanoparticle Res.* **2011**, *13* (4), 1747–1757.

(191) Zhou, J.; Song, D.; Mergelsberg, S. T.; Wang, Y.; Adhikari, N. M.; Lahiri, N.; Zhao, Y.; Chen, P.; Wang, Z.; Zhang, X.; Rosso, K. M. Facet-Dependent Dispersion and Aggregation of Aqueous Hematite Nanoparticles. *Sci. Adv.* **2024**, *10* (7), 60–62.

(192) Soltani, N.; Saion, E.; Hussein, M. Z.; Erfani, M.; Abedini, A.; Bahmanrokh, G.; Navasery, M.; Vaziri, P. Visible Light-Induced Degradation of Methylene Blue in the Presence of Photocatalytic ZnS and CdS Nanoparticles. *Int. J. Mol. Sci.* **2012**, *13* (10), 12242–12258.

(193) Kariofillis, S. K.; Jiang, S.; Żurański, A. M.; Gandhi, S. S.; Martinez Alvarado, J. I.; Doyle, A. G. Using Data Science To Guide Aryl Bromide Substrate Scope Analysis in a Ni/Photoredox-Catalyzed Cross-Coupling with Acetals as Alcohol-Derived Radical Sources. *J. Am. Chem. Soc.* **2022**, *144* (2), 1045–1055.

(194) Kossoy, E.; Diskin-Posner, Y.; Leitus, G.; Milstein, D. Selective Acceptorless Conversion of Primary Alcohols to Acetals and Dihydrogen Catalyzed by the Ruthenium(II) Complex $Ru(PPh_3)_2(NCCH_3)_2(SO_4)$. *Adv. Synth. Catal.* **2012**, *354* (2–3), 497–504.

(195) Sahoo, A. R.; Jiang, F.; Bruneau, C.; Sharma, G. V. M.; Suresh, S.; Achard, M. Acetals from Primary Alcohols with the Use of Tridentate Proton Responsive Phosphinepyridonate Iridium Catalysts. *RSC Adv.* **2016**, *6* (102), 100554–100558.

(196) Feng, T.; Zhang, S.; Li, C.; Li, T. One-Step Solvent-Free Aerobic Oxidation of Aliphatic Alcohols to Esters Using a Tandem Sc-Ru⊂MOF Catalyst. *Green Chem.* **2022**, *24* (4), 1474–1480.

(197) Fleming, B. I.; Bolker, H. I. The Reduction of Acetals with Cobalt Carbonyl Catalysts. *Can. J. Chem.* **1976**, *54* (5), 685–694.

(198) Sahoo, A. R.; Jiang, F.; Bruneau, C.; Sharma, G. V. M.; Suresh, S.; Roisnel, T.; Dorcet, V.; Achard, M. Phosphine-Pyridonate Ligands Containing Octahedral Ruthenium Complexes: Access to Esters and Formic Acid. *Catal. Sci. Technol.* **2017**, *7* (16), 3492–3498.

(199) Szymoniak, J.; Besançon, J.; Moïse, C. Tandem Carbonyl Coupling-Rearrangements Promoted by the Niobium(III) Reagent. Dual Reductive and Lewis Acid Properties of $NbCl_3$(DME). *Tetrahedron* **1992**, *48* (19), 3867–3876.

(200) Lee, H.-H.; Chen, S. Reactions of Diastereomeric 2,4,5-Triphenyl-1,3-Dioxolans with N-Bromosuccinimide and t-Butyl Perbenzoate. *J. Chem. Soc. Perkin Trans. 1* **1978**, *1* (3), 270–274.

(201) Chakraborti, A. K.; Chankeshwara, S. V. Counterattack Mode Differential Acetylative Deprotection of Phenylmethyl Ethers: Applications to Solid Phase Organic Reactions. *J. Org. Chem.* **2009**, *74* (3), 1367–1370.

(202) Rauniyar, V.; Hall, D. G. Catalytic Enantioselective and Catalyst-Controlled Diastereofacial-Selective Additions of Allyl- and Crotylboronates to Aldehydes Using Chiral Brønsted Acids. *Angew. Chemie - Int. Ed.* **2006**, *45* (15), 2426–2428.

(203) Superchi, S.; Contursi, M.; Rosini, C. Monobenzylether of (R,R)-1,2-Diphenylethane-1,2-Diol as Chiral Auxiliary in the Diastereoselective Reduction of α-Ketoesters. *Tetrahedron* **1998**, *54* (37), 11247–11254.

(204) Kündig, E. P.; Enriquez Garcia, A.; Lomberget, T.; Perez Garcia, P.; Romanens, P. Truncated Cinchona Alkaloids as Catalysts in Enantioselective Monobenzoylation of Meso-1,2-Diols. *Chem. Commun.* **2008**, No. 30, 3519–3521.

(205) Muramatsu, W.; William, J. M.; Onomura, O. Selective Monobenzoylation of 1,2- and 1,3-Diols Catalyzed by Me_2SnCl_2 in Water (Organic Solvent Free) under Mild Conditions. *J. Org. Chem.* **2012**, *77* (1), 754–759.

(206) Castells, J.; Pujol, F.; Llitjós, H.; Moreno-Mañas, M. Oxidative Benzoin Reactions. *Tetrahedron* **1982**, *38* (3), 337–346.

(207) Cutulic, S. P. Y.; Findlay, N. J.; Zhou, S. Z.; Chrystal, E. J. T.; Murphy, J. A. Metal-Free Reductive

Cleavage of C-O σ-Bonds in Acyloin Derivatives by an Organic Neutral Super-Electron-Donor. *J. Org. Chem.* **2009**, *74* (22), 8713–8718.

(208) Zheng, Z.-R.; Kjær, N. T.; Lund, H.; Plé, G.; Mesaros, E.; Mihis, A.; Søtofte, I.; Långström, B. Base-Induced Rearrangement of O-Benzoylbenzaldehyde Cyanohydrin to Benzil and the Further Reactions of Benzil. *Acta Chem. Scand.* **1998**, *52* (3), 362–365.

(209) Ortega, N.; Beiring, B.; Urban, S.; Glorius, F. Highly Asymmetric Synthesis of (+)-Corsifuran A. Elucidation of the Electronic Requirements in the Ruthenium-NHC Catalyzed Hydrogenation of Benzofurans. *Tetrahedron* **2012**, *68* (26), 5185–5192.

(210) Ortega, N.; Urban, S.; Beiring, B.; Glorius, F. Ruthenium NHC Catalyzed Highly Asymmetric Hydrogenation of Benzofurans. *Angew. Chemie - Int. Ed.* **2012**, *51* (7), 1710–1713.

(211) Moure, M. J.; Sanmartin, R.; Dominguez, E. Benzofurans from Benzophenones and Dimethylacetamide: Copper-Promoted Cascade Formation of Furan O1-C2 and C2-C3 Bonds under Oxidative Conditions. *Angew. Chemie - Int. Ed.* **2012**, *51* (13), 3220–3224.

(212) Zhu, X. R.; Deng, C. L. Nickel-Catalyzed Intramolecular Nucleophilic Addition of Aryl Halides to Aryl Ketones for the Synthesis of Benzofuran Derivatives. *Synth.* **2021**, *53* (10), 1842–1848.

(213) Vebrel, J.; Roche, M.; Gore, J. Comportement de Quelques Arylbenzo[b]-furannes Sous l'Impact Électronique. *Org. Mass Spectrom.* **1977**, *12* (12), 751–755.

(214) Ma, Z.; Zhou, M.; Ma, L.; Zhang, M. Synthesis of Benzofurans from the Cyclodehydration of α-Phenoxy Ketones Mediated by Eaton's Reagent. *J. Chem. Res.* **2020**, *44* (7–8), 426–436.

(215) Davies, W.; Middleton, S. Cyclodehydration Processes. Part I. Benzofuran Derivatives Formed by Cyclisation of ω-Aryloxyacetophenones. *J. Chem. Soc.* **1958**, 822–825.

(216) Davies, W.; Middleton, S. Cyclodehydration Processes. Part II. Migration of a Phenyl Group during Cyclisation of ω-Phenoxyacetophenone. *J. Chem. Soc.* **1959**, 3544–3547.

(217) Tomioka, H.; Nakanishi, K.; Izawa, Y. Generation and Reactions of 2-Alkoxydiphenylcarbenes in Fluid Solution and Rigid Matrices. *J. Chem. Soc. Perkin Trans. 1* **1991**, *45* (2), 465.

(218) Parkanyi, C.; Lablache-Combier, A.; Marko, I.; Ofenberg, H. Photoreduction of Substituted Benzo[b]Furans by Aliphatic Amines. *J. Org. Chem.* **1976**, *41* (1), 151–153.

(219) Findlay, N. J.; Park, S. R.; Schoenebeck, F.; Cahard, E.; Zhou, S. Z.; Berlouis, L. E. A.; Spicer, M. D.; Tuttle, T.; Murphy, J. A. Reductions of Challenging Organic Substrates by a Nickel Complex of a Noninnocent Crown Carbene Ligand. *J. Am. Chem. Soc.* **2010**, *132* (44), 15462–15464.

(220) Strunz, G. M.; Kazinoti, P. I. Butenolides from Citraconic Anhydride and Acetophenone: Rearrangement to a 2,3-Dihydro-3-Furanone Related to Bullatenone. *Can. J. Chem.* **1976**, *54* (3), 415–417.

(221) So, J. H.; Boudjouk, P.; Park, M. K. Reductive Coupling of Carbonyl Compounds with Zinc and Trimethylchlorosilane to Produce O-Silylated Pinacols. Effect of Ultrasonic Waves. *J. Org. Chem.* **1988**, *53* (25), 5871–5875.

(222) Xie, Y. X.; Song, R. J.; Liu, Y.; Liu, Y. Y.; Xiang, J. N.; Li, J. H. Copper-Catalyzed α-Aminoxylation of Ketones with 2,2,6,6- Tetramethylpiperidine-1-Oxyl (TEMPO). *Adv. Synth. Catal.* **2013**, *355* (17), 3387–3390.

(223) Zhang, M.; Li, Z.; Feng, Y.; Xin, X.; Yang, G. Y.; Lv, H. Highly Selective Hydrogenolysis of Lignin β-O-4 Models by a Coupled Polyoxometalate/CdS Photocatalytic System. *Green Chem.* **2023**, *25* (23), 10091–10100.

(224) Xu, Q.; Xie, H.; Chen, P.; Yu, L.; Chen, J.; Hu, X. Organohalide-Catalyzed Dehydrative O-Alkylation between Alcohols: A Facile Etherification Method for Aliphatic Ether Synthesis. *Green Chem.* **2015**, *17* (5), 2774–2779.

(225) Noji, M.; Ohno, T.; Fuji, K.; Futaba, N.; Tajima, H.; Ishii, K. Secondary Benzylation Using Benzyl

Alcohols Catalyzed by Lanthanoid, Scandium, and Hafnium Triflate. *J. Org. Chem.* **2003**, *68* (24), 9340–9347.

(226) Delgado-Abad, T.; Martínez-Ferrer, J.; Acerete, R.; Asensio, G.; Mello, R.; González-Núñez, M. E. SN1 Reactions in Supercritical Carbon Dioxide in the Presence of Alcohols: The Role of Preferential Solvation. *Org. Biomol. Chem.* **2016**, *14* (27), 6554–6560.

(227) Black, P. J.; Edwards, M. G.; Williams, J. M. J. Borrowing Hydrogen: Indirect "Wittig" Olefination for the Formation of C–C Bonds from Alcohols. *European J. Org. Chem.* **2006**, *2006* (19), 4367–4378.

(228) Felstead, R.; Gibson, S. E.; Rooney, A.; Tse, E. S. Y. A Stereocontrolled Approach to Ethers with Two α Stereocentres. *European J. Org. Chem.* **2008**, No. 29, 4963–4971.

(229) Jereb, M.; Vražič, D.; Zupan, M. Dual Behavior of Alcohols in Iodine-Catalyzed Esterification under Solvent-Free Reaction Conditions. *Tetrahedron Lett.* **2009**, *50* (20), 2347–2352.

(230) Chu, J. H.; Chen, S. T.; Chiang, M. F.; Wu, M. J. Palladium-Catalyzed Direct Ortho Aroylation of 2-Phenoxypyridines with Aldehydes and Catalytic Mechanism Investigation. *Organometallics* **2015**, *34* (5), 953–966.

(231) Enthaler, S. Zinc-Catalyzed Depolymerization of End-of-Life Polysiloxanes. *Angew. Chemie - Int. Ed.* **2014**, *53* (10), 2716–2721.

(232) Mohite, A. R.; Phatake, R. S.; Dubey, P.; Agbaria, M.; Shames, A. I.; Lemcoff, N. G.; Reany, O. Thiourea-Mediated Halogenation of Alcohols. *J. Org. Chem.* **2020**, *85* (20), 12901–12911.

(233) Huy, P. H.; Motsch, S.; Kappler, S. M. Formamides as Lewis Base Catalysts in SNReactions—Efficient Transformation of Alcohols into Chlorides, Amines, and Ethers. *Angew. Chemie - Int. Ed.* **2016**, *55* (34), 10145–10149.

(234) Siavashi, N. Y.; Akhlaghinia, B.; Zarghani, M. Sulfonated Nanohydroxyapatite Functionalized with

2-Aminoethyl Dihydrogen Phosphate (HAP@AEPH$_2$-SO$_3$H) as a Reusable Solid Acid for Direct Esterification of Carboxylic Acids with Alcohols. *Res. Chem. Intermed.* **2016**, *42* (6), 5789–5806.

(235) Ohshima, T.; Iwasaki, T.; Maegawa, Y.; Yoshiyama, A.; Mashima, K. Enzyme-like Chemoselective Acylation of Alcohols in the Presence of Amines Catalyzed by a Tetranuclear Zinc Cluster. *J. Am. Chem. Soc.* **2008**, *130* (10), 2944–2945.

(236) Bellezza, F.; Cipiciani, A.; Cruciani, G.; Fringuelli, F. The Importance of Ester and Alkoxy Type Functionalities for the Chemo- and Enantio-Recognition of Substrates by Hydrolysis with Candida Rugosa Lipase. *J. Chem. Soc. Perkin Trans. 1* **2000**, *1* (24), 4439–4444.

(237) Weng, S. S.; Ke, C. S.; Chen, F. K.; Lyu, Y. F.; Lin, G. Y. Transesterification Catalyzed by Iron(III) β-Diketonate Species. *Tetrahedron* **2011**, *67* (9), 1640–1648.

(238) Madabhushi, S.; Mallu, K. K. R.; Chinthala, N.; Beeram, C. R.; Vangipuram, V. S. Efficient and Chemoselective Acetalization and Thioacetalization of Carbonyls and Subsequent Deprotection Using InF$_3$ as a Reusable Catalyst. *Tetrahedron Lett.* **2012**, *53* (6), 697–701.

(239) Tank, R.; Pathak, U.; Vimal, M.; Bhattacharyya, S.; Pandey, L. K. Hydrogen Peroxide Mediated Efficient Amidation and Esterification of Aldehydes: Scope and Selectivity. *Green Chem.* **2011**, *13* (12), 3350–3354.

(240) Zhang, Z.; Sadakane, M.; Murayama, T.; Izumi, S.; Yasuda, N.; Sakaguchi, N.; Ueda, W. Tetrahedral Connection of ε-Keggin-Type Polyoxometalates to Form an All-Inorganic Octahedral Molecular Sieve with an Intrinsic 3D Pore System. *Inorg. Chem.* **2014**, *53* (2), 903–911.

(241) Barbosa, S. L.; Ottone, M.; Santos, M. C.; Junior, G. C.; Lima, C. D.; Glososki, G. C.; Lopes, N. P.; Klein, S. I. Benzyl Benzoate and Dibenzyl Ether from of Benzoic Acid and Benzyl Alcohol under Microwave Irradiation Using a SiO$_2$-SO$_3$H Catalyst. *Catal. Commun.* **2015**, *68*, 97–100.

(242) Nowicka, E.; Hofmann, J. P.; Parker, S. F.; Sankar, M.; Lari, G. M.; Kondrat, S. A.; Knight, D. W.;

Bethell, D.; Weckhuysen, B. M.; Hutchings, G. J. In Situ Spectroscopic Investigation of Oxidative Dehydrogenation and Disproportionation of Benzyl Alcohol. *Phys. Chem. Chem. Phys.* **2013**, *15* (29), 12147–12155.

(243) Dimitratos, N.; Lopez-Sanchez, J. A.; Morgan, D.; Carley, A. F.; Tiruvalam, R.; Kiely, C. J.; Bethell, D.; Hutchings, G. J. Solvent-Free Oxidation of Benzyl Alcohol Using Au-Pd Catalysts Prepared by Sol Immobilisation. *Phys. Chem. Chem. Phys.* **2009**, *11* (25), 5142–5153.

(244) Chen, Y.; Zheng, H.; Guo, Z.; Zhou, C.; Wang, C.; Borgna, A.; Yang, Y. Pd Catalysts Supported on MnCeOx Mixed Oxides and Their Catalytic Application in Solvent-Free Aerobic Oxidation of Benzyl Alcohol: Support Composition and Structure Sensitivity. *J. Catal.* **2011**, *283* (1), 34–44.

(245) Li, G.; Enache, D. I.; Edwards, J.; Carley, A. F.; Knight, D. W.; Hutchings, G. J. Solvent-Free Oxidation of Benzyl Alcohol with Oxygen Using Zeolite-Supported Au and Au-Pd Catalysts. *Catal. Letters* **2006**, *110* (1–2), 7–13.

(246) Firouzabadi, H.; Iranpoor, N.; Jafarpour, M. $ZrCl_4$ Dispersed on Dry Silica Gel Provides a Useful Reagent for S-Alkylation of Thiols with Alcohols under Solvent-Free Conditions. *Tetrahedron Lett.* **2006**, *47* (1), 93–97.

(247) Sorribes, I.; Corma, A. Nanolayered Cobalt-Molybdenum Sulphides (Co-Mo-S) Catalyse Borrowing Hydrogen C-S Bond Formation Reactions of Thiols or H_2S with Alcohols. *Chem. Sci.* **2019**, *10* (10), 3130–3142.

(248) Corma, A.; Navas, J.; Rõdenas, T.; Sabater, M. J. One-Pot Palladium-Catalyzed Borrowing Hydrogen Synthesis of Thioethers. *Chem. - A Eur. J.* **2013**, *19* (51), 17464–17471.

(249) An, S. J.; Kang, M. J.; Lee, H.; Kim, H. S. Tunable Selectivity of Photocatalytic Benzyl Alcohol Transformation over Ag-Ion-Exchanged CdS Nanowires. *ACS Sustain. Chem. Eng.* **2023**, *11* (11), 4364–4373.

(250) Hansen, S. H.; Sydnes, L. K.; Wiggen, U.; Öhman, L.-O.; Ruiz, J.; Colacio, E.; Mulichak, A. M.; Alminger, T.; Erickson, M.; Grundevik, I.; Hagin, I.; Hoffman, K.-J.; Johansson, S.; Larsson, S.; Löfberg, I.; Ohlson, K.; Persson, B.; Skånberg, I.; Tekenbergs-Hjelte, L. Photochemical Oxidation of Benzyl Alcohol. *Acta Chem. Scand.* **1989**, *43*, 395–398.

(251) Savara, A.; Chan-Thaw, C. E.; Rossetti, I.; Villa, A.; Prati, L. Benzyl Alcohol Oxidation on Carbon-Supported Pd Nanoparticles: Elucidating the Reaction Mechanism. *ChemCatChem* **2014**, *6* (12), 3464–3473.

(252) Quattlebaum, W. M.; Toussaint, W. J.; Dunn, J. T. Deoxygenation of Certain Aldehydes and Ketones: Preparation of Butadiene and Styrene. *J. Am. Chem. Soc.* **1947**, *69* (3), 593–599.

(253) Kijeński, J.; Gliński, M.; Czarnecki, J. Reduction of Alkyl Alkyl, Aryl Alkyl and Cyclic Ketones by Catalytic Hydrogen Transfer over Magnesium Oxide. *J. Chem. Soc. Perkin Trans. 2* **1991**, *2* (11), 1695–1698.

(254) Nose, A.; Kudo, T. Studies of Reduction of Various Organic Compounds with the Nickel(II) Chloride-Zinc System. *Chem. Pharm. Bull.* **1990**, *38* (8), 2097–2101.

(255) Ono, A.; Maruyama, T.; Suzuki, N. Hydrogenation of Diaryl and Arylalkyl Ketones by Sodium Borohydride and Aluminum Chloride. *Synth. Commun.* **1987**, *17* (8), 1001–1005.

(256) Sivcev, V. P.; Volcho, K. P.; Salakhutdinov, N. F.; Anikeev, V. I. Transformations of Acetophenone and Its Derivatives in Supercritical Fluid Isopropanol/CO_2 in a Continuous Flow Reactor in the Presence of Alumina. *J. Supercrit. Fluids* **2012**, *70*, 35–39.

(257) Brienza, F.; Van Aelst, K.; Thielemans, K.; Sels, B. F.; Debecker, D. P.; Cybulska, I. Enhancing Lignin Depolymerizationviaa Dithionite-Assisted Organosolv Fractionation of Birch Sawdust. *Green Chem.* **2021**, *23* (9), 3268–3276.

(258) Guo, H.; Zhang, B.; Li, C.; Peng, C.; Dai, T.; Xie, H.; Wang, A.; Zhang, T. Tungsten Carbide: A

Remarkably Efficient Catalyst for the Selective Cleavage of Lignin C−O Bonds. *ChemSusChem* **2016**, *9* (22), 3220–3229.

(259) Wu, X.; Jiao, W.; Li, B. Z.; Li, Y.; Zhang, Y.; Wang, Q.; Tang, Y. Decomposition of a β-O-4 Lignin Model Compound over Solid Cs-Substituted Polyoxometalates in Anhydrous Ethanol: Acidity or Redox Property Dependence? *Cuihua Xuebao/Chinese J. Catal.* **2017**, *38* (7), 1216–1228.

(260) Marvi, O.; Fekri, L. Z.; Takhti, M. Montmorillonite K10 and KSF Clays as Acidic and Green Catalysts for Effective Esterification of Phenols and Alcohols under MWI. *Russ. J. Gen. Chem.* **2014**, *84* (9), 1837–1840.

(261) Son, S.; Toste, F. D. Non-Oxidative Vanadium-Catalyzed Co Bond Cleavage: Application to Degradation of Lignin Model Compounds. *Angew. Chemie - Int. Ed.* **2010**, *49* (22), 3791–3794.

(262) Zhou, X.; Mitra, J.; Rauchfuss, T. B. Lignol Cleavage by Pd/C under Mild Conditions and without Hydrogen: A Role for Benzylic C=H Activation? *ChemSusChem* **2014**, *7* (6), 1623–1626.

(263) Harms, R. G.; Markovits, I. I. E.; Drees, M.; Herrmann, H. C. M. W. A.; Cokoja, M.; Kühn, F. E. Cleavage of C-O Bonds in Lignin Model Compounds Catalyzed by Methyldioxorhenium in Homogeneous Phase. *ChemSusChem* **2014**, *7* (2), 429–434.

(264) Guo, F.; Wang, L.; Sun, H.; Li, M.; Shi, W. High-Efficiency Photocatalytic Water Splitting by a N-Doped Porous g-C_3N_4 Nanosheet Polymer Photocatalyst Derived from Urea and: N,N-Dimethylformamide. *Inorg. Chem. Front.* **2020**, *7* (8), 1770–1779.

(265) Galkin, M. V.; Dahlstrand, C.; Samec, J. S. M. Mild and Robust Redox-Neutral Pd/C-Catalyzed Lignol β-O-4′ Bond Cleavage Through a Low-Energy-Barrier Pathway. *ChemSusChem* **2015**, *8* (13), 2187–2192.

(266) Kerr, J. A. Bond Dissociation Energies by Kinetic Methods. *Chem. Rev.* **1966**, *66* (5), 465–500.

(267) Benson, S. W. Papers — III Bond Energies. *J. Chem. Educ.* **1965**, *42* (9), 502–518.

(268) Choi, Y. S.; Singh, R.; Zhang, J.; Balasubramanian, G.; Sturgeon, M. R.; Katahira, R.; Chupka, G.; Beckham, G. T.; Shanks, B. H. Pyrolysis Reaction Networks for Lignin Model Compounds: Unraveling Thermal Deconstruction of β-O-4 and α-O-4 Compounds. *Green Chem.* **2016**, *18* (6), 1762–1773.

(269) Ota, E.; Wang, H.; Frye, N. L.; Knowles, R. R. A Redox Strategy for Light-Driven, Out-of-Equilibrium Isomerizations and Application to Catalytic C-C Bond Cleavage Reactions. *J. Am. Chem. Soc.* **2019**, *141* (4), 1457–1462.

(270) Liu, W.; Wu, Q.; Wang, M.; Huang, Y.; Hu, P. Iron-Catalyzed C-C Single-Bond Cleavage of Alcohols. *Org. Lett.* **2021**, *23* (21), 8413–8418.

(271) Gao, Y.; Zhang, J.; Chen, X.; Ma, D.; Yan, N. A Metal-Free, Carbon-Based Catalytic System for the Oxidation of Lignin Model Compounds and Lignin. *Chempluschem* **2014**, *79* (6), 825–834.

(272) Rao, C. H.; Wei, H. R.; Miao, X. L.; Jia, M. Z.; Yao, X. R.; Zheng, X. Y.; Zhang, J. Selective Cleavage of Cα-Cβ Bonds in Lignin Models Using a Bifunctional Pyridinium Photocatalyst via a PCET Process. *Green Chem.* **2023**, *25* (10), 3974–3981.

(273) Meshram, H. M.; Chandra Sekhar, K.; Ganesh, Y. S. S.; Yadav, J. S. Clay Catalyzed Facile Cyclodehydration Under Microwave: Synthesis of 3-Substituted Benzofurans. *Synlett* **2000**, *2000* (09), 1273–1274.

(274) Kim, I.; Lee, S. H.; Lee, S. BCl_3-Promoted Synthesis of Benzofurans. *Tetrahedron Lett.* **2008**, *49* (46), 6579–6584.

(275) Habermann, J.; Ley, S. V.; Smits, R. Three-Step Synthesis of an Array of Substituted Benzofurans Using Polymer-Supported Reagents. *J. Chem. Soc. - Perkin Trans. 1* **1999**, *1* (17), 2421–2423.

(276) Shi, L.; Fan, C. A.; Tu, Y. Q.; Wang, M.; Zhang, F. M. Novel and Efficient Ni-Mediated Pinacol Coupling of Carbonyl Compounds. *Tetrahedron* **2004**, *60* (12), 2851–2855.

(277) Naumann, R.; Goez, M. How the Sustainable Solvent Water Unleashes the Photoredox Catalytic Potential of Ruthenium Polypyridyl Complexes for Pinacol Couplings. *Green Chem.* **2019**, *21* (16), 4470–4474.

(278) Banik, B. K.; Banik, I.; Aounallah, N.; Castillo, M. Samarium-Induced Convenient Reductive Dimerization of Aromatic Ketones in Aqueous Methanol: A Mechanistic Approach. *Tetrahedron Lett.* **2005**, *46* (41), 7065–7068.

(279) Mukaiyama, T.; Kagayama, A.; Shiina, I. Efficient Method for Pinacol Coupling of Aromatic and Aliphatic Ketones by Using Titanium(II) Chloride and Zinc in the Presence of Pivalonitrile. *Chemistry Letters*. 1998, pp 1107–1108.

(280) Netto-Ferreira, J. C.; Avellar, I. G. J.; Scaiano, J. C. Effect of Ring Substitution on the Photochemistry of α-(Aryloxy)Acetophenones. *J. Org. Chem.* **1990**, *55* (1), 89–92.

(281) Huang, Y.; Pagé, D.; Wayner, D. D. M.; Mulder, P. Radical-Induced Degradation of a Lignin Model Compound. Decomposition of 1-Phenyl-2-Phenoxyethanol. *Can. J. Chem.* **1995**, *73* (11), 2079–2085.

(282) Liu, Q.; Wang, R. G.; Song, H. J.; Liu, Y. X.; Wang, Q. M. Synthesis of 1,4-Dicarbonyl Compounds by Visible-Light-Mediated Cross-Coupling Reactions of α-Chlorocarbonyls and Enol Acetates. *Adv. Synth. Catal.* **2020**, *362* (20), 4391–4396.

(283) Cui, T.; Ma, L.; Wang, S.; Ye, C.; Liang, X.; Zhang, Z.; Meng, G.; Zheng, L.; Hu, H. S.; Zhang, J.; Duan, H.; Wang, D.; Li, Y. Atomically Dispersed Pt-N_3C_1 Sites Enabling Efficient and Selective Electrocatalytic C-C Bond Cleavage in Lignin Models under Ambient Conditions. *J. Am. Chem. Soc.* **2021**, *143* (25), 9429–9439.

(284) Chen, H.; Hong, D.; Wan, K.; Wang, J.; Niu, B.; Zhang, Y.; Long, D. Urchin-like Nb_2O_5 Hollow Microspheres Enabling Efficient and Selective Photocatalytic C–C Bond Cleavage in Lignin Models

under Ambient Conditions. *Chinese Chem. Lett.* **2022**, *33* (9), 4357–4362.

(285) Andersson, O.; Kemerink, M. Enhancing Open-Circuit Voltage in Gradient Organic Solar Cells by Rectifying Thermalization Losses. *Sol. RRL* **2020**, *4* (12), 2000400.

(286) Yadav, D.; Pauly, F.; Trushin, M. Charge-Carrier Thermalization in Bulk and Monolayer CdTe from First Principles. *Phys. Rev. B* **2021**, *103* (12), 125113.

(287) Tamulaitis, G. Origin of Carrier Heating in Semiconductor Nanocrystals: Excess Energy of Photoexcited Electrons or Auger Processes? *J. Phys. Condens. Matter* **1998**, *10* (45), 10307–10316.

(288) Chen, Y.; Shu, T.; Lai, T.; Wu, H. Excitation-Density and Excess-Energy Dependence of Ultrafast Dynamics of Photoexcited Carriers in Intrinsic Bulk CdTe. *Results Phys.* **2021**, *31*, 105047.

(289) Shin, T.; Cho, K. S.; Yun, D. J.; Kim, J.; Li, X. S.; Moon, E. S.; Baik, C. W.; Kim, S. Il; Kim, M.; Choi, J. H.; Park, G. S.; Shin, J. K.; Hwang, S.; Jung, T. S. Exciton Recombination, Energy-, and Charge Transfer in Single- and Multilayer Quantum-Dot Films on Silver Plasmonic Resonators. *Sci. Rep.* **2016**, *6*, 1–11.

Appendix A. Mass spectra and calibration curves of known products

The experimental mass spectra of toluene and styrene (Figure A.1) were collected for the purpose of headspace GC-MS qualitative analysis.

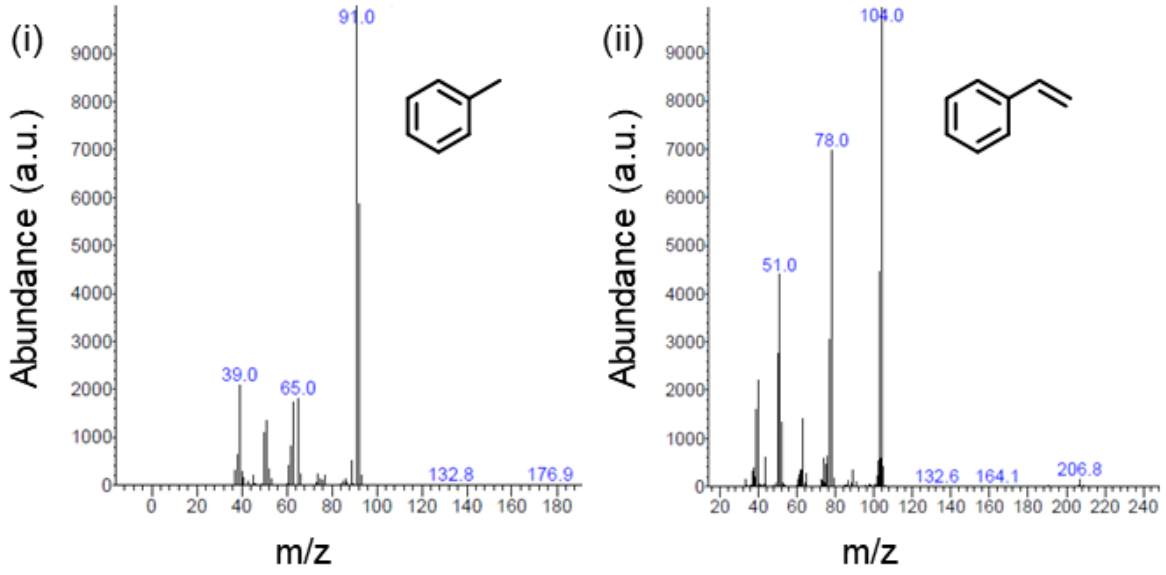

Figure A.1. Experimental reference mass spectrum of (i) toluene and (ii) styrene.

During the generation of GC-MS calibration curves, the chromatograms were collected. A representative chromatogram is generated for all known compounds (Figure A.2).

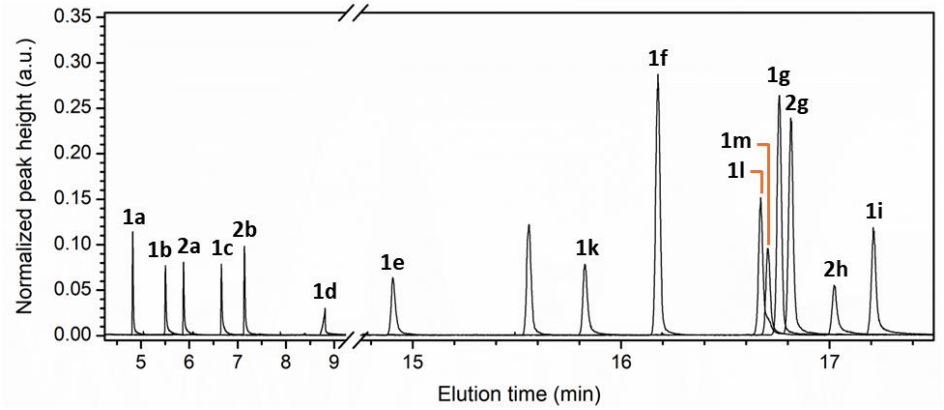

Figure A.2. Reference chromatogram of known compounds.

The stilbene peak at 15.56 minutes in the chromatogram was identified but not labelled as this compound was not present during any of the experiments outlined in Chapters 3 and 4. The pentachlorobenzene peak, representing the internal standard, at 13.41 minutes was omitted for clarity. The elution times of each known compound was recorded and summarized in Table A.1.

Table A.1. Reference elution times and structures of known compounds.

Elution time (min)	Compound	Label	Elution time (min)	Compound	Label
4.83		**1a**	15.83	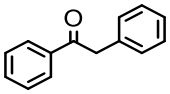	**1k**
5.50	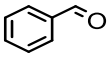	**1b**	16.18	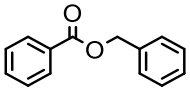	**1f**
5.88	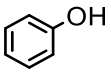	**2a**	16.67	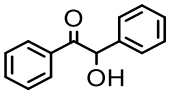	**1l**
6.67	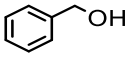	**1c**	16.71	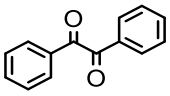	**1m**
7.14		**2b**	16.77	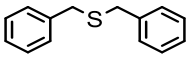	**1g**
8.78	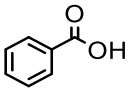	**1d**	16.81	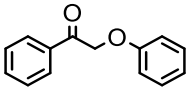	**2g**
14.90	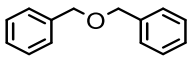	**1e**	17.02	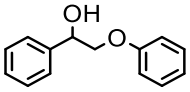	**2h**
15.56	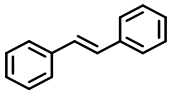	**N/A**	17.21	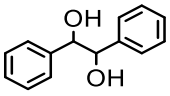	**1i**

The reference mass spectra of each known compound were also collected based on their associated GC chromatogram peaks. Furthermore, calibration curves for the known compounds were generated to enable quantification of GC chromatogram peaks. The reference mass spectra and calibration curves of the known compounds are illustrated in Figures A.3 to A.13.

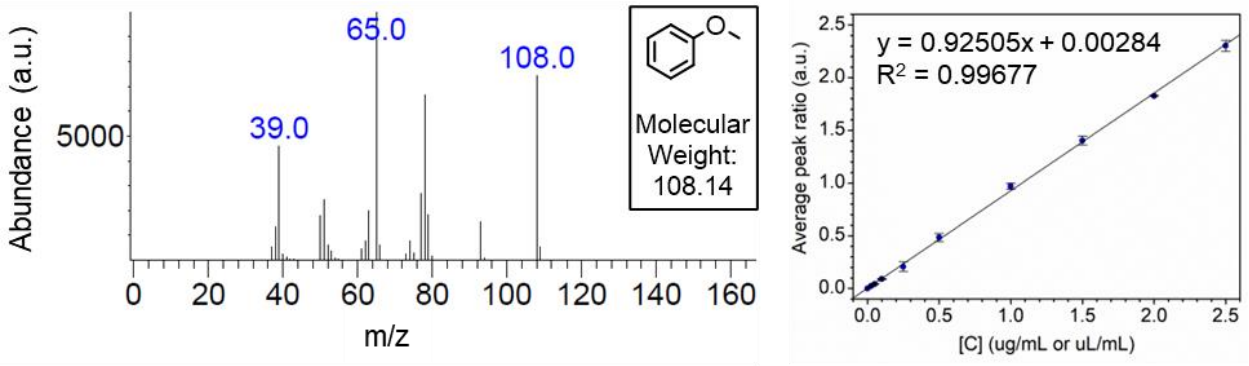

*Figure A.3. Experimental reference mass spectrum (left) and GC calibration curve (right) of anisole (**1a**).*

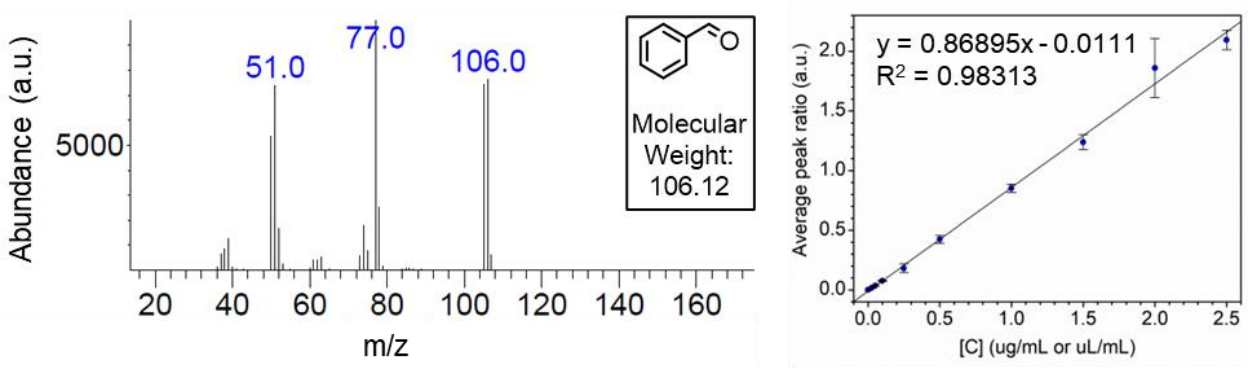

*Figure A.4. Experimental reference mass spectrum (left) and calibration curve (right) of benzaldehyde (**1b**).*

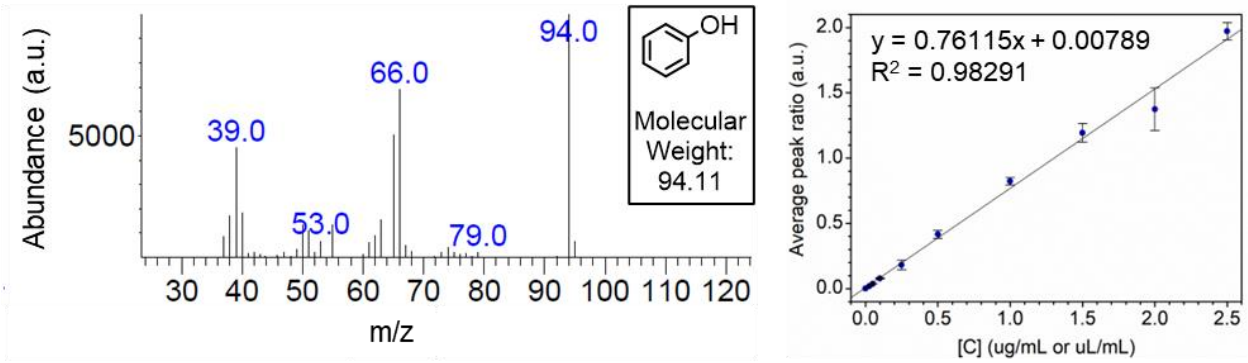

*Figure A.5. Experimental reference mass spectrum (left) and calibration curve (right) of phenol (**2a**).*

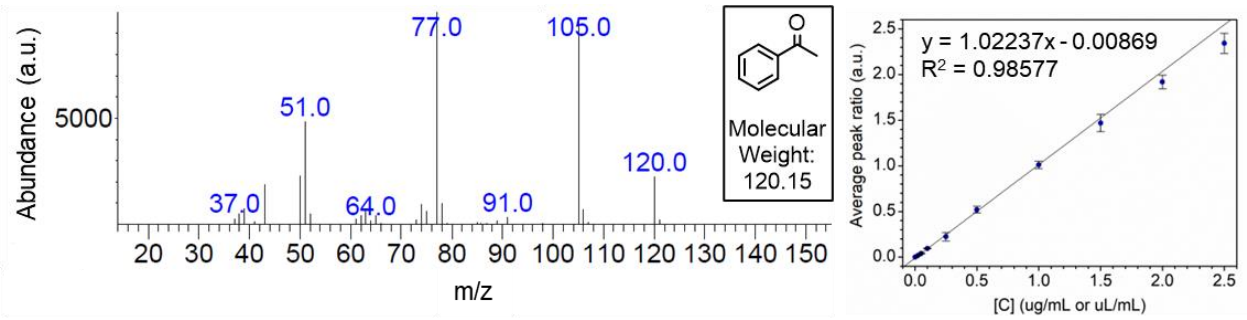

*Figure A.6. Experimental reference mass spectrum (left) and calibration curve (right) of acetophenone (**2b**).*

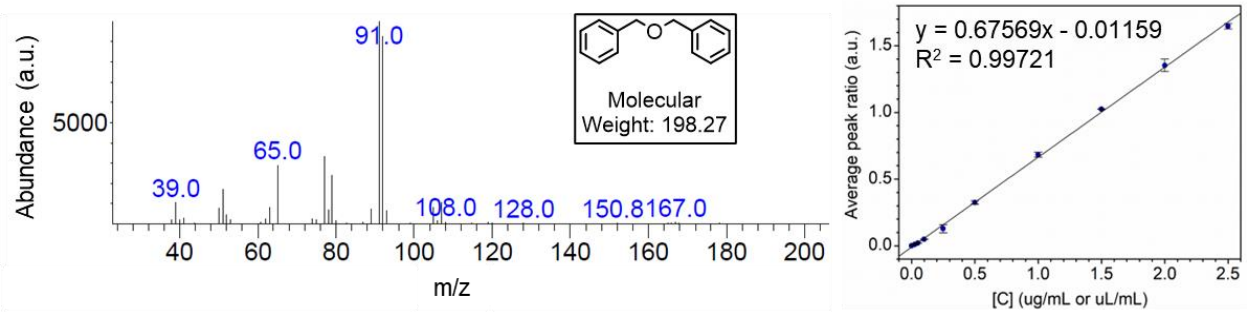

*Figure A.7. Experimental reference mass spectrum (left) and calibration curve (right) of dibenzyl ether (**1e**).*

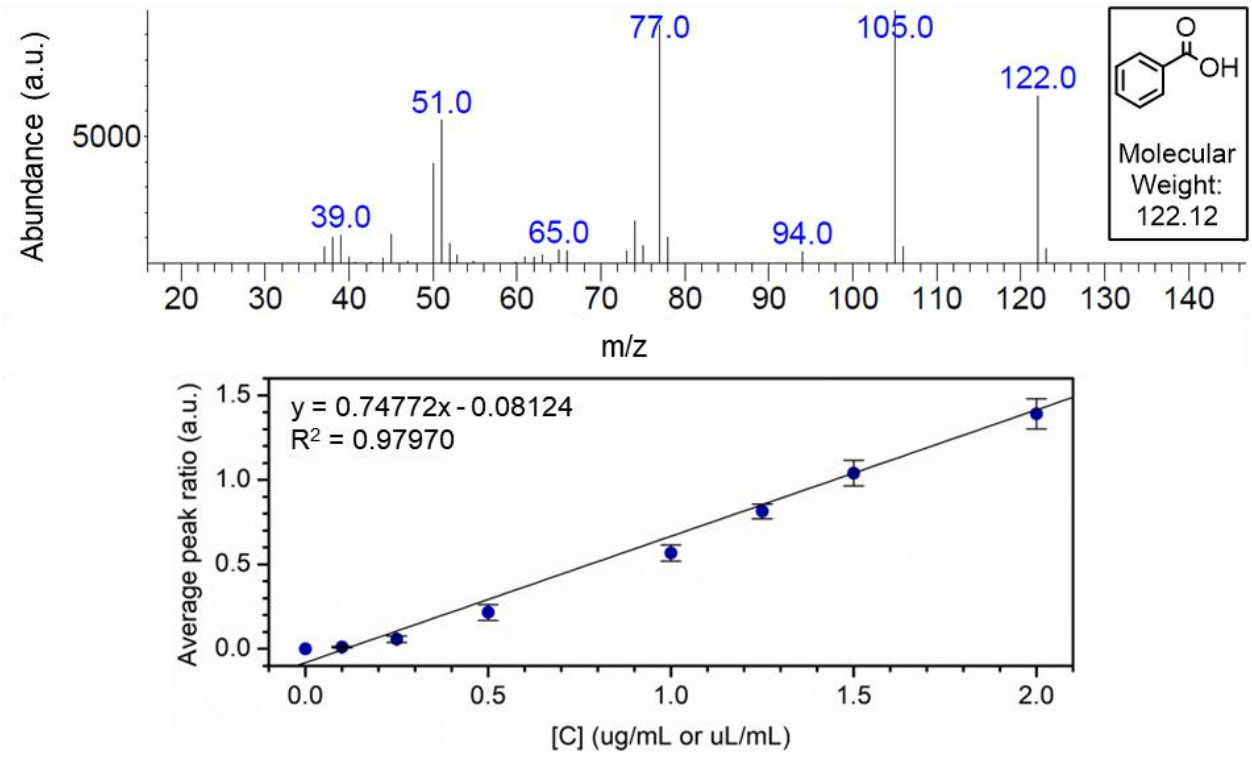

*Figure A.8. Experimental reference mass spectrum (top) and calibration curve (bottom) of benzoic acid (**1d**).*

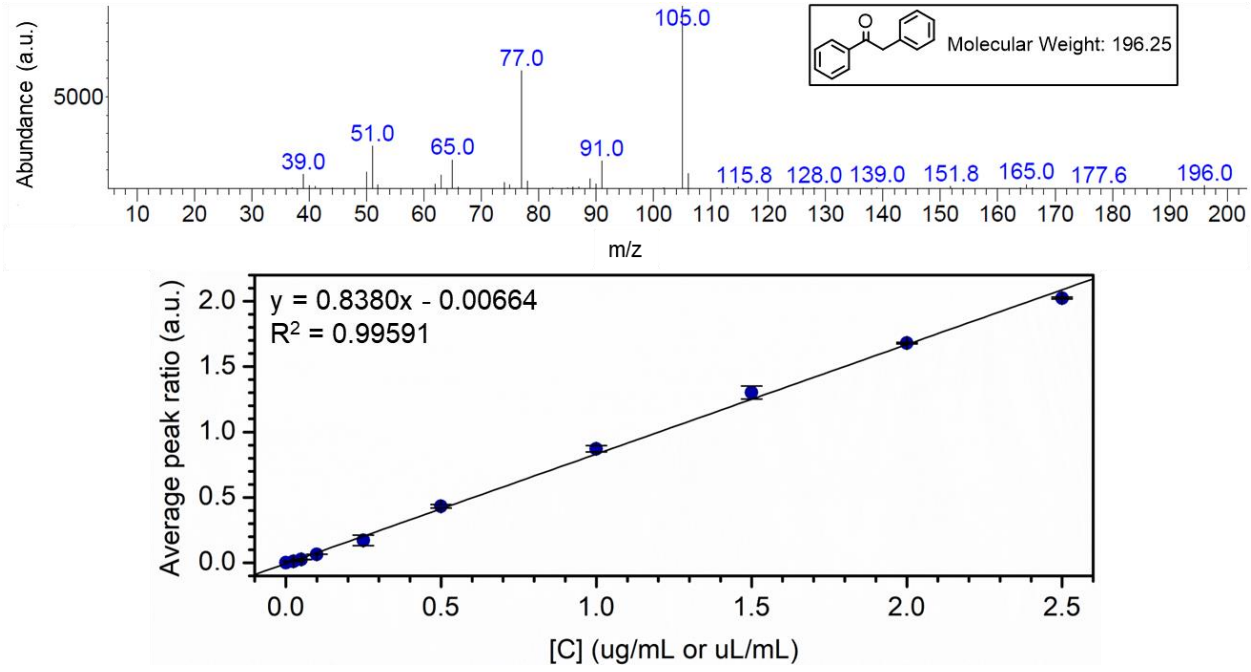

*Figure A.9. Experimental reference mass spectrum (top) and calibration curve (bottom) of deoxybenzoin (**1k**).*

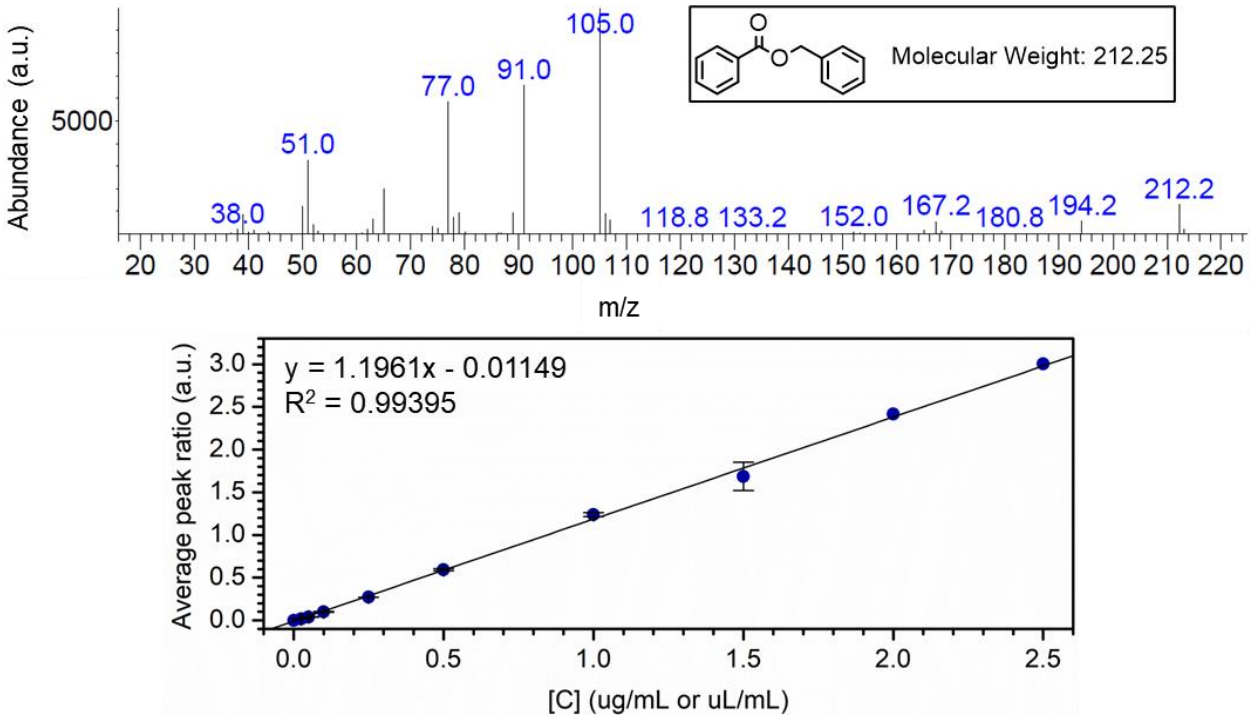

*Figure A.10. Experimental reference mass spectrum (left) and calibration curve (right) of benzyl benzoate (**1f**).*

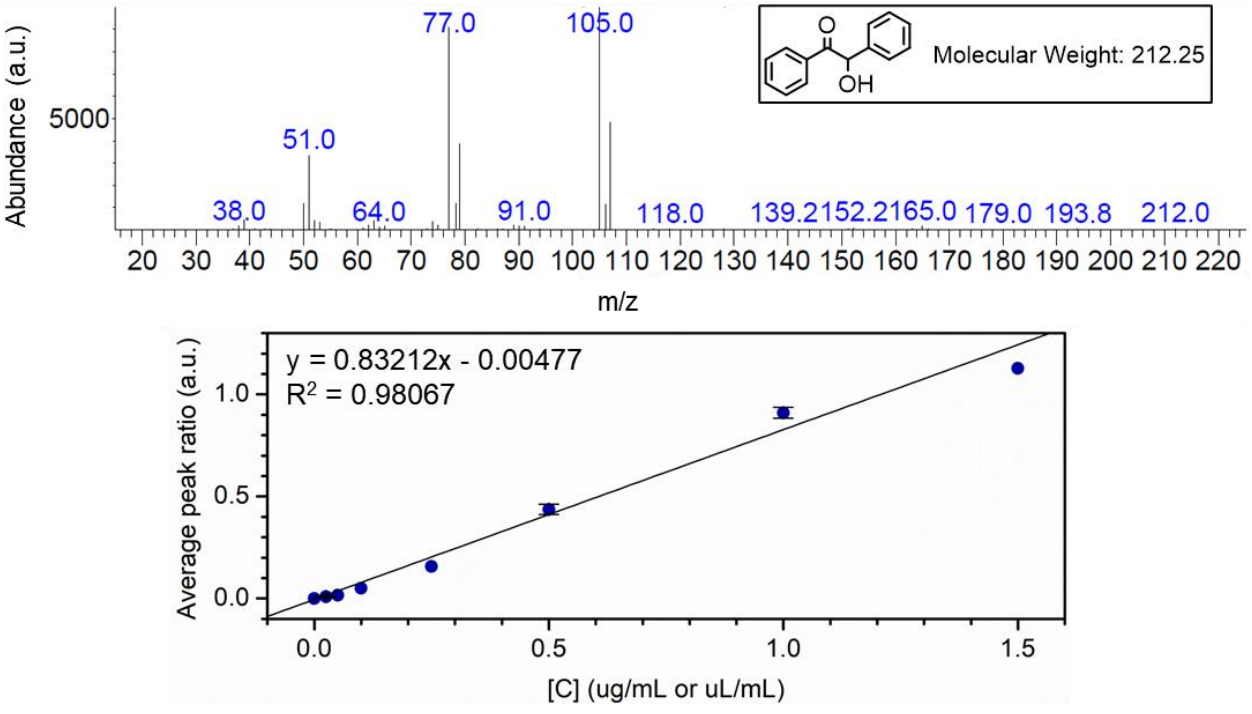

*Figure A.11. Experimental reference mass spectrum (left) and calibration curve (right) of benzoin (**1l**).*

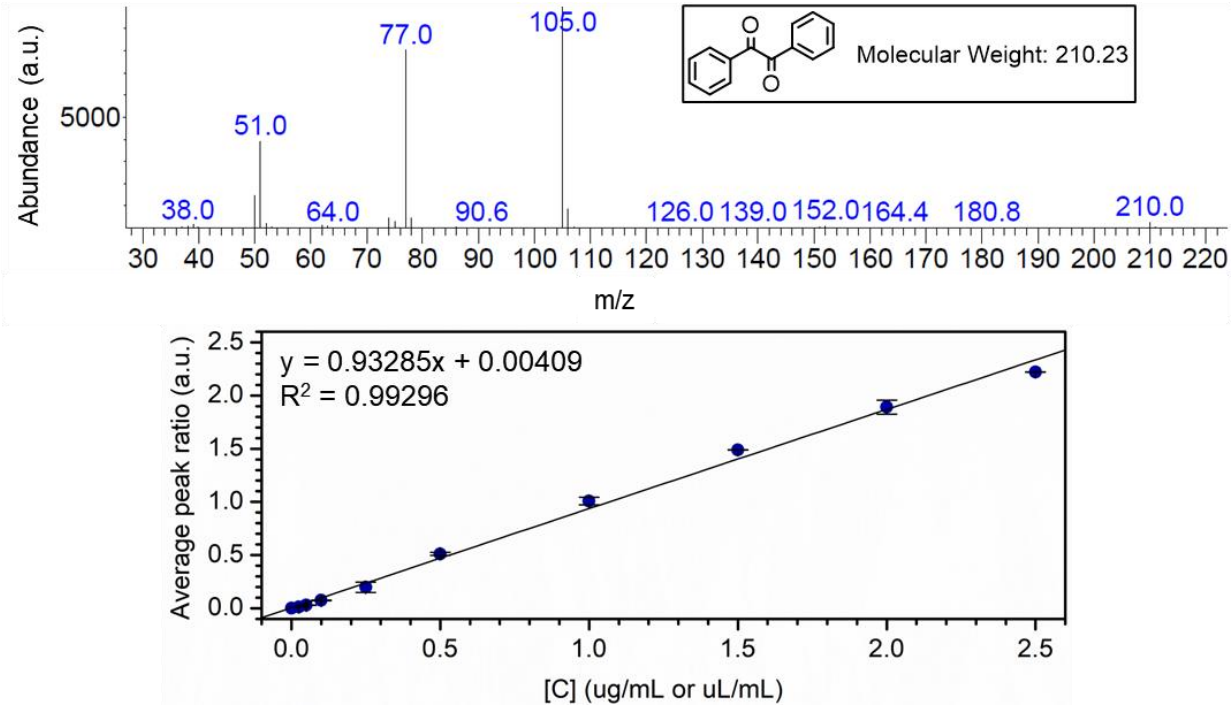

*Figure A.12. Experimental reference mass spectrum (left) and calibration curve (right) of benzil (**1m**).*

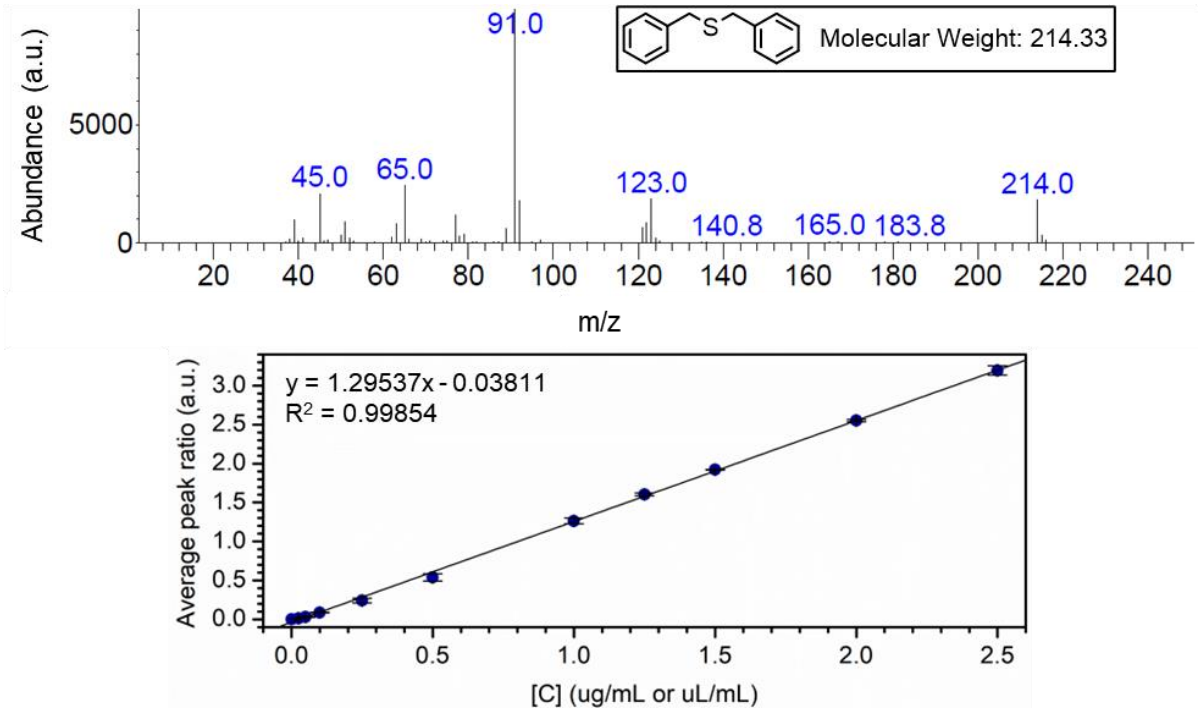

*Figure A.13. Experimental reference mass spectrum (top) and calibration curve (bottom) of dibenzyl sulfide (**1g**).*

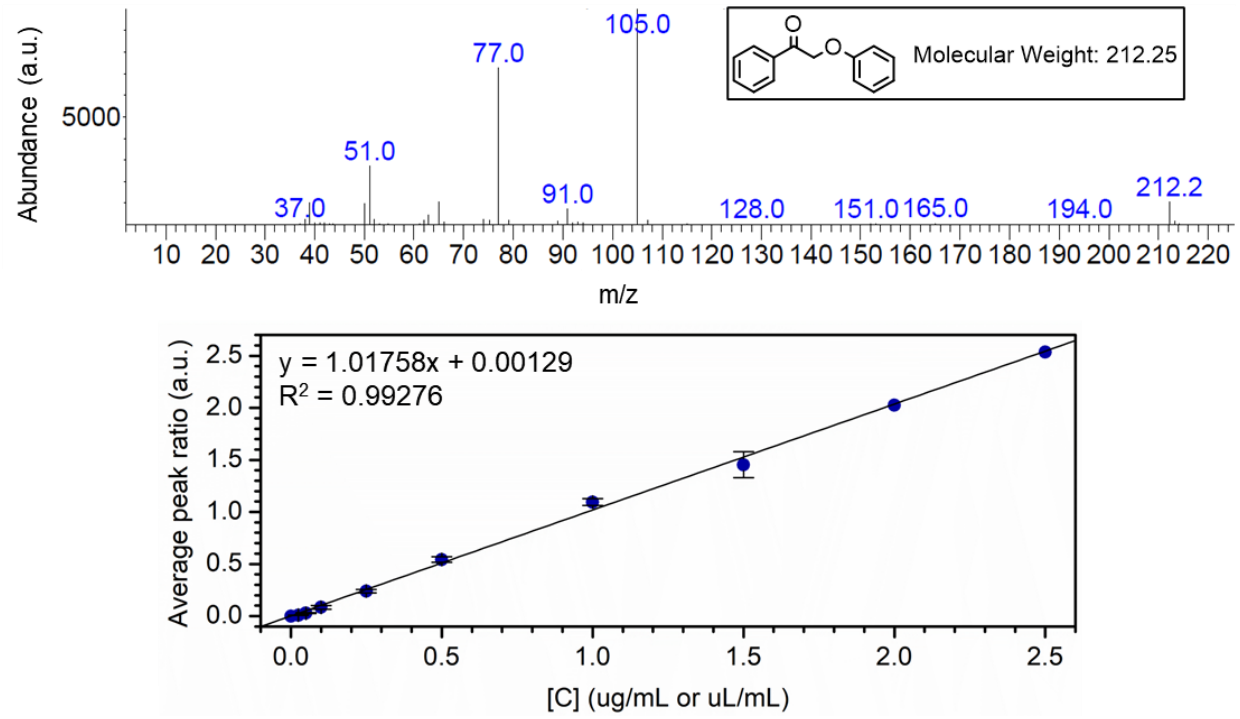

*Figure A.14. Experimental reference mass spectrum (top) and calibration curve (bottom) of PP-one (**2g**).*

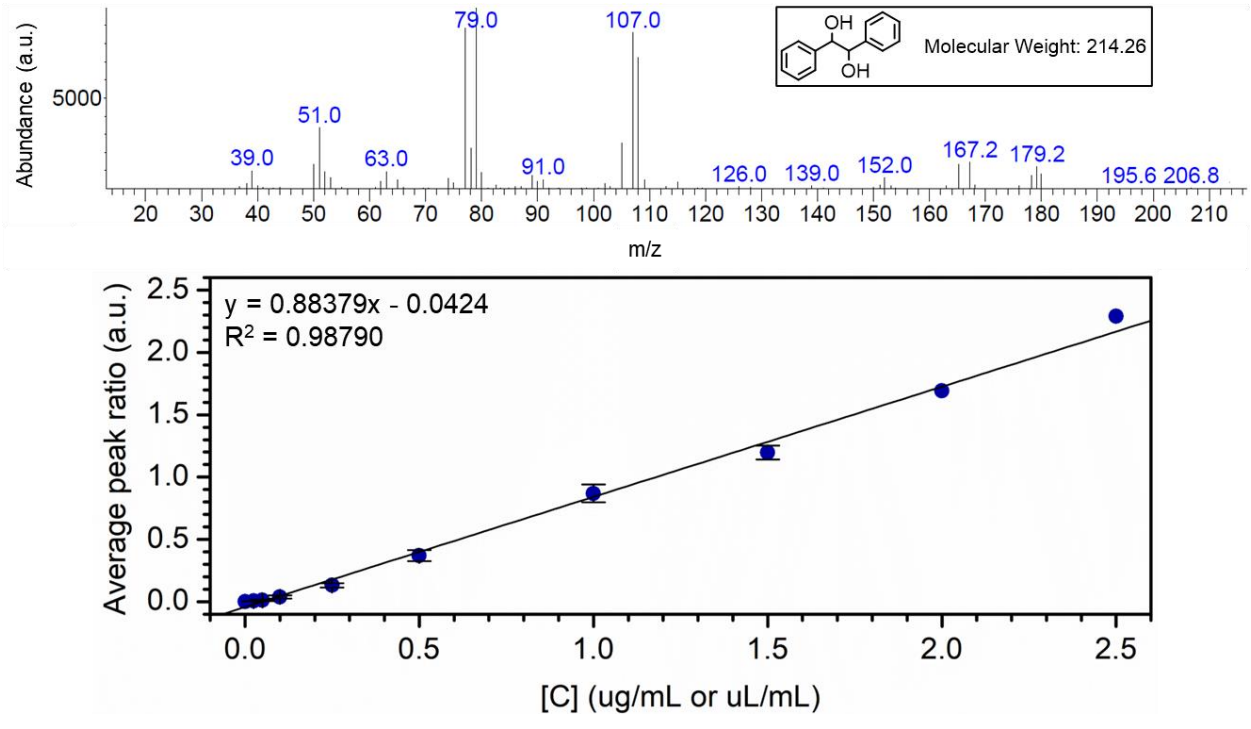

*Figure A.15. Experimental reference mass spectrum (top) and calibration curve (bottom) of hydrobenzoin (**1i**).*

The reference mass spectra as well as the GC calibration curves for the two starting materials, benzyl alcohol and PP-ol, were also obtained and depicted in Figures A.16 and A.17.

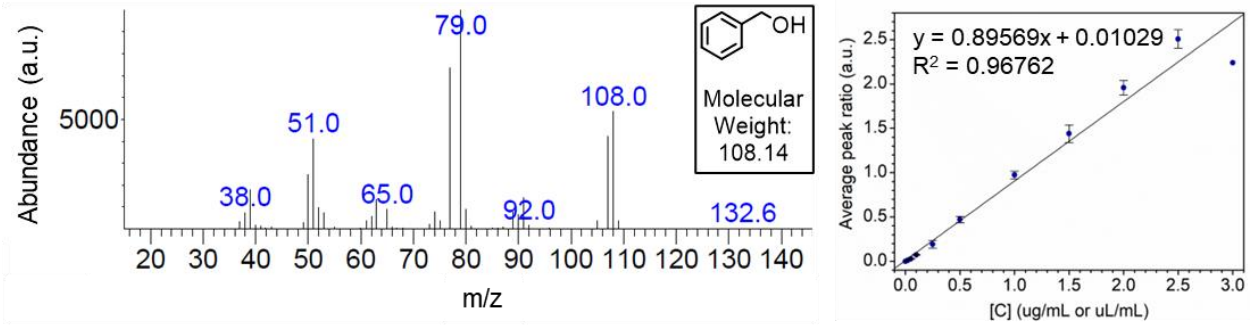

*Figure A.16. Experimental reference mass spectrum (left) and calibration curve (right) of benzyl alcohol (**1c**).*

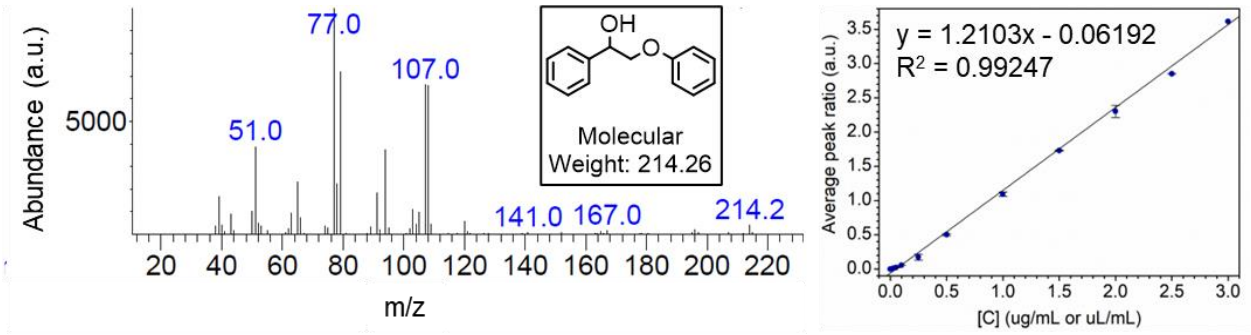

*Figure A.17. Experimental reference mass spectrum (left) and calibration curve (right) of PP-ol (**2h**).*

Appendix B. Additional data for Chapter 3

Chapter 3 identified CdS-7 as the optimal catalyst for future experiments. The representative GC chromatogram (Figure B.1) of the PP-ol/CdS-7 system depicts all possible products of PP-ol conversion under the experimental conditions specified in Chapter 3 of this Thesis. Substituting CdS-7 with the other synthesized photocatalysts resulted in variations in concentrations of products. In very few cases, anisole and benzaldehyde (not pictured) were found in the final reaction mixture.

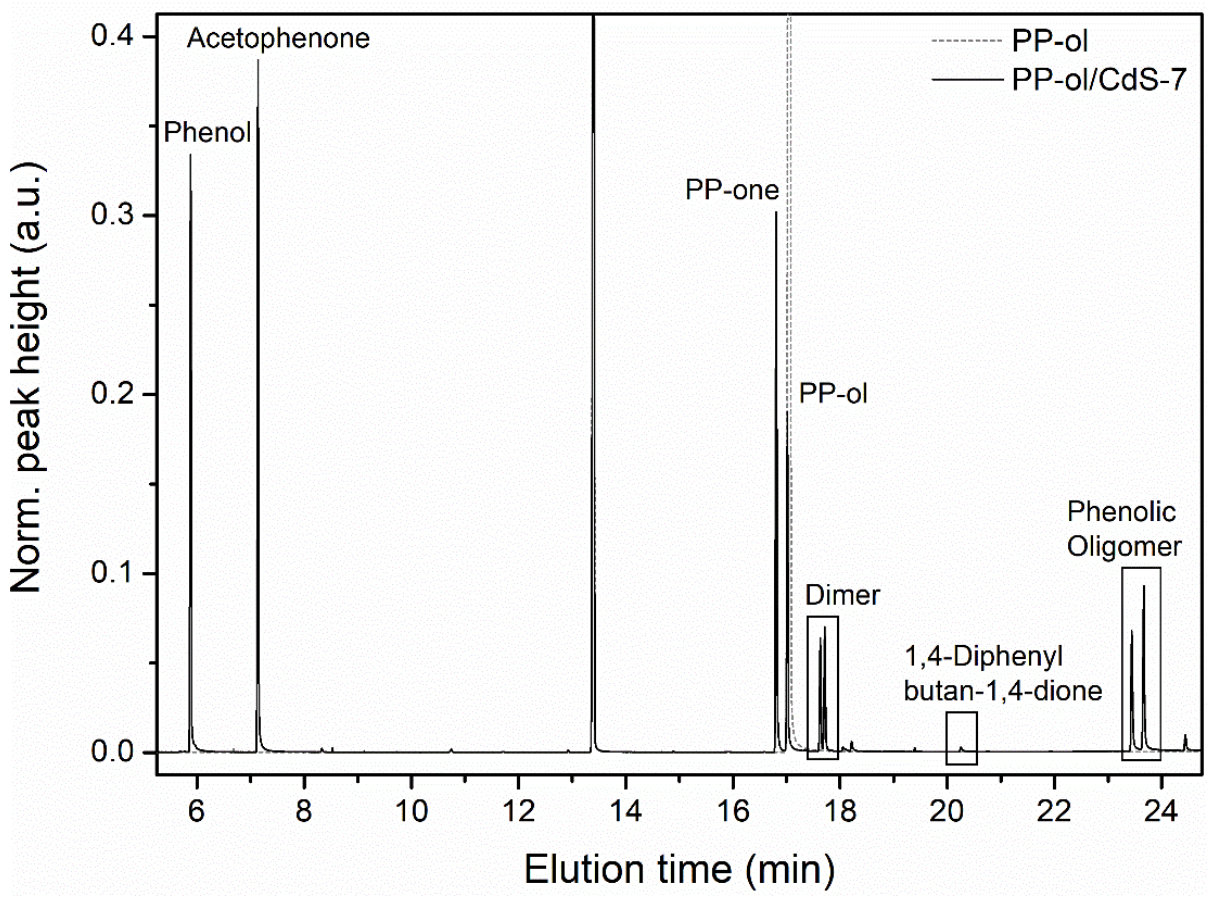

Figure B.1. GC chromatogram of PP-ol/CdS-7 reaction mixture at the end of the reaction. The dashed lines represent the starting PP-ol.

To determine the relationship, if any, of specific reaction pathways with PP-ol conversion, several scatter plots were generated from the experimentally determined concentrations of PP-ol conversion products. Figure B.2 illustrates that increasing PP-ol conversion is related to a high phenol-to-acetophenone ratio,

which suggests that active CdS photocatalysts, aside from catalyzing PP-ol conversion, could potentially catalyze the reaction of acetophenone to form other byproducts. In addition, increased PP-ol conversion is also associated with a higher rate of β-O-4 cleavage reactions as opposed to PP-ol oxidation to PP-one. This would suggest that, overall, PP-one remains a minor product of PP-ol decomposition.

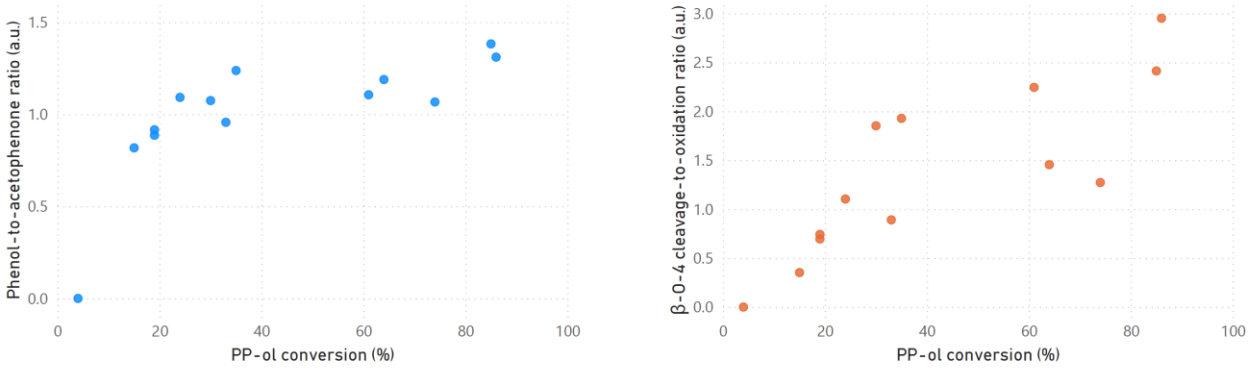

Figure B.2. Phenol-to-acetophenone (left) and β-O-4 cleavage-to-oxidation (right) ratios versus PP-ol conversion.

Similar analysis was also done to elucidate the relationship between decomposition (β-O-4 cleavage or oxidation to PP-one) and coupling reactions as a function of PP-ol conversion, as depicted in Figure B.3. In all cases, all the synthesized photocatalysts favored PP-ol decomposition, however, there did not seem to be apparent patterns to the formation of larger oligomers. Indeed, increased photocatalytic activity did not necessarily lead to increased coupling reactions.

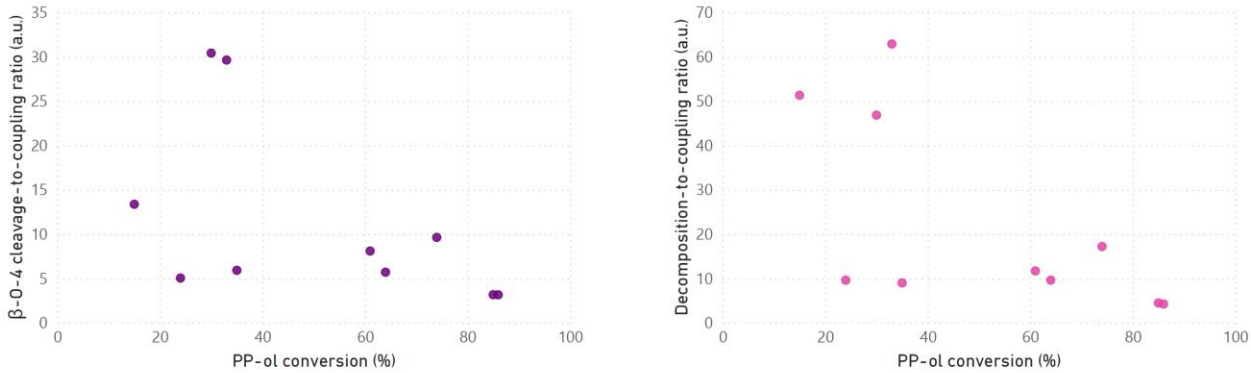

Figure B.3. *β-O-4 cleavage-to-coupling ratio (left) and PP-ol decomposition-to-coupling ratio (right) versus PP-ol conversion. Undefined values were omitted from both plots.*

Appendix C. Repetition of synthesis and characterization of unused CdS

In Chapter 3, synthesis for some of the CdS catalysts were repeated to determine the reproducibility of synthesis procedures. The CdS NPs outlined in this Appendix were characterized but not used for any photocatalytic experiments.

C-1. Synthesis of CdS QDs

As stated in Chapter 3, synthesis of CdS-1, CdS-2, and CdS-3 was conducted using the same method, and the procedure was repeated once more to yield CdS-A1 (Figure C.1). In the case of the latter, the NPs exhibited high BET surface area (174 m^2/g) and similar particle size as the catalysts outlined in Chapter 3, apart from CdS-2. Generally, it was found that NPs synthesized using this method exhibited significant differences in specific surface areas and crystalline phases, and there were observable challenges in producing NPs with similar features.

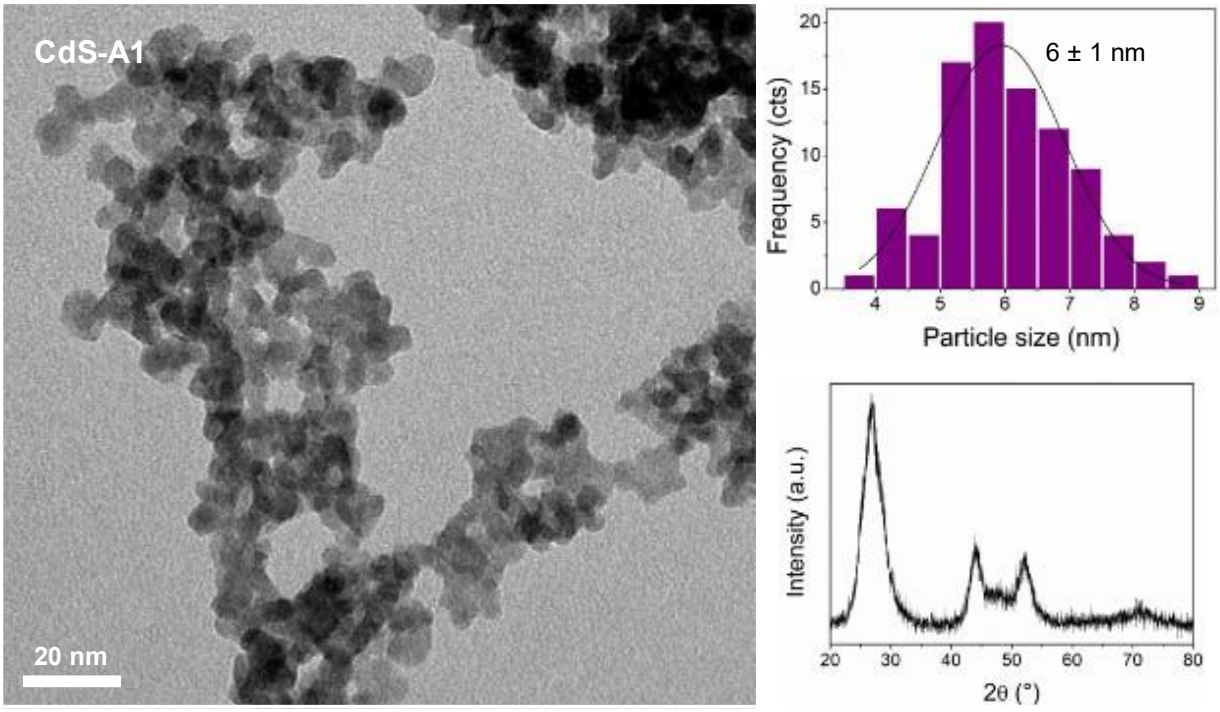

Figure C.1. (Clockwise, from left) TEM image, particle size distribution, and XRD pattern of CdS-A1. Synthesis procedure followed that of CdS-1, CdS-2, CdS-3 without any modifications.

C-2. Synthesis of CdS nanoflorets

The synthesis procedure of CdS-9, CdS-12, and CdS-13 was also repeated and the resulting CdS NPs are illustrated in Figures C.2 and C.3, labelled as CdS-A2 and CdS-A3 respectively. While the latter two CdS NPs showcased the same cauliflower-like morphology as expected, as visible from the particle size distributions, there was significant fluctuations in the sizes of the resulting CdS NPs.

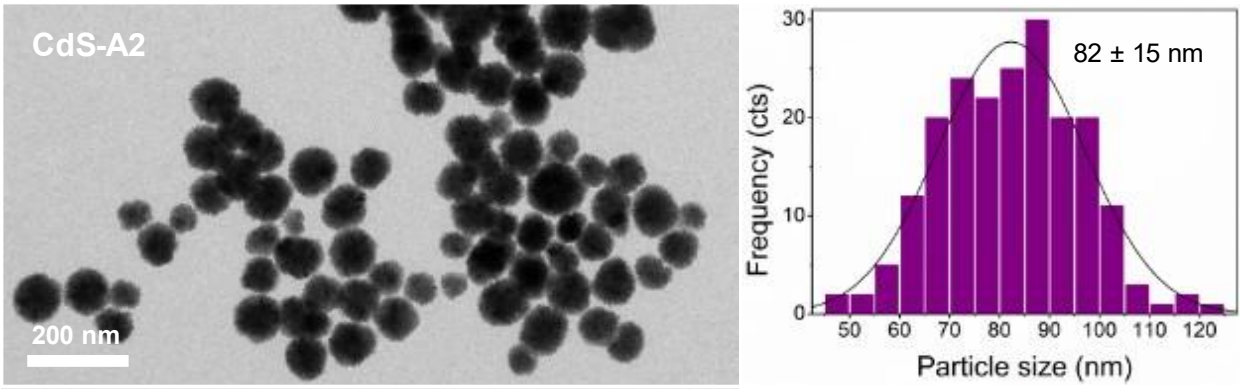

Figure C.2. TEM image (left) and particle size distribution (right) of CdS-A2. Synthesis procedure followed that of CdS-9, CdS-12, CdS-13 without any modifications.

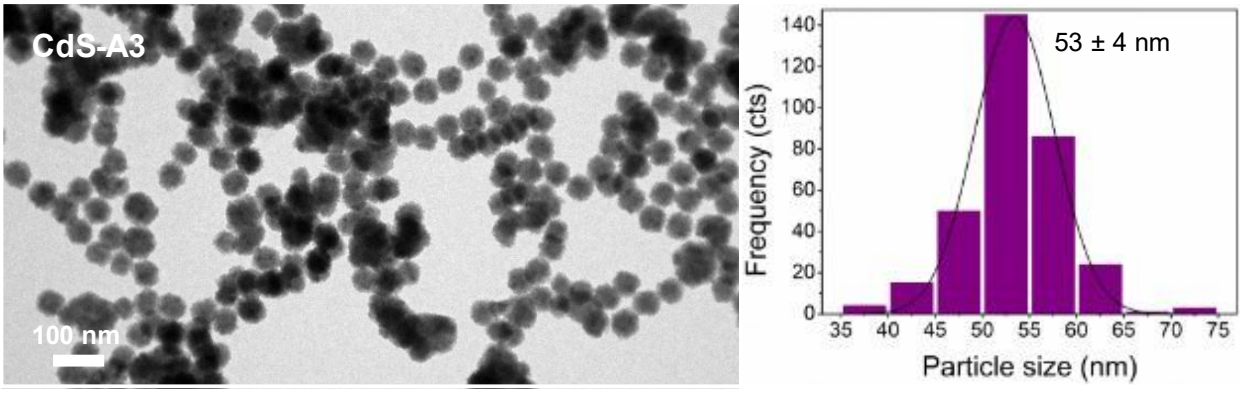

Figure C.3. TEM image (left) and particle size distribution (right) of CdS-A3. Synthesis procedure followed that of CdS-9, CdS-12, CdS-13 without any modifications.

Appendix D. Additional characterization of **CdS-c**, **CdS-m**, and **CdS-h**

During the characterization of the CdS NPs, the EDS spectra for **CdS-c**, **CdS-m**, and **CdS-h** were collected using a JEOL JEM-2100F FETEM to determine elemental composition and illustrated in Figure D.1. To note, carbon-supported copper grids were employed during TEM/EDS measurements, and this is likely the reason why the EDS spectra show carbon (C) and copper (Cu) peaks. These peaks are not attributed to the synthesized CdS NPs.

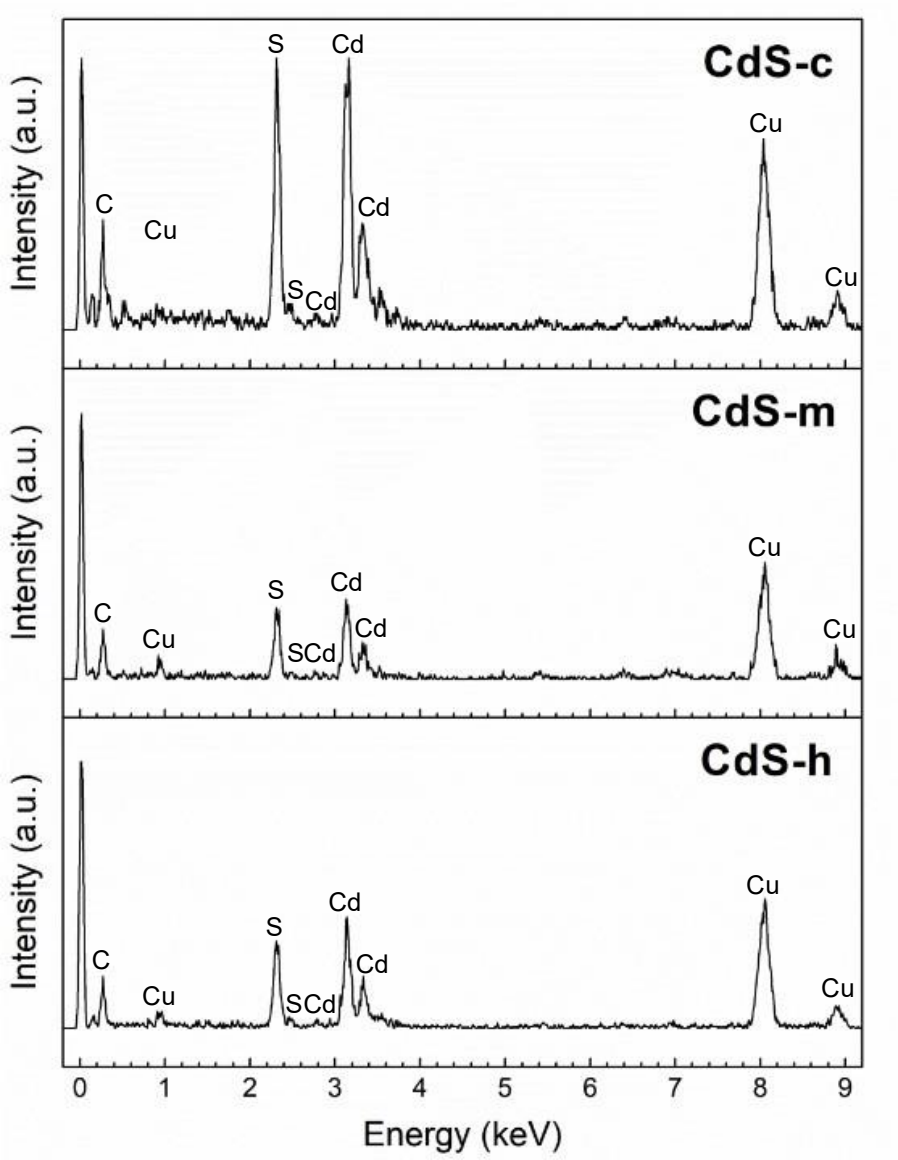

*Figure D.1. EDS spectra of **CdS-c**, **CdS-m**, and **CdS-h**.*

SEM images were also obtained for the CdS NPs using a JEOL JSM-7500F field emission scanning electron microscope (FESEM) and are illustrated in Figures D.2 to D.4, which show that the CdS NPs aggregate into amorphous clusters. Due to the small size of the synthesized NPs, morphologies could not be visualized clearly using SEM.

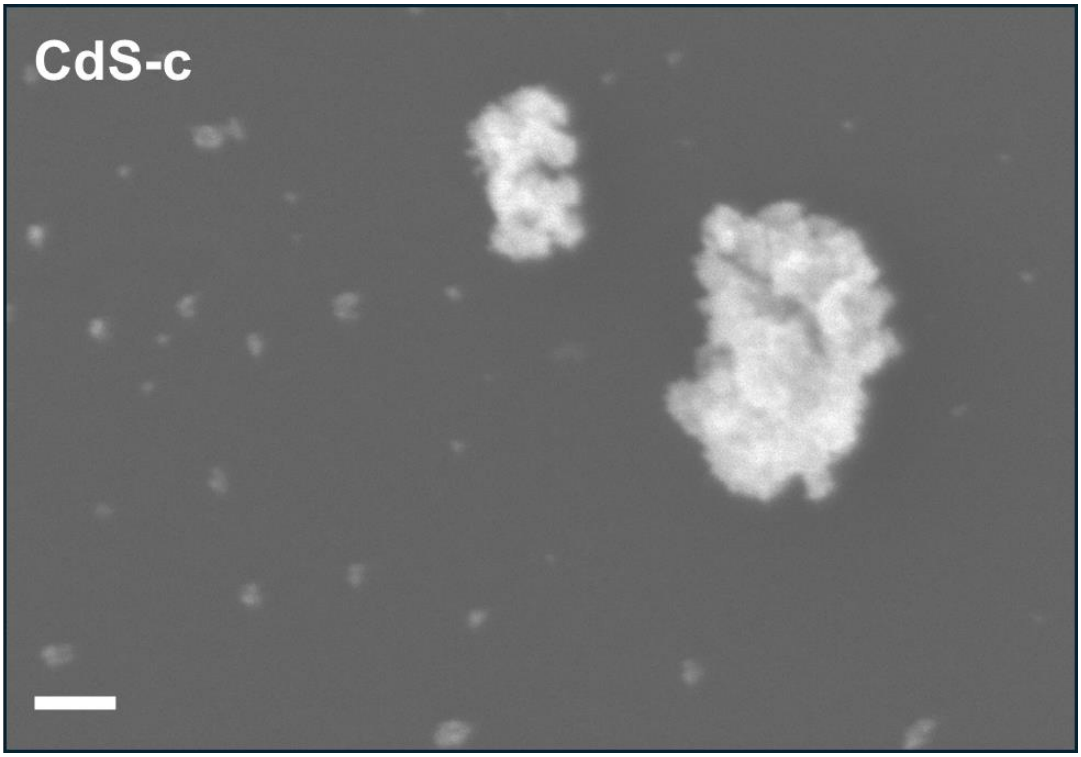

Figure D.2. SEM image of CdS-c (scale bar: 100 nm).

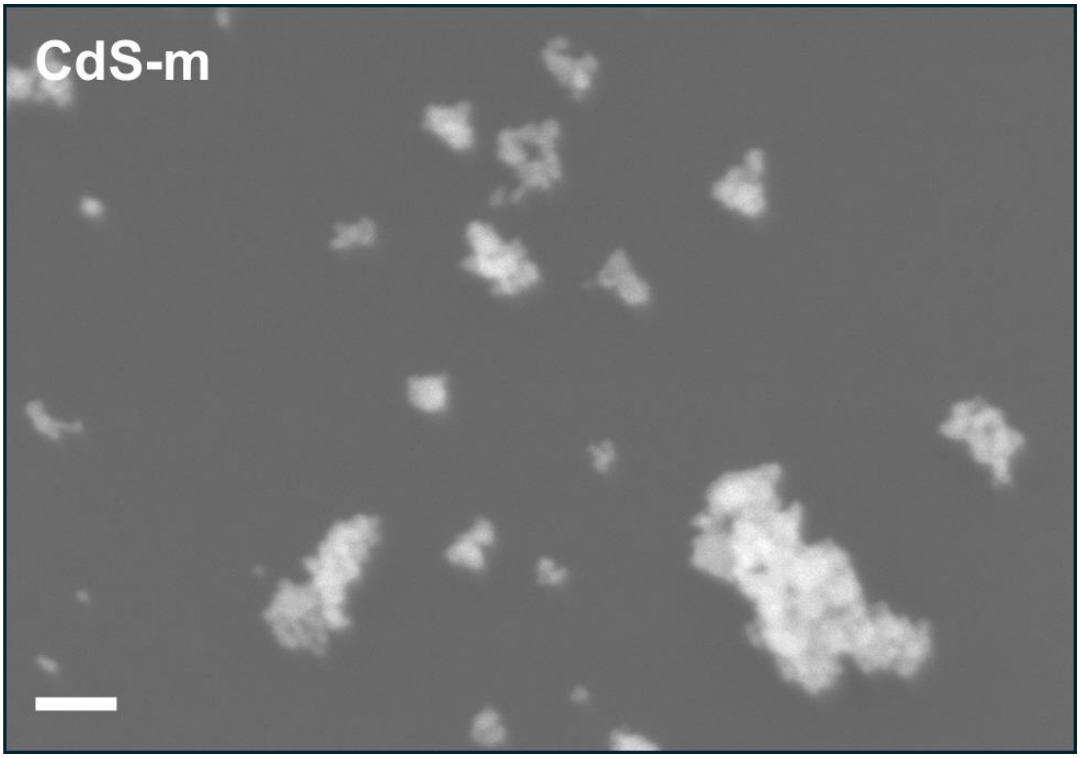

Figure D.3. SEM image of CdS-m (scale bar: 100 nm)

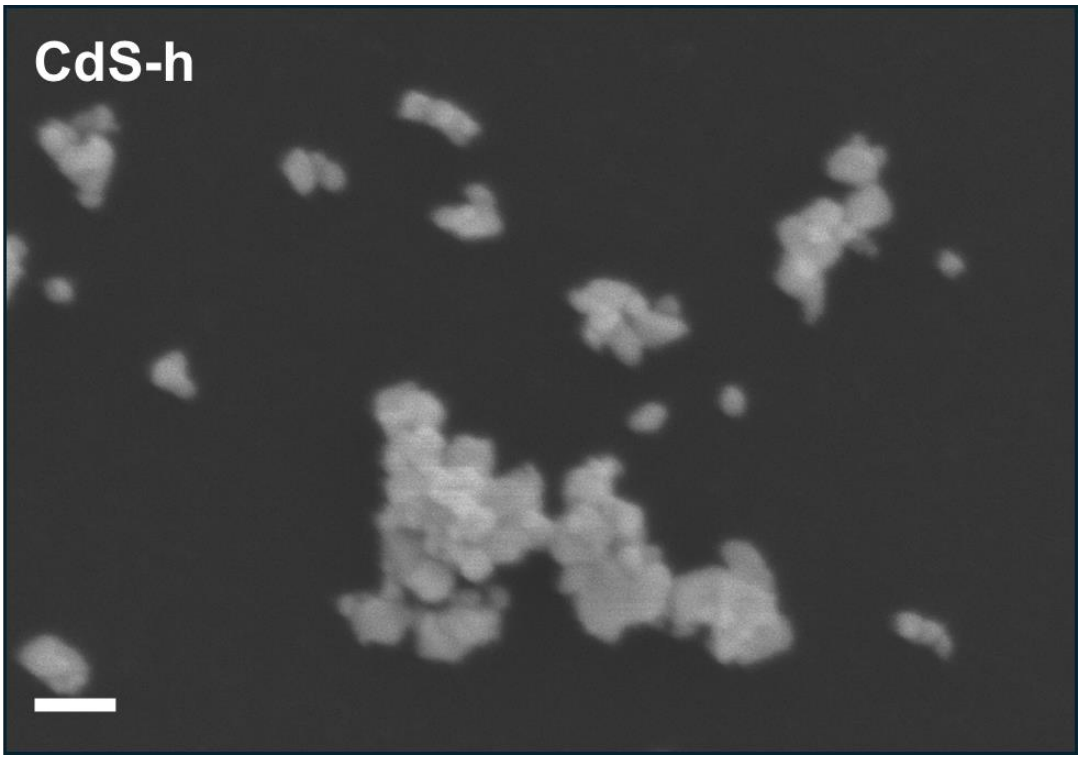

Figure D.4. *SEM image of CdS-h (scale bar: 100 nm).*

Appendix E. Additional GC-MS data for solvent-free benzyl alcohol and PP-ol conversion experiments

Control experiments for the thermal and photocatalytic conversion of benzyl alcohol and PP-ol were conducted. Figures E.1 and E.2 show the recorded GC chromatograms of the control experiments that did not show conversion of the starting material and where therefore omitted from discussions in Chapter 4.

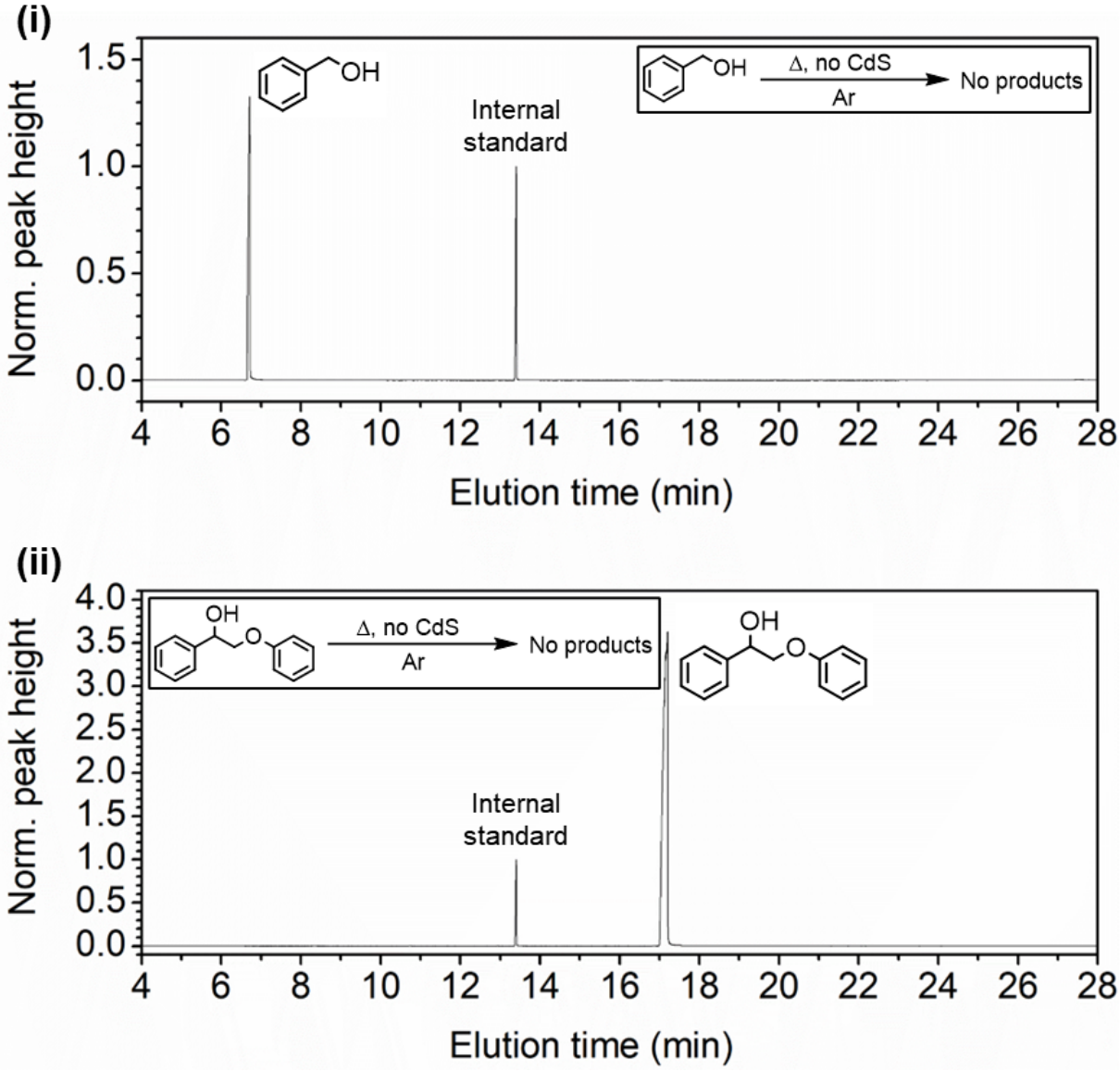

Figure E.1. GC chromatogram of (i) benzyl alcohol and (ii) PP-ol control experiment after 24h under heating without CdS. No products of conversion were observed.

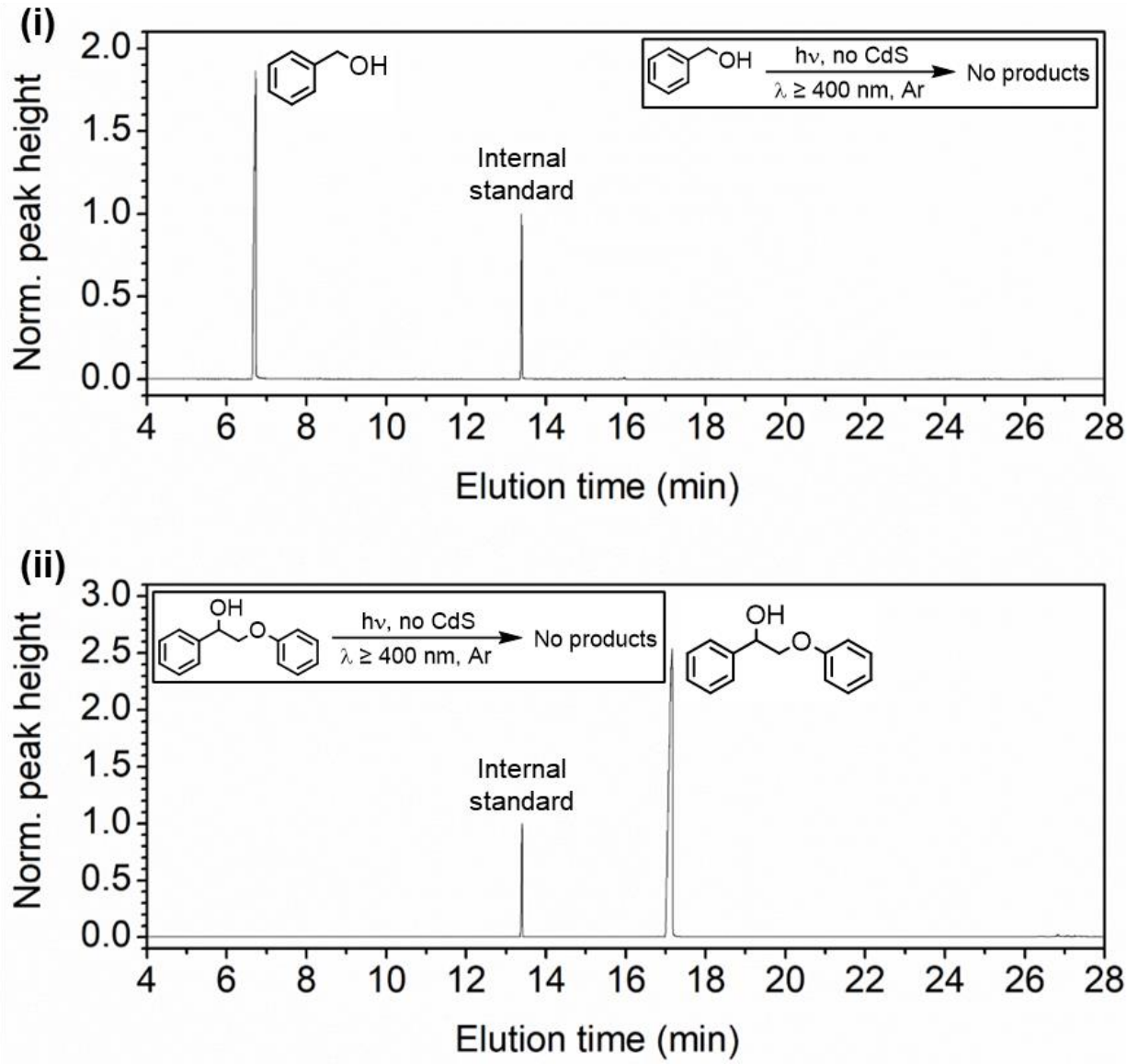

Figure E.2. GC chromatogram of (i) benzyl alcohol and (ii) PP-ol control experiment after 24h under visible light irradiation without CdS. No products of conversion were observed.

In addition to liquid GC-MS samples, qualitative analysis was also conducted on the headspace GC-MS of the control experiments. Figure E.3 showcases control experiments in which toluene and styrene were not observed from benzyl alcohol and PP-ol decomposition, respectively.

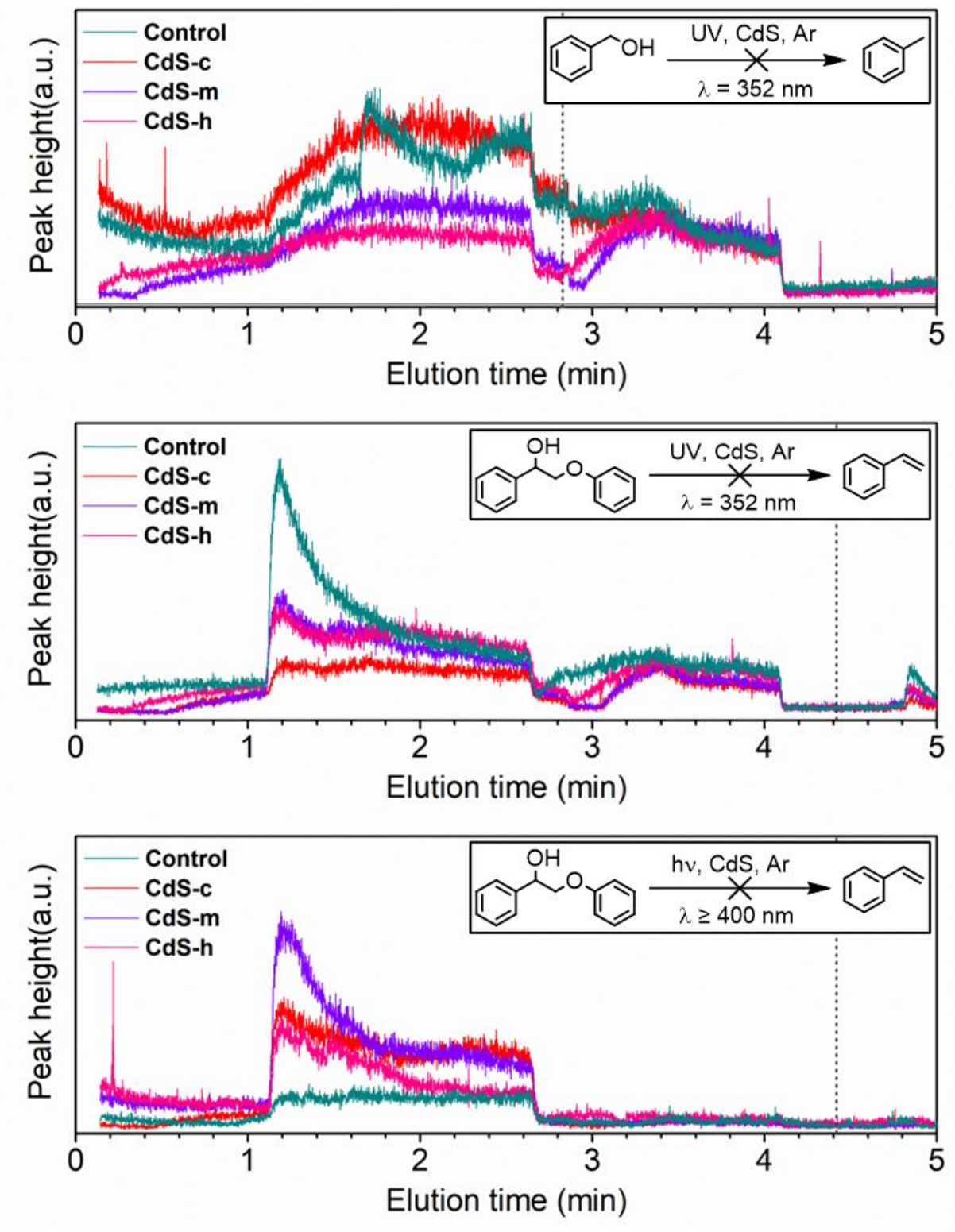

Figure E.3. Headspace GC chromatogram of (i) benzyl alcohol and (ii) PP-ol under UV irradiation and (iii) PP-ol under visible light irradiation after 24 hours. The dotted lines represent the position of the expected product (toluene or styrene) peaks. The expected toluene and styrene peaks were absent.

Appendix F. Validation of **CdS-c**, **CdS-m**, and **CdS-h** synthesis procedures, and characterization of unused CdS

In Chapter 4, synthesis procedures were repeated for validation purposes. As a result, additional CdS NPs were synthesized, which were characterized but not used in any catalysis experiments.

F-1. Testing the reproducibility of **CdS-m** synthesis

To ensure reproducibility, the synthesis of mixed phase CdS was repeated, using the same procedure that led to the production of CdS-7 (Chapter 3) and **CdS-m** (Chapter 4) in the Thesis, and Cd-Am1 depicted in Figure F.1. The mixed crystalline phase of this sample was confirmed through XRD. TEM imaging and measurement of particle sizes confirmed that the morphology of CdS-Am1 is similar, if not identical to the CdS NPs described in the Thesis, with similar particle sizes as well.

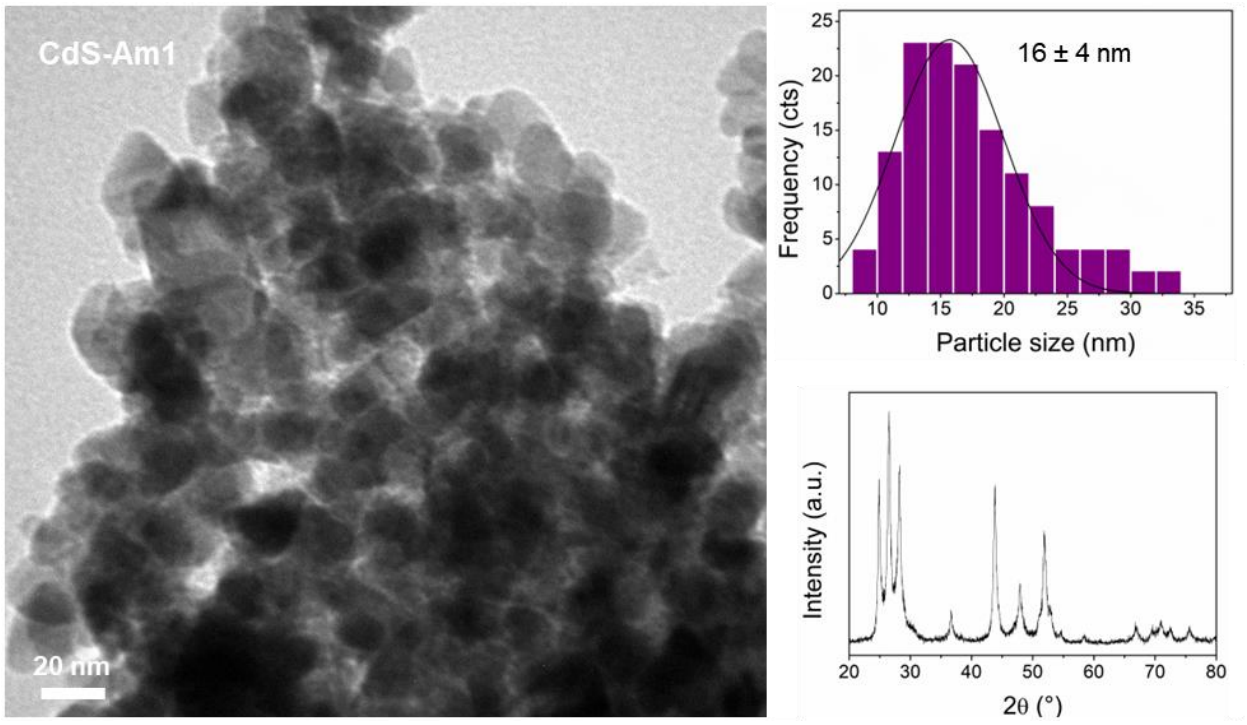

*Figure F.1. (Clockwise, from left) TEM image, particle size distribution, and XRD pattern of CdS-Am1. Synthesis procedure followed that of CdS-7 (Chapter 3) and **CdS-m** (Chapter 4) without any modifications.*

F-2. Optimization of **CdS-c** synthesis temperature

As the seminal work[186] referenced for CdS synthesis in Chapter 4 did not describe experimental conditions leading to the production of cubic CdS NPs, some synthesis optimization experiments were conducted to determine the best conditions to synthesize cubic NPs. It is generally known that cubic CdS can be produced in mild conditions, which includes room temperature synthesis. However, in our systems, this was not possible; due to the low solubility of sodium sulfide nonahydrate ($Na_2S \cdot 9H_2O$), the sulfur precursor, some mild heating needed to be applied. Therefore, some temperature optimization experiments were conducted, where the synthesis procedure for **CdS-m** was repeated with some modifications. Namely, once the sulfur precursor was completely dissolved and the mixture was totally outgassed, the temperature was lowered to 95 °C. This change led to the generation of CdS-Ac1 (Figure F.2). Small bumps around 36° and 48° in the XRD pattern suggested the onset of hexagonal CdS, which was not ideal.

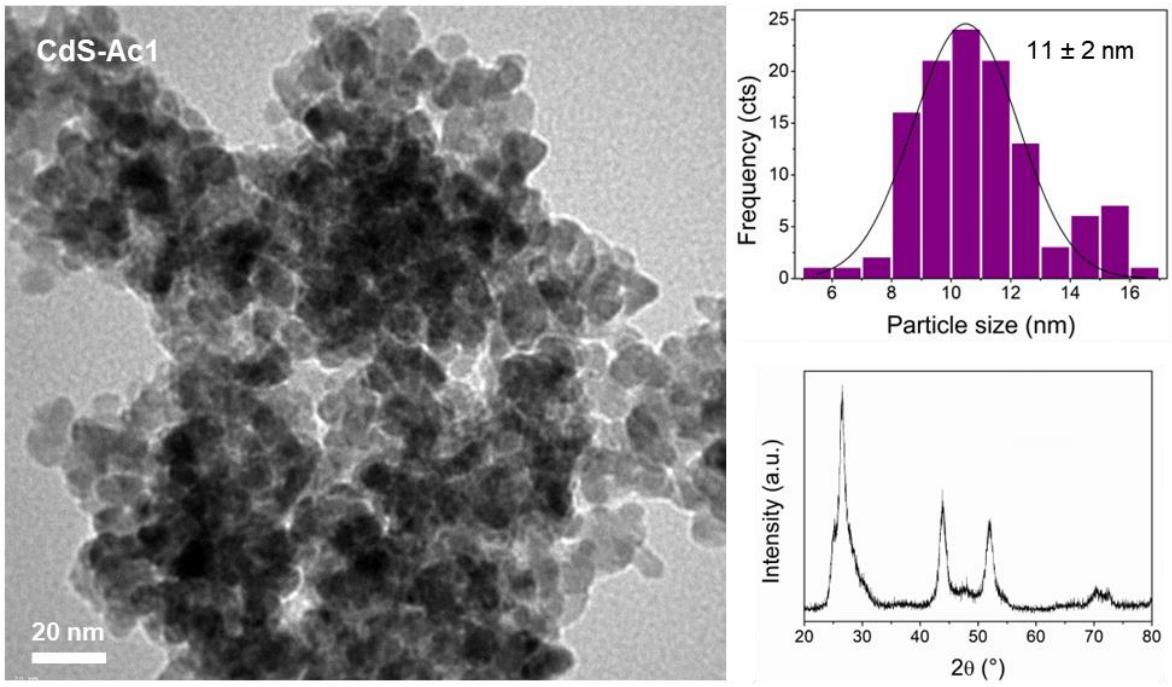

*Figure F.2. (Clockwise, from left) TEM image, particle size distribution, and XRD pattern of CdS-Ac1. Synthesis procedure followed that of **CdS-c** (Chapter 4) with some modifications (temperature set at 95 °C instead of 80 °C).*

To obtain phase-pure cubic CdS, the synthesis temperature was lowered to 80 °C, resulting in the production of CdS-Ac2 (Figure F.3). The modified procedure was repeated and yielded CdS-Ac3 (Figure F.4). Both had XRD patterns that showed pure cubic phase CdS. Ultimately, the results of these exploratory experiments established the **CdS-c** synthesis procedure described in Chapter 4 of this Thesis.

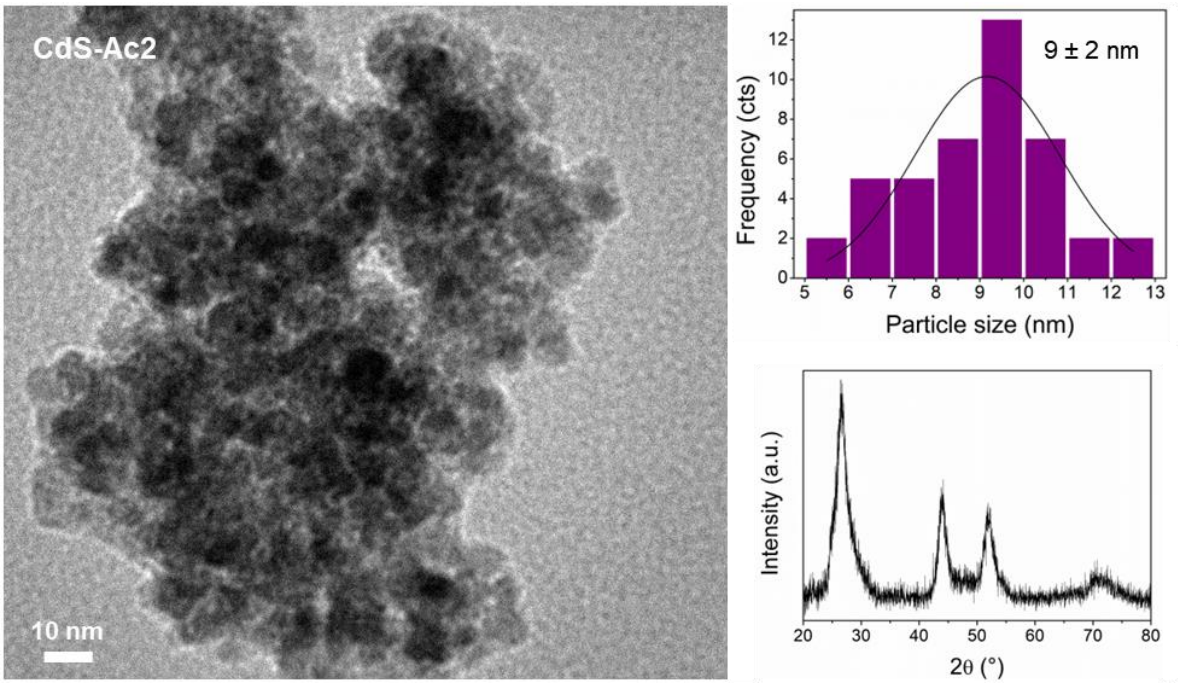

*Figure F.3 (Clockwise, from left) TEM image, particle size distribution, and XRD pattern of CdS-Ac2. Synthesis procedure followed that of **CdS-c** (Chapter 4) with no modifications.*

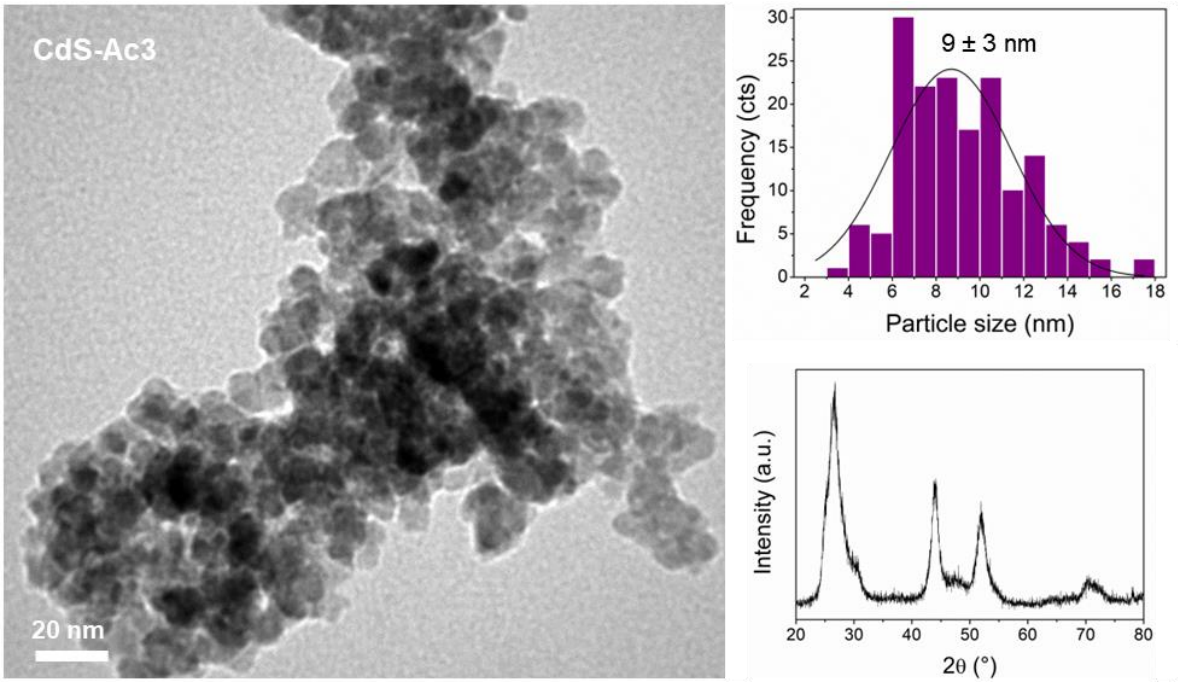

*Figure F.4. (Clockwise, from left) TEM image, particle size distribution, and XRD pattern of CdS-Ac3. Synthesis procedure followed that of **CdS-c** (Chapter 4) with no modifications.*

F-3. Repetition of **CdS-h** synthesis

Regarding the hexagonal CdS catalyst, the initial attempt of the synthesis procedure led to the formation of CdS-Ah1 depicted in Figure F.5. While the XRD pattern for CdS-Ah1 showed high crystallinity and phase purity, one concern was the broad size distribution. The synthesis procedure was then repeated, yielding CdS-h which had an identical XRD pattern and similar particle size with a lower size distribution.

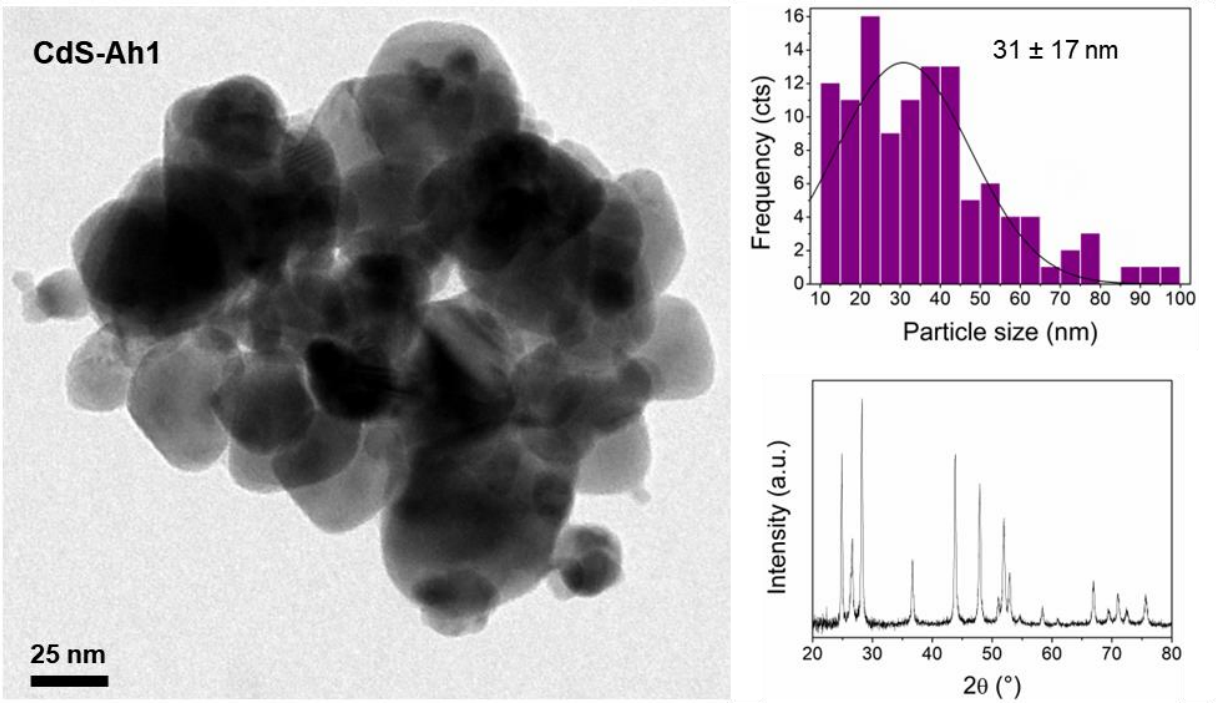

*Figure F.5. (Clockwise, from left) TEM image, particle size distribution, and XRD pattern of CdS-Ah1. Synthesis procedure followed that of **CdS-h** (Chapter 4) with no modifications.*

Outside the scope of the Thesis, an exploration on the effect of solvent and sulfur injection rate was conducted. In a series of two experiments, the synthesis procedure to obtain hexagonal CdS was performed exactly as outlined in the reference work; that is, tetraethylene glycol was used as the solvent during CdS synthesis, rather than the triethylene glycol as described in Chapter 4. Of note, the reference work[86] emphasized the effect of cadmium addition rate on the resulting CdS morphology.

In the first experiment yielding CdS-Ah2 (Figure F.6), the cadmium precursor solution was quickly injected to the sulfur precursor solution. This one-shot injection is the same rate of injection that was described in Chapter 4, which was used as a way of obtaining smaller NPs to maximize specific surface area. The authors of the reference work reported that a fast injection rate resulted in the formation of nanocones, which we observed when the procedure was reproduced. Some smaller spherical and triangular NPs were also observed.

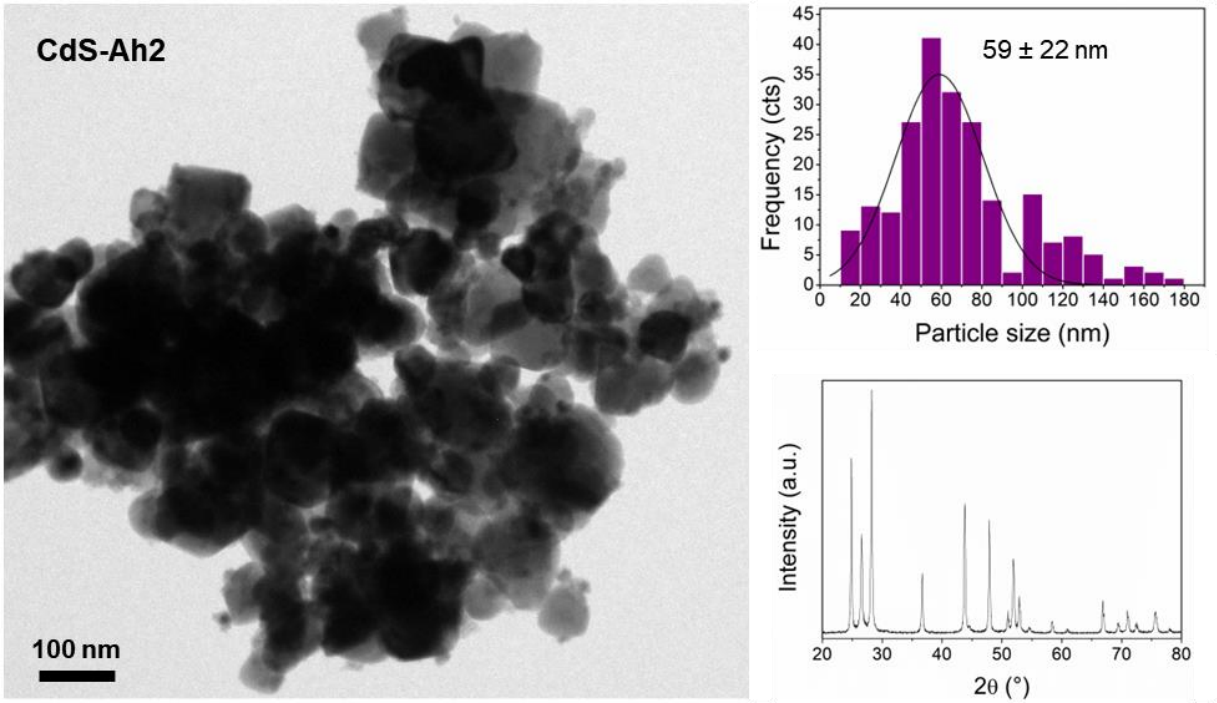

Figure F.6. (Clockwise, from left) TEM image, particle size distribution, and XRD pattern of CdS-Ah2. Synthesis procedure described in literature (fast Cd^{2+} injection rate).

In the second experiment, the cadmium precursor was slowly injected at a rate of 0.5 mmol/h, to yield CdS-Ah3 (Figure F.7). According to literature, slow addition should have resulted in the formation of hexagonal nanoplates, but in the case of our experiment, only a couple of them were observed. They also did not appear to be flat NPs. The dominant morphology appeared to be larger, triangular NPs with some smaller spherical NPs as well as nanocones. Particle sizes were also larger and with broader size distribution relative to CdS-Ah2.

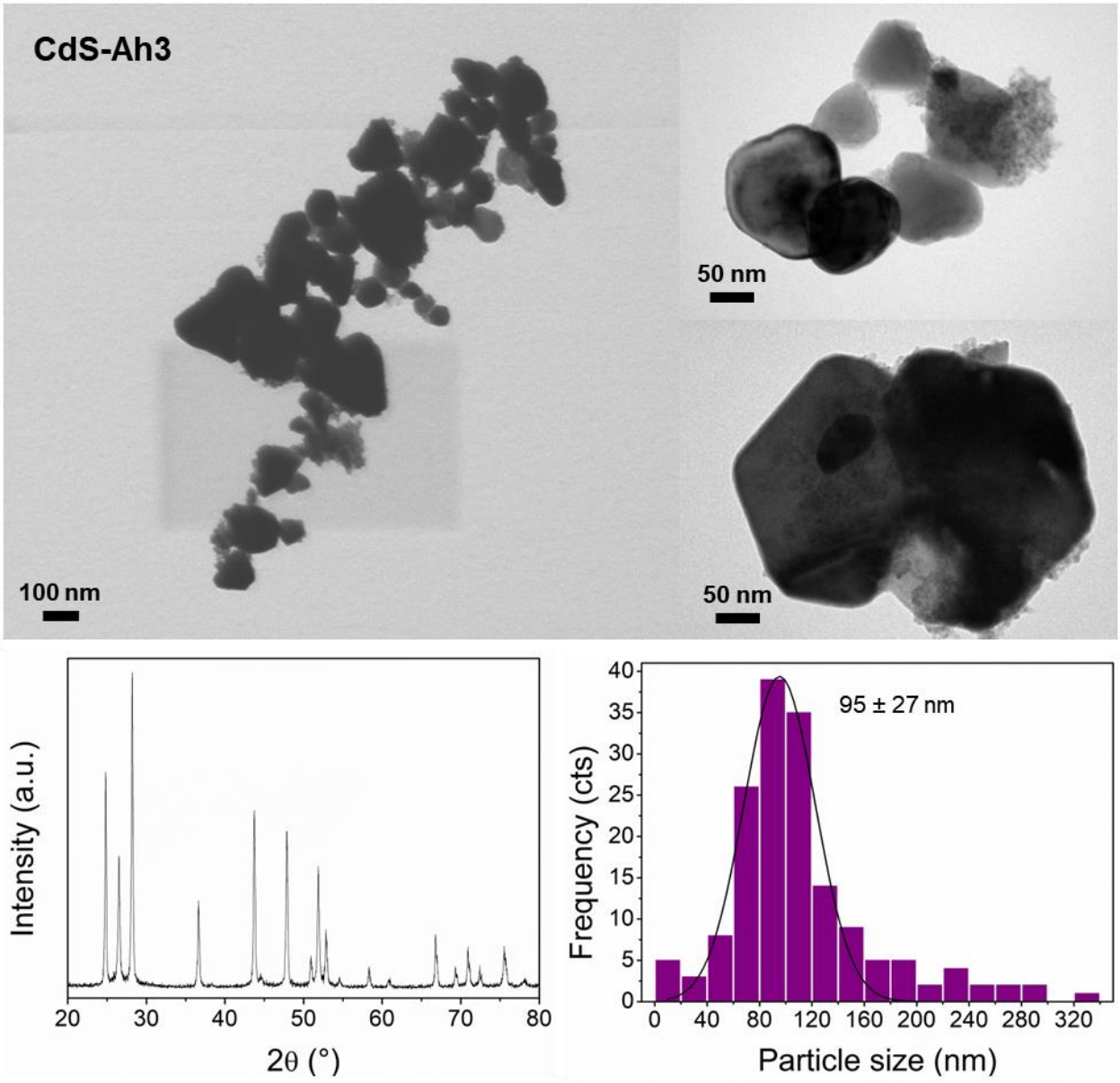

Figure F.7. (Clockwise, from top left) TEM images, particle size distribution, and XRD pattern of CdS-Ah3. Synthesis procedure described in literature (slow Cd^{2+} injection rate).

F-4. References

(1) Wang, X.; Liu, M.; Zhou, Z.; Guo, L. Toward Facet Engineering of CdS Nanocrystals and Their Shape-Dependent Photocatalytic Activities. *J. Phys. Chem. C* **2015**, *119* (35), 20555–20560.

Appendix G. Additional work

G-1. Synthesis of CuS NPs

CuS quantum dots (QDs) were synthesized according to a reported approach with modifications.[1] Thiourea (5.0 mmol) was dissolved in 30 mL of ethylene glycol to prepare a sulfur stock solution. In a separate flask, copper (II) chloride dihydrate (5.0 mmol) and tetramethylammonium hydroxide (10.0 mmol) were dissolved in 30 mL of ethylene glycol and heated to 100 °C. Under vigorous stirring, the sulfur precursor solution was quickly injected into the flask. The reaction was heated to 155 °C and stirring was maintained for 2 hours, followed by refluxing at 194 °C for an additional hour before cooling down to room temperature. The solution was then centrifuged and washed with water and methanol to obtain dark blue solids, which were dried under vacuum at 60 °C for 4 hours. The product was characterized by TEM and XRD (Figure G.1) and identified as hexagonal CuS. The BET surface area was determined to be 77.5 m^2/g.

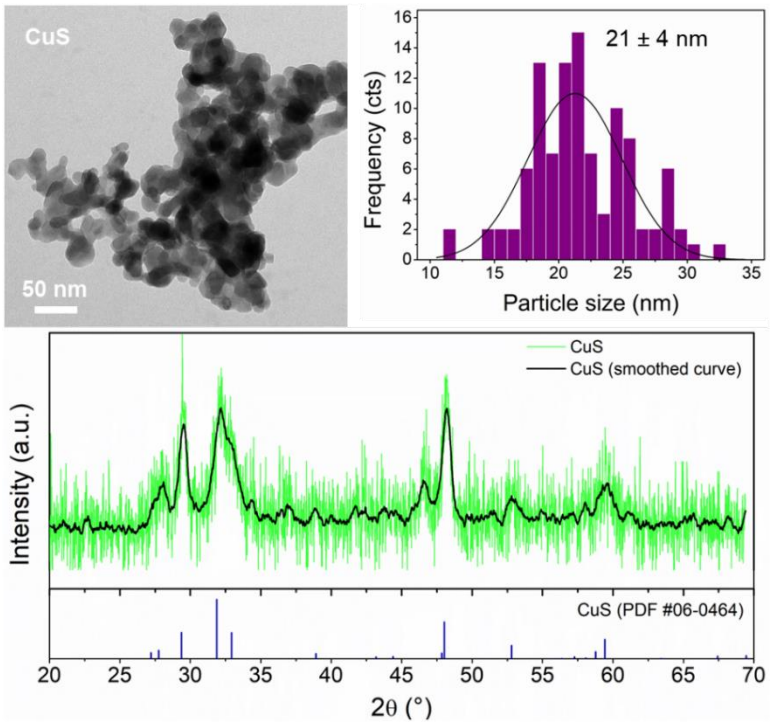

Figure G.1. (Clockwise, from top left) TEM image, particle size distribution, and XRD pattern of CuS (PDF card no. 06-0464). The recorded XRD pattern (green) was smoothed (black) using a Savitzky-Golay filter for clarity and stacked above the reference XRD pattern (blue).

G-2. Synthesis of CdS-A4

CdS nanocrystals were synthesized following a procedure reported in literature, with minor modifications.[2] Anhydrous cadmium chloride ($CdCl_2$, 0.22 mmol) and thiourea ($(NH_2)_2CS$, 1.26 mmol) were dissolved in 60 mL of ethanol under magnetic stirring at 160 °C. In parallel, sodium hydroxide (NaOH, 0.50 mmol) was dissolved in 20 mL of ethanol, and this solution was rapidly pipetted into the cadmium-containing solution. The mixture was refluxed at 160 °C for 10 hours. The resulting yellow precipitates were collected by filtration and washed multiple times with distilled water before being dried under vacuum at 60 °C for 4 hours. The product was characterized by TEM and XRD (Figure G.2).

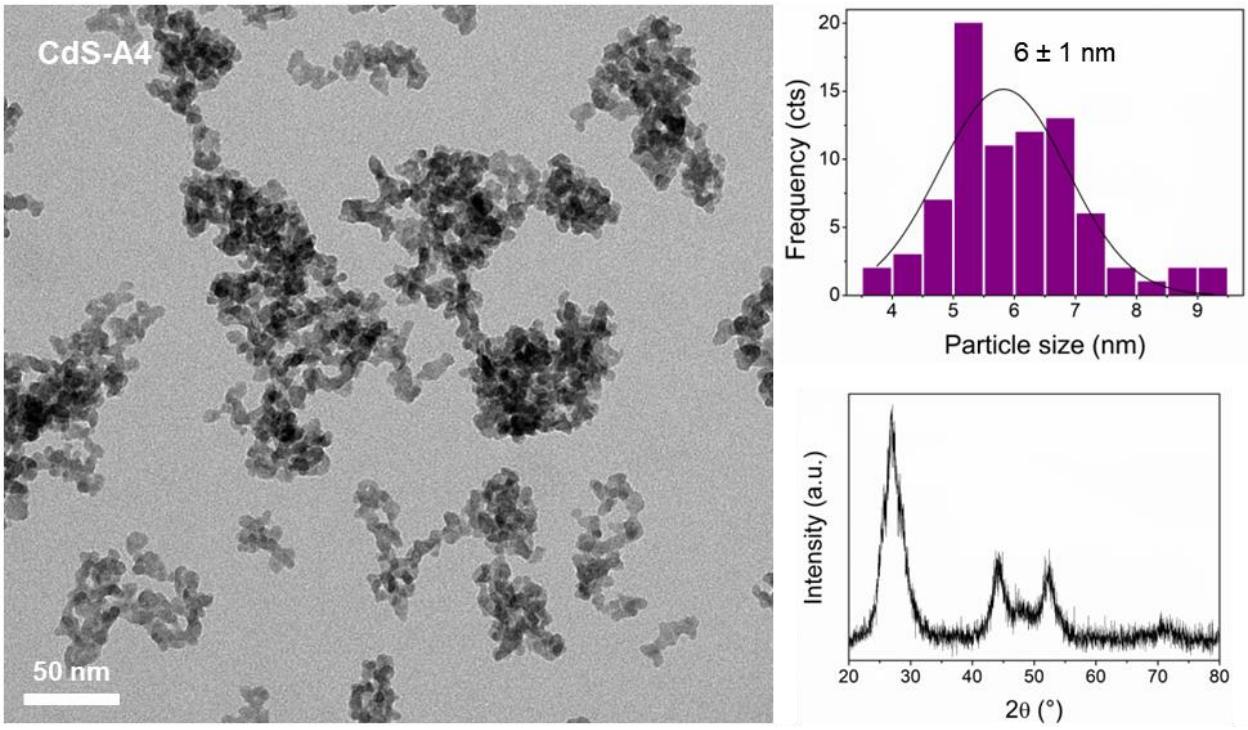

Figure G.2. (Clockwise, from left) TEM image, particle size distribution, and XRD pattern of CdS-A4.

G-3. References

(1) Wang, A.; Wang, W.; Chen, J.; Mao, R.; Pang, Y.; Li, Y.; Chen, W.; Chen, D.; Hao, D.; Ni, B. J.; Saunders, M.; Jia, G. Dominant Polar Surfaces of Colloidal II-VI Wurtzite Semiconductor Nanocrystals Enabled by Cation Exchange. *J. Phys. Chem. Lett.* **2020**, *11* (13), 4990–4997.

(2) Lee, H. L.; Issam, A. M.; Belmahi, M.; Assouar, M. B.; Rinnert, H.; Alnot, M. Synthesis and Characterizations of Bare Cds Nanocrystals Using Chemical Precipitation Method for Photoluminescence Application. *J. Nanomater.* **2009**, 2009.